ILMATIETEEN LAITOS
METEOROLOGISKA INSTITUTET
FINNISH METEOROLOGICAL INSTITUTE

181
CONTRIBUTIONS

WINDS AND WINDSTORMS IN NORTHERN EUROPE AND FINLAND

TERHI K. LAURILA

FINNISH METEOROLOGICAL INSTITUTE
CONTRIBUTIONS

No. 181

Winds and Windstorms in Northern Europe and Finland

Terhi K. Laurila

Institute for Atmospheric and Earth System Research
Faculty of Science
University of Helsinki
Helsinki, Finland

ACADEMIC DISSERTATION in meteorology

To be presented, with the permission of the Faculty of Science of the University of Helsinki, for public criticism in E204 auditorium at Physicum (Gustaf Hällströmin katu 2, Helsinki) on June 2nd, 2022 at 1 o'clock in the afternoon.

Finnish Meteorological Institute
Helsinki, 2022

Author
Terhi K. Laurila
Weather and Climate Change Impact Research
Finnish Meteorological Institute, Finland
terhi.laurila@fmi.fi

Supervisors
Docent Victoria A. Sinclair, Ph.D.
Institute for Atmospheric and Earth System Research
University of Helsinki, Finland

Research Professor Hilppa Gregow, Ph.D.
Weather and Climate Change Impact Research
Finnish Meteorological Institute, Finland

Pre-examiners
Senior Scientist Benjamin Harvey, Ph.D.
Department of Meteorology
University of Reading, United Kingdom

Senior Scientist Lukas Papritz, Ph.D.
Institute for Atmospheric and Climate Science
ETH Zurich, Switzerland

Custos
Docent Victoria A. Sinclair, Ph.D.
Institute for Atmospheric and Earth System Research
University of Helsinki, Finland

Opponent
Professor Joaquim Pinto, Ph.D.
Institute of Meteorology and Climate Research
Karlsruhe Institute of Technology, Germany

ISBN 978-952-336-155-3 (paperback)
ISBN 978-952-336-154-6 (pdf)
ISSN 0782-6117

Edita Prima Oy
Helsinki 2022

ILMATIETEEN LAITOS
METEOROLOGISKA INSTITUTET
FINNISH METEOROLOGICAL INSTITUTE

Published by	Series title, number and report code of publication
Finnish Meteorological Institute (Erik Palménin aukio 1), P.O. Box 503 FIN-00101 Helsinki, Finland	Finnish Meteorological Institute Contributions 181, FMI-CONT-181 Date: April 2022

Author	ORCID iD
Terhi K. Laurila	0000-0002-0903-7331

Title

Winds and Windstorms in Northern Europe and Finland

Abstract

Strong winds can cause large impacts and damage to society. Many sectors, such as wind energy, forestry and insurance, are highly affected by winds. Thus, preparedness and adaptation to winds and windstorms is essential in both weather (days) and climate (decades) time scales. The aim of this thesis is to better understand the near-surface mean and extreme wind climate in northern Europe and Finland and the role of extratropical cyclones in contributing to the extreme winds.

This thesis investigated the main characteristics of wind and windstorm climate in northern Europe and Finland over a 40-year period. The wind and windstorm climate was found to have large inter-annual and decadal variability and no significant linear trends. The well-known seasonal cycle was detected: winds in northern Europe are up to 30 % stronger in winter than in summer and while there are on average 5–6 windstorms per month in winter in northern Europe there are none in summer months. A more surprising result was that the number of all extratropical cyclones does not vary between seasons. Windstorms were found to be the most frequent over the Barents Sea whereas weaker extratropical cyclones occur over the land areas in northern Europe.

The development and structure of strong winds in windstorms in northern Europe and Finland were examined. The results show that the strongest wind gusts associated with windstorms shift and extend from the warm sector to behind the cold front during the evolution. The cold-season (Oct–Mar) windstorms are overall stronger and spatially larger than warm-season (Apr–Sep) windstorms. For example, the central pressure is on average 9 hPa deeper and the maximum wind gust 2 ms^{-1} stronger in cold-season windstorms than in warm-season windstorms. Analysing a case study of storm Mauri, a damaging windstorm in Finland in September 1982, shows that an individual windstorm development can vary largely from the climate's general concept. The case study also found that during storm Mauri the wind speeds over land areas in Finland are underestimated in the weather model by 2–13 ms^{-1} compared to observations, but the location of strong winds is correctly predicted.

Lastly, this thesis investigated what meteorological factors affect the intensity of windstorms in northern Europe. This was studied by using an ensemble sensitivity method. The sensitivities of windstorm intensity to all studied meteorological factors were 20–75 % higher in the cold season than in the warm season. This implies that cold-season windstorms are potentially better predictable than warm-season windstorms. The strongest impact to the intensity of northern Europe windstorms is from the low-level temperature gradient which is therefore an important variable to follow when forecasting windstorms.

The results from this thesis highlight the importance of examining long-term inter-annual variations, instead of just linear trends, to get a broader understanding of the climate. Moreover, the results emphasize the need of both general conceptual models and individual case studies to better understand the large variety of windstorm development paths.

Publishing unit

Weather and Climate Change Impact Research / Finnish Meteorological Institute

Classification (UDC)	Keywords
551.515.1, 551.55, 551.58	wind, windstorm, extratropical cyclone, climate, trend, weather, reanalysis
ISSN and series title	ISBN
0782-6117 Finnish Meteorological Institute Contributions	978-952-336-155-3 (paperback) 978-952-336-154-6 (pdf)
DOI	Language / Pages
https://doi.org/10.35614/isbn.9789523361546	English / 57

ILMATIETEEN LAITOS
METEOROLOGISKA INSTITUTET
FINNISH METEOROLOGICAL INSTITUTE

Julkaisija	Julkaisun sarja, numero ja raporttikoodi
Ilmatieteen laitos (Erik Palménin aukio 1) PL 503, 00101 Helsinki	Finnish Meteorological Institute Contributions 181, FMI-CONT-181 Päiväys: Huhtikuu 2022

Tekijä	ORCID iD
Terhi K. Laurila	0000-0002-0903-7331

Nimeke

Pohjois-Euroopan ja Suomen tuulisuus ja myrskyt

Tiivistelmä

Voimakkaat tuulet voivat aiheuttaa vaikutuksia ja tuhoja yhteiskunnalle. Tuulisuus vaikuttaa moniin aloihin, kuten tuulienergia-, metsä- ja vakuutussektoreihin. Varautuminen ja sopeutuminen tuuliin ja myrskyihin ovat näin ollen tärkeitä sekä sään (päiviä) että ilmaston (vuosikymmeniä) aikaskaaloissa. Tämän väitöskirjan tavoitteena on ymmärtää paremmin maanpinnan läheisten keski- ja äärituulten ilmastoa Pohjois-Euroopassa ja Suomessa sekä keskileveysasteiden matalapaineiden roolia äärituulten aiheuttajana.

Tässä väitöskirjassa tutkittiin Pohjois-Euroopan ja Suomen tuuli- ja myrskyilmaston tyypillisiä piirteitä 40 vuoden jaksolta. Tuuli- ja myrskyilmastolle havaittiin tyypilliseksi suuri vuosien ja vuosikymmenien välinen vaihtelu ilman merkitseviä pitkänajan trendejä. Tutkimuksessa osoitettiin tiedetty kausivaihtelu: tuulet ovat Pohjois-Euroopassa jopa 30 % voimakkaampia talvella kuin kesällä, ja talvikuukausina Pohjois-Euroopassa esiintyy keskimäärin 5–6 myrskyä kuukaudessa kun taas kesäkuukausina ei yhtään. Yllättävämpi tulos oli, että kaikkien matalapaineiden määrässä ei löydetty kausittaista vaihtelua. Myrskyjä havaittiin esiintyvän eniten Barentsin meren yllä kun taas heikommat matalapaineet esiintyvät Pohjois-Euroopan maa-alueilla.

Työssä tutkittiin Pohjois-Euroopan myrskyihin liittyvien voimakkaiden tuulten kehittymistä ja rakennetta. Tulokset osoittavat, että voimakkaimmat myrskyihin liittyvät puuskat siirtyvät ja leviävät lämpimästä sektorista kylmän rintaman taakse myrskyn kehittymisen aikana. Kylmän vuodenajan (loka–maaliskuu) myrskyt ovat yleisesti voimakkaampia ja alueellisesti laajempia kuin lämpimän vuodenajan (huhti–syyskuu) myrskyt. Esimerkiksi myrskyn minimipaine on keskimäärin 9 hPa matalampi ja maksimipuuska 2 ms^{-1} voimakkaampi kylmänä kuin lämpimänä vuodenaikana. Tapaustutkimus Mauri-myrskystä, tuhoisasta myrskystä Suomessa 22.9.1982, osoittaa, että yksittäisen myrskyn kehitys voi poiketa suuresti ilmaston yleisestä kehitysmallista. Tapaustutkimuksessa selvisi myös, että säämalli aliarvioi Suomen maa-alueilla Mauri-myrskyn tuulennopeuksia 2–13 ms^{-1} havaintoihin verrattuna, mutta voimakkaiden tuulten sijainnit on ennustettu oikein.

Viimeisimpänä väitöskirjassa tutkittiin mitkä meteorologiset tekijät vaikuttavat myrskyn voimakkuuteen Pohjois-Euroopassa. Tätä tutkittiin käyttämällä nk. parviherkkyysmenetelmää. Myrskyn voimakkuuden herkkyydet kaikkiin tutkittuihin meteorologisiin tekijöihin olivat 20–75 % korkeampia kylmänä kuin lämpimänä vuodenaikana. Tämä viittaa siihen, että kylmän vuodenajan myrskyt ovat potentiaalisesti paremmin ennustettavissa kuin lämpimän vuodenajan myrskyt. Pohjois-Euroopan myrskyjen voimakkuuteen vaikuttaa eniten alailmakehän vaakasuuntainen lämpötilaero, joka täten on tärkeä seurattava muuttuja myrskyjä ennustettaessa.

Tämän väitöskirjan tulokset korostavat tärkeyttä tarkastella pitkänajan vuosien välistä vaihtelua pelkkien lineaaristen trendien sijaan, jotta ilmastoa ymmärrettäisiin laajemmin. Lisäksi tulokset korostavat tarvetta sekä yleisille käsitemalleille että yksitäisille tapaustutkimuksille, jotta myrskyjen moninaisia kehityspolkuja ymmärrettäisiin paremmin.

Julkaisijayksikkö

Sään ja ilmastonmuutoksen vaikutustutkimus / Ilmatieteen laitos

Luokitus (UDK)	Asiasanat
551.515.1, 551.55, 551.58	tuuli, myrsky, keskileveysasteiden matalapaine, ilmasto, trendi, sää, uusanalyysi

ISSN ja avainnimeke	ISBN
0782-6117 Finnish Meteorological Institute Contributions	978-952-336-155-3 (paperback) 978-952-336-154-6 (pdf)

DOI	Kieli	Sivumäärä
https://doi.org/10.35614/isbn.9789523361546	Englanti	57

PREFACE

I would like to first thank my supervisors Doc. Victoria Sinclair and Research Prof. Hilppa Gregow. Victoria, you have always found time to help and your deep knowledge on both the atmospheric science and technical matters has given me the best possible basis to carry out my work. I am very grateful for your support even, and especially, on those times when I have been struggling. Hilppa, your advice and broad view of the thesis topic has given inspiration and new perspectives to do this research. I am thankful of your encouragement and enthusiasm for my work and helping me grow as a scientist. I wish to thank my co-author Joona Cornér for your contribution. I thank Prof. Heikki Järvinen for acting as my responsible professor during my whole PhD and taking care of many practicalities of the defence. I am grateful to Prof. Joaquim Pinto for serving as my opponent and Dr. Benjamin Harvey and Dr. Lukas Papritz for pre-examining this thesis.

I thank Satakunta Region Fund from the Finnish Cultural Fund for a one-year personal grant for my thesis. This financial support allowed me to concentrate on my thesis and it greatly helped me to get the work forward. This work has additionally been supported by several projects and funding agencies: Academy of Finland (CLIPS project and Flagship Programme), SAFIR2018 Programme (EXWE project), ERA4CS Consortium (WINDSURFER project) and MONITUHO project.

This research was conducted in Weather and Climate Change Impact Research unit in Finnish Meteorological Institute. I thank Antti Mäkelä who took me to his group in 2015 and has been supporting this journey ever since. I also thank Anna Luomaranta, my new group leader, for the flexibility and help while I was finishing my PhD. I thank all my co-workers for the morning coffee breaks, badminton games, chin-up sessions and all the fun moments that have given joy to the workdays and have been much needed during this process. The peer-support from my fellow PhD students has been priceless and our booth at Dynamicum has always being a safe place to share experiences, cries and laughs.

Finally, I want to thank my friends and family for the endless encouragement during this process. You have never stopped believing in me, even when I had my doubts, and by now I have already a collection of hundred ways to use the sword and hat which you were sure I will get one day. Lastly, I want to give my most heartfelt thanks to Minttu, Jutta and Ilona: thank you for always being there beside me, I truly don't know what I would have done without you.

Terhi Laurila
Helsinki, April 2022

CONTENTS

List of original publications

I **Laurila, T. K.**, Sinclair, V. A. and Gregow, H. (2021a). Climatology, variability, and trends in near-surface wind speeds over the North Atlantic and Europe during 1979–2018 based on ERA5. *International Journal of Climatology*, **41**:(4), 2253–2278, doi:10.1002/joc.6957

II **Laurila, T. K.**, Gregow, H., Cornér, J. and Sinclair, V. A. (2021b). Characteristics of extratropical cyclones and precursors to windstorms in northern Europe. *Weather and Climate Dynamics*, **2**:(4), 1111–1130, doi:10.5194/wcd-2-1111-2021

III **Laurila, T. K.**, Sinclair, V. A. and Gregow, H. (2020). The Extratropical transition of hurricane Debby (1982) and the subsequent development of an intense windstorm over Finland. *Monthly Weather Review*, **148**:(1), 377–401, doi:10.1175/MWR-D-19-0035.1

1. Introduction

Strong winds can cause a large amount of damage and high impacts to society (e.g. Wernli et al., 2002; Suursaar et al., 2006; Gregow et al., 2017; Holley, 2021; Tervo et al., 2021), such as power outages, forest damage and destruction to property. Extratropical cyclones – also called mid-latitude cyclones or low-pressure systems – that cause strong winds (i.e. windstorms) are the main cause of insured losses in Europe (Munich Re, 2017). Winds play an essential part in for example wind energy, forestry and insurance sectors. Therefore, it is crucial to prepare and adapt to winds and windstorms in both weather and climate time scales. Weather scale refers to a time scale from one day to around one week whereas climate scale indicates a period of multiple decades. In this thesis, climate scale refers to past 40-year climate and hence to climatology.

In addition to regulating our everyday weather, winds and extratropical cyclones have an important role in the atmosphere. They transport moisture, heat and momentum from lower latitudes towards poles and between the surface and the atmosphere. Extratropical cyclones occur in the mid-latitudes and they are driven by the meridional temperature difference between tropics and poles. The size of extratropical cyclones ranges from hundreds to thousands of kilometres and they typically have an asymmetrical structure with fronts (Fig. 1). Since the meridional temperature difference between tropics and poles is the greatest during winter the strongest extratropical cyclones in the Northern Hemisphere occur typically in winter time (e.g. Hoskins and Hodges, 2019). In this thesis windstorms are considered as strong extratropical cyclones that are large in scale and they should not be mixed with small-scale local thunderstorms.

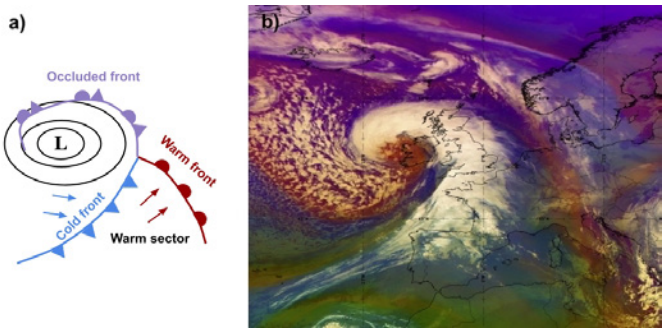

Figure 1. *a) A schematic figure of a typical frontal structure of an extratropical cyclone, L denotes the low-pressure centre and arrows the wind directions. Figure by Terhi Laurila. b) A satellite image of an extratropical cyclone: storm Barra on 7 December 2021 09 UTC. © EUMETSAT.*

In the Northern Hemisphere, the main storm track regions i.e. areas with high extratropical cyclone activity occur in the North Atlantic and the North Pacific and the secondary storm track regions occur in the Mediterranean and Siberia (e.g. Hoskins and Hodges, 2002; Priestley et al., 2020). The North Atlantic storm track region extends from the Rocky Mountains in North America to northern Europe. While extratropical cyclones in the main North Atlantic and North Pacific storm track regions have been extensively studied (e.g. Hoskins and Hodges, 2002; Ulbrich et al., 2009; Hodges et al., 2011; Priestley et al., 2020) those located at the end of the storm track regions have received less attention. Hence, this thesis intends to bring more knowledge to the extratropical cyclone research regarding this less studied region in northern Europe.

Northern Europe in this thesis is defined to include Norway, Sweden, Finland, Estonia, Latvia and parts of the Norwegian, Barents and Baltic seas (Fig. 2). This region contains a mix of sea areas and different topographical features with Scandinavian Mountains dominating the western land areas in Norway and Sweden. In Finland, over 75 % of land is covered with forests making it the most forested country in Europe. Regarding windiness, although northern Europe is located at the end of the North Atlantic storm track this region also experiences damaging windstorms. Some examples are storm Anatol in 1999 (Ulbrich et al., 2001), storm Dagmar, also know as storm Tapani, in 2011 (Kufeoglu and Lehtonen, 2014) and storm Aila in 2020 (Rantanen et al., 2021).

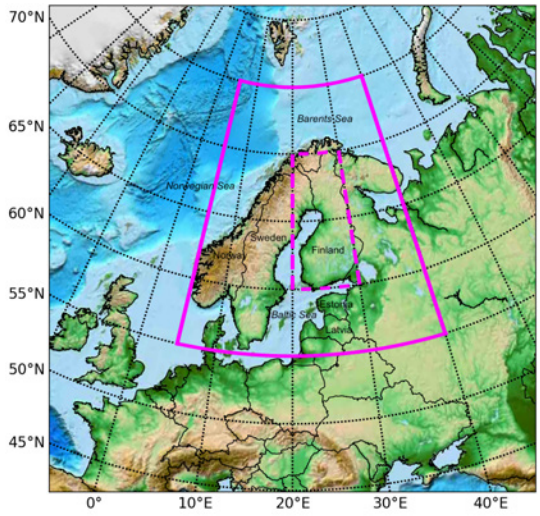

Figure 2. *Topography map and the boxes of northern Europe (solid) and Finland (dashed) used in this thesis.*

Since winds and extratropical cyclones have an important role on our weather and climate system, a better understanding of the phenomena is gained when both time scales are considered. The climate scale can show a general view of the occurrence and variability of winds and windstorms. However, to understand the structure and evolution of the phenomenon it must be investigated on a short-term weather scale. Since the cases can vary largely between each other, it is important to also investigate individual windstorm cases.

Aims of this thesis

The general aim of this thesis is to increase the understanding of the near-surface mean and extreme wind climate and the role of extratropical cyclones in contributing to the extreme winds. This thesis focuses on northern Europe and partly specifically on Finland and considers both weather and climate time scales. This general aim is addressed through the following three research questions:

1. **What are the main characteristics of wind and windstorm climate in northern Europe and Finland and can we detect any long-term trends? (Papers I and II)**
   For these aims, the climatology, variability and trends of near-surface wind speeds, extratropical cyclones and windstorms are investigated by using reanalysis data over 40 years. To determine possible seasonal variations, the wind speed climate is examined on a monthly scale and extratropical cyclones and windstorms separately for the cold and warm seasons.

2. **How does the spatial structure of windstorms in northern Europe and Finland change during the evolution? (Papers II and III)**
   This aim is addressed in a climatological perspective by examining the general spatio-temporal structure of windstorms in northern Europe. Additionally, this aim is determined in a case study perspective by analysing the development of a windstorm event in Finland with numerical weather prediction model simulations.

3. **What meteorological factors affect the intensity of windstorms in northern Europe and Finland? (Papers II and III)**
   This final aim is investigated by analysing the sensitivity of windstorm intensity to different meteorological factors. As a measure of intensity, both the minimum mean sea level pressure and the maximum 10-m wind gust are considered. In addition, this aim can be assessed from the case study by comparing the different numerical weather prediction model simulations.

2. Background

2.1. Atmospheric circulation and jet stream in the mid-latitudes

Winds are a result from an uneven heating from the sun to different parts of the Earth. The equator gets more solar energy than poles and winds exist to balance this difference. In the mid-latitudes in the Northern Hemisphere (approximately 30–60°N), atmospheric circulation is seen as the Ferrel cell where air sinks at the lower latitudes around 30°N and rises at the higher latitudes around 60°N. This produces surface winds that would flow from south to north but due to the Coriolis effect the winds are deflected to the right. This results in the westerlies: the planetary winds in the mid-latitudes that blow from west/south-west to east (Fig. 3a). The other circulation cells produce trade winds at the lower latitudes and easterlies at the higher latitudes that flow from an easterly direction (Fig. 3a).

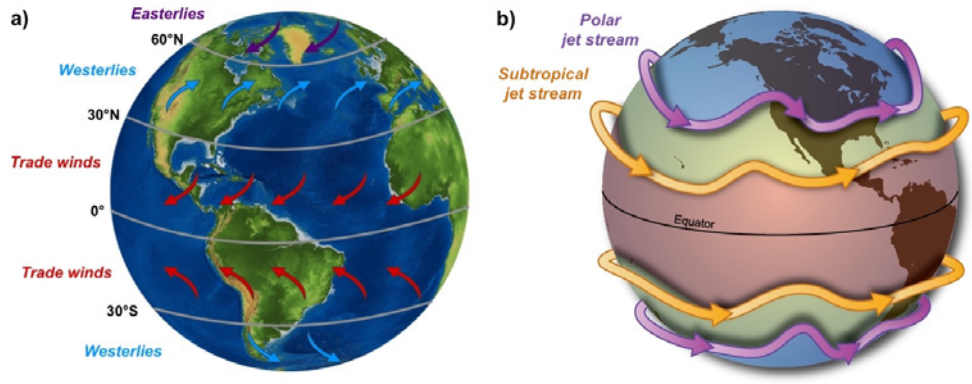

Figure 3. *a) A schematic figure of planetary winds. Figure by Terhi Laurila. b) A schematic figure of jet streams. Figure adopted from National Weather Service / NOAA.*

Jet streams are narrow and meandering ribbons of strong winds near the tropopause (around 8–16 km altitude) that move from west to east following the direction of the Earth rotation. The main jet streams locate between the circulation cells: the subtropical jet stream at lower latitudes around 30°N and the polar jet stream in the mid-latitudes at around 60°N (Fig. 3b). These main jet streams are results from different physical mechanisms. The subtropical jet stream is driven by the angular momentum transport that accelerates the poleward moving air at upper levels and the transport is caused by the thermally direct circulation cell (Held and Hou, 1980). The polar jet stream, also called as the

eddy-driven jet stream, is driven by the convergence of momentum flux from transient atmospheric disturbances i.e. eddies (Held, 1975). The eddies occur in the mid-latitudes in regions with strong meridional temperature gradient called baroclinic regions. The baroclinic zone separates the cold polar air from the warm tropical air. The baroclinic zone is a region where extratropical cyclones develop and occur and thus, the polar jet stream (hereinafter referred to as the jet stream) is closely linked to extratropical cyclones.

2.2. Extratropical cyclones

Extratropical cyclones can form through cyclogenesis or extratropical transition. The latter, and much rarer, evolution path is described in the following Section 2.2.1. Cyclogenesis means the formation and development of an extratropical cyclone, and the main ingredient for cyclogenesis is baroclinic instability or baroclinicity (Charney, 1947; Eady, 1949). Baroclinicity is associated with a large meridional temperature gradient in the mid-latitudes where small disturbances can grow in the mean flow. In this process, atmospheric available potential energy is converted into kinetic energy (Lorenz, 1955). These growing disturbances develop into extratropical cyclones.

While cyclogenesis is driven by the baroclinicity there are other ingredients that can affect the development and strength of extratropical cyclones: upper-level forcing and diabatic heating. At upper-levels, the jet stream has a large role where the surface cyclone tends to develop. The right entrance and left exit regions in the jet stream are associated with upper-level divergence which causes ascending air. Thus, they are favourable regions for the surface cyclone to intensify. The meandering jet stream creates troughs where the jet stream curves equatorward and ridges where the jet stream curves poleward. A trough is associated with low-pressure areas and a cyclonic / positive potential vorticity (PV) anomaly. In contrast, a ridge is associated with high-pressure areas and an anticyclonic / negative PV anomaly. Upper-level divergence occurs downstream of an upper-level trough due to positive vorticity advection. This means that the development of a surface cyclone enhances and intensifies when it is located downstream of an upper-level trough i.e. the surface cyclone and the upper-level trough are tilted westward with height.

While the baroclinic process is essential for extratropical cyclone development diabatic processes can significantly intensify the cyclone (e.g. Ahmadi-Givi et al., 2004; Grams et al., 2011; Martínez-Alvarado et al., 2016). In a diabatic process an air parcel exchanges heat with the environment; in extratropical cyclones, this

is most importantly seen as latent heat release which occurs when water vapour condenses to liquid water in cloud formation. A concept of PV framework was developed by Hoskins et al. (1985) and it is useful in examining the role of diabatic heating in extratropical cyclones. PV is conserved in an adiabatic and baroclinic flow and therefore any changes in PV are due to diabatic processes. Latent heat release produces a positive PV anomaly in the lower troposphere which enhances the cyclonic circulation (Hoskins et al., 1985). Moreover, latent heat release can produce a negative PV anomaly i.e. reduce the PV in the upper troposphere which can enhance the upper-level ridge downstream of the surface cyclone. Therefore, a higher moisture content increases the latent heat release and leads to more intense extratropical cyclones.

There are two commonly known conceptual models on the structure and development of extratropical cyclones: the Norwegian cyclone model (Bjerknes, 1919; Bjerknes and Solberg, 1922) and the Shapiro-Keyser cyclone model (Shapiro and Keyser, 1990). They describe how a disturbance in a baroclinic zone, or a frontal wave, develops and forms cold and warm fronts. In the Norwegian cyclone model, a cold front moves faster than a warm front and eventually the cold front catches the warm front and by merging they form an occluded front. In the Shapiro-Keyser cyclone model, a cold front is situated nearly perpendicular compared to a warm front creating a so-called T-bone structure. A bent-back front develops when the warm front extends westward behind the low-pressure centre and finally by wrapping around the centre it forms a warm seclusion. Based on Schultz et al. (1998), extratropical cyclones at the end of the North Atlantic storm track are more similar to the Norwegian cyclone model.

2.2.1. Extratropical transition

Extratropical transition is a process where a tropical cyclone travels to mid-latitudes, is affected by the changes in the environment (e.g. increasing baroclinicity, increasing Coriolis effect and colder waters) and transforms into an extratropical cyclone (Palmén, 1958; Hart and Evans, 2001; Jones et al., 2003). Almost half of tropical cyclones in the Atlantic undergo extratropical transition (Hart and Evans, 2001). Transitioned cyclones can cause high-impact and damaging weather on the east coast of North America and Canada (e.g. Palmén, 1958; Ma et al., 2003; Galarneau et al., 2013) but also in Europe. Some examples are hurricane Iris in 1995 that reached north-western Europe (Thorncroft and Jones, 2000), hurricane Lili in 1996 that caused impacts to the United Kingdom (Browning et al., 1998; Agustí-Panareda et al., 2005) and more recently hurricane Ophelia in 2017 that damaged Ireland and the United Kingdom

and lead to three fatalities (Stewart, 2018; Rantanen et al., 2020). However, in northern Europe only less than 1 % of all extratropical cyclones are transitioned cyclones (Sainsbury et al., 2020). When considering those extratropical cyclones in northern Europe which have storm force winds (> 25 m s^{-1}) the proportion of transitioned cyclones becomes significantly larger, approximately 9 % (Sainsbury et al., 2020). In Finland, the only known damaging windstorm which has been thought to be a transitioned cyclone is storm Mauri from September 1982.

During the extratropical transition process, a tropical cyclone loses its symmetrical, eye-shaped structure and turns asymmetrical with a frontal structure commonly seen in extratropical cyclones (Klein et al., 2000; Evans et al., 2017). Tropical cyclones are warm-core cyclones which means that the temperature near the surface cyclone centre is warmer than the surroundings and that the winds are the strongest close to the surface and decrease with height. In contrast, extratropical cyclones are typically cold-core cyclones which indicates a lower temperature near the cyclone centre and winds increasing with height. By analysing these structural changes, Hart (2003) and Evans and Hart (2003) developed a cyclone phase space diagram and defined that the extratropical transition starts when a cyclone changes from symmetrical to asymmetrical and the transition is complete when a warm-core cyclone changes to a cold-core cyclone.

There are multiple ways a transitioned cyclone can affect the mid-latitudes. The most direct way is that the cyclone interacts with a pre-existing upper-level trough and re-intensifies as an extratropical cyclone (Evans et al., 2017). A transitioning cyclone can also impact the mid-latitudes, even before the extratropical transition is complete, by modifying the downstream flow (Keller et al., 2019). This is usually seen as ridge building, trough amplification and jet streak modification immediately downstream of the transitioning cyclone (Keller et al., 2019). The downstream modification of transitioning cyclones have been found in climatological studies (Archambault et al., 2013), idealised experiments (Riemer et al., 2008) and in case studies (Agustí-Panareda et al., 2004; Grams et al., 2013). Moreover, a transitioned cyclone can impact mid-latitudes even farther downstream by modifying the upper-tropospheric flow and eventually leading to a formation of new cyclones and possible high-impact weather (Riemer et al., 2008; Archambault et al., 2013). More unusually, a transitioned cyclone can travel to mid-latitudes as a diabatic Rossby wave. A diabatic Rossby wave is a low-level PV anomaly in a moist and baroclinic environment (e.g. Moore and Montgomery, 2004, 2005). It can maintain itself due to constant production of diabatic PV downstream of the original location of the low-level PV anomaly (Moore and Montgomery, 2004, 2005). This way a diabatic Rossby wave, which can be a transitioned cyclone, do not need upper-level forcing to re-develop.

2.2.2. Detecting extratropical cyclones

Extratropical cyclones are commonly detected using the Eulerian approach or the Lagrangian approach (Hoskins and Hodges, 2002). The Eulerian approach is based on basic statistics that are applied to a meteorological field that describes the occurrence and location of a cyclone, usually mean sea level pressure (MSLP) or 850-hPa relative vorticity (Blackmon, 1976). Eulerian methods are applied to spatially fixed grids and therefore they are suitable to use in gridded datasets. The Eulerian approach is easy to calculate and it gives general information about the cyclone activity. However, it does not provide any details about individual cyclones.

The Lagrangian approach identifies individual cyclones by finding a localised minimum or maximum of a meteorological field (usually MSLP or 850-hPa relative vorticity) and tracking its location through time (e.g. Murray and Simmonds, 1991; Hodges, 1995; Wernli and Schwierz, 2006). The Lagrangian approach enables us to investigate each cyclone and its properties separately and to provide cyclone-specific analysis. The results may depend on the chosen tracking algorithm. For example, the resulting tracks can differ depending on which variable a cyclone location is identified from: a MSLP-based tracking often identifies large-scale extratropical cyclones while tracking based on the 850-hPa relative vorticity captures additionally smaller-scale phenomena (Neu et al., 2013). Furthermore, the minimum MSLP and the maximum 850-hPa relative vorticity are not co-located and thus the estimated location of the cyclone centre may differ.

2.3. Use of reanalysis data in climate studies

Reanalysis is a gridded dataset that combines atmospheric observations and a numerical weather prediction model. It provides the best estimate of the atmospheric state of the past weather and climate. Therefore, reanalysis is a relevant and commonly used source for climate studies and assessments.

There are multiple benefits in using reanalysis data. Reanalysis has a gridded and often global coverage and therefore we can examine large regions anywhere in the globe and are not restricted to locations with in-situ observations. The data in reanalysis is homogeneous in time; for example in wind studies, this is a major advantage in comparison to wind observations which are affected by, for example, the changes in the station location, instrument height and observation environment. Reanalysis datasets cover long time periods, usually

multiple decades, and thus are very valuable in studying long-term, climatological variations and trends. When producing the reanalysis the same numerical weather prediction model version is used for the historical and present data. This enables an independence from the model development through time and hence the increasing skill of the numerical weather model does not affect the reanalysis.

While there are apparent advantages in the use of reanalysis a disadvantage is the coarse spatial and temporal resolution. Because of that, some smaller-scale phenomena may not be accurately or at all captured. Likewise, the most extreme values may not be obtained since the values are smoothed over a relatively large grid size (for example 80 km in ERA-Interim reanalysis and 30 km in ERA5 reanalysis). However, there has been great improvement in the temporal resolution: while the analysis fields in ERA-Interim are output every 6 hours in ERA5 they are produced every hour.

3. Data and models

Large-scale features, such as extratropical cyclones studied in this thesis, are usually well identified in reanalysis. Since extratropical cyclones can be thousands of kilometers wide and travel across countries and oceans, reanalysis is able to cover the whole life-cycle. However, as discussed in Section 2.3, smaller meso-scale sized extratropical cyclones may not be well captured. Therefore, simulations from a higher resolution numerical weather prediction model can be useful to detect more details. However, the intensity of extratropical cyclones has been found to be underestimated in most of the ensemble prediction systems (Froude, 2010). Hence, it is additionally valuable to compare the modelled fields of e.g. wind speed to available observations.

3.1. Reanalysis data

In this thesis, global atmospheric reanalyses are used that are produced by the European Centre for Medium Range Weather Forecasts (ECMWF). In **Papers I** and **II**, the fifth and newest generation reanalysis called ERA5 is used. ERA5 replaced the previous reanalysis called ERA-Interim. The synoptic overview in **Paper III** is analysed with ERA-Interim since ERA5 was not yet available when conducting the study.

ERA-Interim (Dee et al., 2011) and ERA5 (Hersbach et al., 2020) are based on the Integrated Forecasting System (IFS), ERA-Interim with Cycle 31r2 and ERA5 with Cycle 41r2. Both reanalyses use a four-dimensional variational (4D-Var) data assimilation system. In ERA-Interim, the horizontal resolution is approximately 80 km and vertically there are 60 levels up to 0.1 hPa. The analysis fields are available 6 hourly and forecast fields 3 hourly. The spatial and temporal resolutions are higher in ERA5 than in ERA-Interim. In ERA5, the horizontal resolution is approximately 30 km, there are 137 vertical levels up to 0.01 hPa and the analysis and forecast fields are available hourly. When performing the studies in this thesis, both reanalyses covered a period from 1979 onwards. Later, ERA5 has been extended to cover also a period from 1950–1978.

For **Papers I**, **II** and **III**, range of variables were obtained from the reanalyses both on pressure levels and on a single, "surface" level. All obtained variables are instantaneous except the maximum 10-m wind gust which is a maximum since the previous post-processing. The computation of 10-m wind speeds and 10-m wind gusts in IFS are briefly explained in Section 3.2.1.

3.2. OpenIFS model

In **Paper III**, numerical simulations were performed with the OpenIFS model which is developed by ECMWF. The IFS is a global numerical weather prediction model and it produces the operational weather forecasts by ECMWF. OpenIFS (Szépszó and Carver, 2018; Szépszó et al., 2019) is a version of IFS which is available to research institutions. OpenIFS includes the same dynamics, physical parametrizations, land surface model and wave model as the full IFS but it does not include the data assimilation system nor ocean model. In **Paper III**, Cycle 40r1v1 version of OpenIFS was used and the simulations were initialised from ERA-Interim. The simulations were run with a horizontal resolution of 16 km and vertically with 137 levels. The simulations were conducted with a 10-min time step and the model fields were output hourly.

To investigate the meso- and synoptic-scale dynamic evolution of ex-Debby and storm Mauri in **Paper III**, three simulations were performed with different initialization dates: 00 UTC 17 September 1982, 00 UTC 19 September 1982 and 00 UTC 21 September 1982. In the 17 and 19 September simulations, after two days the errors develop and large differences appear compared to ERA-Interim. Therefore, simulations that are initialised at different dates were used to analyse different phases of the evolution of ex-Debby and storm Mauri.

3.2.1. Computation of 10-m winds in IFS

In IFS, and therefore also in OpenIFS, the 10-m wind speeds and 10-m wind gusts are parameterized. Parameterization in numerical weather prediction models means that variables that are too small in scale to be resolved directly with dynamical equations are modelled with simplified equations. The 10-m wind speed in IFS is created to be comparable to wind speed observations from SYNOP stations. As required by the World Meteorological Organization (WMO), SYNOP stations are usually in open terrain and hence well exposed to wind. Therefore, the wind speeds in SYNOP observations may not represent the winds for a large area, e.g. a grid box in a model. Inside a model grid box, the terrain can vary largely and the wind observations are affected by the local features such as forest, vegetation and buildings that cause higher roughness than open terrain. For that reason, IFS contains an exposure correction which is applied to grid boxes with a high roughness length in order to fix the modelled wind speeds to be comparable to SYNOP observations. Therefore, the wind speeds at some locations can be higher in IFS than in reality but in general the modelled wind speeds should be well compatible with observations.

The 10-m wind gust in IFS is, similarly to the 10-m wind speed, designed to correspond to the definition by WMO. The 10-m wind gust (WG_{10}) in IFS is calculated by summing up three components:

$$WG_{10} = WS_{10} + C_{ugn}u_{*} + C_{conv}max(0, WS_{850} - WS_{950}) \quad (1)$$

where WS_{10} is the 10-m wind speed, C_{ugn} is an empirically derived parameter with a value of 7.71, u_{*} is the friction velocity, C_{conv} is the convective mixing parameter with a value of 0.6, and WS_{850} and WS_{950} are the wind speeds at 850-hPa and 950-hPa respectively (ECMWF, 2015). The second component in Eq. 1 describes the turbulent-driven wind gusts which contains the impact from surface roughness, and hence surface friction, and boundary layer stability. The third component in Eq. 1 describes the wind gusts caused by the convective downdrafts which can occur when higher momentum air is transported downward in convective situations. Thus, the 10-m wind gusts are elevated from the 10-m wind speeds by turbulent and convective factors.

3.3. Observations

In **Paper III**, the wind speed observations from Finnish Meteorological Institute (FMI) were obtained from 22 September 1982 when storm Mauri occurred over Finland. Observations of 10-m wind speeds were available from 130 automated and manual weather stations but wind gust observations were not made at that time. The wind speed observations in 1982 are 10-min average SYNOP observations that were made every 3 h or 6 h. Hence, it is likely that the strongest wind speeds during storm Mauri are not included in the FMI's observations due to the limited temporal and spatial coverage.

4. METHODS

4.1. CLIMATOLOGICAL DIAGNOSTICS

In this thesis, the climatology is analysed over a 40-year period; years from 1979–2018 in the wind speed study (**Paper I**) and years from 1980–2019 in the extratropical cyclone and windstorm study (**Paper II**). In **Paper I**, the wind speed climate is analysed for each month and in **Paper II**, extratropical cyclones and windstorms are investigated separately for the cold season (October–March) and the warm season (April–September). Hence, the seasonal variations and differences can be determined. Both the mean and extreme climate are investigated: for the wind speeds, the extreme is examined with the 98th percentile wind speed at each grid point. Furthermore, the climatological extremeness of the winds is studied by defining an extreme wind factor (EWF, the 98th percentile divided by the mean). The EWF measures how extreme the extreme winds are in relation to the mean winds. The mean and extreme extratropical cyclone climatology was created by tracking all the cyclones in northern Europe and classifying them all as either a windstorm or a non-windstorm (see Section 4.3 for more details). Furthermore, a group "all extratropical cyclones", which includes all identified extratropical cyclones, is defined and analysed. In **Paper I**, in addition to analysing statistical values over the whole 40-year period, the decadal variability is investigated by dividing the period to four 10-year periods. These periods are 1979–1988, 1989–1998, 1999–2008 and 2009–2018 but they are referred to as 1980s, 1990s, 2000s and 2010s for clarity.

The linear trends in 10-m wind speeds and the number of extratropical cyclones presented in **Papers I** and **II** were analysed by using the Mann-Kendall test (Mann, 1945; Kendall, 1970) which tests whether the trend is statistically significant. The trends are tested at a 5 % (p-value <0.05) significance level. The wind speed time series in Finland (20–30°E, 60–70°N, Fig. 2) were created by calculating the mean and the 98th percentile wind speeds at each grid point inside the box and then averaging the values over the box. The linear trends in the numbers of extratropical cyclones and windstorms are calculated for a box over northern Europe (55–75°N, 5–40°E, Fig. 2). The selection of cyclones and a threshold for a windstorm are explained in Section 4.3.

4.2. EXTRATROPICAL CYCLONE IDENTIFICATION

In **Paper I**, storm tracks were identified by using the Eulerian approach to get a general overview of the extratropical cyclone activity. First, the 6-hourly

MSLP from ERA5 was detrended in order to remove an underlying trend by subtracting the trend from the data. Then, a 2–6 day bandpass filter was applied to the detrended MSLP data. Then, the bandpass-filtered MSLP was used to calculate the monthly standard deviations. This standard deviation of the 2–6 day bandpass-filtered MSLP shows the main paths where the extratropical cyclones travel i.e. the storm track regions.

In **Paper II**, storm tracks were identified by using the Lagrangian approach to obtain information about individual extratropical cyclones and cyclone-specific characteristics such as the track density and minimum MSLP. The cyclones were tracked with the TRACK algorithm (Hodges, 1994, 1995, 1999) by using 3-hourly MSLP field from ERA5. Before tracking, the MSLP field was smoothed to T63 resolution (180 km) to reduce the noise in the field and the wavenumbers smaller than 5 were removed to exclude the large planetary-scale waves. Tracks that are short-lived (last less than 1 day) and stationary (move less than 500 km during their lifetime) were excluded to only include mobile and not overly short-lived systems. At each time step of each track, the coordinates and value of the minimum MSLP of the cyclone centre were found from the native resolution (30 km) MSLP field. To investigate the wind gusts associated with extratropical cyclones, at each time step of the track additionally the maximum 10-m wind gust within a 6 degree geodesic radius from the cyclone centre was found. The results in **Paper II** showing the windstorm structure supports the choice of 6 degrees as a suitable radius to determine the associated wind gusts.

4.3. Extratropical cyclone classes

All extratropical cyclones were classified either as a windstorm or a non-windstorm based on which extratropical cyclones have extremely strong wind gusts. Since the investigation focused on extratropical cyclones in northern Europe, the study includes those tracks that have at least one location point inside the northern Europe box (55–75°N, 5–40°E, Fig. 2). The threshold for a windstorm is calculated from the wind gust distribution which includes the maximum 10-m wind gust values within 6 degrees of the cyclone centre at each time step when the cyclone centre of the track is inside the northern Europe box. This means that in the wind gust distribution there can be multiple wind gust values per track and that the maximum 10-m wind gust can be located at a maximum of 6 degrees outside the northern Europe box.

The threshold for a windstorm was chosen to be the 90^{th} percentile of the wind gust distribution i.e. 27.2 m s^{-1} since this results in a reasonable number of

windstorms to analyse. The 90th percentile was calculated covering the whole year; although the study examines the cold and warm seasons separately, by choosing just one threshold makes it possible to more easily compare the seasons (the 90th percentile is higher in the cold season than in the warm season which would lead to warm-season windstorms including extratropical cyclones with weaker wind gusts than cold-season windstorms). In **Paper II**, the climatological characteristics were analysed for these three cyclone classes: 1) all extratropical cyclones (i.e. extratropical cyclones that have at least one track point inside the northern Europe box), 2) windstorms (i.e. extratropical cyclones which have wind gusts of at least 27.2 m s^{-1} when the cyclone centre in inside northern Europe), and 3) non-windstorms (i.e. all extratropical cyclones minus windstorms). In total, the set of cyclones consisted of 5 966 extratropical cyclones of which 1 381 are windstorms and 4 585 are non-windstorms.

4.4. Cyclone composites

The spatio-temporal evolution and precursors to windstorms in **Paper II** are investigated by creating cyclone composites. A cyclone composite is the average of many cyclones and therefore it emphasises the most typical features of the cyclones. The composites are created for different meteorological parameters and they are converted to a normalised time axis relative to 1) the time of the minimum MSLP and 2) the time of the maximum 10-m wind gust. The time of the minimum MSLP is the time when the minimum MSLP value during the whole lifetime of the cyclone is obtained. However, since the focus is on wind gusts in northern Europe, the time of the maximum 10-m wind gust is defined to be the time when the maximum 10-m wind gust is obtained while the cyclone centre is inside the northern Europe box. To create the cyclone composites, first the windstorms are interpolated into a spherical grid where the cyclone centre is in the middle. Then, all the cyclones are rotated to a cyclone-relative coordinate so that the propagation direction is towards east. Finally, the composite of a chosen meteorological parameter is produced by taking an average over that parameter of each individual windstorm.

4.5. Ensemble sensitivity analysis

Ensemble sensitivity analysis is a method which can be applied to examine precursors to windstorms. The basic idea is to use linear regression between the windstorm intensity and precursor fields and to find statistical correlations. This method has been used to find precursors in few previous cyclone studies

e.g. for intense Mediterranean cyclones (Garcies and Homar, 2009) and for extratropical cyclones in the east and west North Atlantic (Dacre et al., 2012). While the ensemble sensitivity analysis is limited by its assumption of linear relationship between the windstorm intensity and the precursor, it is computationally straightforward and can give general guidance, for example, of what parameters are important when forecasting windstorms.

In the ensemble sensitivity analysis, the correlation is calculated between the precursor field, x, and a so-called response function, J. In **Paper II**, two response functions were defined to investigate two different measures of windstorm intensity: 1) the minimum MSLP and 2) the maximum 10-m wind gust. The MSLP represents the commonly used intensity parameter and the wind gust represents the parameter that typically causes the damage and impacts. The sensitivity S is calculated by multiplying three components:

$$S_{i,j} = m_{i,j}\alpha_{i,j}\sigma_{i,j} \tag{2}$$

where m is the linear regression slope, α is a correction factor, and σ is the standard deviation of the precursor. The linear regression is calculated between the response function J and the precursor x at each grid point (i, j) which results in the linear regression slope m:

$$m_{i,j} = \left(\frac{\delta J}{\delta x}\right)_{i,j}. \tag{3}$$

In order to alter the sensitivity S in grid points with weak correlations, the correlation factor α is defined:

$$\alpha_{i,j} = \begin{cases} 1 & \text{if } r^2_{i,j} \geq r^2_{min}, \\ \frac{r^2_{i,j}}{r^2_{min}} & \text{if } r^2_{i,j} < r^2_{min} \end{cases} \tag{4}$$

where $r_{i,j}$ is the correlation coefficient and r_{min} is the threshold that determines which correlation coefficient values modify the sensitivity S. In **Paper II**, and in similar way to Dacre and Gray (2013), r^2_{min} is set to 0.05 and therefore the sensitivity S is scaled down in all grid points where the correlation coefficient is less than 0.224.

The last component in the sensitivity Eq. 2 is the standard deviation of the precursor, σ. It is calculated over both seasons so that they are comparable to each other. When the sensitivity S is multiplied with the standard deviation σ the final sensitivity becomes the same unit as the response function. This further means that the resulting sensitivity describes how the response function changes when the precursor field is increased by one standard deviation.

In practice, the linear regression slope m determines the sign of the sensitivity while the correlation factor α and the standard deviation σ can modify the magnitude of the sensitivity. Negative sensitivity means that there is a negative correlation between the precursor and the response function. When the minimum MSLP is investigated as the response function, negative sensitivity indicates that an increase in the precursor is associated with a decrease in the minimum MSLP and hence with a stronger windstorm (in regards to MSLP). In the same way, when the maximum 10-m wind gust is investigated as the response function, negative sensitivity indicates that an increase in the precursor is associated with a decrease in the maximum wind gust. In contrast, this however indicates a weaker windstorm (in regards to wind gust). Therefore, the same sign in the sensitivity implies an opposite windstorm evolution and this is important to notice when comparing the sensitivities of these two response functions.

The precursors examined in **Paper II** are the 850-hPa potential temperature anomaly (as being the primary driver of extratropical cyclones), total column water vapour (TCWV, to investigate the influence of moisture), 300-hPa wind speed (to examine the effect of the jet stream) and 300-hPa PV (to investigate the impact of the upper-level troughs and ridges). All precursors are used as absolute values except the 850-hPa potential temperature which is calculated to an anomaly to determine the strength of the temperature gradient. The anomaly is computed separately for each windstorm: first the 850-hPa potential temperature is averaged over the whole 18 degree radius composite and then this average value is subtracted from each grid point in that windstorm.

5. Overview of the results

5.1. Climatology of wind speeds, extratropical cyclones and windstorms in northern Europe

The mean wind speeds in the whole North Atlantic and Europe region reveal a distinct land-sea contrast and a seasonal variability (Fig. 4). The strongest winds occur over the ocean in the North Atlantic storm track region (contours in Fig. 4) and during winter months. The mean wind speeds over the North Atlantic are around 40 % stronger and over Europe on average 30 % stronger in winter than in summer. Some smaller-scale, local wind phenomena are also visible, e.g. the mistral and etesians wind phenomena in the northern and eastern Mediterranean Sea. These same main features are visible in the extreme (i.e. the 98th percentile) wind climate (see Fig. 2 in **Paper I**).

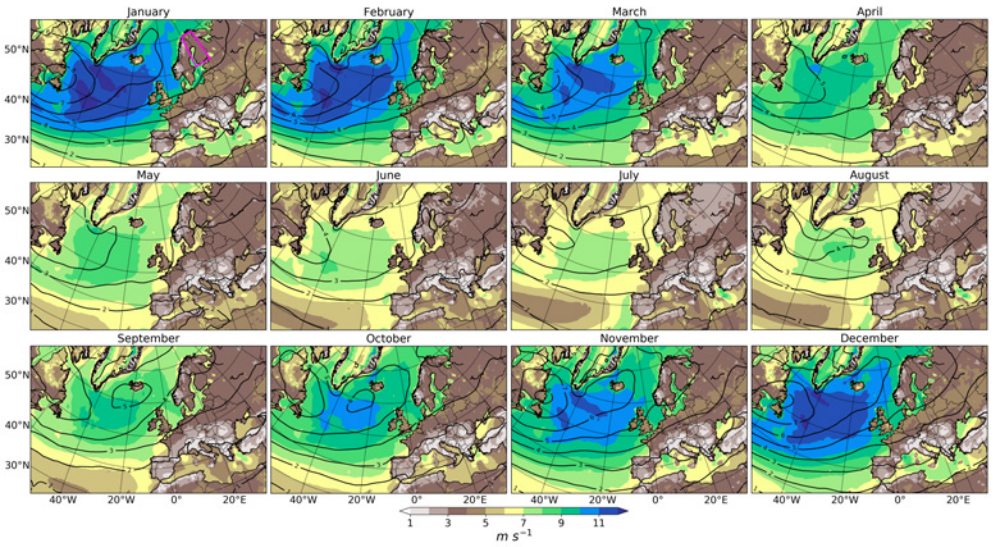

Figure 4. *Monthly mean values of 10-m wind speed (colours, m s^{-1}) and standard deviation of 2–6 day bandpass filtered mean sea level pressure (contours, hPa) from 1979–2018. The magenta box over Finland shown in the January map is used in the time series and trend analysis. Figure modified from* ***Paper I****.*

Regarding the wind climate in northern Europe, the mean and extreme winds show a seasonal variation with up to 30 % stronger winds in winter than in summer. The absolute mean winds in winter are around 4 m s^{-1} and in summer around 3 m s^{-1} (Fig. 4). A large difference in wind climate between northern

Europe and other parts of Europe is found in the EWF seasonality. The EWF values in northern Europe are the highest in summer whereas in southern Europe the highest EWF values are in winter. Moreover, the EWF values in southern Europe are larger than in northern Europe throughout the year. This firstly implies that strong winds in summer in northern Europe are rare and hence relatively extreme when they occur. In contrast, high winds in southern Europe are relatively extreme in winter. Secondly, this implies that high winds in northern Europe are more common than in southern Europe.

A notable detail in the ERA5 wind climate in northern Europe is the low wind speeds over Scandinavian Mountains. Previous studies have shown that the modelled wind speeds in mountainous regions in Norway (Thyness et al., 2017) and in Sweden (Minola et al., 2020) are underestimated compared to observations. This may be caused by, for example, too coarse resolution of the reanalysis, high subgrid variability in topography or the handling of surface roughness in the model. Hence, the near-surface wind speeds in the mountainous regions in northern Europe are likely poorly represented in ERA5.

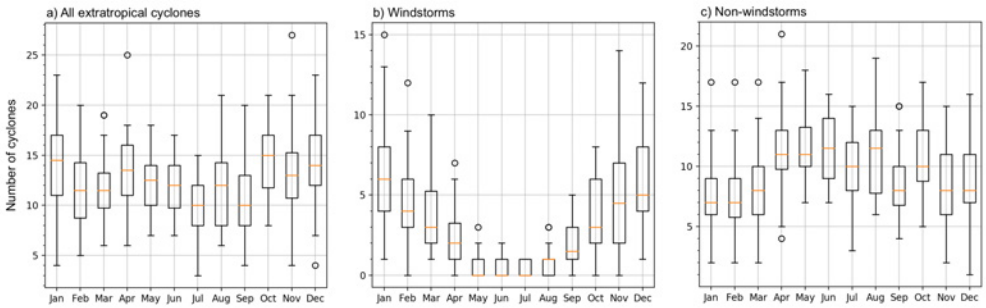

Figure 5. *Monthly distribution of a) all extratropical cyclones, b) windstorms, and c) non-windstorms in northern Europe. Orange lines are medians and boxes show first and third quartiles. Figure adopted from* ***Paper II****.*

The result from **Paper I** that high wind events are more common in winter and rare in summer in northern Europe is further confirmed from **Paper II** which shows that windstorms mostly occur during winter (Fig. 5b). On average, there are 5–6 windstorms per month in December and January but no windstorms at all between May and July. In contrast, there are more non-windstorms in summer than in winter months (Fig. 5c). Therefore, and more surprisingly, the overall number of extratropical cyclones in northern Europe does not largely vary between seasons (Fig. 5a).

Extratropical cyclones that influence northern Europe occur during their

lifetime zonally between the east coast of the United States and eastern Siberia and meridionally between the Greenland Sea and the Mediterranean Sea (Figs. 6a and 6b). In the cold season, the highest track densities are over the Barents Sea and south-eastern parts of northern Europe (Fig. 6a) whereas in the warm season, the tracks most frequently occur over the land areas in northern Europe (Fig. 6b). There is a distinct difference in the location of occurrence between windstorms and non-windstorms. Windstorms are the most frequent over the Barents Sea (Figs. 6c and 6d) while non-windstorms mostly over the land areas in northern Europe (Figs. 6e and 6f). Hence, windstorms tend to occur at higher latitudes than weaker extratropical cyclones.

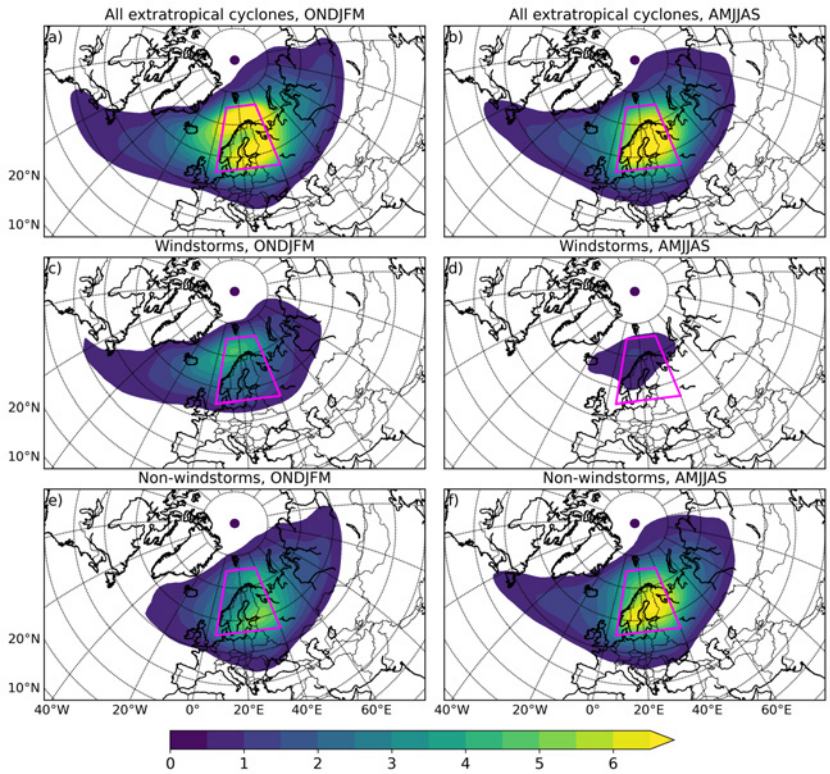

Figure 6. *Track density (number of cyclones per month per 5° spherical cap ≈ 10^6 km^2) of a,b) all extratropical cyclones, c,d) windstorms, and e,f) non-windstorms. The magenta box shows the northern Europe box where the tracks in this study are selected to occur. Figure modified from* ***Paper II****.*

In addition to seasonal variability and track density, **Paper II** examined other cyclone characteristics as well. Extratropical cyclones propagate mostly towards

the east over northern Europe and this does not differ between seasons or between windstorms and non-windstorms. Extratropical cyclones in the warm season live on average 3.6 days and are thus slightly longer living than extratropical cyclones in the cold season which last 3.4 days. Moreover, the difference in lifetimes is larger between windstorms and non-windstorms; the average lifetime of windstorms (4.0 days in both seasons) is longer than the average lifetime of non-windstorms (3.0 days in the cold season and 3.6 days in the warm season). Regarding the maximum 10-m wind gusts associated with the cyclones, they occur on average between 0–3 h after the minimum MSLP occurs. The highest maximum 10-m wind gusts are stronger in cold season windstorms (up to 52 m s^{-1}) than in warm season windstorms (up to 38 m s^{-1}).

5.2. Variability and trends in wind speeds, extratropical cyclones and windstorms in northern Europe

The decadal near-surface wind speeds in the whole North Atlantic and Europe region show large decadal variabilities (see Figs. 6, 7, S1 and S2 in **Paper I**). The highest variations are in winter months and the weakest in summer. There are no long-term trends evident in any of the three geographic regions that were considered in **Paper I** and different decades exhibit varying signs in wind speed anomalies at different locations.

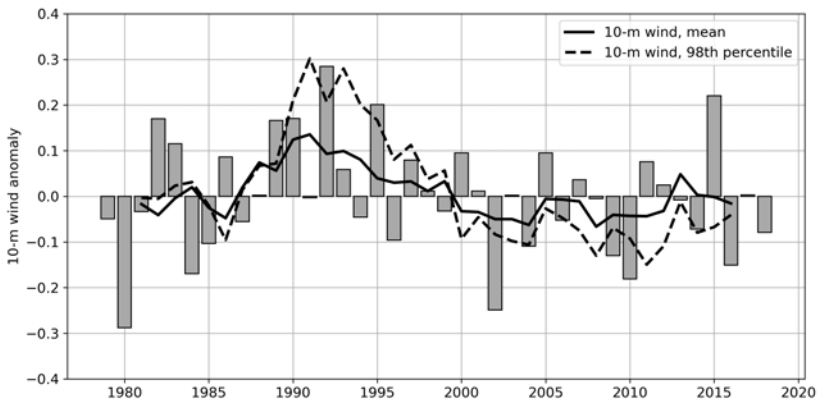

Figure 7. *Annual 10-m wind speed anomalies (yearly mean value minus the 1979–2018 mean value (3.8 m s^{-1}), gray bars) and 5-year running means of the mean (solid line) and the 98^{th} percentile (dashed line) wind speeds in Finland (the box is shown in Fig. 4). Figure modified from* ***Paper I****.*

In northern Europe, winters in the 1990s were windier than on average while winters in the 1980s and 2010s had weaker winds. Specifically in Finland, the large inter-annual and decadal variability is distinct in the annual wind speed anomalies (Fig. 7). The mean annual wind speed in Finland is 3.8 m s^{-1} and therefore, as an example, an anomaly of 0.3 m s^{-1} refers to a 8 % change compared to the average. The wind speeds were stronger than on average during 1990–1995 and in contrast, a period between 2000–2015 had weaker wind speeds. This variability in annual wind speeds in Finland from ERA5 corresponds well to the annual wind speed variability based on observations (Laapas and Venäläinen, 2017). The 5-year running means in Fig. 7 reveal that the mean and extreme winds have similar time evolution but the extreme winds have larger variability than the mean winds. The long-term linear trends in mean and extreme wind speeds in Finland are small in magnitude and not statistically significant based on the Mann-Kendall test at 5 % significance level. This is valid on an annual scale as well as separately for each month. Hence, the wind speed climate in northern Europe does not have linear trends during the 40-year period but is characterised by a natural and large inter-annual variability.

The large year-to-year variability is also apparent in the annual number of extratropical cyclones and windstorms in northern Europe during the 40-year period (Fig. 8). The 1980s had more extratropical cyclones overall than on average which for the most part was caused by an increased number of non-windstorms. There were also more windstorms in northern Europe between 1987–1995 compared to the 40-year mean. In contrast, a decrease in the overall number of extratropical cyclones occurred during 1995–2005 when there were particularly less windstorms than on average.

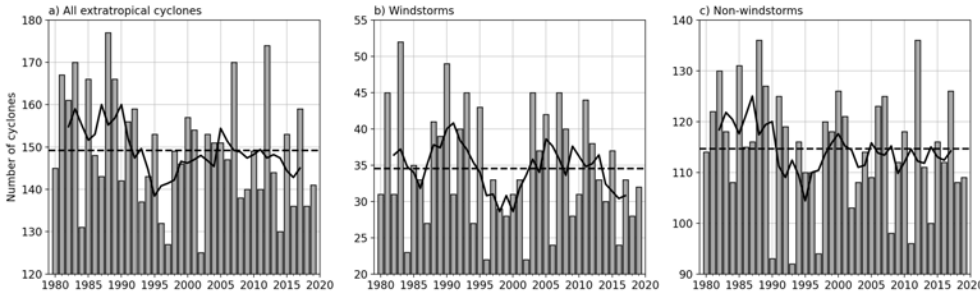

Figure 8. *Annual absolute numbers of a) all extratropical cyclones, b) windstorms, and c) non-windstorms in northern Europe in 1980–2019. Bars show the annual values, solid lines are 5-year running means and dashed lines are annual means. Figure adopted from* ***Paper II****.*

The linear trends in the numbers of all extratropical cyclones, windstorms and non-windstorms in northern Europe are not significant with the 5 % level in the Mann-Kendall test. However, with a 7 % level the decreasing trend in the number of all extratropical cyclones (Fig. 8a) would be significant. Overall, extratropical cyclone and windstorm climate in northern Europe is similar to wind speed climate in northern Europe especially in terms of large inter-annual variability and no distinct long-term trends.

Since the near-surface wind speeds show decadal variability, **Paper I** further attempted to find physical reasons to explain these variations. The decadal changes were investigated for MSLP, 300-hPa wind speed and storm tracks (produced by the Eulerian approach, see Section 4.2) and it was found that they all contribute to the changes in 10-m wind speeds. For example in the 1990s in February, northern Europe had stronger than average 10-m winds. During that decade, the MSLP gradient between the northern and southern parts of the North Atlantic was stronger than on average. Furthermore, the jet stream (determined from the 300-hPa wind speed field) and storm tracks were extended more poleward and eastward than on average. In conclusion, the decadal near-surface wind speed variations in the North Atlantic and Europe region are well explained by the strength of the pressure gradient across the north-south direction in the North Atlantic and the position of the jet stream and storm tracks.

5.3. Spatio-temporal evolution and precursors to windstorms in northern Europe

5.3.1. Climatological perspective for spatio-temporal evolution

The spatial structure during the evolution of northern Europe windstorms is investigated in **Paper II** with cyclone composites showing the MSLP, 850-hPa potential temperature (from which the frontal structure can be determined) and 10-m wind gust. The composites are examined at -48 h, -24 h, 0 h and +24 h offset times that are relative to the time of the minimum MSLP.

Two days before the minimum MSLP, both cold- and warm-season windstorms already have a closed low-pressure centre and a noticeable frontal structure with a cold front located upstream of the cyclone centre and a warm front downstream of the cyclone centre (Figs. 9a and 9e). The highest 10-m wind gusts are located between the cold and warm fronts in the warm sector where the pressure gradient is the strongest. One day before the minimum MSLP, the windstorm further intensifies with a decreasing central pressure and increasing pressure and potential

temperature gradients (Figs. 9b and 9f). The region of the strongest wind gusts expands from the warm sector to also cover areas behind the cold front. At the time of the minimum MSLP, the frontal structure reaches its mature stage indicated by the warm front that begins to wrap around the cyclone centre (Figs. 9c and 9g). The pressure gradient and the wind gusts are the strongest at this time. The extent of the highest wind gusts is spread from the warm sector to behind the cold front. One day after the minimum MSLP, the pressure and potential temperature gradients and the maximum wind gusts have weakened (Figs. 9d and 9h).

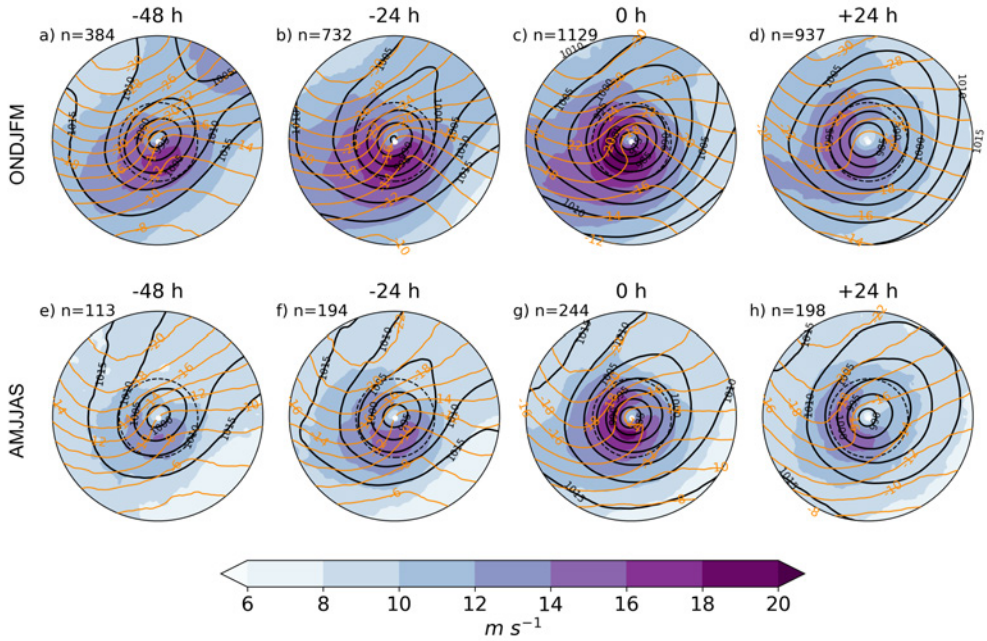

Figure 9. *The maximum 10-m wind gust (colours, m s^{-1}), mean sea level pressure (black contours, 5 hPa interval) and 850-hPa potential temperature (orange contours, 2 °C interval) composites of windstorms during the cold season (October–March, top row) and the warm season (April–September, bottom row). The offset times are relative to the time of the minimum mean sea level pressure: a) -48 h, b) -24 h, c) 0 h, and d) +24 h. The number in each panel is the number of individual windstorms in each composite. The radius of the plots is 18° and the 6° radius is marked with a dashed circle. Figure modified from* ***Paper II****.*

The structure and evolution of northern Europe windstorms are similar in the cold and warm seasons, however, there are differences in the intensity and the spatial scale. Cold-season windstorms are stronger than warm-season

windstorms in terms of all investigated measures: the central pressure is on average 9 hPa deeper, pressure and potential temperature gradients are stronger and the maximum 10-m wind gust is on average 2 m s^{-1} higher. In addition, the area that exceeds wind gusts of 16 m s^{-1} in the composites is 18 % in cold-season windstorms (Fig. 9c) and 10 % in warm-season windstorms (Fig. 9g). Therefore, the spatial extent of the strong wind gusts is larger in windstorms in the cold season than in the warm season.

5.3.2. Climatological perspective for precursors

The precursors that affect the intensity of windstorms in northern Europe were examined in **Paper II** using the ensemble sensitivity method (see Section 4.5). The intensity was investigated with two measures: the minimum MSLP and the maximum 10-m wind gust. **Paper II** analysed the sensitivities at -72 h, -48 h, and -24 h before the time of maximum intensity (the minimum MSLP or the maximum 10-m wind gust) and the strongest sensitivities were generally found 48 h before the time of maximum intensity. Hence, the results presented here are with sensitivities two days before the time of maximum intensity, and the other offset times can be seen from **Paper II**.

Two days before the minimum MSLP, the frontal structure is evident (Figs. 10a and 10e) which was also seen in the cyclone composites (Figs. 9a and 9e). The sensitivity to the 850-hPa potential temperature anomaly shows a dipole with negative sensitivity over the warm sector and positive sensitivity over the cold sector. This means that an increase in the 850-hPa potential temperature anomaly is associated with a lower minimum MSLP in the warm sector but a higher minimum MSLP in the cold sector. In other words, a lower minimum MSLP is attained when the low-level temperature is warmer in the warm sector and colder in the cold sector. This implies that a windstorm is more intense in terms of MSLP when the temperature gradient is stronger. The TCWV pattern resembles the frontal structure and the highest amount of moisture is located in the warm sector (Figs. 10b and 10f). Negative sensitivity over the warm sector indicates that higher amount of moisture in that region is associated with a lower minimum MSLP and hence a stronger windstorm.

Investigating the upper levels, two days before the minimum MSLP the cyclone centre is positioned towards the left exit region of the jet stream (Figs. 10c and 10g) which is a region enhancing the surface cyclone development. The highest negative sensitivities are located north-east of the cyclone centre. This implies that a stronger windstorm occurs when the jet stream is extended towards north-east

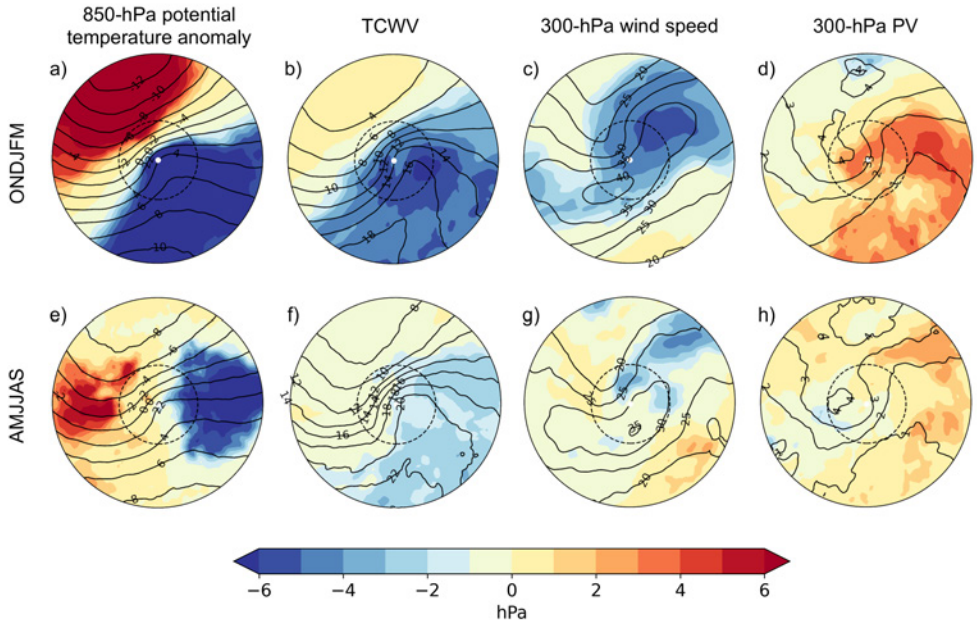

Figure 10. *Sensitivity (colours, hPa) of the minimum MSLP 48 h before the minimum MSLP to a,e) 850-hPa potential temperature anomaly, b,f) TCWV, c,g) 300-hPa wind speed, and d,h) 300-hPa PV. Top row shows the cold season and bottom row the warm season. The contours are the composite means of each variable. The radius of the plots is 18° and the 6° radius is marked with a dashed circle. Figure modified from* ***Paper II****.*

of the cyclone centre which may be caused by a tilted i.e. more meridional jet stream. The last examined precursor is the 300-hPa PV. The upper-level trough (denoted by high PV values) occurs upstream of the cyclone centre creating a westward tilt between the upper-level trough and the surface cyclone which usually intensifies the cyclone (Figs. 10d and 10h). The upper-level ridge is also evident with low PV values downstream of the cyclone centre. Positive sensitivity downstream of the cyclone centre indicates that higher PV is associated with a higher minimum MSLP and hence a weaker windstorm. Other way around, a windstorm is stronger when downstream of the cyclone centre the PV is lower which indicates a stronger upper-level ridge or higher tropopause which increases the PV gradient and therefore steepens the tropopause.

The synoptic situation two days before the maximum wind gust (Fig. 11) is largely similar to that two days before the minimum MSLP (Fig. 10). Likewise,

the sensitivities have overall similar patterns although with contrary signs; this is sensible since negative sensitivity in the minimum MSLP indicates the same windstorm evolution as positive sensitivity in the maximum wind gust (see Section 4.5). A stronger temperature gradient, more moisture in the warm sector and north-east extended jet stream are all associated with higher maximum wind gusts and hence a stronger windstorm. However, the sensitivity to the 300-hPa PV is mostly weak.

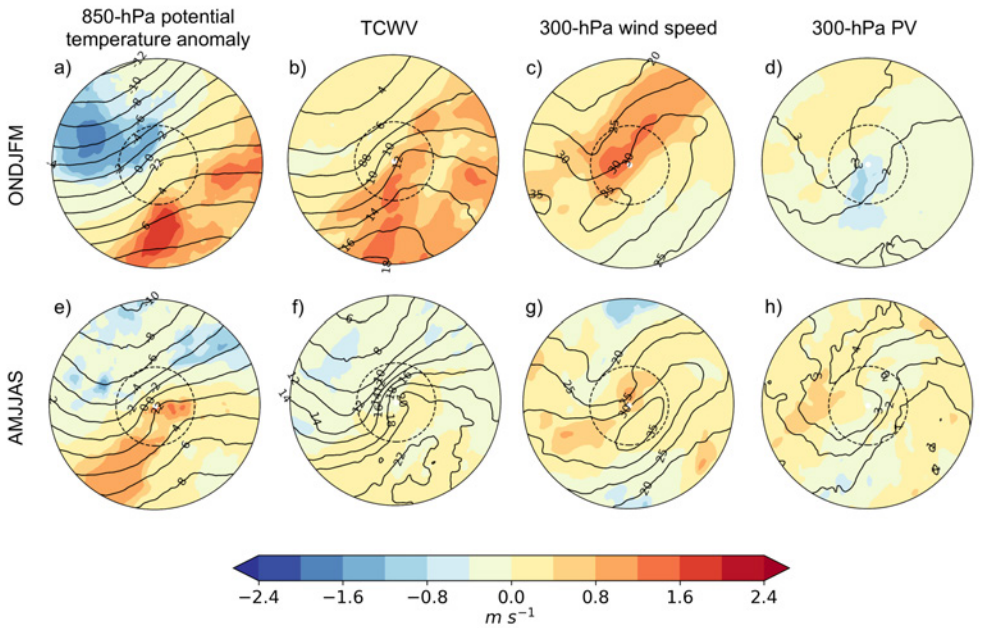

Figure 11. *Sensitivity (colours, m s^{-1}) of the maximum 10-m wind gust 48 h before the maximum wind gust to a,e) 850-hPa potential temperature anomaly, b,f) TCWV, c,g) 300-hPa wind speed, and d,h) 300-hPa PV. Top row shows the cold season and bottom row the warm season. The contours are the composite means of each variable. The radius of the plots is 18° and the 6° radius is marked with a dashed circle. Figure modified from* ***Paper II****.*

The sensitivity fields of both the minimum MSLP and the maximum wind gust show overall similar patterns in both seasons. However, the sensitivities are higher in the cold season than in the warm season. For example, an increase of one standard deviation in the TCWV decreases the minimum MSLP by 7 hPa in the cold season and 3 hPa in the warm season (Figs. 10b and 10f). Similarly, an increase of one standard deviation in the TCWV increases the maximum wind

gust by 1.6 m s^{-1} in the cold season and 0.4 m s^{-1} in the warm season (Figs. 11b and 11f). Higher sensitivity indicates that cold-season windstorms are possibly better predictable than warm-season windstorms. In addition, the sensitivities of the minimum MSLP are higher than the sensitivities of the maximum wind gusts indicating that the minimum MSLP of windstorms is probably easier to predict than the maximum wind gust. Of all the four precursors, the 850-hPa potential temperature anomaly i.e. the temperature gradient has the highest sensitivities in terms of both the minimum MSLP and the maximum wind gust. Therefore, this variable is important for forecasting the windstorm intensity.

5.3.3. Case study perspective

While the cyclone composite results describe the general features in the structure and evolution of northern Europe windstorms, an individual windstorm event can develop in a quite different way. **Paper III** investigated a unique windstorm case in Finland in 1982, named storm Mauri, which caused lot of damage and two fatalities. The uniqueness of this event comes from its origin; storm Mauri is thought to be the only named (i.e. damaging) windstorm in Finland which was a remnant of a hurricane. Therefore, **Paper III** aimed to get a better understanding on the development of ex-hurricane Debby and the subsequent storm Mauri. Moreover, **Paper III** examined the winds over Finland during storm Mauri and how well the wind speeds were represented in the OpenIFS model.

Paper III gave a short synoptic overview of this case using ERA-Interim reanalysis and analysed it in more detail with higher spatial and temporal resolution from the OpenIFS model simulations. Debby formed on 13 September 1982 near the Dominican Republic and moved north-east alongside the east coast of the United States (Clark, 1983). The extratropical transition of Debby started on 17 September (see Fig. 2 in **Paper III**) and on 18 September, there were two extratropical cyclones present in the North Atlantic (labelled as "ETC1" and "ETC2" in Fig. 12a). The completion of the extratropical transition occurred on 19 September transforming Debby to an extratropical cyclone, now called "ex-Debby". After this, ex-Debby travelled rapidly across the North Atlantic and at the same time the two extratropical cyclones in the North Atlantic merged to one large low-pressure system between Iceland and the United Kingdom (labelled as "ETC" in Fig. 12b). When ex-Debby reached the United Kingdom on 21 September, it re-intensified and took a more northerly path towards northern Europe while the other low-pressure system remained over the Norwegian Sea (Fig. 12c). On 22 September, ERA-Interim shows two low-pressure centres and the one associated with ex-Debby located in northern Finland and was named storm Mauri (Fig. 12d).

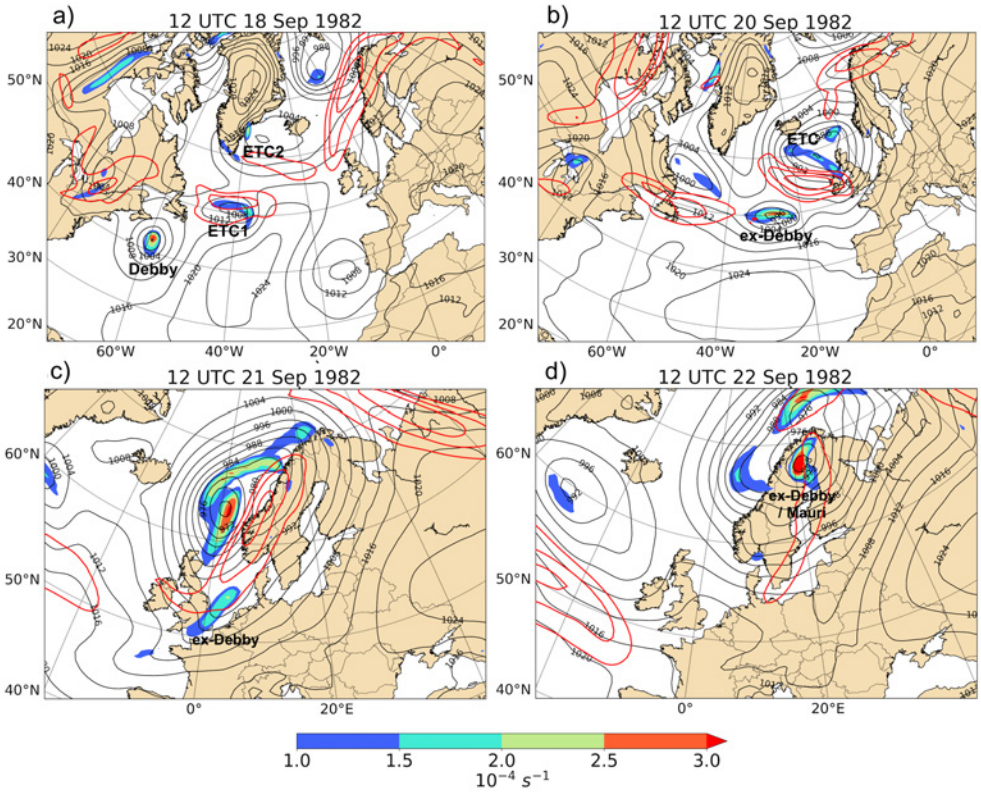

Figure 12. *850-hPa relative vorticity (colours, s^{-1}), 300-hPa wind speed (red contours at 40, 50 and 60 m s^{-1}), and MSLP (black contours at 4-hPa interval) from ERA-Interim on a) 18 Sep 12 UTC, b) 20 Sep 12 UTC, c) 21 Sep 12 UTC, and d) 22 Sep 12 UTC. Figure modified from* ***Paper III****. © American Meteorological Society, used with permission.*

As noted in Section 3.2, the OpenIFS simulations performed on 17 and 19 September diverged from the reanalysis only after two days indicating that the predictability of this case was poor and this caused us to use multiple OpenIFS forecasts to cover the whole life cycle of Debby and Mauri. The OpenIFS forecast from 17 September was used to examine if Debby impacted the downstream flow already before Debby's transition. The outflow from Debby was found to have amplified the ridge building and accelerated the jet stream, similarly than in typhoon Jangmi (Grams et al., 2013). A significant point, however, was that although an upper-level trough was present just upstream, Debby did not re-intensify. Earlier studies have noted that the exact phasing

between an upper-level trough and a surface tropical cyclone is highly sensitive in determining whether the tropical cyclone will re-intensify (Ritchie and Elsberry, 2007; Riemer et al., 2008; Riboldi et al., 2019). Hence, a slightly different phasing between Debby and the upper-level trough could have lead to a totally different development of ex-Debby.

ERA-Interim and the OpenIFS forecast from 19 September show that during 19–21 September ex-Debby travelled rapidly across the North Atlantic without re-intensifying. Further analysis revealed that ex-Debby had similarities to a diabatic Rossby wave. Ex-Debby was found to fulfill most of the criteria for diabatic Rossby wave characteristics developed by Boettcher and Wernli (2013). The lack of re-intensification while moving over the North Atlantic was due to the upper-level trough being too far west compared to the location of ex-Debby to provide upper-level forcing. However, ex-Debby started to rapidly intensify when it reached the United Kingdom. At this stage, ex-Debby was still a small meso-scale sized feature. Another upper-level trough approached from the north-west and the OpenIFS forecast from 21 September shows that on 21 September a favourable phasing i.e. a westward tilt with the low-level PV anomaly of ex-Debby enabled the interaction and forcing from upper levels.

Paper III additionally investigated what caused the strong winds over Finland during storm Mauri. This was done by examining the three components in Eq. 1 separately: the 10-m wind speed, turbulent mixing and convectively-driven downdrafts. While the strongest 10-m wind speeds were associated with the strongest pressure gradient over the Bay of Bothnia (Fig. 13), the wind gusts were enhanced due to both other components. The wind gusts driven by turbulent mixing were evident over land behind the cold front which is logical since the surface roughness / friction is higher over land than over sea. The wind gusts driven by convective downdrafts were apparent in the warm sector suggesting that convection was present in this region. The turbulent-driven gusts covered a larger area over Finland whereas the convectively-driven gusts were relatively localised. In general, these results emphasise that the strong winds in windstorms can be caused by multiple factors.

Finally, **Paper III** examined how the wind speeds over Finland during storm Mauri were resolved in the model compared to observations. The highest recorded 10-m wind speed on 22 September 1982 was 23 m s^{-1} and it was observed in three weather stations over land areas in central and northern Finland (Fig. 13a). The highest 10-m wind speed in OpenIFS forecast from 21 September is 22 m s^{-1} over the Bay of Bothnia and 14 m s^{-1} over land. In northern Finland, the observed winds range generally between 16–23 m s^{-1} but the modelled wind speeds are

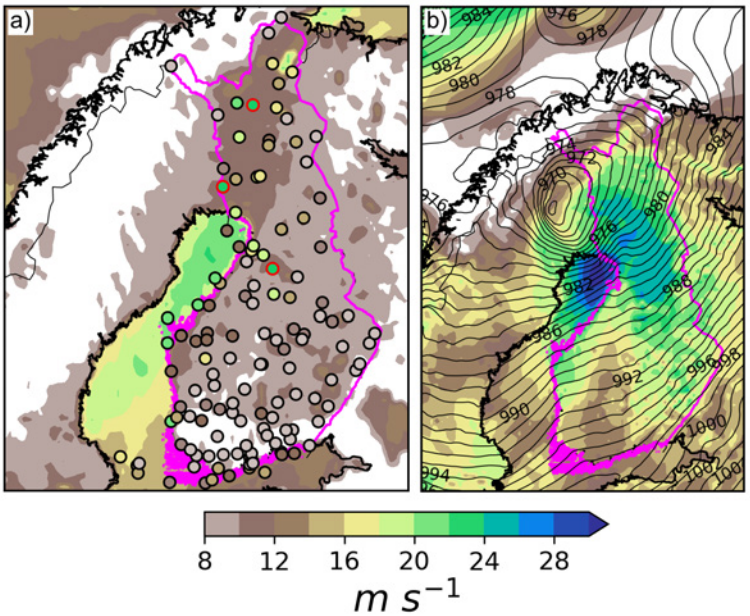

Figure 13. *a) Maximum observed 10-minute average 10-m wind speeds during 22 Sep 1982 from Finnish Meteorological Institute's weather stations (circles) and from OpenIFS simulation initialized on 21 Sep (colours). The red circles denote the three stations that observed the highest values of 23 m* s^{-1}*. b) Maximum 10-m wind gust (colours) during the previous hour and mean sea level pressure (contours at 1-hPa interval) on 22 Sep 1982 12 UTC from OpenIFS simulation initialized on 21 Sep. Borders of Finland are colored magenta. Figure modified from* ***Paper III****. © American Meteorological Society, used with permission.*

between 10–14 m s^{-1}. Thus, the model underestimates the wind speeds over land by 2–13 m s^{-1} but over sea and coastal areas the modelled winds are in better agreement with the observations. While the underestimation over land is evident, however, the locations of the strongest wind speeds are correctly predicted.

6. Discussion

The research questions presented in Section 1 are answered below with some further discussion.

What are the main characteristics of wind and windstorm climate in northern Europe and Finland and can we detect any long-term trends?

Papers I and **II** show that the wind and windstorm climate in northern Europe is characterised by a seasonality with the highest wind speeds and most windstorms occurring during winter. Since high wind events in summer are rare, they are relatively extreme when they do occur. However, the number of all extratropical cyclones does not show any seasonality in northern Europe. Commonly, it is stated that extratropical cyclones in the Northern Hemisphere are more frequent during winter than in summer (e.g. Ulbrich et al., 2009). This is, however, mostly prominent in the core of the North Atlantic storm track region whereas northern Europe and Finland are located at the end of the storm track region where the seasonality is small (Hoskins and Hodges, 2019; Priestley et al., 2020).

The results from this thesis show that during a recent 40-year period (years 1979–2018 in **Paper I** and 1980–2019 in **Paper II**), there are no significant, linear trends in the mean and extreme wind speeds or in the number of extratropical cyclones and windstorms in northern Europe and Finland with a 5 % significance level. Instead, the wind and windstorm climate exhibits large inter-annual and decadal variability. Due to the large inter-annual variability, the long-term linear trends depend strongly on the chosen time period and the chosen geographic region.

During the last few decades, the long-term wind speeds over the global land areas indicated a decreasing trend which was termed stilling (Vautard et al., 2010). This global stilling was found to be explained by changes in atmospheric circulation and the increase in surface roughness, and the surface roughness can increase due to for example urbanisation, forest growth or land use changes in agriculture (Vautard et al., 2010; Wu et al., 2018). However, the global stilling reversed after 2010, and in Europe the reversal occurred in 2003 (Zeng et al., 2019). The reversal of global stilling supports the results of this thesis that there are no long-term linear trends in the 10-m wind speeds.

Regarding trends in the number of extratropical cyclones in northern Europe, no consistent trends have been found among different studies. A review by Feser et al. (2015) found that in the region surrounding the Baltic Sea (including the

Baltic Sea, Estonia, Latvia, Lithuania and most of Finland, Sweden and Norway) there are as many studies showing increasing and decreasing long-term trends as well as large number of studies showing no trends at all. The inconsistency in trends is seen in both reanalysis-based and observation-based studies (Feser et al., 2015). A more recent study by Wickström et al. (2020) found a decrease in the extratropical cyclone density in the southern Barents Sea (the region overlaps with the north-eastern part of the northern Europe box defined in this thesis) during winters in 1979–2016 which was significant with a 10 % level in the Mann-Kendall test. This supports the decreasing trend in the number of all extratropical cyclones in northern Europe found in this thesis which is significant with a 10 % level. The study by Wickström et al. (2020) additionally found a significant increasing trend in the extratropical cyclone density over Svalbard which may indicate a poleward shift in storm tracks due to climate change. The aspect of climate change is discussed more in the last paragraphs of this section. Overall, the comparison between studies is difficult since the chosen time period and region have a large effect on the sign and magnitude of linear trends.

Comparing wind and windstorm climates is not straightforward. If a month has weaker wind speeds than the long-term average it does not mean that a damaging windstorm could not have occurred. For example, this thesis shows that a period between 1995–2005 had mostly weaker wind speeds and less windstorms than on average in northern Europe but during those years northern Europe was hit with few of the most intense and damaging windstorms: storm Anatol in 1999 (Ulbrich et al., 2001) and storm Gudrun in 2005 (Suursaar et al., 2006). In addition, other weather systems, for example thunderstorms, can also cause strong winds than extratropical cyclones. When comparing the annual time series of mean and extreme wind speeds and the numbers of extratropical cyclones and windstorms shown in this thesis it can be concluded that the time series do not exactly match. However, the studied regions for these time series are different; wind speeds are analysed over land over Finland while windstorms are analysed over the whole northern Europe. Moreover, the results show that windstorms are the most frequent in the Barents and Norwegian seas which means that all windstorms are likely not affecting Finland. Therefore, as mentioned already above, the choice of the region makes a direct comparison difficult. In spite of that, the common feature for the long-term changes in winds and windstorms in northern Europe and Finland is the large, natural variability and the lack of linear trends.

How does the spatial structure of windstorms in northern Europe and Finland change during the evolution?

Cyclone composites in **Paper II** show that the wind gusts move and extend from the warm sector to behind the cold front during the windstorm evolution. This is also seen in an individual windstorm event of storm Mauri in **Paper III** where the highest 10-m wind speeds are caused by the strong pressure gradient and the wind gusts in the warm sector were strengthened by convectively-driven downdrafts and behind the cold front by turbulent mixing. This location of the strongest gusts agrees with an aqua-planet study by Sinclair et al. (2020) who found a similar shift in the location of the maximum 900-hPa wind speeds with the 200 strongest extratropical cyclones. This result also agrees with Hewson and Neu (2015) who developed a conceptual model of the life-cycle and structure of strong winds in extratropical cyclones based on 29 historic and damaging windstorms in Europe. Hewson and Neu (2015) found three regions of strong winds which all have different features and they occur at different times in the life-cycle. The warm conveyor belt jet occurs in the warm sector and develops already in the early stage in the life-cycle. This warm jet can additionally be enhanced by convective downdrafts (Hewson and Neu, 2015) which is a feature found in the case of storm Mauri in **Paper III**. The sting jet occurs right before the maximum cyclone intensity just ahead and behind the cold front at the end of the bent-back front. The sting jet has the strongest and most damaging winds of the three wind regions although it is spatially the smallest and most short-living. The last wind region is the cold conveyor belt jet which develops right before the maximum cyclone intensity in the cold airmass behind the bent-back front. Although all of the three wind features do not often occur in the same extratropical cyclone (Hewson and Neu, 2015) the location of the strong winds during the extratropical cyclone evolution supports the results from this thesis.

Paper II additionally shows that the temperature gradient, pressure gradient and the wind gusts are stronger, the minimum pressure is deeper and the wind gusts are more widely spread (i.e. the wind gust footprint is larger) in cold-season windstorms than in warm-season windstorms. More generally, the cold-season windstorms are typically stronger and spatially larger than warm-season windstorms. Earlier studies have shown that the radius size of extratropical cyclones is smaller in summer than in winter (Simmonds, 2000; Rudeva and Gulev, 2007). By using different intensity measures for vorticity and meridional wind in the lower and upper troposphere, Hoskins and Hodges (2019) showed that also the intensity is weaker in summer than in winter in extratropical cyclones in the Northern Hemisphere with all the investigated measures. Considering the windstorm footprint, Hawcroft et al. (2012) found that

the precipitation footprint was larger in wintertime extratropical cyclones than in summertime extratropical cyclones. This is in line with our result regarding the wind gust footprint.

What meteorological factors affect the intensity of windstorms in northern Europe and Finland?

The composite sensitivities studied in **Paper II** reveal that from the investigated four meteorological factors the 850-hPa potential temperature anomaly i.e. the low-level temperature gradient has the strongest impact on the windstorm intensity in northern Europe. Hence, attention should be paid especially to this variable when forecasting windstorms in northern Europe. The windstorms are also, although to a lesser degree, sensitive to the other examined meteorological factors - total column water vapour, 300-hPa wind speed and 300-hPa potential vorticity - from which the 300-hPa potential vorticity has the weakest impact. Especially in the warm season (April–September), windstorms are mainly not sensitive to the upper-level potential vorticity field and hence to the upper-level trough/ridge. In contrast, the windstorm case examined in **Paper III** occurred in September and was found to be strongly dependant on the phasing with the upper-level trough in order to develop into an intense windstorm in Finland. This result highlights the case-to-case variability which is smoothed in climatological investigations and leads to the need of more case studies to better understand the detailed development of individual windstorms. Nonetheless, the composite results emphasise the general features in northern Europe windstorms and provide concepts of typical windstorm characteristics to forecasters.

The ensemble sensitivity analysis in the precursor investigation in **Paper II** uses correlation which means that the results cannot be interpreted as causalities. One option to solve this is to remove the influence of the cyclone before the linear regression so that the cyclone itself does not affect the precursor field. This method was applied by Dacre et al. (2019) who used a 10-day bandpass-filtered field as the background precursor. However, the sensitivity results without any modification / cyclone removal are more useful in weather forecasting because forecasters follow the full fields of the precursor variables rather than just the background fields. The ensemble sensitivity method has been used in other cyclone studies (e.g. Garcies and Homar, 2009; Dacre and Gray, 2013) that also have not applied any isolation of the cyclone influence from the precursor field. Although the causality would have added value to the results the knowledge of correlations is nevertheless important in determining which precursors have a relationship with the windstorm intensity.

The meteorological factors affect windstorm intensity with different magnitudes depending on the season and the measure of intensity. The sensitivities are around 20–75 % higher in cold-season windstorms than in warm-season windstorms which implies that northern Europe windstorms are possibly better predictable in the cold season than in the warm season. This may be due to the smaller sample size (windstorms are rare in summer) and higher variability between cases. The result that cold-season windstorms are deeper, stronger and spatially larger than warm-season windstorms may also affect the predictability. Moreover, diabatic processes may be more important in warm-season windstorms due to higher moisture content potential in warmer temperatures. Since diabatic processes in numerical models are parameterized they have a critical impact on the predictability skill (Bauer et al., 2015). However, contradictory to the indication from the result from this thesis, Froude et al. (2007) found that extratropical cyclones in the Northern Hemisphere have higher predictability skill in summer seasons than in winter seasons. This was especially seen in the intensity (in terms of 850-hPa relative vorticity) but slightly also in the cyclone position (Froude et al., 2007). However, the research of windstorm predictability considers almost solely wintertime (e.g. Boisserie et al., 2016; Pantillon et al., 2017), and there is a gap in the literature investigating predictability in summer windstorms and comparisons between winter and summer seasons.

In addition to the cold season having higher sensitivities than the warm season, the minimum mean sea level pressure of windstorms has higher sensitivities and thus potentially better predictability than the maximum 10-m wind gust of windstorms. This may by explained by the different scales and types of these variables: the mean sea level pressure is a prognostic variable (i.e. directly resolved in the model) and much larger-scale and smoother-distributed field compared to the wind gusts which are parameterized and can be relatively localised and turbulent. A good example of a poorly predictable warm-season / autumn windstorm in Finland is storm Mauri; all OpenIFS forecasts performed in **Paper III** diverged from reanalysis after only two days. Since ex-Debby, the preceding ex-hurricane that impacted the development of Mauri, was more of a meso-scale sized cyclone during its critical moment in the evolution, coarse resolution models can struggle in capturing and correctly predicting these kind of cyclones. Even the resolution of many reanalysis is not enough to resolve the smaller-scale cyclones like polar lows or mesocyclones (Uotila et al., 2009; Laffineur et al., 2014; Pezza et al., 2016). One example of coarser resolution models is climate models and thus they are likely limited to only represent the large-scale extratropical cyclones.

In this thesis, windstorms are selected to occur in a box over northern Europe which includes surrounding sea areas. Because of this, most of the windstorms (defined based on strong wind gusts in this box) occur over ocean due to decreased surface friction. Since this thesis is focused more on the dynamics and structure of windstorms this choice for a windstorm threshold is suitable. From an impact point of view, however, it would be valuable to examine windstorms that have caused strong wind gusts over land. The results from this thesis also indicate that windstorms are possibly harder to predict in the warm season when they are rare and have a smaller wind gust footprint than in the cold season when the are more common and the wind gust footprint is larger. However, windstorms in the warm season are likely more damaging and can cause more impacts because the ground is not frozen to anchor the roots of trees and there are leaves on trees causing more area for the wind to grip. Therefore, in the future, windstorms in northern Europe could be studied more from an impact perspective.

Climate change has its impacts also on winds and extratropical cyclones. The low-level meridional temperature gradient will decrease because the polar regions are warming more than lower latitudes (Wang et al., 2017). This reduces the low-level baroclinicity and therefore would lead to less or weaker extratropical cyclones and weaker winds. In contrast, some changes have an effect to strengthen extratropical cyclones. The atmospheric moisture content will increase which enhances the latent heat release which further can intensify the extratropical cyclone and lead to heavier precipitation (Yettella and Kay, 2017). Contradictory to the low-levels, the upper-level meridional temperature will increase since the upper-level troposphere is warming in the tropics while the stratosphere is cooling near the poles (Catto et al., 2019). As there are many atmospheric factors affecting simultaneously to opposite directions in the intensity and frequency of extratropical cyclones the future changes have large uncertainties. The recent Sixth Assessment Report by the Intergovernmental Panel on Climate Change (IPCC) summarises that there is high confidence that precipitation associated with extratropical cyclones will increase due to the increasing atmospheric water vapour (Seneviratne et al., 2021). In addition, IPCC reports medium confidence that changes in the intensity (e.g. wind speeds) of extratropical cyclones will be small, although there can be significant changes locally due to the shift in storm track locations (Seneviratne et al., 2021).

Many studies have shown that the polar, eddy-driven jet stream and storm tracks have shifted poleward following the poleward shift in the low-level baroclinicity due to climate change (e.g. Rivière, 2011; Tamarin-Brodsky and Kaspi, 2017; Gulev et al., 2021). Based on results from **Paper II** and Wickström et al. (2020), this may be seen with less extratropical cyclones overall in northern

Europe. Applying the sensitivity results from **Paper II** to the projected changes due to warming climate, a decrease in low-level temperature gradient would indicate a weaker windstorm whereas an increase in moisture content (in terms of total column water vapour) would indicate a more intense windstorm. In line with these opposing effects, **Paper II** shows no changes in the windstorm frequency in northern Europe. Regarding transitioned cyclones, the tropical cyclones are predicted to become more intense and the tropical cyclone development region will expand poleward and eastward (Haarsma, 2021). This can potentially lead to a higher risk of transitioned cyclones, such as storm Mauri examined in **Paper III**, to northern Europe in the future (Haarsma, 2021). The climate projections to mean and extreme wind speeds in northern Europe and Finland do not show large changes except a small increase in autumn at the end of the century (Ruosteenoja et al., 2019). Although the wind and windstorm climate in northern Europe and Finland would not massively change in the future, the windstorm impacts are likely to increase due to shorter frost season and heavier precipitation. This further highlights the importance of more impact-based windstorm research.

7. Main conclusions

Strong winds can cause significant amount of damage and destruction with high impacts to society. The knowledge of the mean wind climate is necessary in order to understand the extreme winds, their causes and to be able to prepare, both in weather (days) and climate (decades) time scales. This thesis aimed to increase the understanding of the near-surface mean and extreme wind climate and how extratropical cyclones contribute to the extreme winds in northern Europe and Finland.

The wind and windstorm climate in northern Europe and Finland has a large inter-annual and decadal variability and no long-term linear trends. The well-known seasonality was found: winds and windstorms are the strongest and most frequent in winter while high wind events in summer are rare. More unexpectedly, the number of all extratropical cyclones in northern Europe does not vary between seasons. Northern Europe is located at the end of the North Atlantic storm track whereas at the core of the storm track the seasonality of extratropical cyclones is evident. Therefore, this thesis wishes to emphasise that the climatologies of winds, extratropical cyclones and windstorms have regional differences. Furthermore, this thesis underlines the importance of examining longer-term variabilities instead of just focusing on linear trends to get a wider perspective of the climate.

This thesis gives a conceptual model on how northern Europe windstorms develop in the cold and warm seasons. Cold-season windstorms were found to be overall stronger and potentially better predictable than warm-season windstorms. In addition, the spatial extent of the wind gusts in windstorms is larger in the cold season than in the warm season. The strongest wind gusts associated with northern Europe windstorms move and extend from the warm sector to behind the cold front during the evolution. Regarding factors affecting the windstorm intensity, the low-level temperature gradient has the strongest impact. These findings are important considering forecasting, giving wind warnings and preparing for impacts. Investigation of a case study of storm Mauri revealed, however, that an individual windstorm event can vary largely from the general features of the climate. Therefore, conceptual models and case studies are both needed for a deeper understanding of the different development paths of windstorms.

8. Review of papers and the author's contribution

Paper I: The aims of this study were to present the near-surface wind speed climate in the North Atlantic and Europe based on ERA5 reanalysis and to investigate inter-annual and decadal variations and long-term linear trends. The results were examined on a monthly scale to determine seasonal details. In addition, the study aims to find physical reasons for the decadal changes in near-surface wind speeds.

Paper II: The aims of this study were to examine climatological characteristics of extratropical cyclones and windstorms in northern Europe based on ERA5 reanalysis and to investigate precursors to northern Europe windstorms. All extratropical cyclones were tracked with a tracking algorithm and classified to windstorms and non-windstorms based on their associated wind gusts in northern Europe. Cyclone composites were created to determine the structural evolution and seasonal differences were identified. The precursors were examined with an ensemble sensitivity analysis which uses linear regression to find correlations between the precursors and the windstorm intensity.

Paper III: The aim of this study was to get more understanding of the development of a unique windstorm event named storm Mauri that occurred in Finland in 1982. The evolution of ex-hurricane Debby and subsequently developed storm Mauri were investigated with a synoptic overview based on ERA-Interim reanalysis and a more detailed meso- and synoptic-scale analysis with OpenIFS model simulations. In addition, the reasons for the strong winds over Finland were investigated.

The author was the main responsible person in all three papers. In **Paper I**, the author conducted all of the data analysis and wrote most of the paper with the help from other co-authors. In **Paper II**, most of the data analysis and writing of the paper was performed by the author. In **Paper III**, the author analysed most of the reanalysis and model simulation results and wrote the paper together with the co-authors.

REFERENCES

Agustí-Panareda, A., Thorncroft, C. D., Craig, G. C. and Gray, S. L. (2004). The extratropical transition of hurricane Irene (1999): A potential-vorticity perspective. *Quarterly Journal of the Royal Meteorological Society*, **130**: (598), 1047–1074.

Agustí-Panareda, A., Gray, S. L., Craig, G. C. and Thorncroft, C. (2005). The Extratropical Transition of Tropical Cyclone Lili (1996) and Its Crucial Contribution to a Moderate Extratropical Development. *Monthly Weather Review*, **133**: (6), 1562–1573.

Ahmadi-Givi, F., Graig, G. C. and Plant, R. S. (2004). The dynamics of a midlatitude cyclone with very strong latent-heat release. *Quarterly Journal of the Royal Meteorological Society*, **130**: (596), 295–323.

Archambault, H. M., Bosart, L. F., Keyser, D. and Cordeira, J. M. (2013). A Climatological Analysis of the Extratropical Flow Response to Recurving Western North Pacific Tropical Cyclones. *Monthly Weather Review*, **141**: (7), 2325–2346.

Bauer, P., Thorpe, A. and Brunet, G. (2015). The quiet revolution of numerical weather prediction. *Nature*, **525**: (7567), 47–55.

Bjerknes, J. (1919). On the structure of moving cyclones. *Geofys. Publ.*, **1**: (2), 1–8.

Bjerknes, J. and Solberg, H. (1922). Life cycle of cyclones and the polar front theory of atmospheric circulation. *Geofys. Publ.*, **3**: (1), 3–18.

Blackmon, M. L. (1976). A Climatological Spectral Study of the 500 mb Geopotential Height of the Northern Hemisphere. *Journal of the Atmospheric Sciences*, **33**: (8), 1607–1623.

Boettcher, M. and Wernli, H. (2013). A 10-yr Climatology of Diabatic Rossby Waves in the Northern Hemisphere. *Monthly Weather Review*, **141**: (3), 1139–1154.

Boisserie, M., Descamps, L. and Arbogast, P. (2016). Calibrated forecasts of extreme windstorms using the Extreme Forecast Index (EFI) and Shift of Tails (SOT). *Weather and Forecasting*, **31**: (5), 1573–1589.

Browning, K. A., Panagi, P. and Vaughan, G. (1998). Analysis of an ex-tropical cyclone after its reintensification as a warm-core extratropical cyclone. *Quarterly Journal of the Royal Meteorological Society*, **124**: (551), 2329–2356.

Catto, J. L., Ackerley, D., Booth, J. F., Champion, A. J., Colle, B. A., Pfahl, S., Pinto, J. G., Quinting, J. F. and Seiler, C. (2019). The future of midlatitude cyclones. *Current Climate Change Reports*, **5**: (4), 407–420.

Charney, J. G. (1947). The dynamics of long waves in a baroclinic westerly current. *Journal of Atmospheric Sciences*, **4**: (5), 136–162.

Clark, G. B. (1983). Atlantic Hurricane Season of 1982. *Monthly Weather Review*, **111**: (5), 1071–1079.

Dacre, H. F. and Gray, S. L. (2013). Quantifying the climatological relationship between extratropical cyclone intensity and atmospheric precursors. *Geophysical Research Letters*, **40**: (10), 2322–2327.

Dacre, H. F., Martínez-Alvarado, O. and Mbengue, C. O. (2019). Linking atmospheric rivers and warm conveyor belt airflows. *Journal of Hydrometeorology*, **20**: (6), 1183–1196.

Dacre, H., Hawcroft, M., Stringer, M. and Hodges, K. (2012). An extratropical cyclone atlas: A tool for illustrating cyclone structure and evolution characteristics. *Bulletin of the American Meteorological Society*, **93**: (10), 1497–1502.

Dee, D. P., Uppala, S. M., Simmons, A. J., Berrisford, P., Poli, P., Kobayashi, S., Andrae, U., Balmaseda, M. A., Balsamo, G., Bauer, P., Bechtold, P., Beljaars, A. C. M., van de Berg, L., Bidlot, J., Bormann, N., Delsol, C., Dragani, R., Fuentes, M., Geer, A. J., ... Vitart, F. (2011). The ERA-Interim reanalysis: configuration and performance of the data assimilation system. *Quarterly Journal of the Royal Meteorological Society*, **137**: (656), 553–597.

Eady, E. T. (1949). Long waves and cyclone waves. *Tellus*, **1**: (3), 33–52.

ECMWF. (2015). Part IV: Physical Processes [Operational implementation 12 May 2015]. *Ifs documentation cy41r1* (pp. 1–190). ECMWF.

Evans, C., Wood, K. M., Aberson, S. D., Archambault, H. M., Milrad, S. M., Bosart, L. F., Corbosiero, K. L., Davis, C. A., Dias Pinto, J. R., Doyle, J., Fogarty, C., Galarneau, T. J., Grams, C. M., Griffin, K. S., Gyakum, J., Hart, R. E., Kitabatake, N., Lentink, H. S., McTaggart-Cowan, R., ... Zhang, F. (2017). The Extratropical Transition of Tropical Cyclones. Part I: Cyclone Evolution and Direct Impacts. *Monthly Weather Review*, **145**: (11), 4317–4344.

Evans, J. L. and Hart, R. E. (2003). Objective Indicators of the Life Cycle Evolution of Extratropical Transition for Atlantic Tropical Cyclones. *Monthly Weather Review*, **131**: (5), 909–925.

Feser, F., Barcikowska, M., Krueger, O., Schenk, F., Weisse, R. and Xia, L. (2015). Storminess over the North Atlantic and northwestern Europe—A review. *Quarterly Journal of the Royal Meteorological Society*, **141**: (687), 350–382.

Froude, L. S. R. (2010). TIGGE: Comparison of the Prediction of Northern Hemisphere Extratropical Cyclones by Different Ensemble Prediction Systems. *Weather and Forecasting*, **25**: (3), 819–836.

Froude, L. S., Bengtsson, L. and Hodges, K. I. (2007). The predictability of extratropical storm tracks and the sensitivity of their prediction to the observing system. *Monthly Weather Review*, **135**: (2), 315–333.

Galarneau, T. J., Davis, C. A. and Shapiro, M. A. (2013). Intensification of Hurricane Sandy (2012) through extratropical warm core seclusion. *Monthly Weather Review*, **141**: (12), 4296–4321.

Garcies, L. and Homar, V. (2009). Ensemble sensitivities of the real atmosphere: application to Mediterranean intense cyclones. *Tellus A*, **61**: (3), 394–406.

Grams, C. M., Jones, S. C., Davis, C. A., Harr, P. A. and Weissmann, M. (2013). The impact of Typhoon Jangmi (2008) on the midlatitude flow. Part I: Upper-level ridgebuilding and modification of the jet. *Quarterly Journal of the Royal Meteorological Society*, **139**: (677), 2148–2164.

Grams, C. M., Wernli, H., Böttcher, M., Čampa, J., Corsmeier, U., Jones, S. C., Keller, J. H., Lenz, C.-J. and Wiegand, L. (2011). The key role of diabatic processes in modifying the upper-tropospheric wave guide: a North Atlantic case-study. *Quarterly Journal of the Royal Meteorological Society*, **137**: (661), 2174–2193.

Gregow, H., Laaksonen, A. and Alper, M. E. (2017). Increasing large scale windstorm damage in Western, Central and Northern European forests, 1951–2010. *Scientific Reports*, **7**: (46397).

Gulev, S., Thorne, P., Ahn, J., Dentener, F., Domingues, C., Gerland, S., Gong, D., Kaufman, D., Nnamchi, H., Quaas, J., Rivera, J., Sathyendranath, S., Smith, S., Trewin, B., von Schuckmann, K. and Vose, R. (2021). Changing state of the climate system [In Press]. *Climate Change 2021: The Physical Science Basis. Contribution of Working Group I to the Sixth Assessment Report*

of the Intergovernmental Panel on Climate Change. Cambridge University Press.

Haarsma, R. (2021). European Windstorm Risk of Post-Tropical Cyclones and the Impact of Climate Change. *Geophysical Research Letters*, **48**: (4), e2020GL091483.

Hart, R. E. (2003). A Cyclone Phase Space Derived from Thermal Wind and Thermal Asymmetry. *Monthly Weather Review*, **131**: (4), 585–616.

Hart, R. E. and Evans, J. L. (2001). A climatology of the extratropical transition of Atlantic tropical cyclones. *Journal of Climate*, **14**: (4), 546–564.

Hawcroft, M. K., Shaffrey, L. C., Hodges, K. I. and Dacre, H. F. (2012). How much Northern Hemisphere precipitation is associated with extratropical cyclones? *Geophysical Research Letters*, **39**: (24).

Held, I. M. (1975). Momentum transport by quasi-geostrophic eddies. *Journal of the Atmospheric Sciences*, **32**: (7), 1494–1497.

Held, I. M. and Hou, A. Y. (1980). Nonlinear axially symmetric circulations in a nearly inviscid atmosphere. *Journal of the Atmospheric Sciences*, **37**: (3), 515–533.

Hersbach, H., Bell, B., Berrisford, P., Hirahara, S., Horányi, A., Muñoz-Sabater, J., Nicolas, J., Peubey, C., Radu, R., Schepers, D., Simmons, A., Soci, C., Abdalla, S., Abellan, X., Balsamo, G., Bechtold, P., Biavati, G., Bidlot, J., Bonavita, M., … Thépaut, J.-N. (2020). The ERA5 Global Reanalysis. *Quarterly Journal of the Royal Meteorological Society*, **146**: (730), 1999–2049.

Hewson, T. D. and Neu, U. (2015). Cyclones, windstorms and the IMILAST project. *Tellus A: Dynamic Meteorology and Oceanography*, **67**: (1), 27128.

Hodges, K. I. (1994). A General Method for Tracking Analysis and Its Application to Meteorological Data. *Monthly Weather Review*, **122**: (11), 2573–2586.

Hodges, K. I. (1995). Feature Tracking on the Unit Sphere. *Monthly Weather Review*, **123**: (12), 3458–3465.

Hodges, K. I. (1999). Adaptive Constraints for Feature Tracking. *Monthly Weather Review*, **127**: (6), 1362–1373.

Hodges, K. I., Lee, R. W. and Bengtsson, L. (2011). A comparison of extratropical cyclones in recent reanalyses ERA-Interim, NASA MERRA, NCEP CFSR, and JRA-25. *Journal of Climate*, **24**: (18), 4888–4906.

Holley, D. M. (2021). The impacts of Storm Odette in eastern England, 24–26 September 2020. *Weather*, **76**: (3), 86–88.

Hoskins, B. J. and Hodges, K. I. (2019). The Annual Cycle of Northern Hemisphere Storm Tracks. Part I: Seasons. *Journal of Climate*, **32**: (6), 1743–1760.

Hoskins, B. J., McIntyre, M. E. and Robertson, A. W. (1985). On the use and significance of isentropic potential vorticity maps. *Quarterly Journal of the Royal Meteorological Society*, **111**: (470), 877–946.

Hoskins, B. J. and Hodges, K. I. (2002). New Perspectives on the Northern Hemisphere Winter Storm Tracks. *Journal of the Atmospheric Sciences*, **59**: (6), 1041–1061.

Jones, S. C., Harr, P. A., Abraham, J., Bosart, L. F., Bowyer, P. J., Evans, J. L., Hanley, D. E., Hanstrum, B. N., Hart, R. E., Lalaurette, F., Sinclair, M. R., Smith, R. K. and Thorncroft, C. (2003). The Extratropical Transition of Tropical Cyclones: Forecast Challenges, Current Understanding, and Future Directions. *Weather and Forecasting*, **18**: (6), 1052–1092.

Keller, J. H., Grams, C. M., Riemer, M., Archambault, H. M., Bosart, L., Doyle, J. D., Evans, J. L., Galarneau, T. J., Griffin, K., Harr, P. A., Kitabatake, N., McTaggart-Cowan, R., Pantillon, F., Quinting, J. F., Reynolds, C. A., Ritchie, E. A., Torn, R. D. and Zhang, F. (2019). The Extratropical Transition of Tropical Cyclones. Part II: Interaction with the Midlatitude Flow, Downstream Impacts, and Implications for Predictability. *Monthly Weather Review*, **147**: (4), 1077–1106.

Kendall, M. G. (1970). *Rank Correlation Methods*. Griffin: London.

Klein, P. M., Harr, P. A. and Elsberry, R. L. (2000). Extratropical Transition of Western North Pacific Tropical Cyclones: An Overview and Conceptual Model of the Transformation Stage. *Weather and Forecasting*, **15**: (4), 373–395.

Kufeoglu, S. and Lehtonen, M. (2014). Cyclone Dagmar of 2011 and its impacts in Finland. *IEEE PES Innovative Smart Grid Technologies, Europe*, 1–6.

Laapas, M. and Venäläinen, A. (2017). Homogenization and trend analysis of monthly mean and maximum wind speed time series in Finland, 1959–2015. *International Journal of Climatology*, **37**: (14), 4803–4813.

Laffineur, T., Claud, C., Chaboureau, J.-P. and Noer, G. (2014). Polar lows over the Nordic Seas: improved representation in ERA-Interim compared to ERA-40 and the impact on downscaled simulations. *Monthly Weather Review*, **142**: (6), 2271–2289.

Lorenz, E. N. (1955). Available potential energy and the maintenance of the general circulation. *Tellus*, **7**: (2), 157–167.

Ma, S., Ritchie, H., Abraham, J., Gyakum, J., McTaggart-Cowan, R. and Fogarty, C. (2003). A study of the extratropical reintensification of former Hurricane Earl using Canadian Meteorological Centre regional analyses and ensemble forecasts. *Monthly Weather Review*, **131**: (7), 1342–1359.

Mann, H. B. (1945). Nonparametric tests against trend. *Econometrica*, **13**: 245–259.

Martínez-Alvarado, O., Gray, S. L. and Methven, J. (2016). Diabatic processes and the evolution of two contrasting summer extratropical cyclones. *Monthly Weather Review*, **144**: (9), 3251–3276.

Minola, L., Zhang, F., Azorin-Molina, C., Pirooz, A. A. S., Flay, R. G. J., Hersbach, H. and Chen, D. (2020). Near-surface mean and gust wind speeds in ERA5 across Sweden: towards an improved gust parametrization. *Climate Dynamics*, **55**: (3), 887–907.

Moore, R. W. and Montgomery, M. T. (2004). Reexamining the Dynamics of Short-Scale, Diabatic Rossby Waves and Their Role in Midlatitude Moist Cyclogenesis. *Journal of the Atmospheric Sciences*, **61**: (6), 754–768.

Moore, R. W. and Montgomery, M. T. (2005). Analysis of an Idealized, Three-Dimensional Diabatic Rossby Vortex: A Coherent Structure of the Moist Baroclinic Atmosphere. *Journal of the Atmospheric Sciences*, **62**: (8), 2703–2725.

Munich Re. (2017). Geo Risks Research, NatCatSERVICE [Available at: http://natcatservice.munichre.com/].

Murray, R. J. and Simmonds, I. (1991). A numerical scheme for tracking cyclone centres from digital data. *Australian Meteorological Magazine*, **39**: (3), 155–166.

Neu, U., Akperov, M. G., Bellenbaum, N., Benestad, R., Blender, R., Caballero, R., Cocozza, A., Dacre, H. F., Feng, Y., Fraedrich, K. et al. (2013). IMILAST: a community effort to intercompare extratropical cyclone detection and tracking algorithms. *Bulletin of the American Meteorological Society*, **94**: (4), 529–547.

Palmén, E. (1958). Vertical circulation and release of kinetic energy during the development of Hurricane Hazel into an extratropical storm. *Tellus A,* **10**: (1).

Pantillon, F., Knippertz, P. and Corsmeier, U. (2017). Revisiting the synoptic-scale predictability of severe European winter storms using ECMWF ensemble reforecasts. *Natural Hazards and Earth System Sciences*, **17**: (10), 1795–1810.

Pezza, A., Sadler, K., Uotila, P., Vihma, T., Mesquita, M. D. and Reid, P. (2016). Southern Hemisphere strong polar mesoscale cyclones in high-resolution datasets. *Climate Dynamics*, **47**: (5-6), 1647–1660.

Priestley, M. D. K., Ackerley, D., Catto, J. L., Hodges, K. I., McDonald, R. E. and Lee, R. W. (2020). An Overview of the Extratropical Storm Tracks in CMIP6 Historical Simulations. *Journal of Climate*, **33**: (15), 6315–6343.

Rantanen, M., Laurila, T. K., Sinclair, V. A. and Gregow, H. (2021). Storm Aila : An unusually strong autumn storm in Finland. *Weather*, **76**: (9), 306–312.

Rantanen, M., Räisänen, J., Sinclair, V. A., Lento, J. and Järvinen, H. (2020). The extratropical transition of Hurricane Ophelia (2017) as diagnosed with a generalized omega equation and vorticity equation. *Tellus A: Dynamic Meteorology and Oceanography*, **72**: (1), 1–26.

Riboldi, J., Grams, C. M., Riemer, M. and Archambault, H. M. (2019). A phase locking perspective on Rossby wave amplification and atmospheric blocking downstream of recurving western North Pacific tropical cyclones. *Monthly Weather Review*, **147**: (2), 567–589.

Riemer, M., Jones, S. C. and Davis, C. A. (2008). The impact of extratropical transition on the downstream flow: An idealized modelling study with a straight jet. *Quarterly Journal of the Royal Meteorological Society*, **134**: (630), 69–91.

Ritchie, E. A. and Elsberry, R. L. (2007). Simulations of the Extratropical Transition of Tropical Cyclones: Phasing between the Upper-Level Trough and Tropical Cyclones. *Monthly Weather Review*, **135**: (3), 862–876.

Rivière, G. (2011). A dynamical interpretation of the poleward shift of the jet streams in global warming scenarios. *Journal of the Atmospheric Sciences*, **68**: (6), 1253–1272.

Rudeva, I. and Gulev, S. K. (2007). Climatology of cyclone size characteristics and their changes during the cyclone life cycle. *Monthly Weather Review*, **135**: (7), 2568–2587.

Ruosteenoja, K., Vihma, T. and Venäläinen, A. (2019). Projected changes in European and North Atlantic seasonal wind climate derived from CMIP5 simulations. *Journal of Climate*, **32**: (19), 6467–6490.

Sainsbury, E. M., Schiemann, R. K. H., Hodges, K. I., Shaffrey, L. C., Baker, A. J. and Bhatia, K. T. (2020). How Important Are Post-Tropical Cyclones for European Windstorm Risk? *Geophysical Research Letters*, **47**: (18), e2020GL089853.

Schultz, D. M., Keyser, D. and Bosart, L. F. (1998). The effect of large-scale flow on low-level frontal structure and evolution in midlatitude cyclones. *Monthly weather review*, **126**: (7), 1767–1791.

Seneviratne, S., Zhang, X., Adnan, M., Badi, W., Dereczynski, C., Luca, A. D., Ghosh, S., Iskandar, I., Kossin, J., Lewis, S., Otto, F., Pinto, I., Satoh, M., Vicente-Serrano, S., Wehner, M. and Zhou, B. (2021). Weather and Climate Extreme Events in a Changing Climate [In Press]. *Climate Change 2021: The Physical Science Basis. Contribution of Working Group I to the Sixth Assessment Report of the Intergovernmental Panel on Climate Change*. Cambridge University Press.

Shapiro, M. A. and Keyser, D. (1990). Fronts, jet streams and the tropopause. *Extratropical cyclones: The erik palmén memorial volume* (pp. 167–191). C. Newton; E. O. Holopainen, Eds., Amer. Meteor. Soc.

Simmonds, I. (2000). Size changes over the life of sea level cyclones in the NCEP reanalysis. *Monthly Weather Review*, **128**: (12), 4118–4125.

Sinclair, V. A., Rantanen, M., Haapanala, P., Räisänen, J. and Järvinen, H. (2020). The characteristics and structure of extra-tropical cyclones in a warmer climate. *Weather and Climate Dynamics*, **1**: (1), 1–25.

Stewart, S. R. (2018). *Tropical Cyclone Report, Hurricane Ophelia* (tech. rep.). National Hurricane Center.

Suursaar, U., Kullas, T., Otsmann, M., Saaremae, I., Kuik, J. and Merilain, M. (2006). Cyclone Gudrun in January 2005 and modelling its hydrodynamic consequences in the Estonian coastal waters. *Boreal Environment Research*, **11**: (2), 143.

Szépszó, G. and Carver, G. (2018). New forecast evaluation tool for OpenIFS. *ECMWF Newsletter*, **156**: 14–15.

Szépszó, G., Sinclair, V. and Carver, G. (2019). Using the ECMWF OpenIFS model and state-of-the-art training techniques in meteorological education. *Advances in Science and Research*, **16**: 39–47.

Tamarin-Brodsky, T. and Kaspi, Y. (2017). Enhanced poleward propagation of storms under climate change. *Nature geoscience*, **10**: (12), 908–913.

Tervo, R., Láng, I., Jung, A. and Mäkelä, A. (2021). Predicting power outages caused by extratropical storms. *Natural Hazards and Earth System Sciences*, **21**: (2), 607–627.

Thorncroft, C. and Jones, S. C. (2000). The Extratropical Transitions of Hurricanes Felix and Iris in 1995. *Monthly Weather Review*, **128**: (4), 947–972.

Thyness, V., Homleid, M., Køltzow, M. and Lien, T. (2017). *Application and verification of ECMWF products 2017* (tech. rep.). Norwegian Meteorological Institute.

Ulbrich, U., Fink, A., Klawa, M. and Pinto, J. G. (2001). Three extreme storms over Europe in December 1999. *Weather*, **56**: (3), 70–80.

Ulbrich, U., Leckebusch, G. and Pinto, J. G. (2009). Extra-tropical cyclones in the present and future climate: a review. *Theoretical and Applied Climatology*, **96**: (1), 117–131.

Uotila, P., Pezza, A., Cassano, J., Keay, K. and Lynch, A. (2009). A comparison of low pressure system statistics derived from a high-resolution NWP output and three reanalysis products over the Southern Ocean. *Journal of Geophysical Research: Atmospheres*, **114**: (D17).

Vautard, R., Cattiaux, J., Yiou, P., Thépaut, J.-N. and Ciais, P. (2010). Northern Hemisphere atmospheric stilling partly attributed to an increase in surface roughness. *Nature Geoscience*, **3**: 756–761.

Wang, J., Kim, H.-M. and Chang, E. K. (2017). Changes in Northern Hemisphere winter storm tracks under the background of Arctic amplification. *Journal of Climate*, **30**: (10), 3705–3724.

Wernli, H., Dirren, S., Liniger, M. A. and Zillig, M. (2002). Dynamical aspects of the life cycle of the winter storm 'Lothar' (24–26 December 1999). *Quarterly Journal of the Royal Meteorological Society*, **128**: (580), 405–429.

Wernli, H. and Schwierz, C. (2006). Surface cyclones in the ERA-40 dataset (1958–2001). Part I: Novel identification method and global climatology. *Journal of the atmospheric sciences*, **63**: (10), 2486–2507.

Wickström, S., Jonassen, M. O., Vihma, T. and Uotila, P. (2020). Trends in cyclones in the high-latitude North Atlantic during 1979–2016. *Quarterly Journal of the Royal Meteorological Society*, **146**: (727), 762–779.

Wu, J., Zha, J., Zhao, D. and Yang, Q. (2018). Changes in terrestrial near-surface wind speed and their possible causes: an overview. *Climate Dynamics*, **51**: 2039–2078.

Yettella, V. and Kay, J. E. (2017). How will precipitation change in extratropical cyclones as the planet warms? Insights from a large initial condition climate model ensemble. *Climate Dynamics*, **49**: (5), 1765–1781.

Zeng, Z., Ziegler, A. D., Searchinger, T., Yang, L., Chen, A., Ju, K., Piao, S., Li, L. Z. X., Ciais, P., Chen, D., Liu, J., Azorin-Molina, C., Chappell, A., Medvigy, D. and Wood, E. F. (2019). A reversal in global terrestrial stilling and its implications for wind energy production. *Nature Climate Change*, **9**: 979–985.

I

International Journal of Climatology, 41(4), 2253–2278,
doi:10.1002/joc.6957

Received: 15 July 2020 | Revised: 30 October 2020 | Accepted: 30 November 2020

DOI: 10.1002/joc.6957

RESEARCH ARTICLE

International Journal of Climatology RMetS

Climatology, variability, and trends in near-surface wind speeds over the North Atlantic and Europe during 1979–2018 based on ERA5

Terhi K. Laurila[1] | **Victoria A. Sinclair**[2] | **Hilppa Gregow**[1]

[1]Weather and Climate Change Impact Research, Finnish Meteorological Institute, Helsinki, Finland

[2]Institute for Atmospheric and Earth System Research/Physics, Faculty of Science, University of Helsinki, Helsinki, Finland

Correspondence
Terhi K. Laurila, Weather and Climate Change Impact Research, Finnish Meteorological Institute, Helsinki, Finland.
Email: terhi.laurila@fmi.fi

Funding information
Academy of Finland, Grant/Award Numbers: 303951, 307331; ERA4CS WINDSURFER; MONITUHO; Satakunnan Rahasto, Grant/Award Number: 75181580

Abstract

This study presents the monthly 10-m wind speed climatology, decadal variability and possible trends in the North Atlantic and Europe from ERA5 reanalysis from 1979 to 2018 and investigates the physical reasons for the decadal variability. Additionally, temporal time series are examined in three locations: the central North Atlantic, Finland and Iberian Peninsula. The 40-year mean and the 98th percentile wind speeds emphasize a distinct land-sea contrast and a seasonal variation with the strongest winds over the ocean and during winter. The strongest winds and the highest variability are associated with the storm tracks and local wind phenomena such as the mistral. The extremeness of the winds is examined with an extreme wind factor (the 98th percentile divided by mean wind speeds) which in all months is higher in southern Europe than in northern Europe. Mostly no linear trends in 10-m wind speeds are identified in the three locations but large annual and decadal variability is evident. The decadal 10-m wind speeds were stronger than average in the 1990s in northern Europe and in the 1980s and 2010s in southern Europe. These decadal changes were largely explained by the positioning of the jet stream and storm tracks and the strength of the north–south pressure gradient in the North Atlantic. The 10-m winds have a positive correlation with the North Atlantic Oscillation in the central North Atlantic and Finland on annual scales and during cold season months and a negative correlation in Iberian Peninsula mostly from July to March. The Atlantic Multi-decadal Oscillation has a moderate negative correlation with the winds in the central North Atlantic but no correlation in Finland and Iberian Peninsula. Overall, our results emphasize that while linear trends in wind speeds may show a general long-term trend, more information on the changes is obtained by analysing long-term variability.

KEYWORDS

climate, climatology, ERA5, trends, variability, wind speed

1 | INTRODUCTION

The knowledge of long-term climatology and variability of 10-m wind speeds is valuable for meteorologists and climate scientists. For example, forecasters need to know the mean wind climate in order to estimate the local extremeness in wind forecasts, and climate model simulations are typically compared and validated against the long-term mean climate. The near-surface winds have an important role in advection and surface fluxes to transfer heat and moisture horizontally and vertically between the atmosphere and the surface. Moreover, information of the near-surface wind speed climate and variability is essential for industries that are dependant or affected by winds such as wind energy, forestry and insurance. For example, Gregow *et al*. (2016) highlight the energy sector's desire for higher resolution and accurate wind datasets.

In addition to global and regional wind atlases, reanalyses are a relevant source for wind assessments. Reanalysis systems provide a consistent analysis of the atmospheric state and aim to utilize observations as extensively as possible (Dee *et al*., 2014). Such datasets are well suited to wind assessments due to their global coverage, homogeneous data and long time periods. Previous studies (e.g., Kaiser-Weiss *et al*., 2015, 2019) have compared in-situ surface wind observations to reanalysis and, in general, it has been shown that the frequency distributions of mean wind speeds are well captured in reanalysis. The long-term wind speed variability and/or trends have been studied with many different reanalyses—e.g., ERA-Interim, MERRA-2, and JRA-55 (Torralba *et al*., 2017), NOAA-20CR (Bett *et al*., 2013) and ERA-40 (Kiss and Jánosi, 2008)—but not yet with the new ERA5 reanalysis (Hersbach *et al*., 2020). The knowledge of the mean climate in ERA5 is needed since it will most likely be used as a basis to compare both historical runs and future projections from climate models (e.g., Priestley *et al*., 2020). Furthermore, ERA5 has been found to outperform MERRA-2 in the wind power modelling (Olauson, 2018) and hence, ERA5 is likely to be used in many wind-related applications.

The long-term surface wind speeds over land have shown a decreasing trend, termed stilling, over the last few decades in 1979–2008 (Vautard *et al*., 2010). However, a reversal in global stilling has been detected after 2010 (Zeng *et al*., 2019). The timing of this reversal varies in different regions and in Europe, the turning point was obtained in 2003 (Zeng *et al*., 2019). Vautard *et al*. (2010) found that 10–50% of the stilling can be explained by atmospheric circulation changes and 25–60% by an increase in surface roughness. Similarly, a recent review by Wu *et al*. (2018) summarizes that the long-term terrestrial wind speed changes are caused by the driving forces (atmospheric circulation) and drag forces (surface friction such as land use and cover change and urbanization, and boundary layer conditions). However, since there are no sudden surface roughness changes in 2010 although a reversal was found, Zeng *et al*. (2019) suggest that the wind speed variability is mainly associated with the decadal variations in large-scale ocean-atmospheric circulations, such as the North Atlantic Oscillation (NAO) in Europe, the Pacific Decadal Oscillation in Asia and the Tropical Northern Atlantic Index in North America.

Previously, climatological studies of 10-m wind speeds (e.g., Bett *et al*., 2013, 2017) have mainly concentrated on long-term linear trends and the variability has been examined over the whole time period with statistical measures (e.g., the standard deviation). Variations of the wind climate between different decades has received less attention and often the decadal variability can be determined from time series using techniques such as Gaussian low-pass filters (Azorin-Molina *et al*., 2014; Minola *et al*., 2016) or piecewise linear regression models (Zeng *et al*., 2019). Such station-based time series studies have been examined separately in multiple European countries (e.g., Azorin-Molina *et al*., 2014; Minola *et al*., 2016; Laapas and Venäläinen, 2017, Zahradníček *et al*., 2019). However, a decadal analysis over a larger domain would provide new information on the large-scale spatial patterns and their changes in each decade. Furthermore, the decadal analysis of 10-m wind speeds can then be compared to spatial and decadal patterns in other atmospheric variables, such as upper-level winds and mean sea level pressure, to study the reasons behind the decadal changes.

Longer range predictions of 10-m wind speeds on multiple time scales (months, years, decades) give value in long-term planning, adaptation and preparedness in societies and many sectors since extreme winds can cause diverse impacts, for example, uproot trees in forests (Gardiner *et al*., 2010; Usbeck *et al*., 2012; Gregow *et al*., 2017) or generate high waves which impact coastlines and offshore infrastructure (Vose *et al*., 2014). As long-term variations in 10-m wind speeds are influenced by changes in the atmospheric circulation, seasonal forecasts of near-surface winds are often based on indices that describe the large-scale atmospheric patterns (Scaife *et al*., 2014). For the North Atlantic and Europe region, a commonly used index is the NAO which is a key source of seasonal predictability skill in many European regions (Scaife *et al*., 2014). On decadal and climatological scales, the Atlantic Multi-decadal Oscillation (AMO) could possibly give some value since the periodical cycle of the AMO is around 70 years (Zhang *et al*., 2019).

The first aim of this study is to present the wind speed climate in the North Atlantic and Europe based on ERA5 and to identify any long-term linear trends. In contrast to many earlier studies, we present monthly averages rather than seasonal or annual averages which likely suppress variability or disguise details. The second aim is to determine if there are decadal variations in the 10-m mean and extreme wind speeds. Since wind speed has a large year-to-year variability, and potentially long-term oscillations, the decadal analysis provides considerably more information than the linear trends. The third and final aim is to investigate physical reasons for possible wind speed changes on the decadal scale in the North Atlantic and Europe, which we do by examining whether 10-m wind speeds correlate with other atmospheric variables and climatic indices. The remainder of this paper is structured as follows. Section 2 describes the data and methods that we use, the wind speed climate is presented in Section 3 and wind speed variability and trends in Section 4. In Section 5 we investigate the physical reasons for the wind speed changes, and finally the conclusions are given in Section 6.

2 | DATA AND METHODS

2.1 | ERA5 reanalysis

ERA5 is the fifth generation atmospheric reanalysis from the European Centre for Medium Range Weather Forecasts (Hersbach *et al*., 2020). ERA5 uses the Integrated Forecasting System (IFS, cycle 41r2) and includes atmosphere, land surface and ocean wave models. In addition to the improved data assimilation system compared to its predecessor ERA-Interim (Dee *et al*., 2011), ERA5 has a higher spatial and temporal resolution. The horizontal resolution in ERA5 is approximately 31 km (TL639 in spectral space) and it has 137 vertical levels (from surface to around 80 km). The analysis and forecast fields are available hourly. Currently ERA5 covers the time period from 1979 onwards but is expected to finally be available from 1950.

In this study, we used 6-hourly data from 1979 to 2018 with 0.25° (∼31 km) horizontal resolution. The variables we obtained are instantaneous 10-m and 300-hPa horizontal wind components and mean sea level pressure.

2.2 | NAO and AMO indices

The NAO (North Atlantic Oscillation) index describes the large-scale circulation pattern in the North Atlantic. When NAO is positive, there is a larger than average pressure difference between the northern and southern Atlantic resulting in warmer, wetter and generally more stormy conditions in northern Europe (Hurrell, 1995). A traditional way to quantify the NAO is to calculate the pressure difference between Iceland and the Azores, however, a station-based method may not capture the large-scale spatial pattern and can be noisy. Hence, it is more common to use a principal component -based method to reduce these limitations. The NAO index used in this study is calculated by applying the Rotated Principal Component Analysis to the monthly standardized 500-hPa height anomalies which is produced by the Climate Prediction Center at the National Oceanic Atmospheric Administration (NOAA, 2020*a*).

The AMO (Atlantic Multi-decadal Oscillation) index describes the sea surface temperature (SST) variability in the North Atlantic. When AMO is in the positive phase, SSTs in the North Atlantic are warmer than on average. This affects Europe during summertime leading to wetter conditions over central and eastern Europe and drought conditions in parts of southern, western and Northern Europe (Ionita *et al*., 2012). However, Yamamoto and Palter (2016) found that during winter the thermodynamic response of AMO to European weather is overruled by the dynamical response from NAO. In this study we use the AMO index calculated from the Kaplan SST dataset (Kaplan *et al*., 1998) detrended and area-averaged over the Atlantic between 0 and 70°N (Enfield *et al*., 2001; NOAA, 2020*b*).

2.3 | Diagnostics and trend analysis

In this study, we consider the wind climatology over the 40-year period (1979–2018). For each month, we calculated the mean (WS_{mean}), the 98th percentile (WS_{98}), standard deviation, and the extreme wind factor (EWF) from the 6-hourly winds, and we define

$$EWF = \frac{WS_{98}}{WS_{mean}}. \quad (1)$$

The standard deviation measures the variations in the mean climate whereas the EWF emphasizes how extreme the extreme winds are relative to the mean at each individual grid point. By definition, EWF must always exceed one as the 98th percentile wind speed is always greater than the mean wind. If the EWF is much larger than one the 98th percentile winds are much stronger than the mean winds implying that the wind speed distribution is wide with a large positive tail. In contrast, a EWF close to one indicates that the 98th percentile winds are not that

extreme compared to the mean and the wind speed distribution is narrow. Therefore, higher EWF values likely lead to more wind damage and impacts.

To examine the decadal variation, we divided the climatological period to four 10-year periods (1979–1988, 1989–1998, 1999–2008, 2009–2018) and calculated the 10-year means separately for each month. Hereinafter these time periods are referred to as 1980s, 1990s, 2000s and 2010s for clarity although the years do not exactly match the decades. The wind speed variation is analysed with relative anomalies (10-year mean value minus 40-year mean value divided by 40-year mean value) whereas the EWF variation is analysed relative to the climatological mean (10-year EWF minus 40-year mean wind speed). We present the monthly results from the cold season (September–February) and the other months are given in the Supporting Information (Figures S1–S4).

In addition to the monthly decadal variability in the North Atlantic and Europe domain, we analysed wind speed time series in more detail in three locations: in the central North Atlantic in the region with the strongest winds, and over land separately in northern and southern parts of Europe where we found opposite wind anomalies in many decades. More precisely, the chosen coordinates for the locations are the central North Atlantic (20–40°W, 45–60°N), Finland (20–30°E, 60–70°N) and Iberian Peninsula (0–9°W, 37–43°N) and the locations are shown as boxes in Figure 1. The time series were produced by first calculating a statistical value (mean, 98th percentile, maximum, standard deviation or EWF) at each grid point and then averaging the values over all grid points in each longitude–latitude box. Since the box over the central North Atlantic is bigger than the ones over Europe, the variability is smoother due to bigger area averaging.

To identify the temporal trends in the three boxes, we applied the Mann-Kendall test (Mann, 1945; Kendall, 1970) which can be used to test the statistical significance of the trends. The magnitude of the trends was determined from the Theil-Sen's slope estimator (Theil, 1950; Sen, 1968). Both the Mann–Kendall test and the Theil-Sen's slope are nonparametric and distribution-free methods. In addition to the trends, we correlated monthly and annual wind speed time series and NAO and AMO indices by using linear least-squares regression and the Wald test. Both the trends and correlations were tested at the significance level of 5% (p-value <0.05).

To investigate the physical reasons, we first investigate the monthly correlation between 10-m and 300-hPa wind speeds (representative of the jet stream level) primarily to determine if the 300-hPa winds are a dominant reason for the 10-m wind speed spatial variability. The 10-m winds are harder to forecast, even at the very short lead times, than 300-hPa wind speeds. In addition, climate models, which are run at coarse resolution, may not accurately capture the current 10-m wind speed climate or future changes. Therefore, by examining the correlation between 10-m and 300-hPa wind speeds, we test whether the 300-hPa wind speeds could be used as a proxy for 10-m winds on monthly scales which further could give potential for extended and longer range forecasting. Secondly, the decadal 10-m wind speed anomalies in February are examined in relation to anomalies of the 300-hPa wind speed, storm tracks and mean sea level pressure (MSLP) to further assess the physical reasons for the decadal variability. This month was chosen because the wind speed anomalies at the decadal scale were the largest in February (shown in Figure 6). Lastly, we investigate whether the temporal variability in 10-m wind speeds at the three locations is correlated with the NAO and AMO.

Storm tracks are commonly analysed with the Eulerian diagnostic of bandpass-filtering (Blackmon, 1976). In our study, we analysed the storm tracks by using the Eulerian measure to 6-hourly MSLP from 1979 to 2018 from ERA5. First, we detrended the MSLP data and then processed the data with 2–6 day bandpass filter. From the bandpass-filtered MSLP, we calculated the monthly standard deviation for the 10-year periods as well as the whole 40-year period.

3 | WIND SPEED CLIMATE

The monthly mean 10-m wind speed over the 40-year period (1979–2018) shows a clear land-sea gradient and a seasonal variation with the strongest winds over the ocean areas and during winter months (Figure 1). Over the North Atlantic, the strongest mean wind speeds during winter months exceed 12 $m \cdot s^{-1}$ whereas in July the highest monthly mean wind speeds are below 8 $m \cdot s^{-1}$. The area of strongest wind speeds over the North Atlantic between 10–50°W and 40–60°N is associated with the main North Atlantic storm track region (contours in Figure 1). During summer months, there is a noticeable area of low wind speeds over the southern North Atlantic between 20–40°W and 25–35°N. These calm winds at the horse latitudes are caused by the divergence between prevailing westerlies on the northern side and trade winds on the southern side.

Over land areas in Europe, the absolute mean wind speed difference between winter and summer months is not as high as over the ocean, mostly between 1 and 2 $m \cdot s^{-1}$ (Figure 1). However, the relative difference is similar with mean winds in winter being around 1.5 times stronger than in summer. There is a narrow band of higher wind speeds spreading horizontally over central

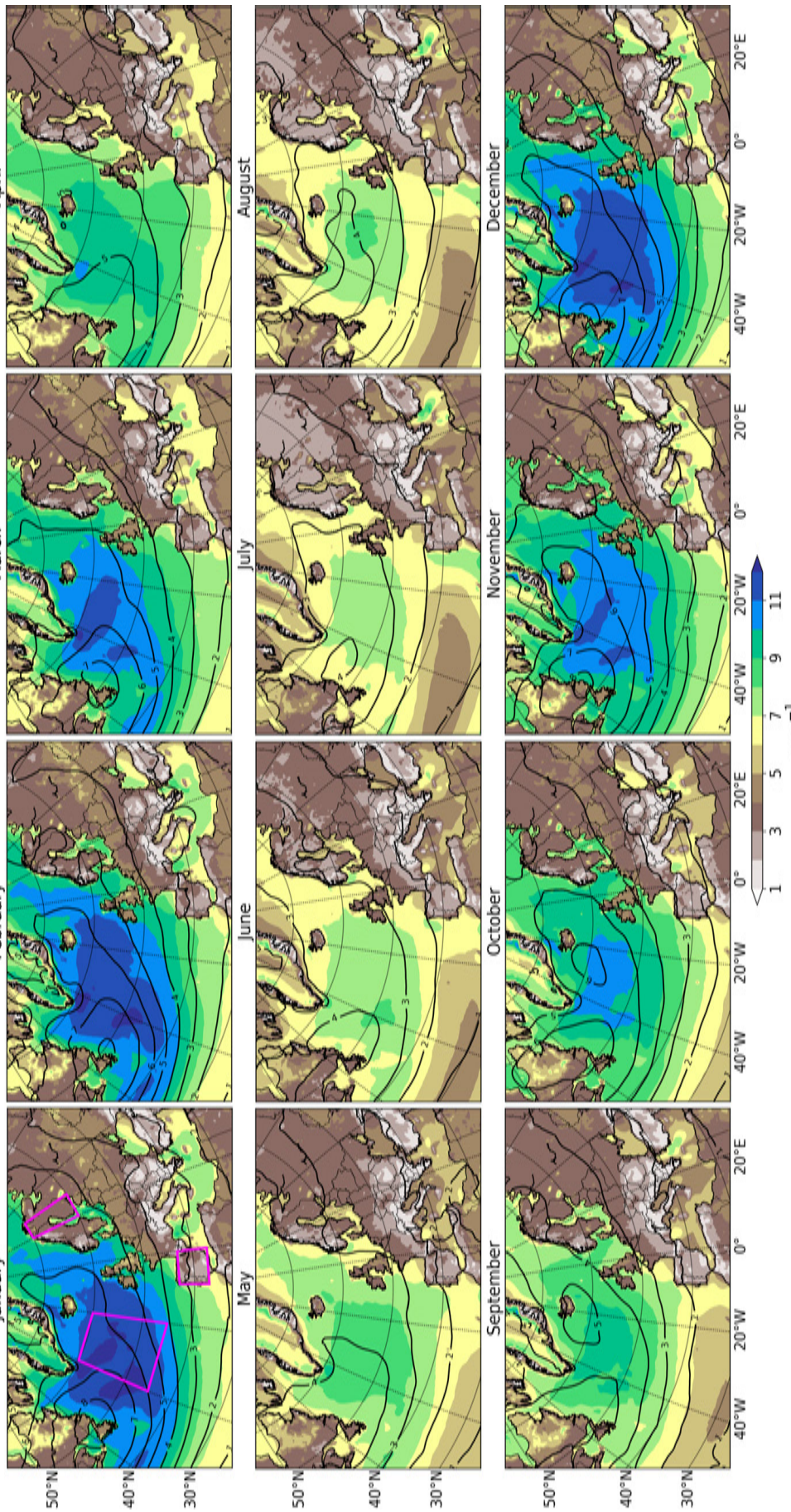

FIGURE 1 Monthly mean values of 10-m wind speed (colours, $m \cdot s^{-1}$) and standard deviation of 2–6 day bandpass filtered mean sea level pressure (contours, hPa) from 1979 to 2018. The magenta boxes shown in the January map are used in time series and trend analysis

Europe most distinctly from October to March. This region is on the southern edge of the storm track (contours in Figure 1) and hence the winds are likely associated with the cyclone activity. The lowest wind speeds over land are found in the high topography regions in the European Alps, Apennines, Pyrenees and Scandinavian Mountains. A similar result is seen in wind climatologies with other reanalyses, for example in NOAA-20CR (Bett *et al*., 2013) and ERA-40 (Kiss and Jánosi, 2008). The IFS is known to have too low wind speeds in complex topography areas in Europe (Hewson, 2020) and for example in Norway, the 10-m winds are underestimated at mountainous stations whereas at coastal stations the observations are quite close to the modelled 10-m wind speeds (Thyness *et al*., 2017). Similarly in Sweden, monthly wind speeds from ERA5 are underestimated in mountain stations by up to 3.5 $m \cdot s^{-1}$ (Minola *et al*., 2020). This issue may be related to the coarse spatial resolution of the reanalysis or how surface roughness is treated in the IFS. In addition, previous studies (Howard and Clark, 2007; Sandu *et al*., 2017) have shown that the orographic drag scheme in numerical models give unrealistically low near-surface wind speeds at high altitudes. In contrast to the low wind speeds over European mountainous regions, the high altitudes in Greenland have high wind speeds. A possible explanation might be that the European mountains have more variability in topography at smaller spatial scales than Greenland does (i.e., more subgrid variability). However, it is out with the scope of this current study to rigorously evaluate the accuracy of ERA5 winds in mountainous areas or to determine causes for the apparently underestimate of the 10-m wind speeds in these regions.

In the monthly mean winds, smaller scale wind features are also visible. In all months there is a localized wind speed maximum in the northern Mediterranean Sea. This is the mistral wind phenomenon that blows from the Rhone Valley towards the Gulf of Lion (Zecchetto and De Biasio, 2007). Another local wind speed maximum is present in the eastern Mediterranean Sea, and is especially evident during summer, when this etesians wind feature is the strongest (Zecchetto and De Biasio, 2007). At the southern tip of Greenland, there is a small wind speed maximum visible during most months but this is most pronounced from February to June. This is most likely associated with tip jets and reverse tip jets which are low-level wind speed maxima occurring when a synoptic-scale cyclone interacts with the high topography of southern Greenland (Moore and Renfrew, 2005). In addition, the southeast Greenland barrier winds are seen as a narrow region of high wind speeds between Greenland and Iceland in Denmark Strait from October to February. This agrees with Sampe and Xie (2007) who found that in winter this region is one of the windiest places in the world's oceans while in summer the occurrence of high wind events is low.

The 98th percentile wind speed over 40-year period (Figure 2) shows similar patterns as the mean wind speed (Figure 1) with a contrast between land and sea areas and a clear seasonal variation. In the North Atlantic storm track region (contours in Figure 1), the highest 98th percentile winds occur between December and March with wind speeds of 20–22 $m \cdot s^{-1}$. The highest 98th percentile winds over land are found during winter in the southern part of Greenland (exceeding 22 $m \cdot s^{-1}$) and in Iceland (14–16 $m \cdot s^{-1}$). The United Kingdom also has high 98th percentile winds during winter (10–12 $m \cdot s^{-1}$). Over continental Europe, the edge of the storm track region is even more noticeable in the 98th percentile winds than in the mean field.

The same local wind features are found with the 98th percentile wind speeds as with the mean. The highest 98th percentile winds of the mistral wind in the Mediterranean Sea are 18–20 $m \cdot s^{-1}$ during winter months while the etesians are more visible during summer with 12–14 $m \cdot s^{-1}$ winds. Tip jets at the south of Greenland as well as the barrier winds in Denmark Strait are evident through all months. The barrier winds are divided into two to three local wind speed maxima that can be seen from the 98th percentile winds while mean wind field did not capture those details. Similarly, these local wind maxima along the southeast coast of Greenland were found by Moore and Renfrew (2005) using SeaWinds scatterometer and Tuononen *et al*. (2015) using Arctic system reanalysis. It is noteworthy that in addition to the mistral, the etesians, tip jets and barrier winds, there are other local wind phenomena in Europe that are not captured by ERA5. For example, the bora winds that occur most commonly during winter in the Adriatic Sea as a downslope wind phenomenon (Zecchetto and Cappa, 2001) are not seen in the monthly wind climate in ERA5.

Over the 40-year period, the smallest EWF values (below 1.8) occur in the North Atlantic storm track region between November and March and over the low wind speed area at the horse latitudes from May to August (Figure 3). This means that the 98th percentile wind speeds in these regions are not that extreme relative to the mean, i.e. the wind speed distribution is narrow. This implies that during winter the storm track region has constantly high wind speeds while during summer at the horse latitudes there are low winds most of the time. However, at the northern border of the horse latitudes between 20–40°W and 30–40°N, there is an area with high EWF values up to 2.4 most distinctly visible from June to September. By comparing Figures 1 and 2, we

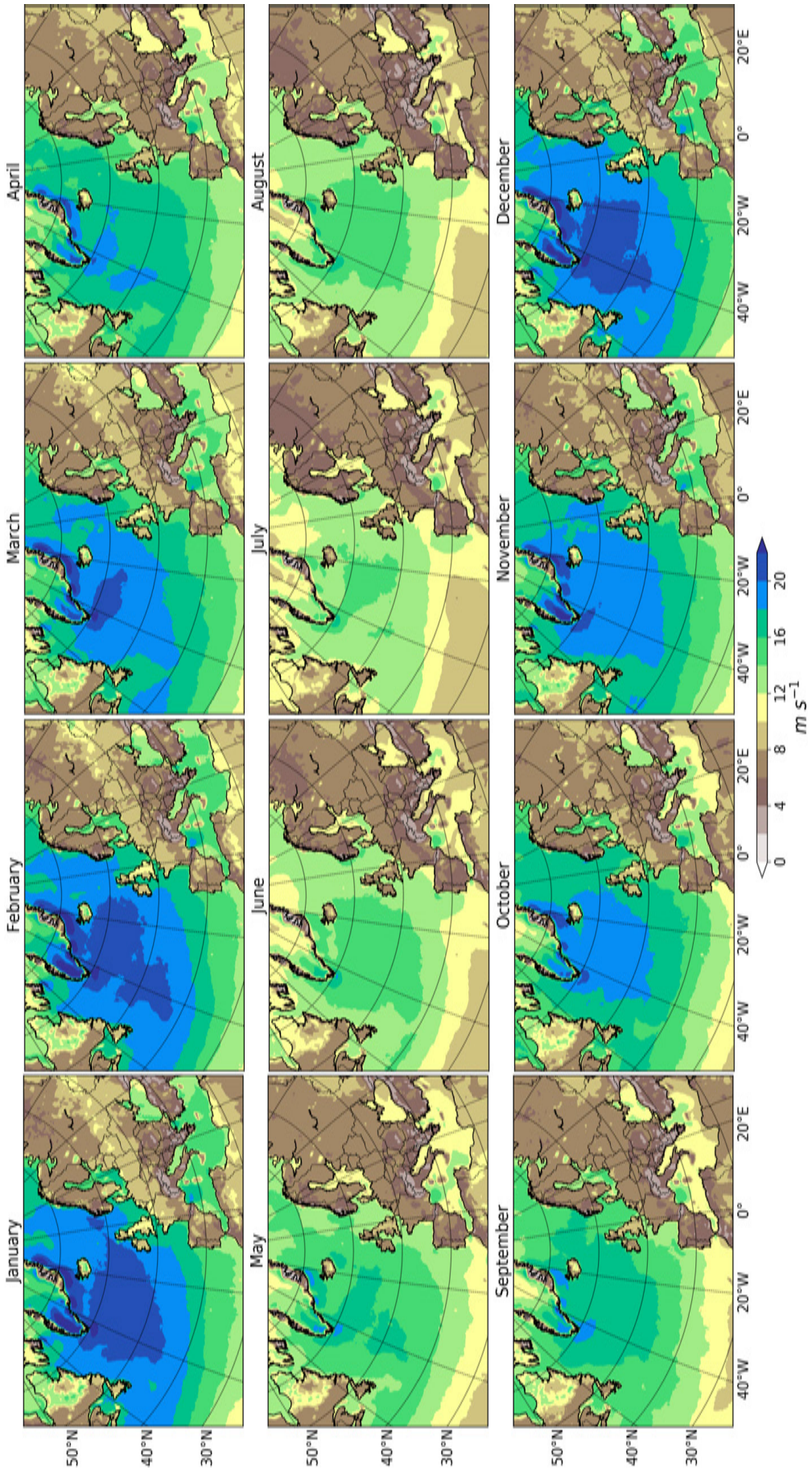

FIGURE 2 Monthly mean values of the 98th percentile of the 10-m wind speed from 1979 to 2018

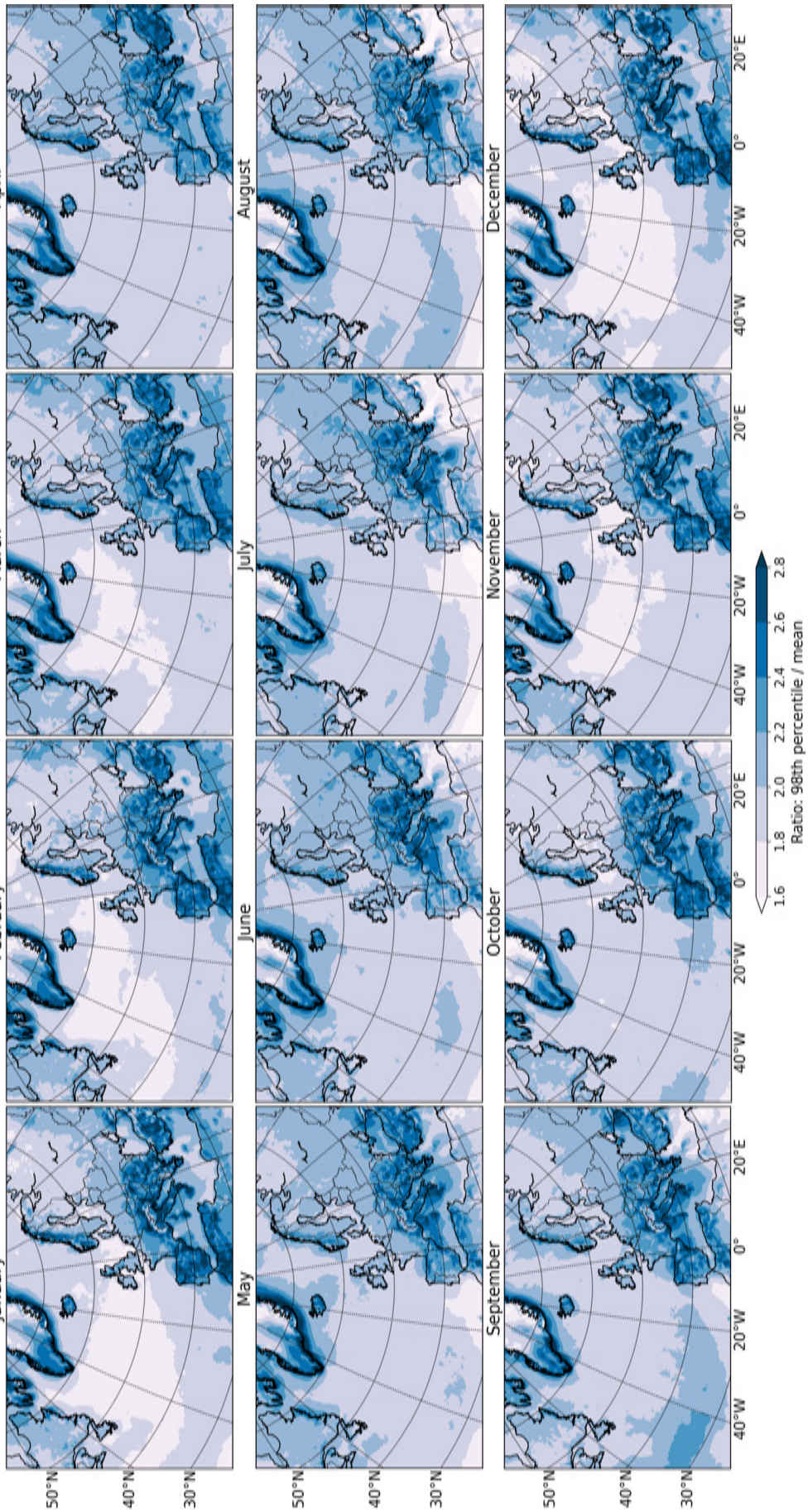

FIGURE 3 Monthly mean values of the 10-m extreme wind factor (EWF) from 1979 to 2018

can see that during those months the border of the low winds does not reach same latitude in the mean and 98th percentile wind speeds. Therefore, while the 98th percentile winds in that region are already getting stronger towards autumn, the mean wind stays relatively low.

Over land, the spatial difference in the EWF values and their seasonality is large (Figure 3). In southern Greenland, Iceland, as well as parts of southern and southeastern Europe such as Italy and Greece, the EWF largely exceeds 2.6 in all months. This implies that the high winds occurring in these regions are very extreme. In Spain and Portugal, the EWF is also as high from September to March but the value drops to 1.8–2.2 during summer. In western Europe, in the United Kingdom and France, the EWF has lower values than in southern Europe but the seasonal variation is similar with higher EWF (up to 2.4) during autumn and winter and lower EWF (down to 1.8) during summer. In contrast, in northern and northeastern Europe, the seasonal variability is the opposite and the EWF difference between seasons is much smaller. For example in Finland, the lowest EWF values of 1.8–2.0 are found from September to March and the highest EWF values of 2.0–2.2 occur during summer. These results indicate that high wind speeds are more common in northern than southern Europe, especially during winter, and therefore the high winds in south are very extreme when they occur. Moreover, it is apparent that the mountains in Norway have very high EWF while the Alps have lower EWF than the surrounding areas. However, as discussed before, we assume that the 10-m winds in mountainous areas in Europe are probably not well represented in ERA5.

To investigate the climatological variability of the 10-m wind speed, Figure 4 shows the standard deviation over the 40-year period. The highest variabilities are found in southern Greenland and its surroundings and over the North Atlantic. These regions were also identified from the mean (Figure 1) and the 98th percentile (Figure 2) wind speeds and they are likely associated with the tip jets, barrier winds and storm tracks. The mistral and the etesians are also evident in the Mediterranean Sea with high values of the standard deviation. This implies that when these phenomena occur the winds are very extreme but otherwise the winds are much calmer.

In addition to the other notable high variability regions, there is also a small, local area in the southwestern coast of Norway which is the most visible during autumn and winter (Figure 4). This location is on the edge of the most frequent storm track region (contours in Figure 1) as well as on the land-sea border. Hence, this area probably has a high wind speed variability due to the storm track shifting: when the storm track is shifted polewards, the winds in this region are extremely high. The southern edge of the storm track region extending through the central Europe is visible in the standard deviation (Figure 4), as well as in the mean (Figure 1) and the 98th percentile (Figure 2) wind speeds, with the highest variability during winter months.

The monthly distributions of 10-m wind speeds at three locations (the central North Atlantic, Finland and Iberian Peninsula) are given in Figure 5. As was evident from the maps, the temporal variation also shows the seasonal variability with the highest winds during winter and the lowest in summer. Comparing all three locations, the central North Atlantic has the highest variability and the highest absolute wind speeds. A significant difference between these locations is in the EWF seasonality: while the central North Atlantic and Finland have the highest EWF during summer, Iberian Peninsula has its EWF peak during winter. In addition, the variation and absolute values of EWF in Iberian Peninsula are much larger than in the other two regions. This indicates that high wind events in summertime in the central North Atlantic and Finland are rare and therefore if they do occur they are relatively extreme. In contrast, the high winds during wintertime in Iberian Peninsula are very extreme compared to the otherwise relatively low mean winds.

4 | WIND SPEED VARIABILITY AND TRENDS

4.1 | Decadal variability in mean winds

Of all months, February has the largest decade-to-decade variability in the 10-m mean wind speed, closely followed by January and March (Figures 6 and S1). Summer months have the weakest anomalies and thus the smallest variability between the four decades (Figure S2). None of the months show a clear decreasing or increasing trend at any location throughout the 40-year time period but there are variations between the different decades at many locations. In each individual decade, January and February have similar spatial patterns in the 10-m wind speed anomaly (Figure 6). In northern Europe in winter (mainly January and February), the mean wind speeds were relatively weak in the 1980s and 2010s whereas the 1990s was the decade of the strongest winds. The decadal changes are the opposite in southern Europe; the 1980s and 2010s had stronger winds while in the 1990s the winds were weaker. In the 1980s, the northern and eastern part of the North Atlantic had weaker winds whereas in the southern part the winds were stronger. The same but opposite dipole pattern occurred in the 1990s with stronger winds in the northern and eastern parts and weaker winds in the southern part of the North

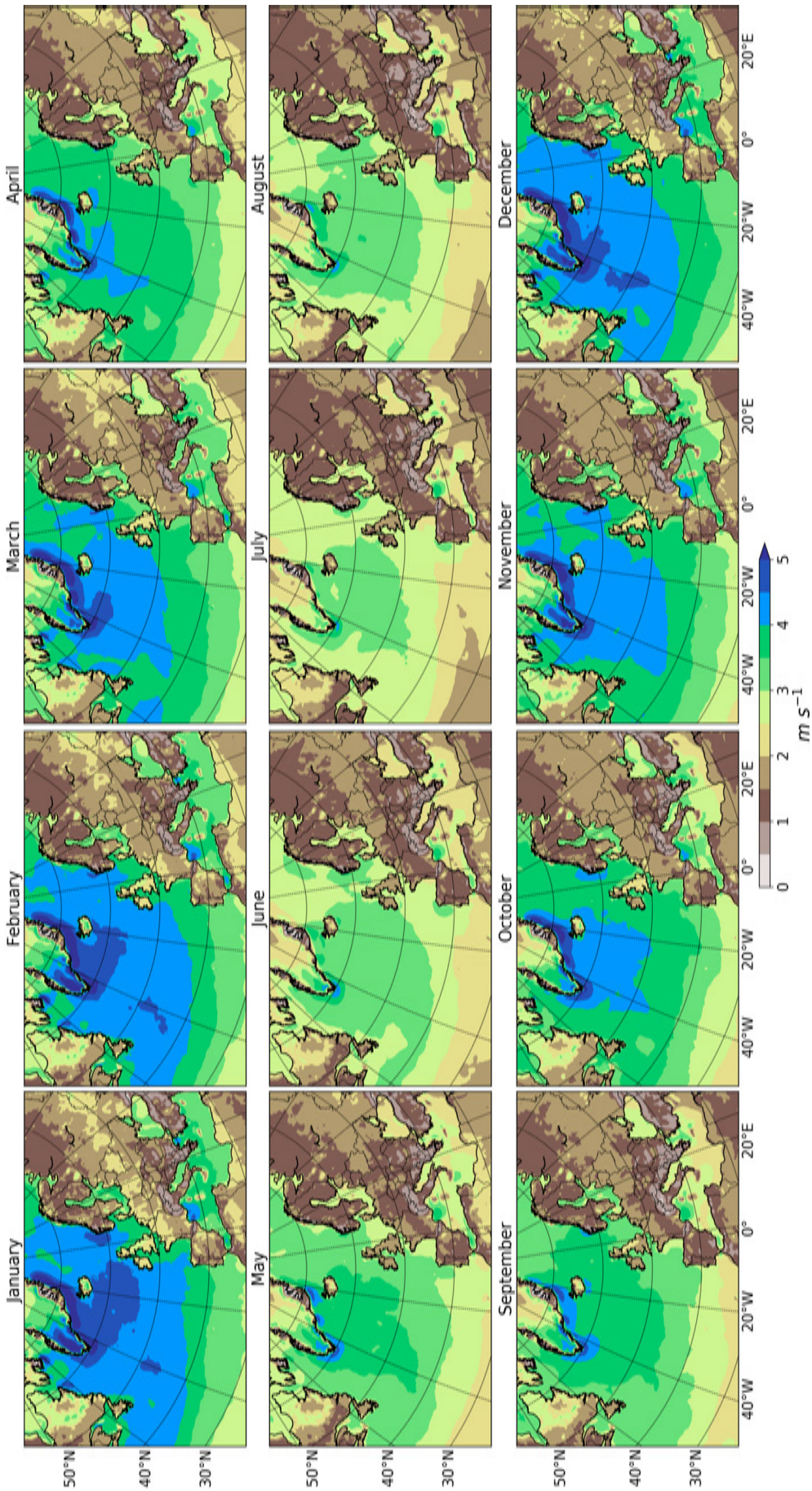

FIGURE 4 Monthly mean values of the standard deviations of 10-m wind speed from 1979 to 2018

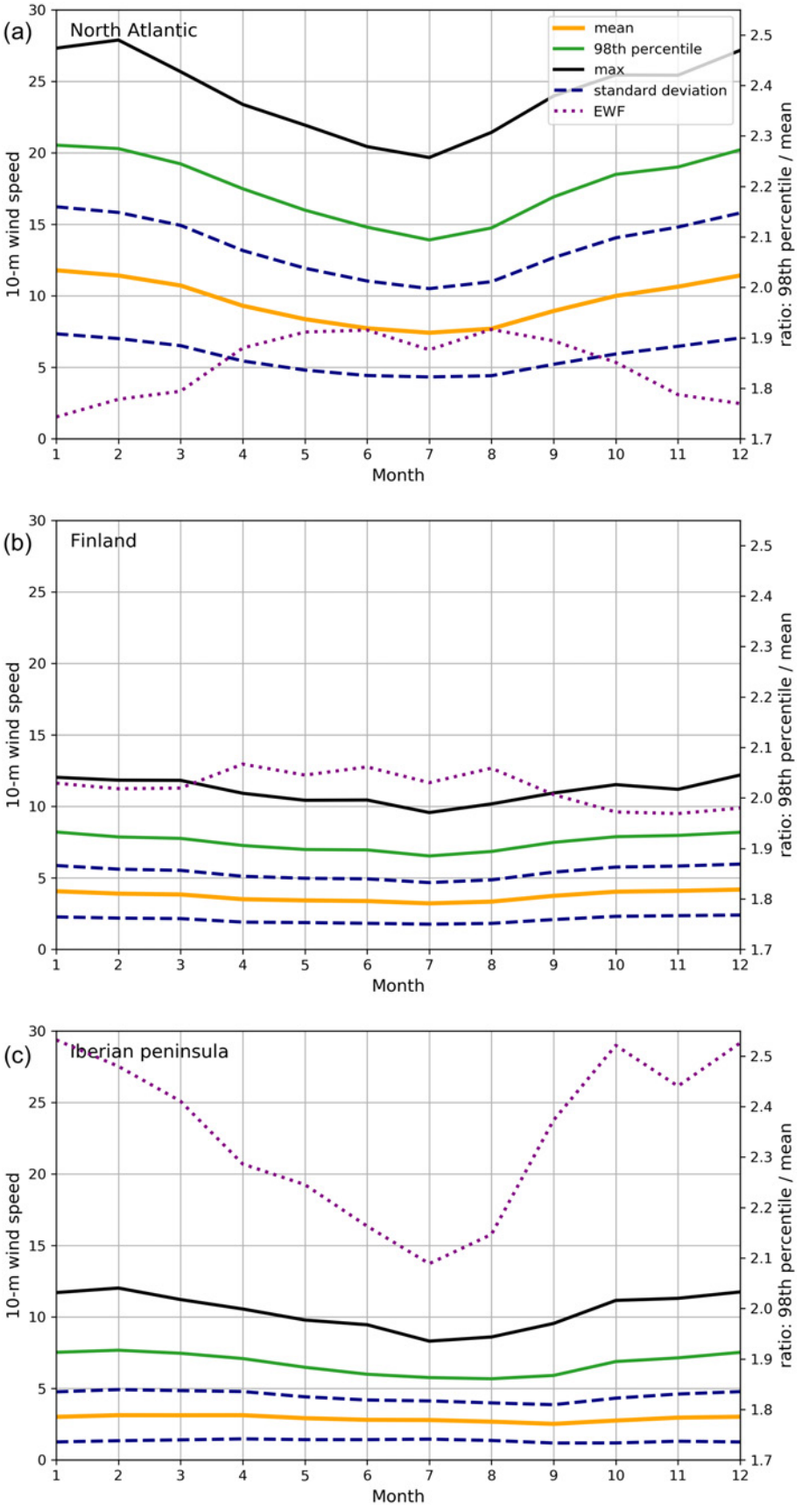

FIGURE 5 Monthly mean (orange), 98th percentile (green), maximum (black), ±1 standard deviation (dashed navy), and extreme wind factor (EWF, dotted purple) of 10-m wind speeds from 1979 to 2018 over (a) the North Atlantic, (b) Finland, and (c) Iberian Peninsula (the boxes are shown in Figure 1)

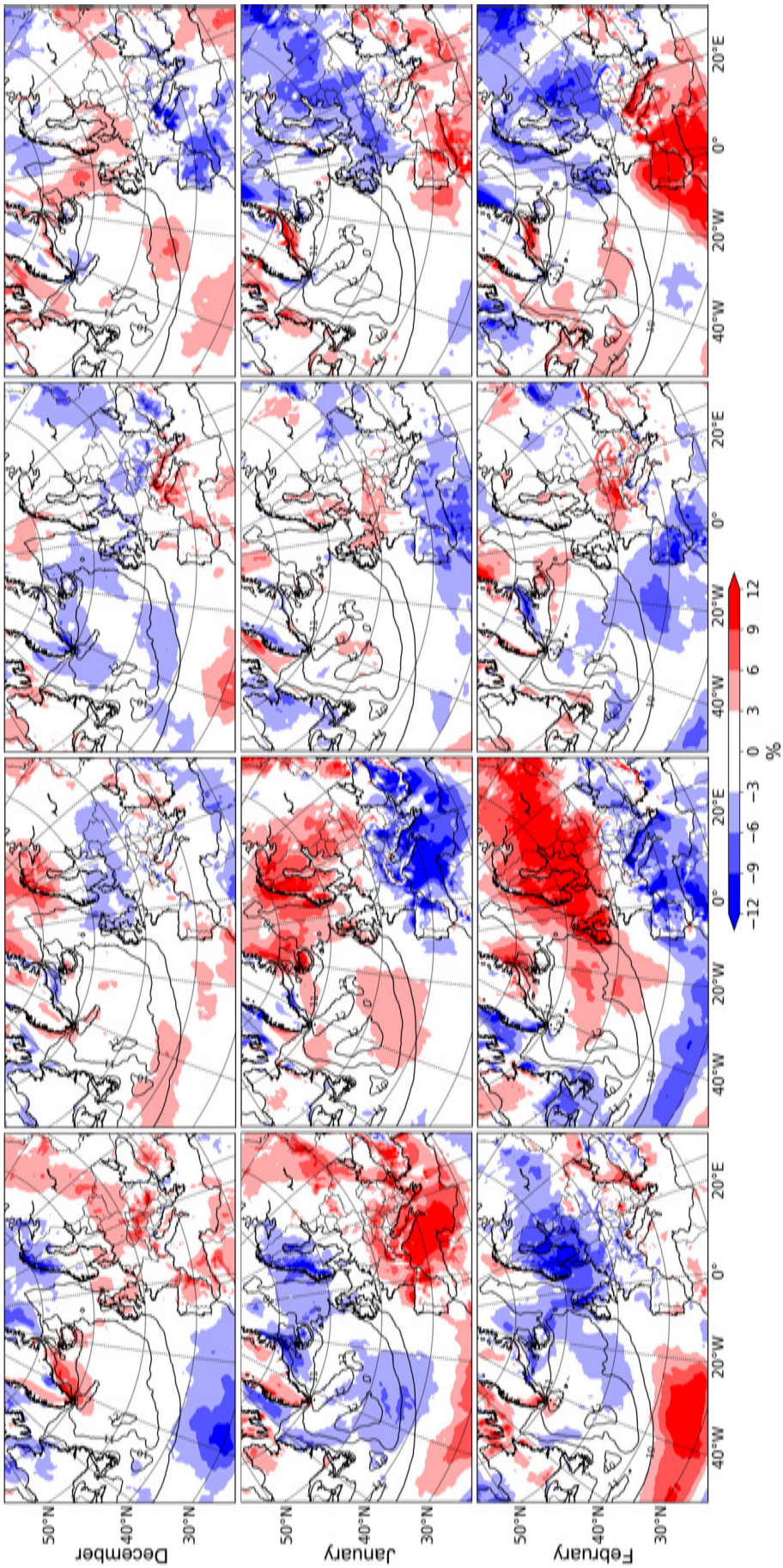

FIGURE 6 Anomalies of the mean 10-m wind speed (colours, $m \cdot s^{-1}$) for December (top row), January (middle row), and February (bottom row) for 10-year periods: 1979–1988 (first column), 1989–1998 (second column), 1999–2008 (third column), and 2009–2018 (fourth column). Contours show the 40-year (1979–2018) means starting at 10 $m \cdot s^{-1}$ (same data as shown by the shading in Figure 1)

Atlantic. The physical reasons behind these decadal variations are investigated in Section 5.

In autumn, the mean 10-m winds in the 1980s were stronger than the 40-year climatological mean in northern Europe and weaker, mainly in September, in southern Europe (Figure 7). In the 1990s, September and October were characterized by stronger than average winds in central and southern Europe while in November, northern Europe had weaker winds. The 2010s were mostly less windy than average in all of Europe. The decadal wind variability in the North Atlantic had a dipole pattern in the 1980s with a positive anomaly in the northern parts and a negative anomaly in the southern parts during September and October. In the North Atlantic, the 1990s mainly had weaker winds than the 40-year average whereas the 2010s had stronger winds. In the 2000s in November, there was a tripole pattern with positive anomalies (i.e., stronger winds) in the southwestern and northeastern parts of the North Atlantic and a negative anomaly (weaker winds) in the central part.

4.2 | Decadal variability in EWF

Overall, the signs and spatial patterns of the 98th percentile wind anomalies (not shown) are similar to the mean winds (Figures 6, 7, S1 and S2) even though the 98th percentile fields are more noisy. However, there are some differences in the decadal variability patterns in the EWF (Figures 8, 9, S3, and S4) compared to the mean and the 98th percentile. Since the decadal EWF is calculated by dividing the 10-year 98th percentile by the 40-year mean, a higher EWF in a certain decade indicates that the 98th percentile winds were more extreme relative to the climatological mean and hence possibly more damaging.

By comparing winter months in difference decades, it is apparent that in northern Europe the EWF was the highest in the 1990s (Figure 8) which is also evident in the monthly distribution of the 98th percentile winds and EWF in Finland (Figure 10c and 10d). This further emphasizes that 1990s winter was extremely stormy in northern Europe. In contrast, the lowest decadal EWF in northern Europe was in February in the 1980s and 2010s. Similarly, January and February in central Europe in the 1990s show high EWF i.e extreme storminess whereas 1980s and 2010s have low EWF. However, in southwestern Europe, the highest EWF is found in January and February in the 2010s which indicates that the wintertime windstorms in the 2010s were more extreme relative to the 40-year climate (Figures 10e and 10f). In the North Atlantic, the most extreme winds occurred in the border of the horse latitudes in February in the 1980s and in December in the 1990s. A key finding, however, is that the decadal EWF variability in the central North Atlantic is rather small compared to the variations over Europe (Figure 10).

In autumn in northern Europe, winds were the most extreme in October and November in the 1980s and in November in the 2000s whereas the lowest EWF occurred in November in the 1990s and in October in the 2000s (Figures 9 and 10c and 10d). In contrast, in southern Europe, September in the 1990s and October in the 2000s stand out as the most extreme storm months in autumn (Figures 9 and 10e and 10f). Over the North Atlantic, there is more EWF variation in the autumn months than in winter with September having the largest variability (Figure 9). The most extreme storms occurred at the horse latitudes in September in the 2010s. Notable in October is that there is a dipole pattern of lower EWF in the central and higher EWF in the southern part of the North Atlantic in the 1990s and 2010s (Figure 9) which is not apparent in the climatological EWF (Figure 3).

4.3 | Temporal trends

The absolute anomalies of the annual (January–December) mean wind speeds with respect to the 40-year mean in the central North Atlantic, Finland, and Iberian Peninsula are presented as time series in Figure 11. As was estimated from the decadal anomaly maps, there are no clear linear trends over the whole 40-year period and the year-to-year variation is large but some longer term variability is visible. In the central North Atlantic (Figure 11a), the 5-year running means of the mean and the 98th percentile winds show a windier period between 1990 and 1995. After 1995 the wind speeds decreased until 2010 after which there has been an increase until 2018. The magnitudes as well as the time evolution of the anomalies for the 98th percentile wind speed in the central North Atlantic are similar to the anomalies in the mean wind speed. Similar annual variability was found in the northeast Atlantic storminess which was analysed from the 95th and 99th percentiles of geostrophic wind speeds calculated from surface pressure observations (Krueger *et al*., 2019). Krueger *et al*. (2019) found a maximum wind speed peak between 1990–1995 and a minimum peak around 2010 which corresponds well to our results from ERA5 in the central North Atlantic (Figure 11a).

In Finland (Figure 11b), there is a bigger difference between the mean and the 98th percentile with the latter having larger variability although the time evolutions are alike. There was a peak of stronger winds around 1990–1995, as was found in the central North Atlantic.

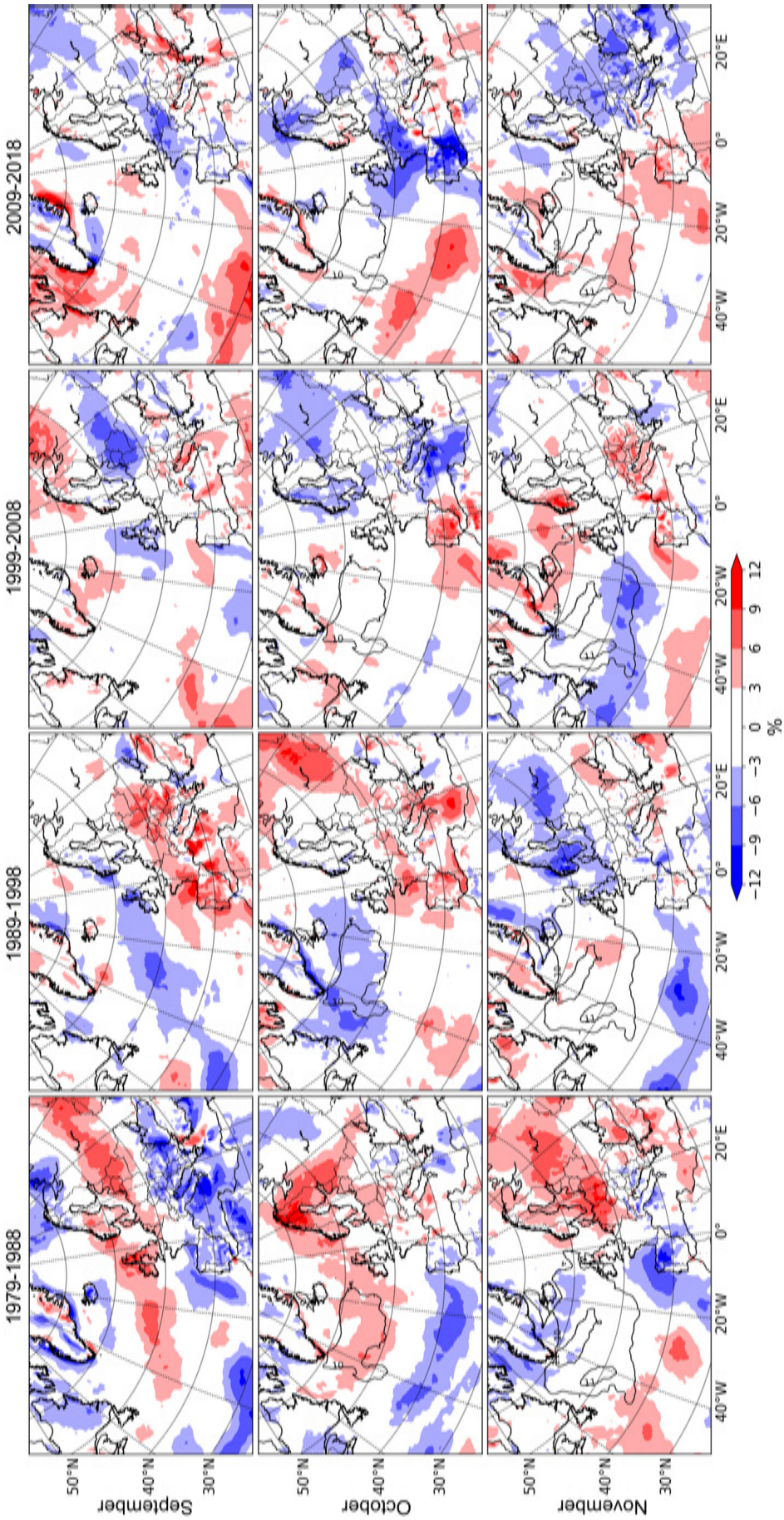

FIGURE 7 Anomalies of the mean 10-m wind speed (colours, $m \cdot s^{-1}$) for September (top row), October (middle row) and November (bottom row) for 10-year periods: 1979–1988 (first column), 1989–1998 (second column), 1999–2008 (third column), and 2009–2018 (fourth column). Contours show the 40-year (1979–2018) means starting at 10 $m \cdot s^{-1}$ (same data as shown by the shading in Figure 1)

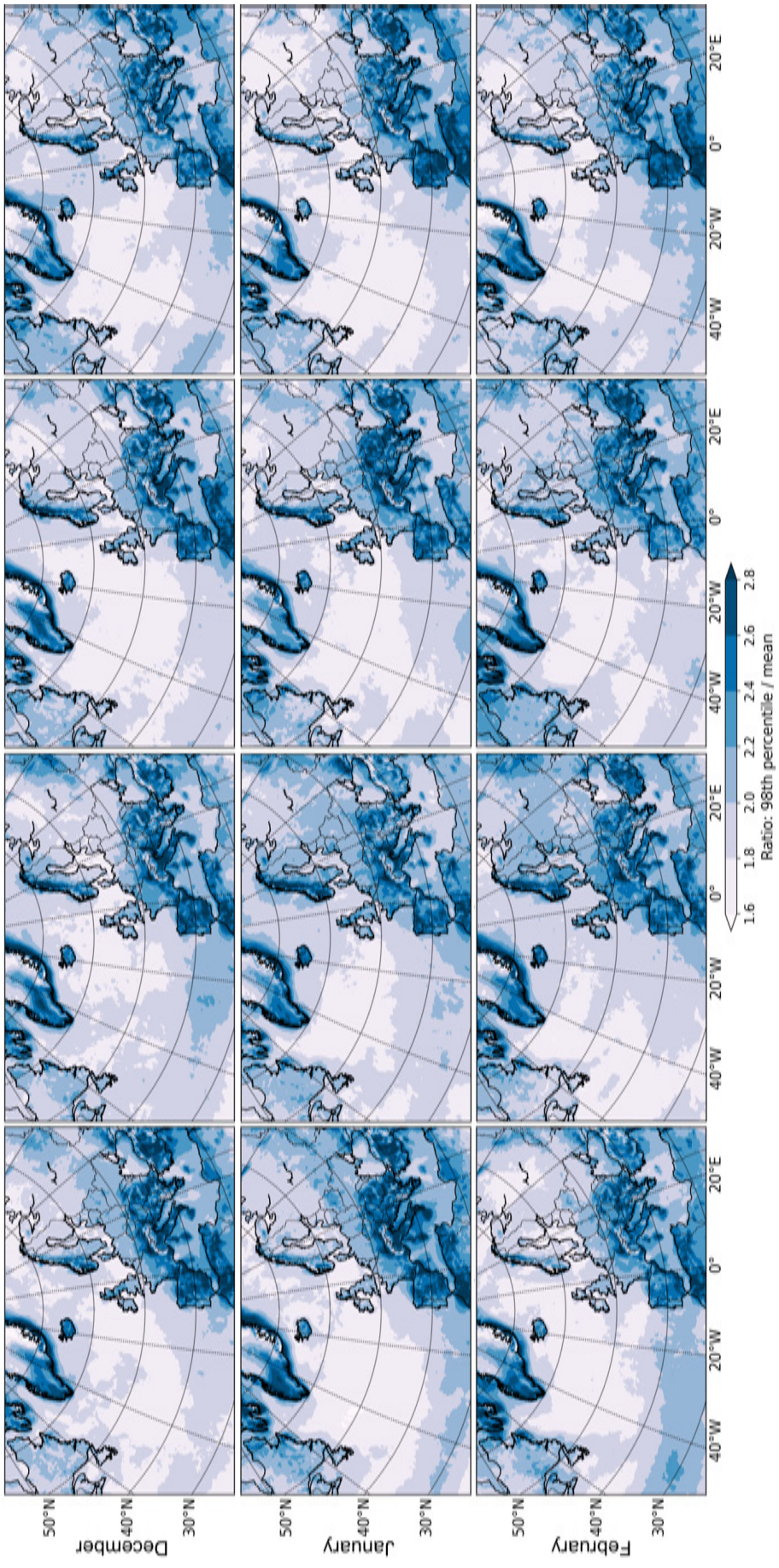

FIGURE 8 10-m extreme wind factor (EWF) (colours, $m \cdot s^{-1}$) for December (top row), January (middle row) and February (bottom row) for 10-year periods: 1979–1988 (first column), 1989–1998 (second column), 1999–2008 (third column), and 2009–2018 (fourth column)

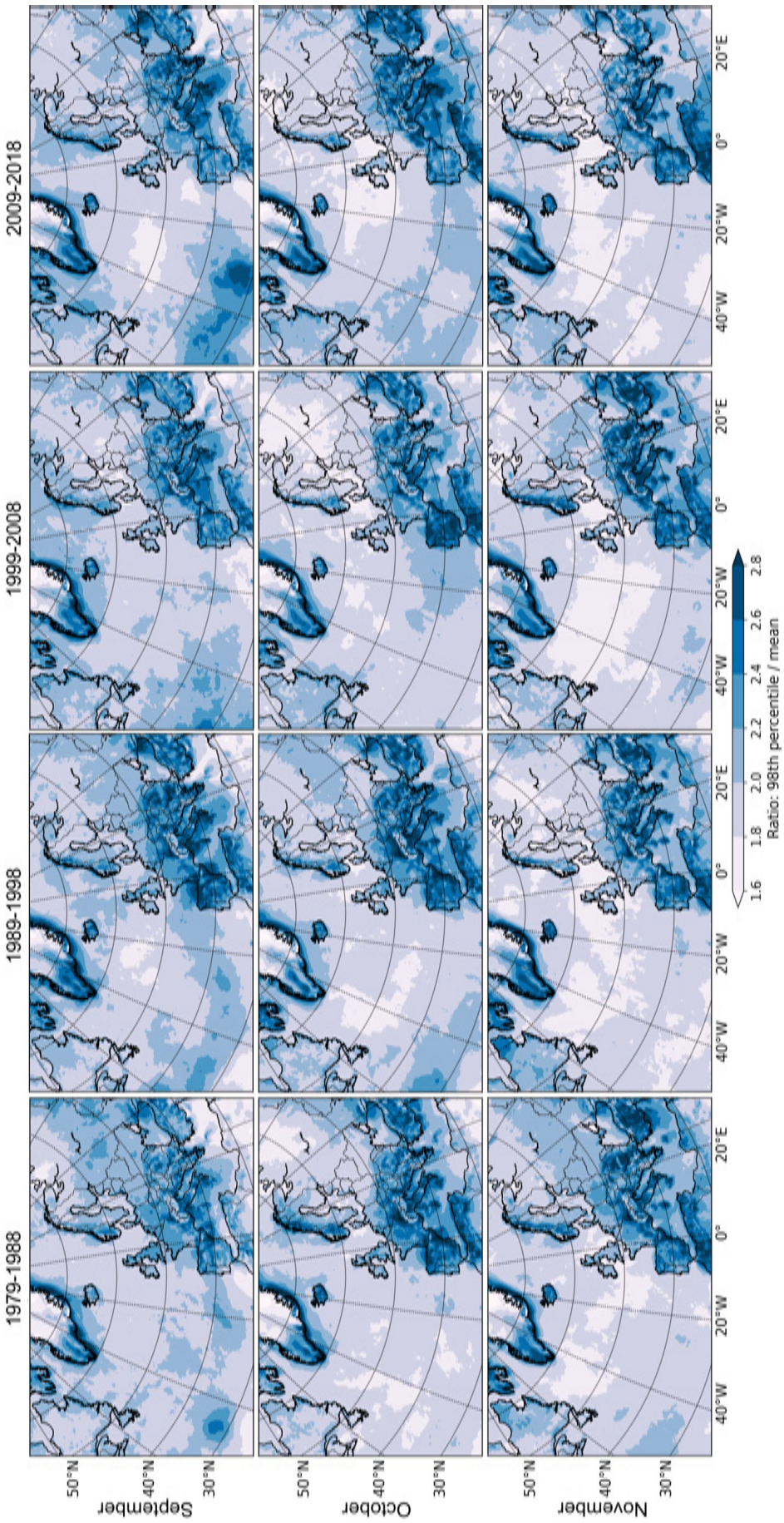

FIGURE 9 10-m extreme wind factor (EWF) (colours, $m \cdot s^{-1}$) for September (top row), October (middle row), and November (bottom row) for 10-year periods: 1979–1988 (first column), 1989–1998 (second column), 1999–2008 (third column), and 2009–2018 (fourth column)

From there forward, there has been a decreasing trend in wind speeds for many decades until around 2014 when a transition to a period with no trends has taken place. The annual mean wind speed variations are similar as in Laapas and Venäläinen, (2017) who used mean and maximum wind speed observations in Finland in 1959–2015 and found positive wind speed anomalies until 1995 and negative anomalies until around 2014. Likewise in our results from ERA5 , Laapas and Venäläinen (2017) found the strongest positive annual anomalies during period 1979–2015 in 1992, 1995, and 2015 and a negative anomaly peak in 2002.

In Iberian Peninsula (Figure 11c), the 5-year running mean of mean winds shows an increasing trend from 1980 to 2000, a decrease until 2006 and again an increase until 2014. The variability is larger in the 98th percentile winds with the most evident negative anomaly, i.e. weaker winds, between 2003 and 2007. Comparing our results from ERA5 to wind speed observations from land stations studied separately for Spain and Portugal in 1961–2011 by Azorin-Molina *et al*. (2014), similar annual variability is seen, for example the negative anomalies in 1997, 1998 and 2011 and positive anomalies in 1979, 1996, and 2001. However, when considering the longer

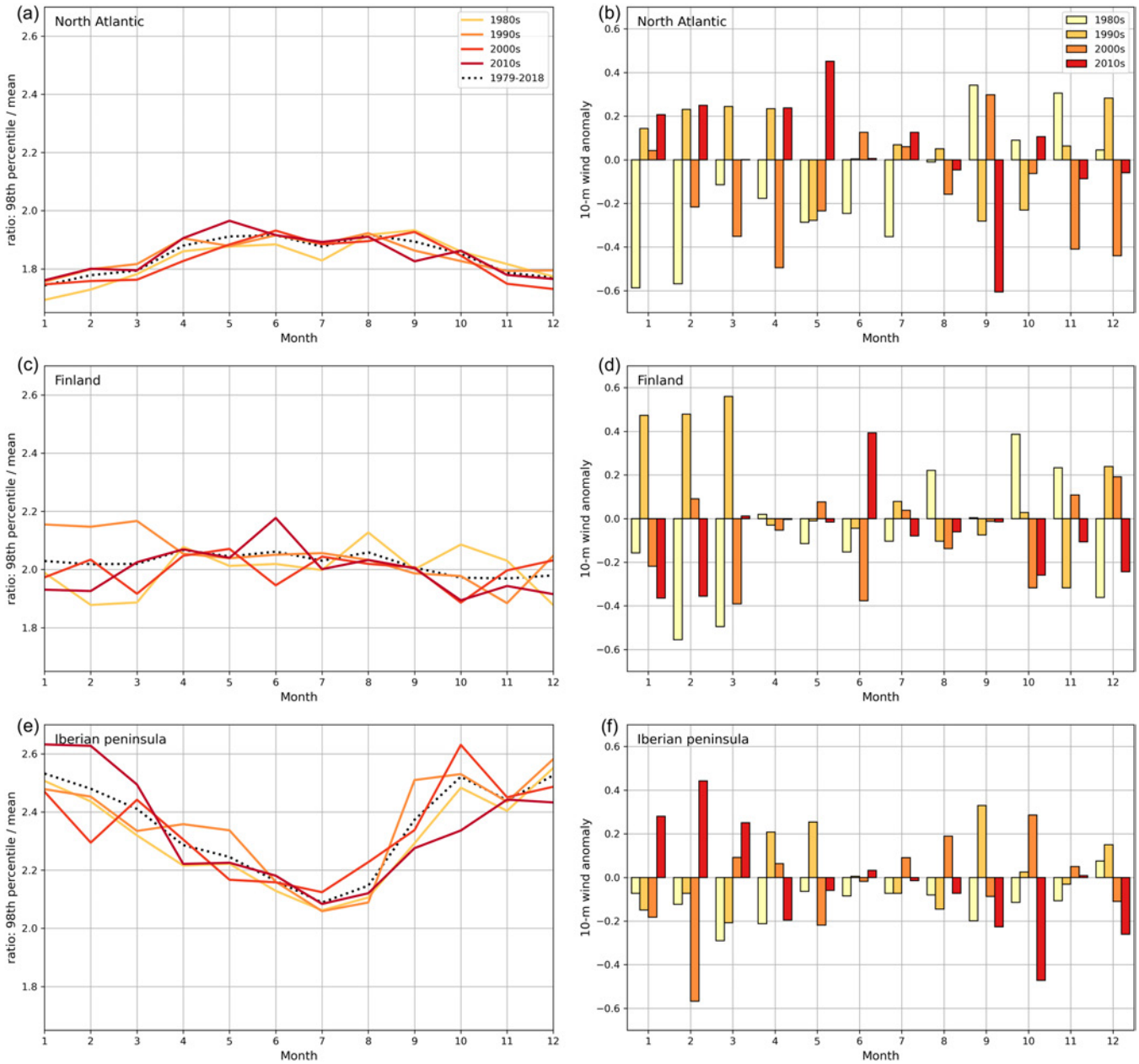

FIGURE 10 Left panel: Monthly extreme wind factor (EWF) for 10-year periods, and right panel: Monthly mean anomalies (10-year value minus 1979–2018 mean value) of the 98th percentile wind speed. Panels (a) and (b) show the North Atlantic; (c) and (d) Finland; and (e) and (f) Iberian Peninsula (location boxes are shown in Figure 1)

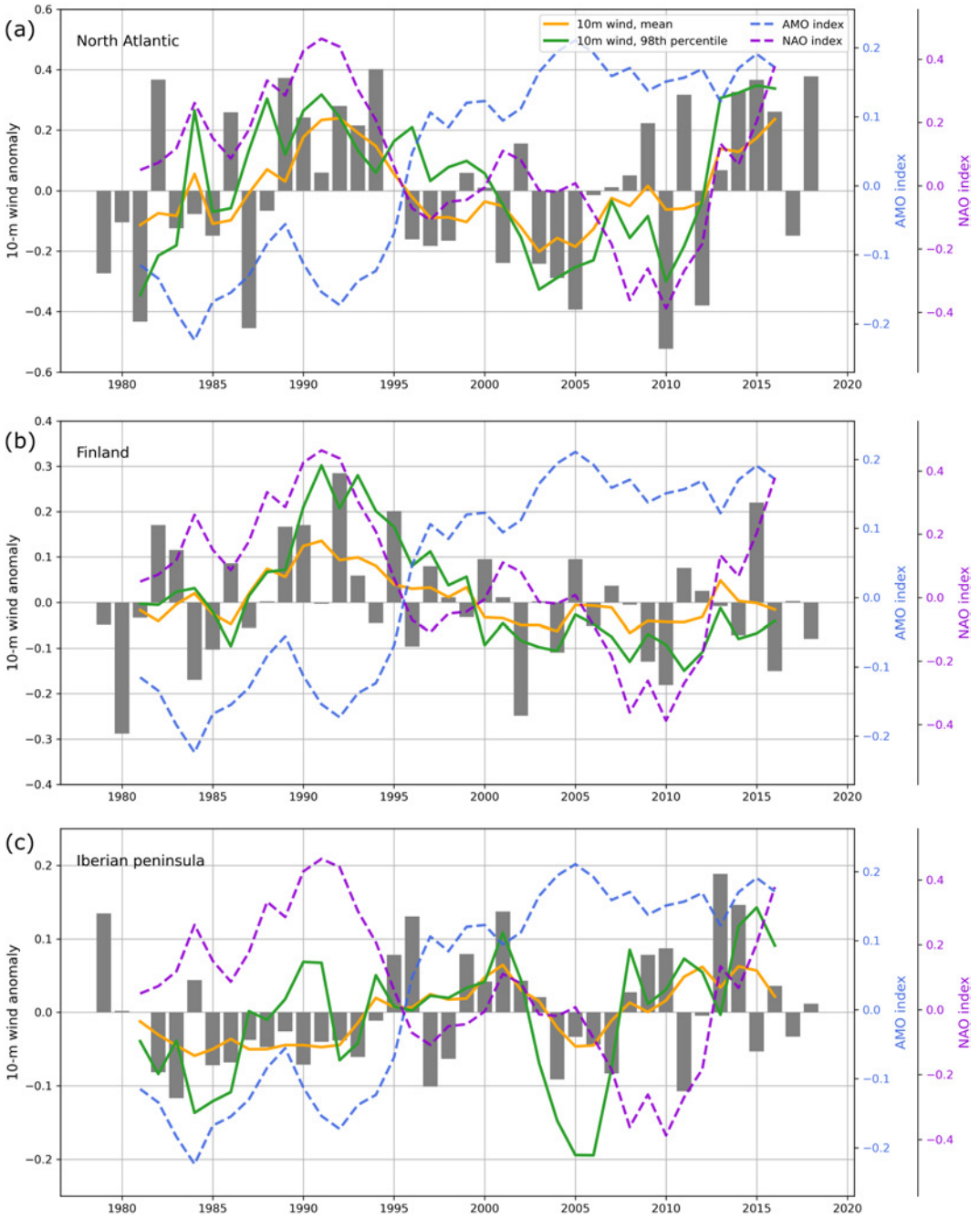

FIGURE 11 Annual 10-m wind speed anomalies (yearly mean value minus the 1979–2018 mean value, grey bars), 5-year running mean of the mean (orange) and 98th percentile (green) 10-m wind speeds, and the AMO (dashed navy) and NAO (dashed purple) indices (also 5-year running means) over (a) the North Atlantic, (b) Finland, and (c) Iberian Peninsula (the boxes are shown in Figure 1). Note that the *y*-axes have different scales

term trends, Azorin-Molina *et al*. (2014) found the period of 1980–2000 to have a declining trend contradictory to our results from ERA5 and the increasing trend from Azorin-Molina *et al*. (2014)) starts around 1998, i.e. 8 years earlier than in our analysis. Azorin-Molina *et al*. (2014) used a 15-year Gaussian low-pass filter and anomalies relative to period 1981–2010 while we used a 5-year running mean relative to 1979–2018 which may explain some differences in the long-term trends in addition to, e.g. surface roughness which has influences in station-based analysis (Vautard *et al*., 2010; Azorin-Molina *et al*., 2014).

The smallest annual variation in wind speeds in these three locations is found in Iberian Peninsula (Figure 11) which is consistent with the fact that it has the lowest wind speeds overall (Figure 5). However, to better compare these

regions we should consider relative anomalies. In relative terms (not shown), the annual anomalies in Figure 11 are largest over Finland (−7.6% to 7.5%) and smallest in the North Atlantic (−5.5% to 4.2%). In Iberian Peninsula, the relative anomalies range from −4.0% to 6.5%.

The wind speed time series revealed some periods with increasing trends and other periods with decreasing trends in all locations (Figure 11). Table 1 shows the annual and monthly linear trends for the whole 40-year time period. The calculated annual mean and the 98th percentile wind trends are positive in the central North Atlantic and Iberian Peninsula and negative in Finland. However, the magnitudes of the trends are small and most importantly the trends are not statistically significant at the 5% level in the Mann-Kendall test. The only statistically significant trends are an increase in mean winds in May in the central North Atlantic and in August in Iberian Peninsula. To conclude, there are no linear wind speed trends over the 40-year period, however, our analysis shows there is pronounced variability between different decades.

5 | PHYSICAL REASONS FOR 10-M WIND SPEED VARIABILITY

5.1 | Correlation between monthly 10-m and 300-hPa wind speeds

To examine how the near-surface and upper-level winds are related we calculated monthly correlation between 10-m and 300-hPa wind speeds from 1979 to 2018 (Figure 12). The highest correlation in all months, being the strongest in winter, is found in the exit region of the jet stream over the North Atlantic. The highest correlation over land occurs in the United Kingdom in December and January and in Iberian Peninsula, Germany and Poland in January. The winds correlate in most of Europe from October to March excluding the eastern parts. From June to July, there is a band from western to northern Europe with high correlation. Therefore, in most of the North Atlantic and Europe, especially in wintertime, the 10-m winds are generally well correlated with the upper-level winds and the jet stream. In contrast, the weakly negative correlations in the coastal areas of Greenland through all months (Figure 12) may indicate that its wind phenomena are the result of local processes (i.e., tip jets and barrier winds) rather than the large-scale atmospheric patterns.

5.2 | Decadal variability in 10-m and 300-hPa wind speed, mean sea level pressure, and storm tracks

The correlation between the 10-m and 300-hPa wind speeds is also seen at the decadal scale in February; where the decade has been windier than average similarly the upper-level winds in that location have been stronger and vice versa (Figure 13). The 1980s in February had weaker 10-m winds in northern Europe which was due to a equatorward shift in the jet stream

TABLE 1 Monthly and annual trends ($m \cdot s^{-1} \cdot decade^{-1}$) of the mean and 98th percentile 10-m wind speeds in the North Atlantic, Finland and Iberian Peninsula (the boxes are shown in Figure 1). Values shown in bold are statistically significant at the 5% level

	North Atlantic		Finland		Iberian Peninsula	
	Mean	98th percentile	Mean	98th percentile	Mean	98th percentile
January	0.110	0.259	0.006	−0.092	0.018	0.080
February	0.054	0.117	0.007	−0.029	0.121	0.206
March	0.036	0.024	0.024	0.066	0.051	0.123
April	0.085	0.083	−0.014	−0.032	−0.026	−0.062
May	**0.146**	0.131	0.031	0.031	−0.014	−0.020
June	0.130	0.096	0.007	0.105	0.030	0.078
July	0.037	0.100	−0.013	−0.045	0.049	0.025
August	−0.033	0.051	−0.028	−0.062	**0.037**	0.054
September	−0.047	−0.143	0.018	0.009	0.013	−0.013
October	−0.087	0.086	−0.088	−0.135	−0.050	−0.117
November	0.040	−0.112	−0.044	−0.073	0.047	0.020
December	0.007	−0.075	0.018	−0.021	−0.108	−0.147
Annual	0.038	0.098	−0.013	−0.028	0.014	0.034

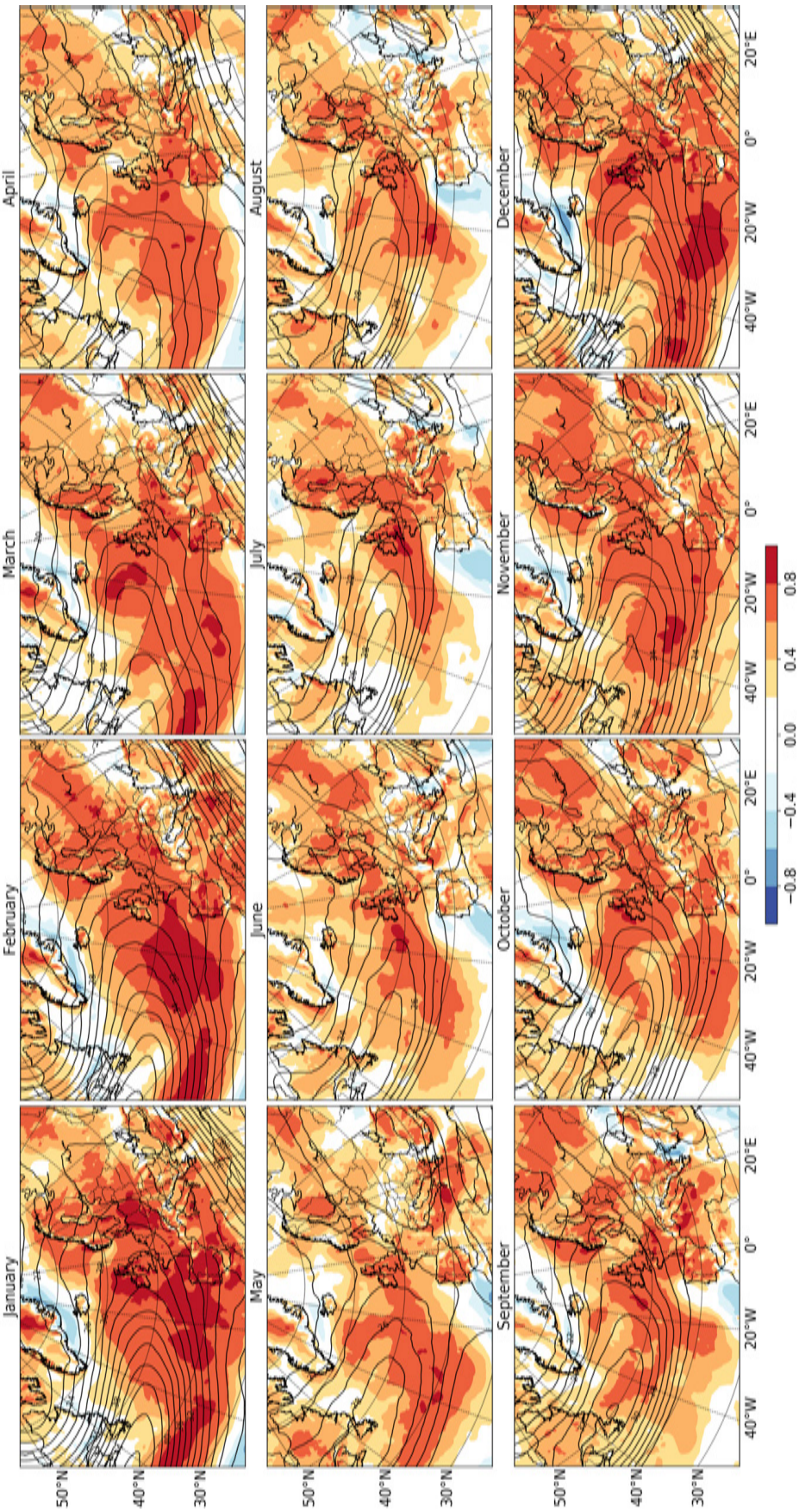

FIGURE 12 Monthly correlation coefficients (shading) between the 10-m and 300-hPa wind speeds from 1979 to 2018. The contours are the monthly mean 300-hPa wind speeds (starting at 20 $m \cdot s^{-1}$ and with a 2 $m \cdot s^{-1}$ contour interval)

and storm tracks and a weaker than average pressure gradient (Figure 13). The tripole pattern in the 300-hPa wind anomaly indicates meridional fluctuation in the jet position which together with the anomalously high surface pressure in Scandinavia implies a tendency towards more blocking events (Rex, 1950). The stronger winds in the southern part of the North Atlantic were in the area of stronger upper-level winds. The extremely stormy February in northern Europe in the 1990s was a result of a stronger, poleward and eastward extended jet stream and storm track region and a stronger than average pressure gradient (Figure 13). Accordingly, the winds were weaker in southern Europe. While in the 1980s and 1990s the dipole anomaly patterns were more north–south oriented, in the 2000s and 2010s the dipole was orientated south-west to north-east. In the 2010s, the polar jet stream was shifted eastward and appears to almost merge with the stronger and northward shifted subtropical jet. In addition, there was a local lower pressure area in southern Europe and higher pressure in northern Europe which potentially indicates an increased tendency of cut-off low and blocking high situations. The storm tracks were shifted south and east. These conditions caused extreme storms in southwestern Europe

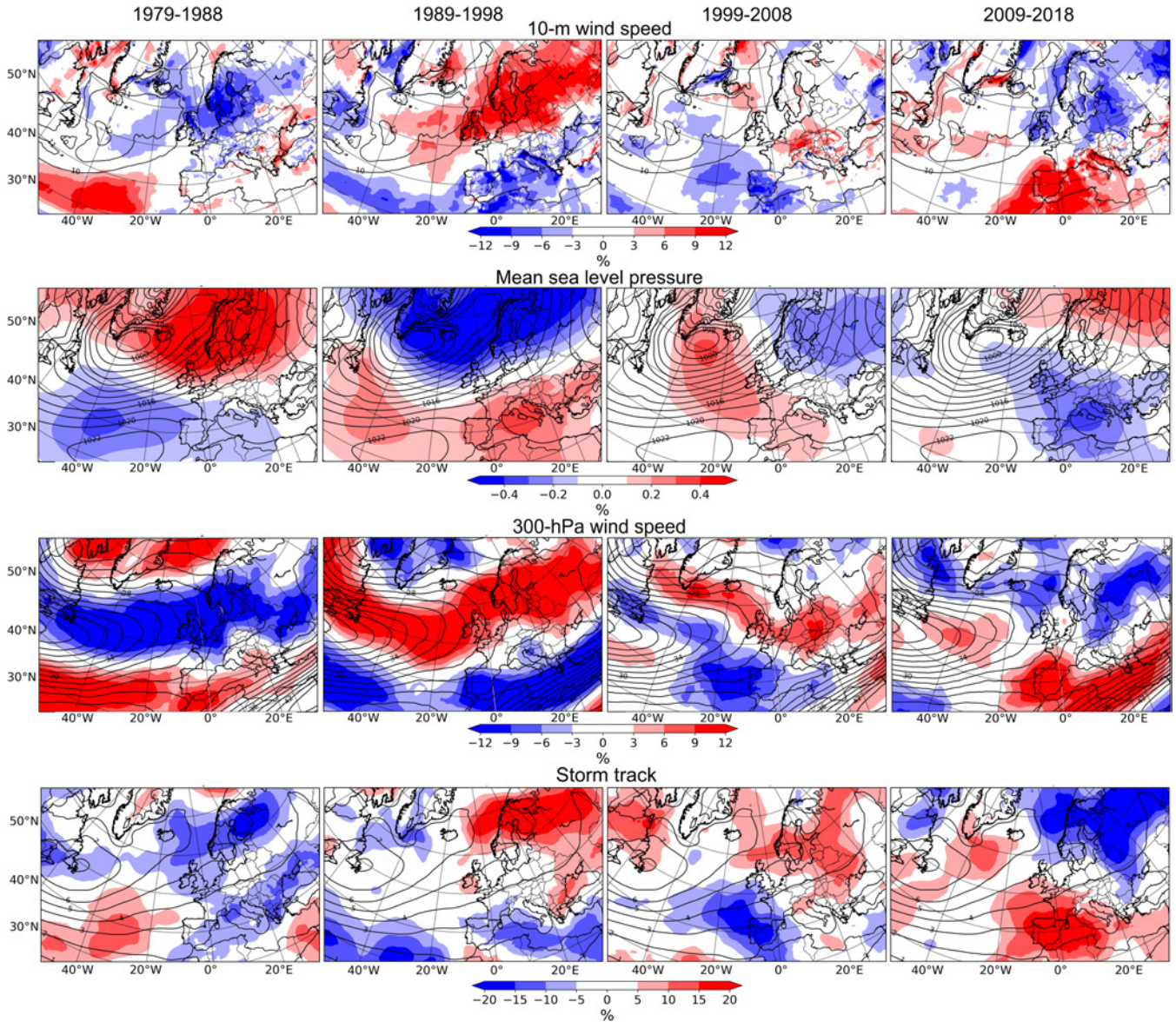

FIGURE 13 Anomalies (colours) and the 40-year means (contours) in February of the mean 10-m wind speed (firts row, contours start at 10 $m \cdot s^{-1}$), mean sea level pressure (second row, contours at 1 hPa interval), 300-hPa wind speed (third row, contours at 2 $m \cdot s^{-1}$ interval), and storm tracks as standard deviation of 2–6 day bandpass filtered mean sea level pressure (fourth row, contours at 1 hPa interval) for 10-year periods: 1979–1988 (frst column), 1989–1998 (second column), 1999–2008 (third column), and 2009–2018 (fourth column)

while the rest of Europe had calmer winds. We similarly investigated the decadal variability in October and found the same consistency between the 10-m wind anomalies and 300-hPa wind, MSLP and storm track anomalies (not shown).

5.3 | Correlation between temporal variability in 10-m wind speed and the NAO and AMO

When annual mean values are considered in the three locations, the temporal changes in wind speeds follow the NAO index really well in the central North Atlantic (Figure 11a) and Finland (Figure 11b) whereas in Iberian Peninsula (Figure 11c) the correlation is weaker. The annual correlations between the NAO index and the mean and the 98th percentile winds are statistically significant in the central North Atlantic (Figure 14a) and Finland (Figure 14c) but not in Iberian Peninsula (Figure 14e). On monthly scales, the correlation is significant in the central North Atlantic from October to May and in Finland from September to March with higher correlations mostly with the mean winds than the 98th percentile. Although the annual NAO does not correlate with the mean or the 98th percentile winds in Iberian Peninsula the majority of the months between July and March do have a significant negative correlation, especially with the mean winds. These results are expected since positive NAO is linked to a stronger than average pressure gradient between the northern and southern North Atlantic which leads to more storminess in northern Europe and less in southern Europe (Hurrell, 1995). The linkage between long-term wind speed changes and the NAO was similarly found by Zeng *et al*. (2019) and Azorin-Molina *et al*. (2018).

The annual AMO index in the 40-year time period appears to have a negative correlation with the NAO index (Figure 11). A positive AMO may induce a negative winter NAO by reducing the SST gradient and hence leading to a decrease in the North Atlantic storm track activity (Sutton *et al*., 2018). However, there is no consensus on how the NAO and AMO are related, and the relationship depends on which dataset and which methods are used (Peings and Magnusdottir, 2014). Our results show that only the annual mean wind speeds in the central North Atlantic have significant negative correlation with the AMO index but the correlation is quite weak (Figure 14b). On the monthly scale, the mean winds in the central North Atlantic are negatively correlated with the AMO in March and November, the 98th percentile winds additionally in April and December. None of the

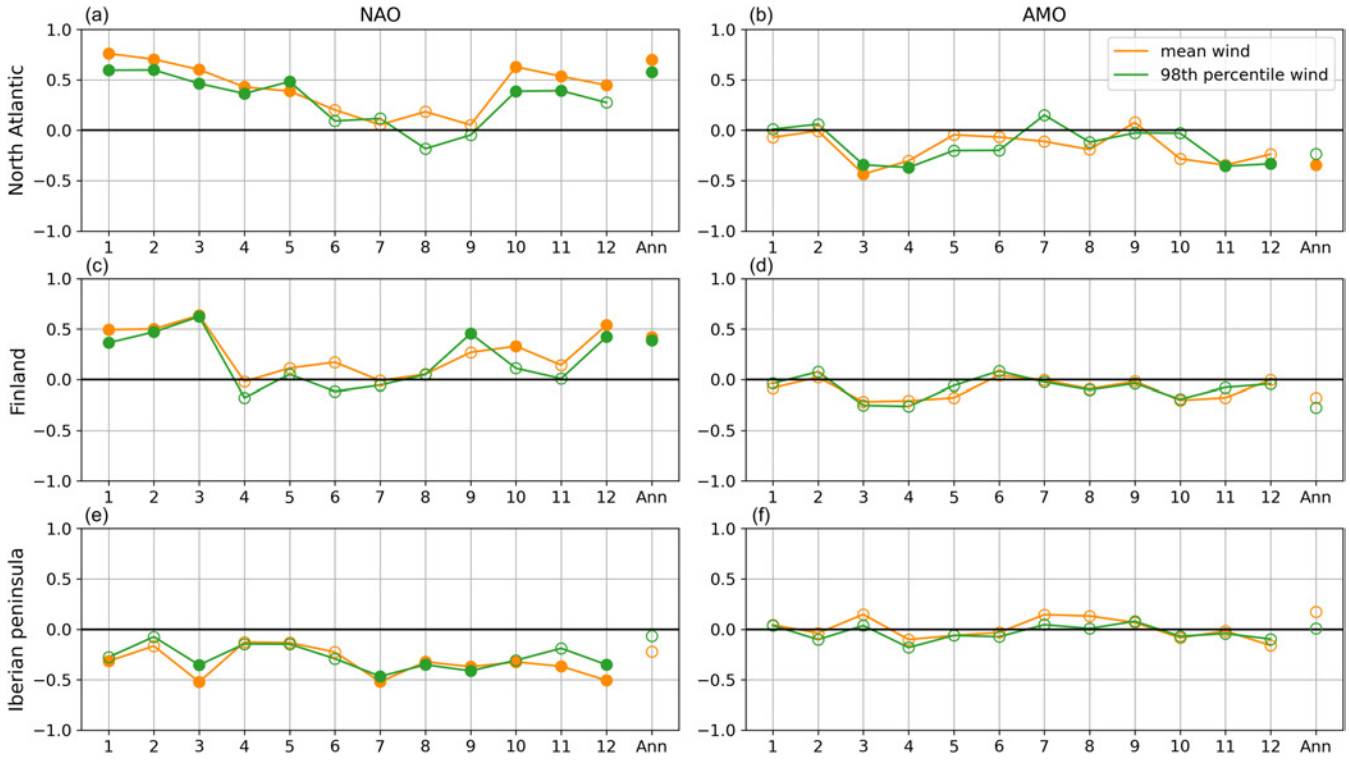

FIGURE 14 Monthly and annual correlation coefficients (circles) between the NAO and AMO indices and the mean (orange) and 98th percentile (green) 10-m wind speeds in (a) and (b) the North Atlantic; (c) and (d) Finland and (e) and (f) Iberian Peninsula (the boxes are shown in Figure 1). Values with filled circles are statistically significant at the 5% level

months nor the annual mean correlate in Finland (Figure 14d) or Iberian Peninsula (Figure 14f). Hence, our results show that while the AMO correlates moderately with the annual wind speeds, as well as few spring and winter months, in the central North Atlantic, there are no correlation in Finland and Iberian Peninsula.

6 | CONCLUSIONS

In this study, we analysed the 10-m wind speed climatology, decadal variability and possible trends in the North Atlantic and Europe in ERA5 reanalysis from 1979 to 2018. Furthermore, we examined the physical reasons for the 10-m wind speed variability. To investigate the extremeness of the wind speeds we defined an extreme wind factor (EWF) which is a ratio of the 98th percentile and mean wind speeds. In addition to spatial and decadal variations in the North Atlantic and Europe domain we studied the temporal changes in wind speeds in three locations: the central North Atlantic, Finland and Iberian Peninsula.

The 10-m wind speed climate in ERA5 shows a distinct land-sea gradient and a seasonal variation with the strongest mean and the 98th percentile winds over the ocean and during winter months. The strongest winds are associated with the storm track region over the ocean in the central North Atlantic and over land in a narrow band across central Europe. The known underestimation of 10-m winds in areas of high topography in numerical models (Howard and Clark, 2007; Hewson, 2020) appears to also be present in ERA5, for example, in the European Alps and Scandinavian Mountains. In the monthly wind climate, ERA5 captures some smaller scale local wind phenomena: the mistral and the etesians in the Mediterranean Sea and tip jets and barrier winds near Greenland. The largest variability, in terms of the standard deviation, is co-located with the highest wind speeds and hence is also associated with the storm tracks and local wind phenomena.

The EWF is low over the central North Atlantic which indicates a narrow wind speed distribution. In Europe, the magnitude and seasonal variation of EWF differs between areas. In all months, the EWF is higher in southern Europe than in northern Europe implying that the wind speed distribution is broader with a more positively skewed tail in southern Europe compared to northern Europe. In the Iberian Peninsula, the EWF is the highest during winter months whereas in Finland the highest values occur during summer. This implies that in Finland, windstorms are more common in winter and high wind events in summertime are more extreme because of their rare occurrence.

The spatial and decadal 10-m wind speed variability was analysed in four 10-year periods and we found differences between the decades with winter months having the largest decade-to-decade variability. The spatial changes in the mean and the 98th percentile wind speed anomalies are similar, however, the spatial changes in the decadal EWF shows differences compared to those. The 10-m mean wind speed anomalies in northern and southern Europe were mostly the opposite at each decade; the 1980s and 2010s had stronger than average winds in southern Europe whereas the 1990s was extremely stormy in northern Europe. In addition to decadal variation in 10-m wind speeds, annual and monthly trends were calculated at the three locations. Our results show that there are mostly no significant linear wind speed trends in the 40-year time period.

Lastly, we investigated what are the physical reasons for the 10-m wind speed variations by examining the monthly correlation with the 300-hPa winds and the decadal variability in February in comparison to the 300-hPa wind speed, MSLP and storm tracks. In addition, the temporal variability was investigated at the three locations in relation to the NAO and the AMO. The 10-m winds correlate well with the 300-hPa wind speeds in most of the North Atlantic and Europe, particularly in cold season months and in the exit region of the jet stream. The weaker than average 10-m winds in northern Europe in winters of 1980s and 2010s were caused by an equatorward shift of the jet stream and storm tracks and a weaker than average pressure gradient over the North Atlantic. In contrast, the extremely windy decade of 1990s in northern Europe, while winds were weaker in southern Europe, was due to a poleward and eastward shifted jet stream and storm tracks and a stronger than average north–south pressure gradient. Hence, the decadal changes in the 10-m wind speeds in the North Atlantic and Europe can be largely explained by the positioning of the jet stream and storm tracks and the strength of the north–south pressure gradient in the North Atlantic.

The 10-m winds in the central North Atlantic and Finland have an expected significant positive correlation with the NAO index on annual timescales as well as during cold season months. The correlation is negative in the Iberian Peninsula and significant in most months between July and March. Of the three locations, the AMO index has a significant negative correlation only in the central North Atlantic on annual scales and in a few months in spring and winter. Therefore, we find that the AMO does not influence the wind speeds over Finland and Iberian Peninsula.

As our results highlight, the annual and decadal variability in wind speeds is large and hence the

climatological anomalies and trends are highly dependent on the chosen time period (Troccoli *et al.*, 2012). The 10-m wind speed variability is related to the large-scale circulation which exhibits decadal variations. Therefore, although the linear trends can reveal an overall trend in long term, a broader view of the wind speed changes are attained by considering the inter-annual or decadal variability.

Climatological studies, such as the one presented here, do have certain limitations. For example, extreme events such as one powerful storm are not necessarily visible and decreasing trends in wind speed do not exclude possible opposite trends in rare extreme events. Furthermore, this study does not attempt to quantitatively determine what type of weather phenomenon the winds are related to. Many previous studies (e.g., Feser *et al.*, 2015; Gregow *et al.*, 2020) have examined trends and characteristics of extratropical cyclones and the winds related to these systems. However, the comparison of wind speed and windstorm climates is difficult and would be a key next step to improve understanding of their linkages.

ACKNOWLEDGEMENTS

This work was supported by the Finnish Cultural Foundation (Satakunta Regional Fund/ Aili Nurminen Fund, grant no. 75181580), MONITUHO project, the EU through the ERA4CS WINDSURFER project, CLIPS project and the Academy of Finland (grant no. 307331).

ORCID

Terhi K. Laurila https://orcid.org/0000-0002-0903-7331
Victoria A. Sinclair https://orcid.org/0000-0002-2125-4726
Hilppa Gregow https://orcid.org/0000-0003-3805-2247

REFERENCES

Azorin-Molina, C., Vicente-Serrano, S.M., McVicar, T.R., Jerez, S., Sanchez-Lorenzo, A., López-Moreno, J.-I., Revuelto, J., Trigo, R.M., Lopez-Bustins, J.A. and Espírito-Santo, F. (2014) Homogenization and assessment of observed near-surface wind speed trends over Spain and Portugal, 1961–2011. *Journal of Climate*, 27(10), 3692–3712.

Azorin-Molina, C., Rehman, S., Guijarro, J.A., McVicar, T.R., Minola, L., Chen, D. and Vicente-Serrano, S.M. (2018) Recent trends in wind speed across Saudi Arabia, 1978-2013: a break in the stilling. *International Journal of Climatology*, 38(S1), e966–e984.

Bett, P., Thornton, H. and Clark, R. (2017) Using the twentieth century reanalysis to assess climate variability for the European wind industry. *Theoretical and Applied Climatology*, 127, 61–80.

Bett, P.E., Thornton, H.E. and Clark, R.T. (2013) European wind variability over 140 yr. *Advances in Science and Research*, 10(1), 51–58.

Blackmon, M.L. (1976) A climatological spectral study of the 500 mb Geopotential height of the Northern Hemisphere. *Journal of the Atmospheric Sciences*, 33(8), 1607–1623.

Dee, D.P., Uppala, S.M., Simmons, A.J., Berrisford, P., Poli, P., Kobayashi, S., Andrae, U., Balmaseda, M.A., Balsamo, G., Bauer, P., Bechtold, P., Beljaars, A.C.M., van de Berg, L., Bidlot, J., Bormann, N., Delsol, C., Dragani, R., Fuentes, M., Geer, A.J., Haimberger, L., Healy, S.B., Hersbach, H., Hólm, E. V., Isaksen, L., Kållberg, P., Köhler, M., Matricardi, M., McNally, A.P., Monge-Sanz, B.M., Morcrette, J.-J., Park, B.-K., Peubey, C., de Rosnay, P., Tavolato, C., Thépaut, J.-N. and Vitart, F. (2011) The ERA-interim reanalysis: configuration and performance of the data assimilation system. *Quarterly Journal of the Royal Meteorological Society*, 137(656), 553–597.

Dee, D.P., Balmaseda, M., Balsamo, G., Engelen, R., Simmons, A.J. and Thépaut, J.-N. (2014) Toward a consistent reanalysis of the climate system. *Bulletin of the American Meteorological Society*, 95(8), 1235–1248.

Enfield, D.B., Mestas-Nuñez, A.M. and Trimble, P.J. (2001) The Atlantic multidecadal oscillation and its relation to rainfall and river flows in the continental U.S. *Geophysical Research Letters*, 28(10), 2077–2080.

Feser, F., Barcikowska, M., Krueger, O., Schenk, F., Weisse, R. and Xia, L. (2015) Storminess over the North Atlantic and northwestern Europe—a review. *Quarterly Journal of the Royal Meteorological Society*, 141(687), 350–382.

Gardiner, B., Blennow, K., Carnus, J.-M., Fleischer, P., Ingemarsson, F., Landmann, G., Lindner, M., Marzano, M., Nicoll, B., Orazio, C., Peyron, J.-L., Reviron, M.-P., Schelhaas, M.-J., Schuck, A., Spielmann, M. and Usbeck, T. (2010) *Destructive Storms in European Forests: Past and Forthcoming Impacts*. Cestas, France: Technical report. European Forest Institute.

Gregow, H., Jylhä, K., Mäkelä, H.M., Aalto, J., Manninen, T., Karlsson, P., Kaiser-Weiss, A.K., Kaspar, F., Poli, P., Tan, D.G. H., Obregon, A. and Su, Z. (2016) Worldwide survey of awareness and needs concerning reanalyses and respondents views on climate services. *Bulletin of the American Meteorological Society*, 97(8), 1461–1473.

Gregow, H., Laaksonen, A. and Alper, M.E. (2017) Increasing large scale windstorm damage in western, central and northern European forests, 1951-2010. *Scientific Reports*, 7, 46397.

Gregow, H., Rantanen, M., Laurila, T.K. and Mäkelä, A. (2020) *Review on winds, extratropical cyclones and their impacts in northern Europe and Finland*. Helsinki, Finland: Technical report. Finnish Meteorological Institute, Reports 2020, p. 3.

Hersbach, H., Bell, B., Berrisford, P., Hirahara, S., Horányi, A., Muñoz-Sabater, J., Nicolas, J., Peubey, C., Radu, R., Schepers, D., Simmons, A., Soci, C., Abdalla, S., Abellan, X., Balsamo, G., Bechtold, P., Biavati, G., Bidlot, J., Bonavita, M., De Chiara, G., Dahlgren, P., Dee, D., Diamantakis, M., Dragani, R., Flemming, J., Forbes, R., Fuentes, M., Geer, A., Haimberger, L., Healy, S., Hogan, R.J., Hólm, E., Janisková, M., Keeley, S., Laloyaux, P., Lopez, P., Lupu, C., Radnoti, G., de Rosnay, P., Rozum, I., Vamborg, F., Villaume, S. and Thépaut, J.-N. (2020) The ERA5 global reanalysis. *Quarterly Journal of the Royal Meteorological Society*, 146(730), 1999–2049.

Hewson, T. (2020) *Use and Verification of ECMWF Products (2019)*. Reading, UK: Technical report. ECMWF Technical Memoranda.

Howard, T. and Clark, P. (2007) Correction and downscaling of NWP wind speed forecasts. *Meteorological Applications*, 14(2), 105–116.

Hurrell, J.W. (1995) Decadal trends in the North Atlantic oscillation: regional temperatures and precipitation. *Science*, 269 (5224), 676–679.

Ionita, M., Lohmann, G., Rimbu, N., Chelcea, S. and Dima, M. (2012) Interannual to decadal summer drought variability over Europe and its relationship to global sea surface temperature. *Climate Dynamics*, 38(1–2), 363–377.

Kaiser-Weiss, A.K., Kaspar, F., Heene, V., Borsche, M., Tan, D.G. H., Poli, P., Obregon, A. and Gregow, H. (2015) Comparison of regional and global reanalysis near-surface winds with station observations over Germany. *Advances in Science and Research*, 12(1), 187–198.

Kaiser-Weiss, A.K., Borsche, M., Niermann, D., Kaspar, F., Lussana, C., Isotta, F.A., van den Besselaar, E., van der Schrier, G. and Undén, P. (2019) Added value of regional reanalyses for climatological applications. *Environmental Research Communications*, 1(7), 071004.

Kaplan, A., Cane, M.A., Kushnir, Y., Clement, A.C., Blumenthal, M.B. and Rajagopalan, B. (1998) Analyses of global sea surface temperature 1856-1991. *Journal of Geophysical Research: Oceans*, 103(C9), 18567–18589.

Kendall, M.G. (1970) *Rank Correlation Methods*. London: Griffin.

Kiss, P. and Jánosi, I.M. (2008) Comprehensive empirical analysis of ERA-40 surface wind speed distribution over Europe. *Energy Conversion and Management*, 49(8), 2142–2151.

Krueger, O., Feser, F. and Weisse, R. (2019) Northeast Atlantic storm activity and its uncertainty from the late nineteenth to the twenty-first century. *Journal of Climate*, 32(6), 1919–1931.

Laapas, M. and Venäläinen, A. (2017) Homogenization and trend analysis of monthly mean and maximum wind speed time series in Finland, 1959-2015. *International Journal of Climatology*, 37(14), 4803–4813.

Mann, H.B. (1945) Nonparametric tests against trend. *Econometrica*, 13, 245–259.

Minola, L., Azorin-Molina, C. and Chen, D. (2016) Homogenization and assessment of observed near-surface wind speed trends across Sweden, 1956-2013. *Journal of Climate*, 29(20), 7397–7415.

Minola, L., Zhang, F., Azorin-Molina, C., Pirooz, A.A.S., Flay, R.G. J., Hersbach, H. and Chen, D. (2020) Near-surface mean and gust wind speeds in ERA5 across Sweden: towards an improved gust parametrization. *Climate Dynamics*, 55(3), 887–907.

Moore, G.W. and Renfrew, I.A. (2005) Tip jets and barrier winds: a QuikSCAT climatology of high wind speed events around Greenland. *Journal of Climate*, 18(18), 3713–3725.

NOAA (2020a). www.cpc.ncep.noaa.gov/products/precip/CWlink/pna/nao.shtml. [Accessed: June 29, 2020].

NOAA (2020b). www.esrl.noaa.gov/psd/data/timeseries/AMO/. [Accessed: June 29, 2020].

Olauson, J. (2018) ERA5: the new champion of wind power modelling? *Renewable Energy*, 126, 322–331.

Peings, Y. and Magnusdottir, G. (2014) Forcing of the wintertime atmospheric circulation by the multidecadal fluctuations of the North Atlantic Ocean. *Environmental Research Letters*, 9(3), 034018.

Priestley, M.D.K., Ackerley, D., Catto, J.L., Hodges, K.I., McDonald, R.E. and Lee, R.W. (2020) An overview of the extratropical storm tracks in CMIP6 historical simulations. *Journal of Climate*, 33(15), 6315–6343.

Rex, D.F. (1950) Blocking action in the middle troposphere and its effect upon regional climate. *Tellus*, 2(4), 275–301.

Sampe, T. and Xie, S.-P. (2007) Mapping High Sea winds from space: a global climatology. *Bulletin of the American Meteorological Society*, 88(12), 1965–1978.

Sandu, I., Zadra, A. and Wedi, N. (2017) Impact of orographic drag on forecast skill. *ECMWF Newsletter*, 150, 18–24.

Scaife, A.A., Arribas, A., Blockley, E., Brookshaw, A., Clark, R.T., Dunstone, N., Eade, R., Fereday, D., Folland, C.K., Gordon, M., Hermanson, L., Knight, J.R., Lea, D.J., MacLachlan, C., Maidens, A., Martin, M., Peterson, A.K., Smith, D., Vellinga, M., Wallace, E., Waters, J. and Williams, A. (2014) Skillful long-range prediction of European and North American winters. *Geophysical Research Letters*, 41(7), 2514–2519.

Sen, P.K. (1968) Estimates of the regression coefficient based on Kendall's tau. *Journal of the American Statistical Association*, 63 (324), 1379–1389.

Sutton, R.T., McCarthy, G.D., Robson, J., Sinha, B., Archibald, A.T. and Gray, L.J. (2018) Atlantic multidecadal variability and the U.K. ACSIS program. *Bulletin of the American Meteorological Society*, 99(2), 415–425.

Theil, H. (1950) A rank-invariant method of linear and polynomial regression analysis, 1–2, *Proceedings of the Royal Netherlands Academy of Sciences*, 53. 386–392 and 521–525.

Thyness, V., Homleid, M., Køltzow, M. and Lien, T. (2017) *Application and Verification of ECMWF Products 2017*. Oslo, Norway: Technical report. Norwegian Meteorological Institute.

Torralba, V., Doblas-Reyes, F.J. and Gonzalez-Reviriego, N. (2017) Uncertainty in recent near-surface wind speed trends: a global reanalysis intercomparison. *Environmental Research Letters*, 12 (11), 114019.

Troccoli, A., Muller, K., Coppin, P., Davy, R., Russell, C. and Hirsch, A.L. (2012) Long-term wind speed trends over Australia. *Journal of Climate*, 25(1), 170–183.

Tuononen, M., Sinclair, V.A. and Vihma, T. (2015) A climatology of low-level jets in the mid-latitudes and polar regions of the Northern Hemisphere. *Atmospheric Science Letters*, 16(4), 492–499.

Usbeck, T., Waldner, P., Dobbertin, M., Ginzler, C., Hoffmann, C., Sutter, F., Steinmeier, C., Volz, R., Schneiter, G. and Rebetez, M. (2012) Relating remotely sensed forest damage data to wind data: storms Lothar (1999) and Vivian (1990) in Switzerland. *Theoretical and Applied Climatology*, 108, 451–462.

Vautard, R., Cattiaux, J., Yiou, P., Thépaut, J.-N. and Ciais, P. (2010) Northern Hemisphere atmospheric stilling partly attributed to an increase in surface roughness. *Nature Geoscience*, 3, 756–761.

Vose, R.S., Applequist, S., Bourassa, M.A., Pryor, S.C., Barthelmie, R.J., Blanton, B., Bromirski, P.D., Brooks, H. E., DeGaetano, A.T., Dole, R.M., Easterling, D.R., Jensen, R.E., Karl, T.R., Katz, R.W., Klink, K., Kruk, M.C., Kunkel, K.E., MacCracken, M.C., Peterson, T.C., Shein, K., Thomas, B.R., Walsh, J.E., Wang, X.L., Wehner, M.F., Wuebbles, D.J. and Young, R.S. (2014) Monitoring and understanding changes in extremes: Extratropical storms, winds, and waves. *Bulletin of the American Meteorological Society*, 95(3), 377–386.

Wu, J., Zha, J., Zhao, D. and Yang, Q. (2018) Changes in terrestrial near-surface wind speed and their possible causes: an overview. *Climate Dynamics*, 51, 2039–2078.

Yamamoto, A. and Palter, J.B. (2016) The absence of an Atlantic imprint on the multidecadal variability of wintertime European temperature. *Nature Communications*, 7, 1–8.

Zahradníček, P., Brázdil, R., Štěpánek, P. and Řezníčková, L. (2019) Differences in wind speeds according to measured and homogenized series in The Czech Republic, 1961-2015. *International Journal of Climatology*, 39(1), 235–250.

Zecchetto, S. and Cappa, C. (2001) The spatial structure of the Mediterranean Sea winds revealed by ERS-1 scatterometer. *International Journal of Remote Sensing*, 22(1), 45–70.

Zecchetto, S. and De Biasio, F. (2007) Sea surface winds over the Mediterranean Basin from satellite data (2000-04): Meso- and local-scale features on annual and seasonal time scales. *Journal of Applied Meteorology and Climatology*, 46(6), 814–827.

Zeng, Z., Ziegler, A.D., Searchinger, T., Yang, L., Chen, A., Ju, K., Piao, S., Li, L.Z.X., Ciais, P., Chen, D., Liu, J., Azorin-Molina, C., Chappell, A., Medvigy, D. and Wood, E.F. (2019) A reversal in global terrestrial stilling and its implications for wind energy production. *Nature Climate Change*, 9, 979–985.

Zhang, R., Sutton, R., Danabasoglu, G., Kwon, Y.-O., Marsh, R., Yeager, S.G., Amrhein, D.E. and Little, C.M. (2019) A review of the role of the Atlantic Meridional overturning circulation in Atlantic multidecadal variability and associated climate impacts. *Reviews of Geophysics*, 57(2), 316–375.

SUPPORTING INFORMATION

Additional supporting information may be found online in the Supporting Information section at the end of this article.

How to cite this article: Laurila TK, Sinclair VA, Gregow H. Climatology, variability, and trends in near-surface wind speeds over the North Atlantic and Europe during 1979–2018 based on ERA5. *Int J Climatol*. 2021;41:2253–2278. https://doi.org/10.1002/joc.6957

Weather and Climate Dynamics, 2(4), 1111–1130,
doi:10.5194/wcd-2-1111-2021

II

Weather Clim. Dynam., 2, 1111–1130, 2021
https://doi.org/10.5194/wcd-2-1111-2021

Weather and Climate Dynamics
Open Access
EGU

Characteristics of extratropical cyclones and precursors to windstorms in northern Europe

Terhi K. Laurila[1], Hilppa Gregow[1], Joona Cornér[2], and Victoria A. Sinclair[2]

[1]Weather and Climate Change Impact Research, Finnish Meteorological Institute, Helsinki, Finland
[2]Institute for Atmospheric and Earth System Research/Physics, Faculty of Science, University of Helsinki, Helsinki, Finland

Correspondence: Terhi K. Laurila (terhi.laurila@fmi.fi)

Received: 5 July 2021 – Discussion started: 12 July 2021
Revised: 28 September 2021 – Accepted: 25 October 2021 – Published: 23 November 2021

Abstract. Extratropical cyclones play a major role in the atmospheric circulation and weather variability and can cause widespread damage and destruction. Extratropical cyclones in northern Europe, which is located at the end of the North Atlantic storm track, have been less studied than extratropical cyclones elsewhere. Our study investigates extratropical cyclones and windstorms in northern Europe (which in this study covers Norway; Sweden; Finland; Estonia; and parts of the Baltic, Norwegian, and Barents seas) by analysing their characteristics, spatial and temporal evolution, and precursors. We examine cold and warm seasons separately to determine seasonal differences. We track all extratropical cyclones in northern Europe, create cyclone composites, and use an ensemble sensitivity method to analyse the precursors. The ensemble sensitivity analysis is a novel method in cyclone studies where linear regression is used to statistically identify what variables possibly influence the subsequent evolution of extratropical cyclones. We investigate windstorm precursors for both the minimum mean sea level pressure (MSLP) and for the maximum 10 m wind gusts. The annual number of extratropical cyclones and windstorms has a large inter-annual variability and no significant linear trends during 1980–2019. Windstorms originate and occur over the Barents and Norwegian seas, whereas weaker extratropical cyclones originate and occur over land areas in northern Europe. During the windstorm evolution, the maximum wind gusts move from the warm sector to behind the cold front following the strongest pressure gradient. Windstorms in both seasons are located on the poleward side of the jet stream. The maximum wind gusts occur nearly at the same time as the minimum MSLP occurs. The cold-season windstorms have higher sensitivities and thus are potentially better predictable than warm-season windstorms, and the minimum MSLP has higher sensitivities than the maximum wind gusts. Of the four examined precursors, both the minimum MSLP and the maximum wind gusts are the most sensitive to the 850 hPa potential temperature anomaly, i.e. the temperature gradient. Hence, this parameter is likely important when predicting windstorms in northern Europe.

1 Introduction

Extratropical cyclones are important phenomena to regulate the daily weather in mid-latitudes and to transport energy and moisture in the atmosphere. They are mainly driven by baroclinicity (Charney, 1947), which is characterized by a strong temperature difference between the poles and Equator. They are associated with precipitation and strong winds, which can lead to high impacts in society (e.g. Suursaar et al., 2006; Kufeoglu and Lehtonen, 2014; Holley, 2021; Tervo et al., 2021; Rantanen et al., 2021), for example floods, power outages, and forest and property damage. Since extratropical cyclones play a crucial role in the atmospheric circulation and weather variability and as a cause for societal and economical impacts, the knowledge and understanding of extratropical cyclone climate and dynamics are essential.

Extratropical cyclones and their tracks have been widely studied in the Northern Hemisphere (e.g. Hoskins and Hodges, 2002; Ulbrich et al., 2009; Hodges et al., 2011; Priestley et al., 2020). It is well known that the main storm track regions in the Northern Hemisphere are located over the North Atlantic and the North Pacific, with secondary storm track regions over the Mediterranean and Siberia (e.g.

Hoskins and Hodges, 2002). The North Atlantic storm track region starts east of the Rocky Mountains in North America and ends in northern Europe (e.g. Hoskins and Hodges, 2002; Priestley et al., 2020). In this study, we consider northern Europe to be a region covering Norway; Sweden; Finland; Estonia; and parts of the Baltic, Norwegian, and Barents seas. In general, extratropical cyclones at the end of all storm track regions are less studied. However, the structure and evolution of such extratropical cyclones may differ from extratropical cyclones elsewhere. Schultz et al. (1998) noted that extratropical cyclones at the end of the North Atlantic storm track generally resemble more of the Norwegian cyclone model (Bjerknes, 1919; Bjerknes and Solberg, 1922) than the Shapiro–Keyser cyclone model (Shapiro and Keyser, 1990), which is reasonable since the Norwegian cyclone model was developed based on cyclones that occur in north-western Europe. Wang and Rogers (2001) found that there are many differences in the dynamical and thermal structure and evolution of strong explosive cyclones in the north-eastern Atlantic compared to the north-western Atlantic. For example, the explosive cyclones in the north-eastern Atlantic have lower static stability but less environmental baroclinicity than explosive cyclones in the north-western Atlantic (Wang and Rogers, 2001).

There are two main ways to identify extratropical cyclones: the Eulerian approach and the Lagrangian approach (Hoskins and Hodges, 2002). The Eulerian approach uses basic statistics such as the variance or standard deviation of a chosen meteorological field (for example mean sea level pressure (MSLP) or 850 hPa relative vorticity), which is bandpass-filtered with synoptic timescales, usually 2–6 d (Blackmon, 1976). While the Eulerian approach is straightforward and gives a general description of the storm track activity it does not provide information about individual extratropical cyclones and their characteristics. The Lagrangian approach is a feature tracking method where a localized minimum or maximum of a meteorological field (for example MSLP or 850 hPa relative vorticity) is identified, and their location in time is tracked (e.g. Hodges, 1994). With the Lagrangian approach it is possible to analyse cyclone-specific characteristics such as the genesis and lifetime. Moreover, additional meteorological variables can be determined along the cyclone track to investigate how they vary during the cyclone evolution.

The spatial and temporal evolution of extratropical cyclones can be analysed by producing cyclone composites. Cyclone compositing allows us to statistically find key features of the structure and development of the chosen set of cyclones. Cyclone composites have been used in extratropical cyclone research for example for creating an extratropical cyclone atlas for the 200 most intense historical extratropical cyclones in the North Atlantic (Dacre et al., 2012) and to investigate how moisture is transported into extratropical cyclones (Dacre et al., 2019). Commonly cyclone composites are used to study the structures in extratropical cyclones, for example for precipitation and clouds (Field and Wood, 2007) and for air–sea turbulent heat fluxes and heat and moisture content (Rudeva and Gulev, 2011). Cyclone composites have also been used to examine extratropical cyclones and their structures in climate models (Catto et al., 2010) and in warming climate (Sinclair et al., 2020).

Since extratropical cyclones are responsible for the daily weather, and their associated heavy rainfall and strong winds can cause damage, it is important that extratropical cyclones and windstorms are accurately predicted. In this study, we define a windstorm to be an extratropical cyclone that has exceptionally strong 10 m winds (see Sect. 3.2 for a full definition). In addition to producing forecasts directly for the parameters of extratropical cyclone intensity (for example MSLP or wind gust), we can use other variables as proxies to predict the windstorm intensity (Krueger and Von Storch, 2011). The use of proxies in forecasting is especially helpful regarding parameters that are small in scale and therefore harder for numerical weather prediction models to accurately predict (Faranda et al., 2017). For forecasting purposes, the proxies should be descriptive of the evolution of windstorms earlier than the most intense phase; i.e. they should act as precursors to windstorms. One way to find precursors to windstorms is to use ensemble sensitivity analysis (which is described in detail in Sect. 3.4), which allows us to quantify how sensitive the subsequent windstorm intensity is to precursor fields. The ensemble sensitivity analysis method was examined by Ancell and Hakim (2007), who analysed the linear connection between perturbed initial conditions and forecast metrics of the wintertime flow pattern on the west coast of North America. The ensemble sensitivity method has also been used to find precursors to intense Mediterranean cyclones (Garcies and Homar, 2009) and to extratropical cyclones in the western and eastern North Atlantic (Dacre et al., 2012). This method is a computationally simple way to identify sensitivities, but it has a limitation of assuming a linear relationship between the precursor and the characteristics of the windstorm being predicted. Nonetheless, the results can provide guidance for forecasters and indicate to which variables the most attention should be paid. From an application point of view, the sensitivities can also be used to assess, for example, likely error propagation or future climate projections. Since the resulting sensitivity shows how much, for example, the windstorm intensity changes if the precursor changes, a similar magnitude change in the precursor caused by an error in the numerical weather model would therefore result in a similar change in the windstorm intensity as the sensitivity results show. Likewise, future studies potentially could estimate how warmer climates would change the windstorm intensity by applying the sensitivity results to how the precursors are projected to change.

In this study, we aim to increase the knowledge of the extratropical cyclone and windstorm climate in northern Europe, which occurs at the end of the North Atlantic storm track. Although many extratropical cyclone studies focus

only on the cold season or winter months (e.g. Hoskins and Hodges, 2002; Pinto et al., 2005), we investigate the results separately for the cold (October–March) and warm (April–September) seasons in order to analyse the seasonal differences. In addition to the climatological properties as temporal frequencies and cyclone characteristics, we extend the study to examine what precursors are relevant in northern Europe windstorms by using ensemble sensitivity analysis. These results may help forecasters to better predict and prepare for windstorms by increasing their understanding of what environments windstorms typically develop in.

The research questions we aim to answer in this paper are as follows. (1) What are the annual and monthly frequencies of extratropical cyclones and windstorms in northern Europe? (2) Are there differences in cyclone characteristics between extratropical cyclones and windstorms and between the cold and warm seasons? (3) How does the spatial and temporal structure of northern Europe windstorms evolve? (4) What precursor has the strongest impact on the minimum MSLP and the maximum wind gust in northern Europe windstorms? The remainder of the paper is structured as follows: first, we introduce the data in Sect. 2 and the methods in Sect. 3. The annual and monthly frequencies of the three cyclone classes (all extratropical cyclones, windstorms, and non-windstorms) are shown in Sect. 4, and different cyclone characteristics are analysed in Sect. 5. Section 6 examines the spatial and temporal evolution of windstorms, and Sect. 7 investigates the precursors to windstorms. The final conclusions are given in Sect. 8.

2 ERA5 reanalysis data

ERA5 is the newest atmospheric reanalysis produced by the European Centre for Medium Range Weather Forecasts (Hersbach et al., 2020), and it is based on the Integrated Forecasting System (IFS; cycle 41r2). ERA5 has a horizontal resolution of 31 km, and vertically it has 137 levels from the surface up to approximately 80 km. ERA5 provides hourly analysis and forecast fields, and while conducting the analysis for this study, ERA5 covered years from 1979 onwards. Recently, there was a release of a back extension, making ERA5 available from 1950 onwards.

In our study, ERA5 data are obtained every 3 h from 1980–2019 (40 years). The variables we obtain are MSLP, the maximum 10 m wind gust (maximum since previous post-processing), 850 hPa temperature, total column water vapour (TCWV), 300 hPa horizontal wind speed components, and 300 hPa potential vorticity (PV). We consider 10 m wind gusts rather than 10 m wind speeds since the impacts and damage regarding extratropical cyclones are usually caused by the strong wind gusts (Gardiner et al., 2013).

3 Methods

3.1 Extratropical cyclone tracking

The cyclones are tracked with the TRACK algorithm (Hodges, 1994, 1995, 1999), and the tracking is based on 3-hourly MSLP from ERA5. The MSLP field is smoothed to T63 resolution (around 180 km) before running TRACK to decrease the noise in the field, and in addition, wavenumbers smaller than 5 are removed in order to exclude the large planetary-scale waves. Many studies use T42 resolution for vorticity-based tracking (e.g. Priestley et al., 2020); however, higher resolution of T63 is generally used for MSLP since its field is smoother than the vorticity field (Hodges et al., 2011). Since we want to investigate large-scale extratropical cyclones, we included only tracks that last at least 1 d and move at least 500 km during their lifetime in order to remove the short-lived and stationary cyclones. After the tracks are created, we then found the locations and values of the minimum MSLP of the cyclone centre at each time step of each track from the native, high-resolution (31 km) data. We also found, for each time step of the track, the maximum 10 m wind gust within a 6° radius because we wanted to find the wind gusts associated with the extratropical cyclones. The results presented in Sect. 6 confirm that the 6° radius used to identify the associated wind gusts is an appropriate choice.

3.2 Extratropical cyclone classes

The classification of the extratropical cyclones is made based on their associated wind gusts. In this study, we include all extratropical cyclones that have at least one point of their track located inside a box (55–75° N, 5–40° E; the box is shown in Fig. 4) during 1980–2019. The wind gust distribution of all extratropical cyclones is created by using the maximum 10 m wind gust within 6°of the cyclone centre at each time step when the cyclone centre of the track is inside the northern Europe box. Thus, there can be more than one gust value per cyclone track, and additionally, the location of the maximum wind gust can be at maximum 6° outside the box (Fig. A2). Figure 1 shows the wind gust distributions covering the whole year (Fig. 1a), the cold season (Fig. 1b), and the warm season (Fig. 1c). All of the distributions are slightly positively skewed; i.e. they have more weight in the right tail. However, the mean and median values are relatively close to each other, and the mean values vary from 22.2 $\mathrm{m\,s^{-1}}$ in the cold season (Fig. 1b) to 18.1 $\mathrm{m\,s^{-1}}$ in the warm season (Fig. 1c). The 90th percentile of the wind gust distribution covering the whole year is 27.2 $\mathrm{m\,s^{-1}}$ (Fig. 1a). While the 90th percentile of wind gusts during the cold (29.4 $\mathrm{m\,s^{-1}}$) and warm (23.6 $\mathrm{m\,s^{-1}}$) seasons differs from the whole-year value, these are relatively near each other compared to the maximum values, which differ from 51.6 $\mathrm{m\,s^{-1}}$ in the cold season to 38.1 $\mathrm{m\,s^{-1}}$ in the warm season.

In order to classify the extratropical cyclones based on their extremeness in wind gusts without depending on the season, we use 27.2 m s^{-1} (i.e. the 90th percentile of wind gusts during the whole year) as a threshold to divide the extratropical cyclones to windstorms and non-windstorms. The choice of 90th percentile as a threshold gives a reasonable number of windstorms for further analysis. When the windstorm threshold is equal in both seasons we can more easily compare the seasons since otherwise the warm-season windstorms would include extratropical cyclones that have lower wind gusts than cold-season windstorms. Furthermore, since our study focuses more on the dynamics and the structure of windstorms rather than impacts, the threshold we use considers wind gusts over the whole northern Europe box rather than only wind gusts over land. Therefore, our final cyclone classes are (1) all extratropical cyclones – all extratropical cyclones that have at least one track point inside the northern Europe box, (2) windstorms – extratropical cyclones whose associated wind gusts are equal to or exceed the 90th percentile when the cyclone centre is inside the northern Europe box, and (3) non-windstorms – extratropical cyclones whose associated wind gusts are below the 90th percentile when the cyclone centre is inside the northern Europe box. Hence, the sum of windstorms and non-windstorms equals all extratropical cyclones.

In this study, we also need to identify, for each windstorm, the time of the minimum MSLP and the time of the maximum 10 m wind gust. The time of the minimum MSLP is the time when the absolute minimum of MSLP occurs along the cyclone track, and therefore the cyclone centre does not need to be located within the northern Europe box at this time. In contrast, as we are interested in investigating wind gusts in northern Europe, we define the time of the maximum 10 m wind gust to be the time that the maximum gust occurs while the cyclone centre is within the northern Europe box. However, as the gusts are taken within a 6° radius of the cyclone centre, the location of the maximum gust can occur just outside of the northern Europe box. The locations of the minimum MSLP and the maximum 10 m wind gust for each windstorm track are shown in the Appendix Figs. A1 and A2.

3.3 Cyclone composites

To further examine the structure and evolution of northern Europe windstorms (identified as described in Sect. 3.2), we create cyclone composites in a similar way as for example Dacre et al. (2012) and Sinclair et al. (2020). The composites are produced for different meteorological variables at different offset times relative to two times: the time of the minimum MSLP and secondly the time of the maximum 10 m wind gust (these times are defined at the end of Sect. 3.2). For the compositing, the windstorms are transformed into a spherical grid (cyclone centre in the middle) and rotated to a cyclone-relative coordinate so that they all travel to the east. The composite for each meteorological variable and offset time is created by averaging that meteorological field of each individual windstorm.

3.4 Ensemble sensitivity analysis

To statistically identify precursors which are strongly correlated with characteristics of windstorms in northern Europe, we use an ensemble sensitivity analysis. In this study, "ensemble" refers to the population of extratropical cyclones that are defined as windstorms. The principle of the ensemble sensitivity method is to calculate the linear regression between a precursor field, x, and the so-called response function, J. In our study, we consider two response functions: (1) the minimum MSLP and (2) the maximum 10 m wind gust. The minimum MSLP was chosen because it is a common variable to represent the intensity of an extratropical cyclone, and the maximum wind gust was chosen because gusts usually cause the high impacts and damage. The minimum MSLP is not directly related to the wind gusts but indirectly by strengthening the pressure gradient, which is associated with stronger wind speeds and hence stronger wind gusts. The ensemble sensitivity analysis is applied to precursors on the cyclone centred radial grid.

The sensitivity S consists of multiplying three components:

$$S_{i,j} = m_{i,j}\alpha_{i,j}\sigma_{i,j}, \tag{1}$$

where m is the linear regression slope, α is a correction factor, and σ is the standard deviation of the precursor. The linear regression slope m is calculated at each grid point (i, j):

$$m_{i,j} = \left(\frac{\delta J}{\delta x}\right)_{i,j}. \tag{2}$$

The correlation factor α modifies the sensitivity S by giving less weight to slope values in those grid points that have weak correlations. This is done by defining α:

$$\alpha_{i,j} = \begin{cases} 1 & \text{if } r^2_{i,j} \geq r^2_{\min}, \\ \frac{r^2_{i,j}}{r^2_{\min}} & \text{if } r^2_{i,j} < r^2_{\min} \end{cases} \tag{3}$$

where $r_{i,j}$ is the correlation coefficient, and $r_{\min}$ is the threshold for correlations that are altered. Similarly to Dacre and Gray (2013), we set $r^2_{\min}$ to be 0.05, which means that for all grid points where the correlation coefficient is less than 0.224, the sensitivity S is reduced.

The standard deviation σ is calculated at each grid point through all windstorms and over both seasons to ensure that the two seasons can be compared to each other. By multiplying with the standard deviation, the sensitivity S obtains the same units as the response function. Therefore, the sensitivity can be interpreted as how the response function (the minimum MSLP / maximum 10 m wind gust) changes when there is an increase of 1 standard deviation in the precursor field.

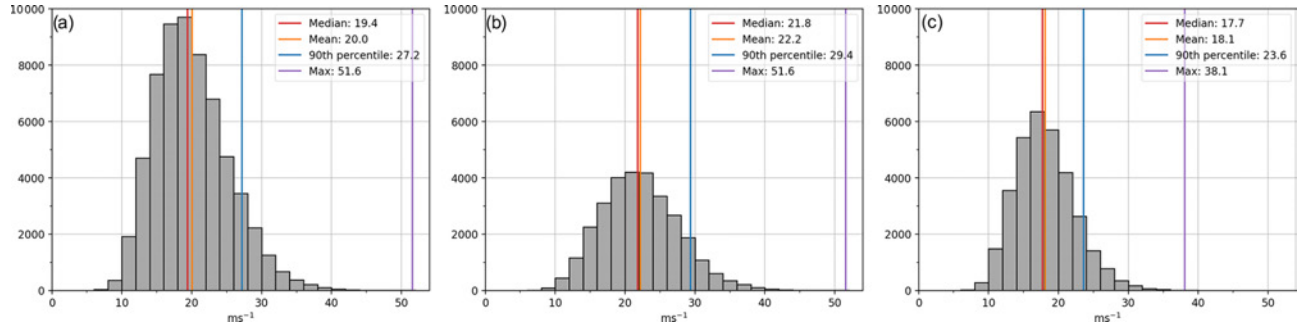

Figure 1. Distribution of the maximum 10 m wind gust within 6° of the cyclone centre at each time step when the cyclone centre of the track is inside the northern Europe box during 1980–2019 covering **(a)** the whole year, **(b)** the cold season (October–March), and **(c)** the warm season (April–September).

The sign of the sensitivity is determined only by the regression slope m, and the magnitude is affected by all three components in Eq. (1). Negative sensitivity means that the precursor x and the response function J are negatively correlated. Regarding the response function of the minimum MSLP, this means that if the precursor increases it is associated with a decrease in the minimum MSLP, i.e. to a stronger windstorm in terms of MSLP. Likewise, regarding the response function of the maximum 10 m wind gust, negative sensitivity means that if the precursor increases it is associated with a decrease in the maximum wind gust. However, this implies that the windstorm gets weaker in terms of wind gusts. This is important to note when comparing the sensitivities of these response functions that the sign of the sensitivity indicates contrary evolution to the windstorm.

In our study, we examine four precursors: 850 hPa potential temperature anomaly, TCWV, 300 hPa wind speed, and 300 hPa PV. We selected these precursors because the 850 hPa potential temperature gradient is a main driver of extratropical cyclones through baroclinicity. TCWV allows us to investigate the availability of moisture that may influence diabatic processes, which further may affect the intensity of an extratropical cyclone. The 300 hPa wind speed describes the jet stream, and the location of an extratropical cyclone in relation to the jet stream is known to influence to the extratropical cyclone development. Lastly, the 300 hPa PV was chosen because the surface cyclone can intensify when it interacts with an upper-level trough, which can be interpreted from the upper-level PV field. The 850 hPa potential temperature is used as an anomaly to assess the strength of the temperature gradient. The anomaly is calculated in each individual windstorm separately by first area-averaging the 850 hPa potential temperature over the 18° radius composite and then subtracting this mean from each grid point in that windstorm. We investigate the precursor fields 24, 48, and 72 h before the time of the minimum MSLP or the maximum 10 m wind gust as defined in Sect. 3.2. These offset times are relevant because they occur at the typical range of extratropical cyclone predictability and evolution. In addition, since the ensemble sensitivity method uses linear correlations the sensitivities are most likely valid at short lead times, whereas at much longer lead times the non-linear affects would dominate.

4 Annual and monthly frequencies of extratropical cyclones, windstorms, and non-windstorms

The annual frequency of extratropical cyclones during 1980–2019 shows a large year-to-year variability in all three cyclone classes (Fig. 2). There are on average 149 extratropical cyclones every year that reach northern Europe (Fig. 2a), of which on average 35 cyclones, i.e. 23 %, are windstorms (Fig. 2c). Although the threshold for windstorms is the 90th percentile of wind gusts, the wind gust distribution can have multiple wind gust values per cyclone since we include all wind gust values at each time step when the cyclone centre is inside the northern Europe box. Hence, the ratio of windstorms can be higher than 10 %. The 40-year linear trends are not statistically significant in any of the three cyclone classes by using the Mann–Kendall test (Mann, 1945; Kendall, 1970) at the 5 % level. However, there is a decreasing trend (−3.7 cyclones per decade) in all extratropical cyclones (Fig. 2a and b) with a p value of 0.067, and therefore the trend would be significant with a 7 % level or higher. However, some time periods stand out with high or low annual number of extratropical cyclones. In the 1980s, there were overall more extratropical cyclones compared to the 40-year average (Fig. 2b), which was mainly due to the increased numbers of non-windstorms (Fig. 2f). In contrast, a longer-term drop in all extratropical cyclones (Fig. 2b) occurred between 1995–2005, during which time the number of windstorms (Fig. 2d) decreased more than the number of non-windstorms. The highest annual numbers of windstorms occurred in 1983 and 1990 (Fig. 2c and d).

In addition to large inter-annual variability, we also investigated the seasonal cycle of the number of extratropical cyclones, windstorms, and non-windstorms (Fig. 3). Regarding all extratropical cyclones in northern Europe (Fig. 3a), the

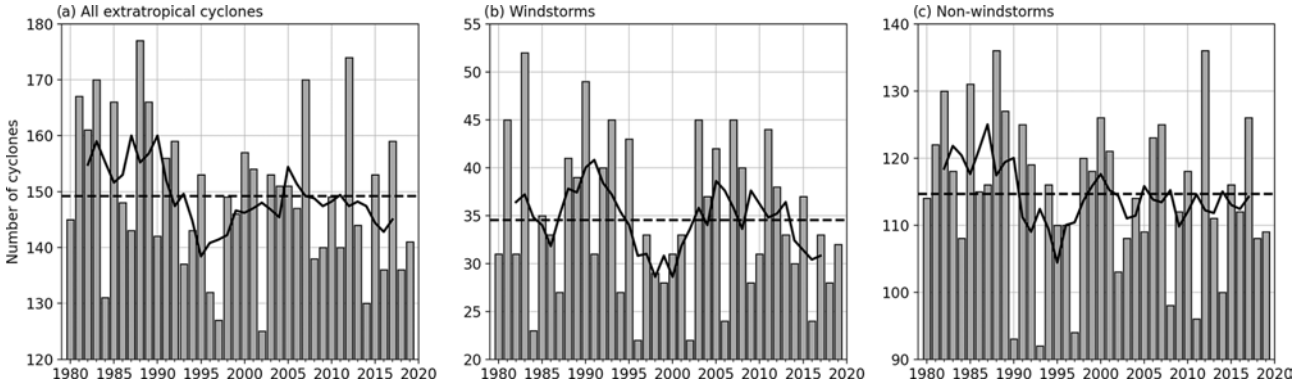

Figure 2. Annual absolute numbers of extratropical cyclones in northern Europe in 1980–2019. Bars show the annual values, solid lines are 5-year running means, and dashed lines are annual means. **(a)** All extratropical cyclones, **(b)** windstorms, and **(c)** non-windstorms.

months from October to January and April have the highest median, between 13–15 extratropical cyclones per month, which means that on average almost every other day in these months an extratropical cyclone travels through northern Europe. The variability in extratropical cyclone numbers within each month (length of whiskers) is the highest during autumn and winter. Nevertheless, the monthly variation in the number of all extratropical cyclones does not have a significantly large seasonal cycle. In contrast, the number of windstorms (Fig. 3b) shows a strong annual cycle, with more windstorms in the cold season and less in the warm season. The highest median values of 5–6 windstorms per month are in January and December, whereas in May, June, and July, there are on average no windstorms at all. The variation in windstorm numbers within the cold-season months is, however, quite large; for example in November, the number of windstorms ranges from 0 to 14. The seasonal cycle for non-windstorms (Fig. 3c) is the opposite of that for windstorms with the highest number of non-windstorms occurring during the warm season from April to August. Therefore, we can conclude that while windstorms are more common in winter, and extratropical cyclones in summer are weaker, the overall number of extratropical cyclones per month in northern Europe does not differ considerably depending on season.

5 Characteristics of extratropical cyclones, windstorms, and non-windstorms

The genesis and track densities are computed by the TRACK code using the spherical kernel method (Hodges, 1996), and the unit of the densities is number of cyclones per season (i.e. 6 months) per unit area, where the unit area is a 5° radius spherical cap ($\approx 10^6$ km^2). In both seasons, the genesis region of all extratropical cyclones that affect northern Europe extends from the east coast of the United States to western Russia and from the Greenland Sea to the Mediterranean Sea (Fig. 4a and b). Most of the extratropical cyclones in the warm season originate over the land areas inside the northern Europe box (Fig. 4b). In the cold season (Fig. 4a), the most dense genesis region is broader, and, in addition to the land areas in northern Europe, most of the extratropical cyclones originate from the Norwegian Sea and the Barents Sea. The genesis over the east coast of the United States is more poleward in the warm season than in the cold season, which is in agreement with Priestley et al. (2020), who found that extratropical cyclones occur more equatorward in the winter than in the summer in the eastern North Atlantic.

When considering windstorms and non-windstorms separately, there are distinct differences. Most of the non-windstorms originate over land areas in northern Europe (Fig. 4e and f), whereas windstorms have their genesis mostly over the Norwegian Sea and the Barents Sea (Fig. 4c and d). This also means that windstorms tend to originate farther away from northern Europe than non-windstorms. In addition, non-windstorms can originate over southern Europe while windstorms do not. In the cold season, the genesis region of windstorms is more zonally spread (Fig. 4c), whereas non-windstorms are more meridionally spread (Fig. 4e). In contrast, in the warm season the genesis region of non-windstorms is zonally spread and includes tracks from the eastern United States (Fig. 4f).

The track densities of all extratropical cyclones are, on a large scale, similar in both seasons, and the highest track density occurs inside the northern Europe box (Fig. 5a and b). Cold-season extratropical cyclones have high track densities over the eastern part of northern Europe and over the Barents Sea (Fig. 5a). There are somewhat fewer tracks over the Scandinavian Mountains, which is likely caused because the Scandinavian Mountains can, to some degree, modify the track of passing extratropical cyclones and even split the cyclone into two low centres (Grönås, 1997). When comparing windstorms and non-windstorms, it is evident that most windstorms have their cyclone centre at higher latitudes than non-windstorms (Fig. 5c–f). The difference is more pronounced in the cold season, when windstorms mostly occur

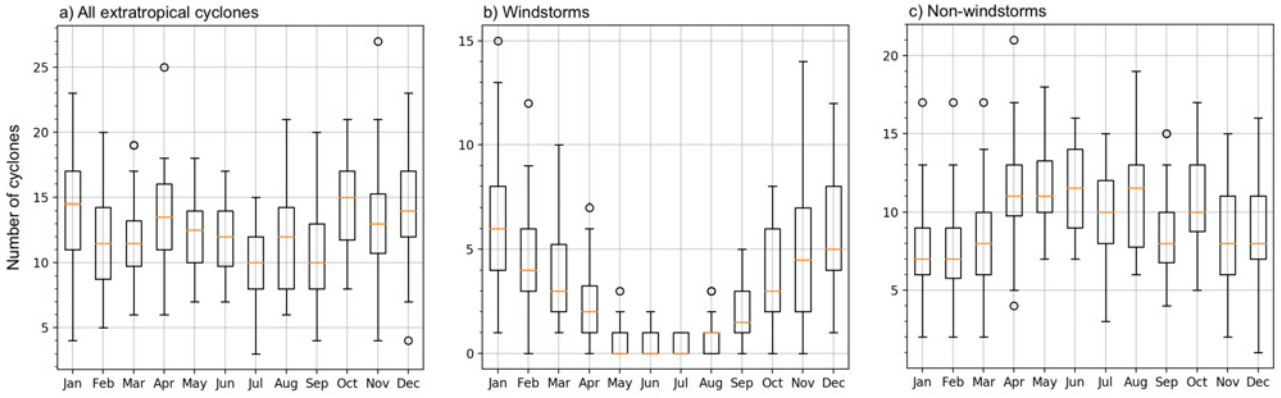

Figure 3. Monthly distribution of cyclones in northern Europe. Orange lines are medians, boxes show first and third quartiles, and whiskers have a first value greater than and a last value less than $Q1 - 1.5 \cdot IQR$ and $Q3 + 1.5 \cdot IQR$, respectively, where Q1 and Q3 are the first and third quartiles and IQR the interquartile range Q3–Q1. **(a)** All extratropical cyclones, **(b)** windstorms, and **(c)** non-windstorms.

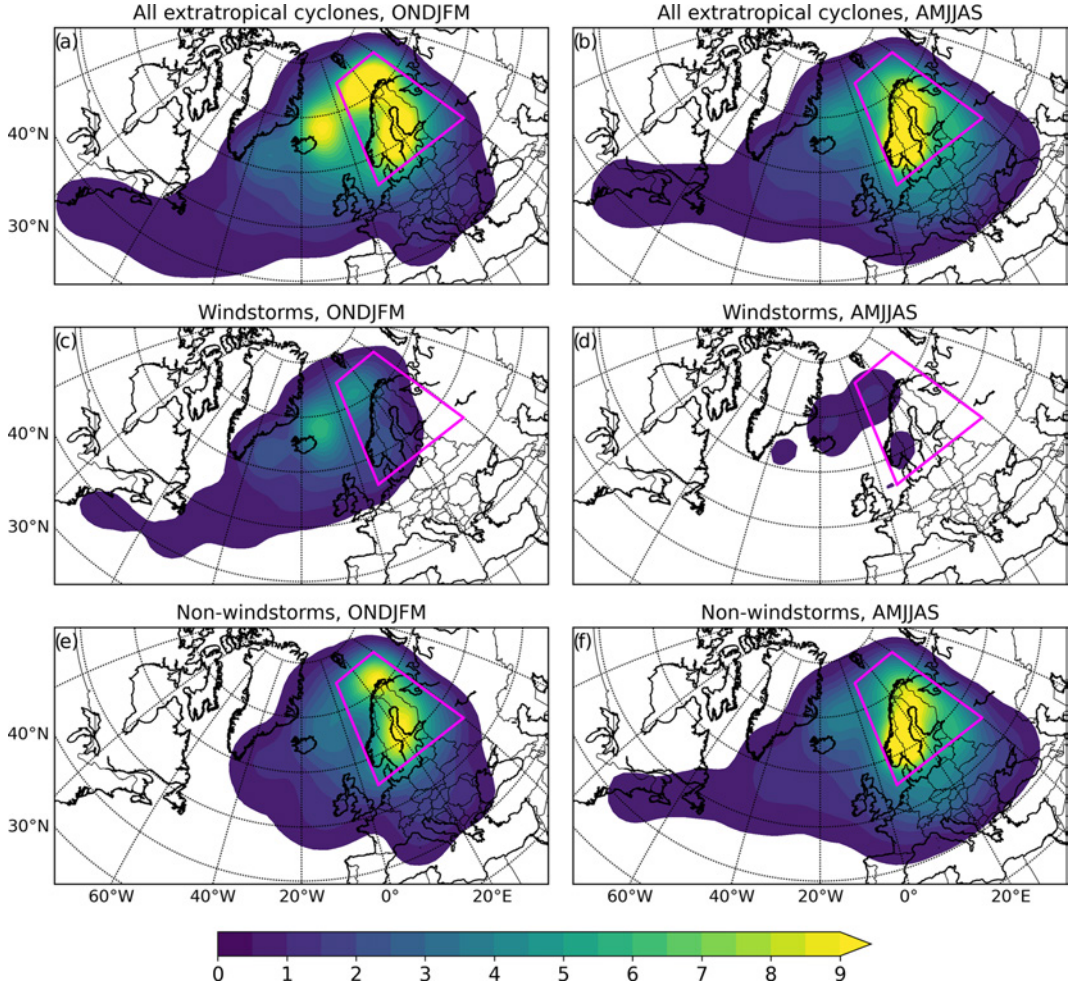

Figure 4. Genesis density (number of cyclones per season (i.e. 6 months) per 5° spherical cap $\approx 10^6$ km^2) of **(a, b)** all extratropical cyclones, **(c, d)** windstorms, and **(e, f)** non-windstorms. The magenta box shows the northern Europe box where the tracks in this study are filtered to occur.

over the Barents Sea (Fig. 5c), while non-windstorms occur over the southern parts of northern Europe (Fig. 5e).

The majority of extratropical cyclones, regardless of the cyclone class (windstorm or non-windstorm) or season, propagate towards the east inside the northern Europe box (not shown). However, each year there is a small portion of extratropical cyclones that propagate towards the west, and this is slightly more visible in the warm season than in the cold season. This is also seen in the genesis density (Fig. 4), where some extratropical cyclones originate on the eastern edge of the northern Europe box.

The median duration of the cyclone lifetime with all extratropical cyclones is 3.4 d in the cold season and 3.6 d in the warm season (not shown). Considering windstorms, the median lifetime is 4 d in both the cold and warm seasons, while non-windstorms have a longer median lifetime in the warm season (3.6 d) than in the cold season (3 d, not shown). Therefore, extratropical cyclones in northern Europe are on average longer-lived in the warm season compared to the cold season and in windstorms compared to non-windstorms. The lifetime of extratropical cyclones, especially in the extremely long-lasting cases, can also be interpreted from the width of the histograms in Fig. 6. In the warm season the histogram is wider (from −13 to 17 d; Fig. 6b), indicating that the lifetimes are longer than in the cold season (from −9 to 10 d; Fig. 6a).

Figure 6 shows the maximum 10 m wind gusts in northern Europe (i.e. the maximum 10 m wind gust when the cyclone centre is inside the northern Europe box) in relation to the time of the minimum MSLP. The highest wind gust values on the y axis are concentrated close to zero on the x axis, which means that the maximum wind gusts occur close to the time of the minimum MSLP. The median occurrence time of the maximum gusts relative to the time of the minimum MSLP is 0 h for all extratropical cyclones and non-windstorms and +3 h for windstorms. There is no differences between the seasons on the median occurrence times. Overall, the occurrence time of the wind gusts is practically very close to the minimum MSLP, and the difference between windstorms and non-windstorms is small. In the cold season, the maximum 10 m wind gusts are higher (up to 52 m s^{-1}) than in the warm season (up to 38 m s^{-1}), which was also seen in the wind gust distributions (Fig. 1). Figure 6 also shows that while the wind gusts are the strongest at the time of the minimum MSLP, after that the wind gusts decrease. This happens especially in windstorms (Fig. 6c and d) where a negative tilt is visible after the time of the minimum MSLP. The negative tilt is not evident in non-windstorms (Fig. 6e and f), but non-windstorms by definition do not have strong wind gusts (there are no wind gust values above 27.2 m s^{-1}).

6 Spatial and temporal evolution of maximum wind gusts, MSLP, and frontal structure in windstorms

The composites of 10 m wind gust, MSLP and 850 hPa potential temperature are shown in Fig. 7 for the cold season and in Fig. 8 for the warm season, and these fields allow us to determine the spatial structure of windstorms in northern Europe. The offset times are relative to the time of the minimum MSLP of each windstorm (defined in Sect. 3.2). We investigate here the offset times at −48, −24, 0, and +24 h since Fig. 6 shows that these times cover the evolution before and after the strongest wind gusts and additionally include enough windstorms to ensure a reasonable number of cyclones in each composite; at the time of the minimum MSLP there are 1129 windstorms in the cold season and 245 windstorms in the warm season.

Already 48 h before the minimum MSLP (Figs. 7a and 8a), a closed low-pressure centre is evident in both seasons. The cold-season composite has a deeper central pressure (994 hPa) and a stronger pressure gradient than the warm-season composite (998 hPa). The frontal structure is visible from the 850 hPa potential temperature composite with a warm front downstream of the cyclone centre and a cold front upstream of the cyclone centre. The strongest wind gusts occur in the warm sector in the region of the strongest pressure gradient. In addition, the strongest wind gusts are located within a 6° radius from the cyclone centre, which supports the choice of selecting the maximum wind gust within 6°. The strongest composite gusts are 17.2 m s^{-1} in the cold season and 14.2 m s^{-1} in the warm season. The region of the strongest gusts is more widely spread in the cold season than in the warm season. This indicates that the windstorms in the cold season are larger in spatial scale than in the warm season.

At 24 h before the minimum MSLP (Figs. 7b and 8b), the central pressure decreases, and the pressure and frontal gradients increase compared to the −48 h offset time. The wind gusts get stronger, while the maximum gust location spreads extending from the warm sector to the cold front. At the time of the minimum MSLP (Figs. 7c and 8c), the central pressure in the cold season is 972 hPa and in the warm season 981 hPa, and the pressure gradient is the strongest equatorward of the cyclone centre. The warm front starts to wrap around the cyclone centre, indicating that the windstorm is reaching its mature stage. The wind gusts are the strongest at this offset time, and the maximum gust values are 20.5 m s^{-1} in the cold season and 18.6 m s^{-1} in the warm season. The location of the maximum wind gusts occurs in a region extending from the warm sector to behind the cold front, where the pressure gradient is the strongest. The maximum wind gusts are still within a 6° radius from the cyclone centre. At 24 h after the minimum MSLP (Figs. 7d and 8d), the central pressure has risen and the frontal structure weakened. The maximum wind gusts have decreased and now occur behind the cold front.

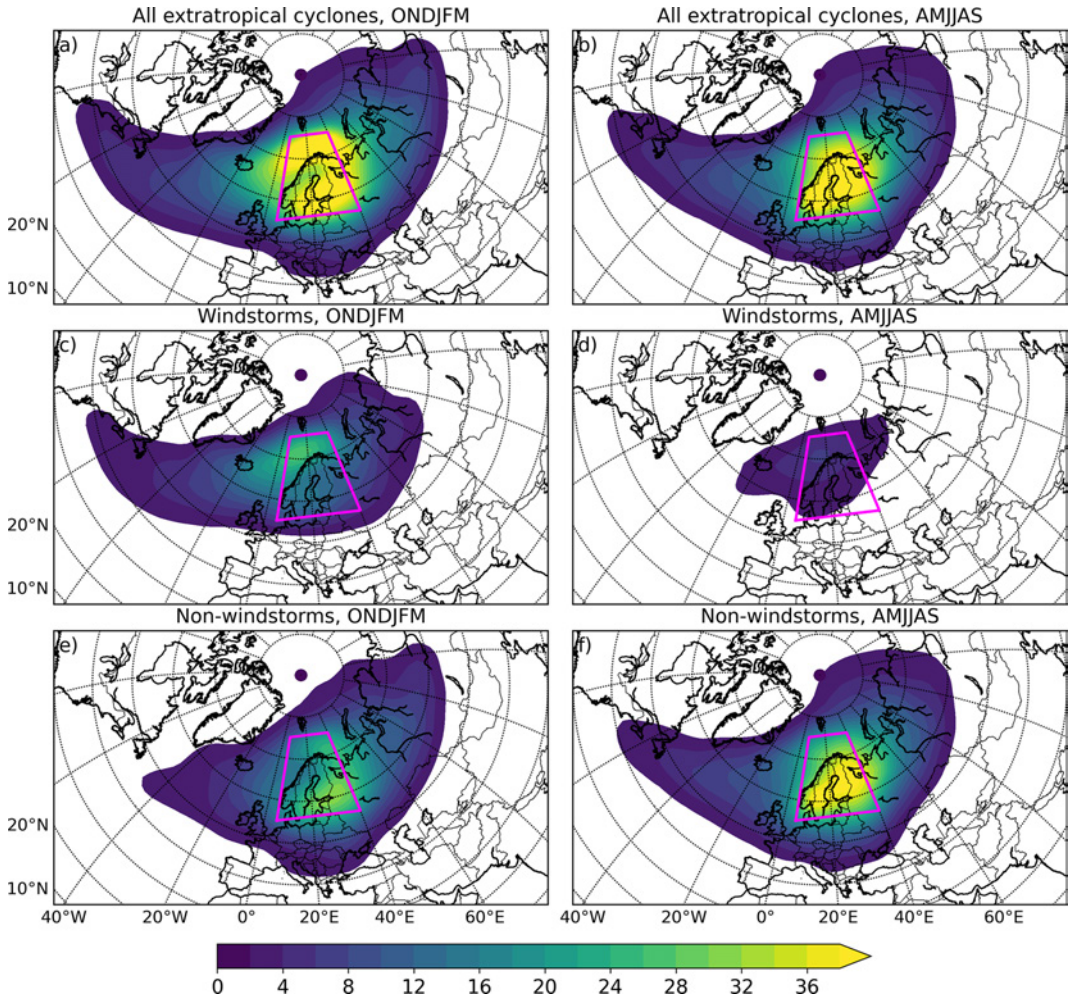

Figure 5. Track density (number of cyclones per season (i.e. 6 months) per 5° spherical cap $\approx 10^6$ km^2) of **(a, b)** all extratropical cyclones, **(c, d)** windstorms, and **(e, f)** non-windstorms. The magenta box shows the northern Europe box where the tracks in this study are filtered to occur.

To conclude, the location of the maximum wind gusts moves from the warm sector to behind the cold front following the location of the strongest pressure gradient during the evolution of the composite windstorm. The wind gusts, pressure gradient, and potential temperature gradient are all stronger and the minimum MSLP deeper in the cold season than in the warm season. In addition, the spatial scale of the windstorm is larger in the cold season than in the warm season.

7 Precursors to windstorms

In this section, we use the ensemble sensitivity analysis to investigate how two response functions, (1) the minimum MSLP and (2) the maximum 10 m wind gust, are sensitive to four different precursors at different offset times. The precursors we examine are 850 hPa potential temperature anomaly, TCWV, 300 hPa wind speed, and 300 hPa PV, and these are analysed 72, 48, and 24 h before the offset time.

7.1 Sensitivity of the minimum MSLP

The offset time in the minimum MSLP sensitivities is relative to the time when the minimum MSLP occurs during the whole lifetime of the windstorm (same as in the composites in Sect. 6). The 850 hPa potential temperature anomaly composites (contours in Fig. 9) show similar frontal structures and seasonal differences as in Figs. 7 and 8, which show the absolute values. In the cold season, the sensitivity to the 850 hPa potential temperature anomaly has a dipole pattern with negative sensitivity in the warm sector and positive sensitivity in the cold sector north of the cyclone centre. Negative sensitivity in the warm sector means that an increase in the 850 hPa potential temperature anomaly in this location is associated with a lower minimum MSLP. The strongest negative sensitivities at −48 h (Fig. 9c) show that an increase

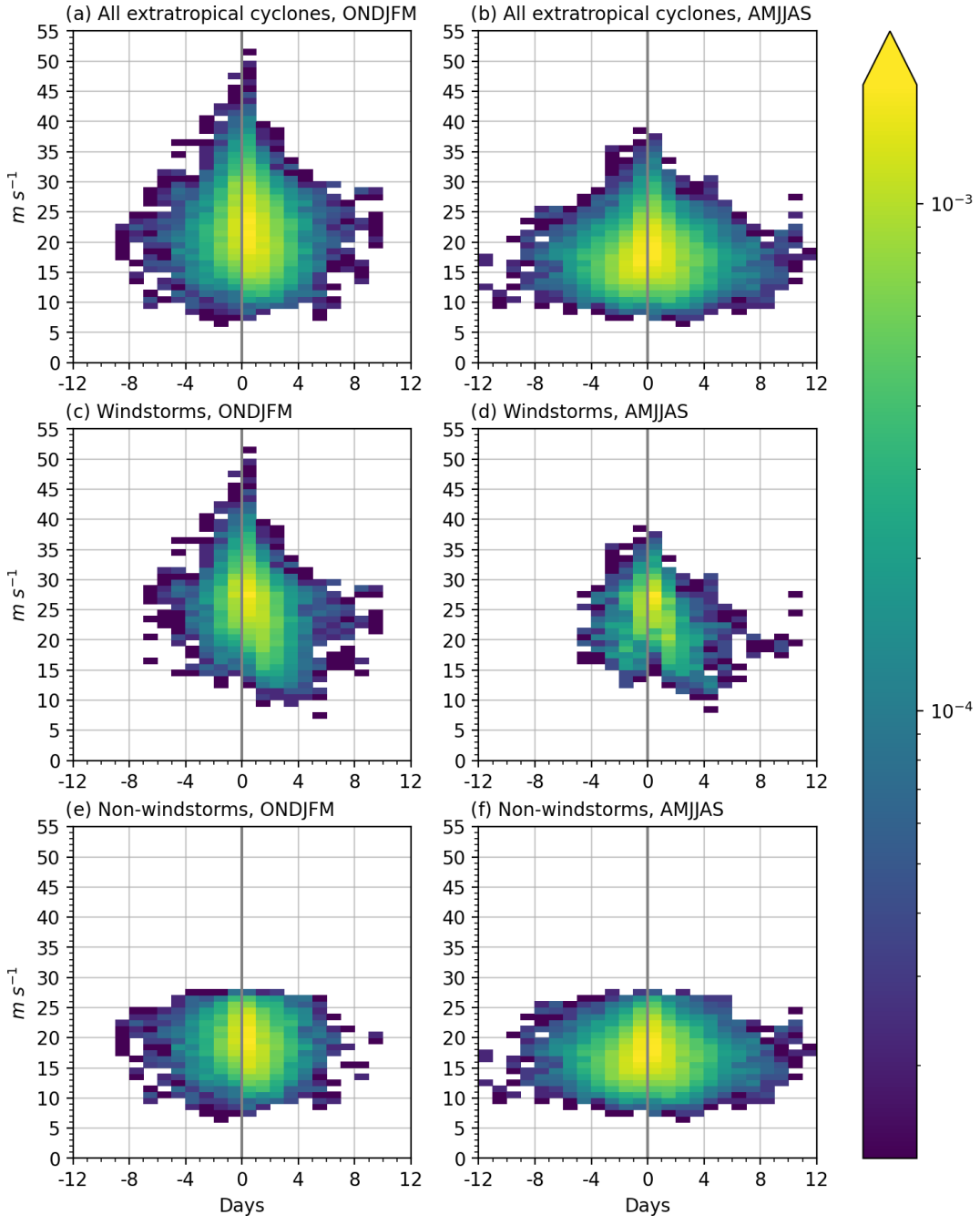

Figure 6. Normalized frequency of the maximum 10 m wind gust ($m\,s^{-1}$) in northern Europe (i.e. the maximum 10 m wind gust when the cyclone centre is inside the northern Europe box) in relation to the time of the minimum mean sea level pressure (MSLP) during the cold season **(a, c, e)** and the warm season **(b, d, f)**: **(a, b)** all extratropical cyclones, **(c, d)** windstorms, and **(e, f)** non-windstorms. Zero on the x axis indicates the time when the minimum MSLP during the track is obtained, and negative (positive) values indicate days before (after) that time. The frequency is normalized by the total number of the points in the tracks, and the colours are in a logarithmic scale. There are three data points with x-axis values over 12 d which are cut from the figure.

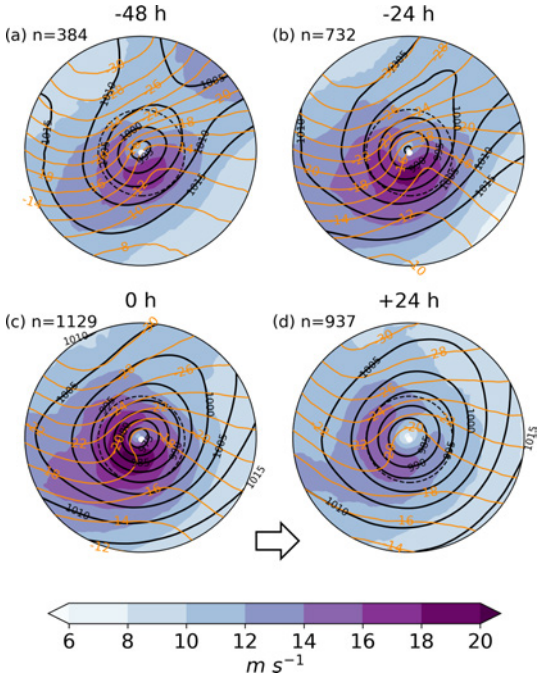

Figure 7. The maximum 10 m wind gust (colours; m s^{-1}), mean sea level pressure (black contours; 5 hPa interval), and 850 hPa potential temperature (orange contours; 2 °C interval) composites of windstorms during the cold season (October–March). The offset times are relative to the time of the minimum mean sea level pressure: **(a)** −48 h, **(b)** −24 **(h, c)** 0 h, and **(d)** +24 h. The number in each panel is the number of individual windstorms in each composite. The radius of the plots is 18°, and the 6° radius is marked with a dashed circle. The arrow shows the propagation direction of the cyclones.

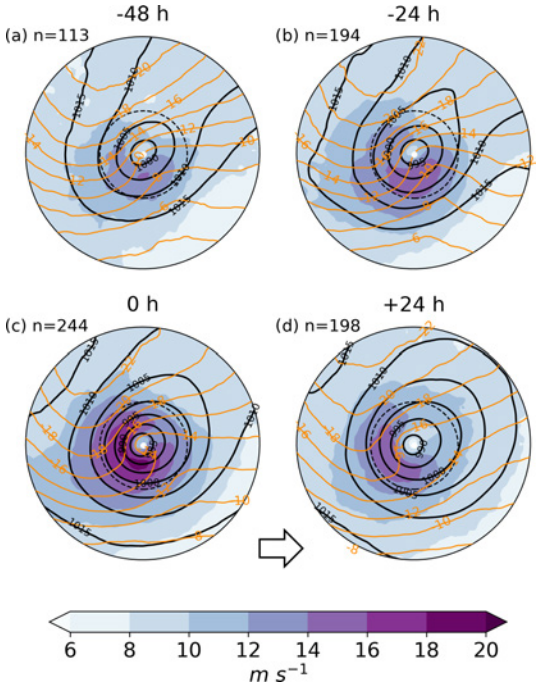

Figure 8. The maximum 10 m wind gust (colours; m s^{-1}), mean sea level pressure (black contours; 5 hPa interval), and 850 hPa potential temperature (orange contours; 2 °C interval) composites of windstorms during the warm season (April–September). The offset times are relative to the time of the minimum mean sea level pressure: **(a)** −48 h, **(b)** −24 h, **(c)** 0 h, and **(d)** +24 h. The number in each panel is the number of individual windstorms in each composite. The radius of the plots is 18°, and the 6° radius is marked with a dashed circle. The arrow shows the propagation direction of the cyclones.

of 1 standard deviation in the 850 hPa potential temperature anomaly decreases the minimum MSLP by more than 13 hPa. Likewise, positive sensitivity in the cold sector means that an increase in the 850 hPa potential temperature anomaly in this location is associated with a higher minimum MSLP, which, in other words, means that a decrease in temperature in the cold sector is associated with a lower minimum MSLP. The strongest positive sensitivities at −72 h (Fig. 9a) and −48 h (Fig. 9c) show that an increase of 1 standard deviation in the 850 hPa potential temperature anomaly increases the minimum MSLP by 10 hPa. This implies that a stronger temperature gradient (i.e. a warmer warm sector and a colder cold sector) is associated with a deeper minimum MSLP and hence with a stronger windstorm in terms of MSLP. This is in agreement with studies that have shown that stronger baroclinicity and thus temperature gradient lead to a stronger extratropical cyclone (Tierney et al., 2018; Rantanen et al., 2019). The dipole pattern is evident in the cold season at all offset times, with the strongest sensitivities at −48 h. In the warm season, the dipole pattern is visible at −48 h (Fig. 9d) and −24 h (Fig. 9f) offset times, and the sensitivity at −48 h is distinctly higher than at −24 h. The minimum MSLP is not sensitive to the 850 hPa potential temperature anomaly at −72 h in the warm season (Fig. 9b).

The TCWV composites (contours in Fig. 10) have a similar pattern to the 850 hPa temperature anomaly composites, and the highest amount of moisture is found south of the cyclone centre in the warm sector. The negative sensitivities south and downstream of the cyclone centre mean that more moisture in the warm sector is associated with a deeper minimum MSLP. The sensitivities are higher in the cold season than in the warm season and have their largest values at −48 h offset time in both seasons. The highest sensitivity in the cold season is at −48 h offset time (Fig. 10c), where an increase of 1 standard deviation in TCWV decreases the minimum MSLP by 6 hPa. These results can be interpreted in a way that more moisture leads to more precipitation, and this leads to more diabatic heating. Furthermore, diabatic heating can then produce low-level positive PV, and this can further intensify the windstorm. Our result is consistent with Dacre et al. (2019), who similarly used ensemble sensitivity analysis to show that downstream moisture (TCWV) leads to an increase in total precipitation.

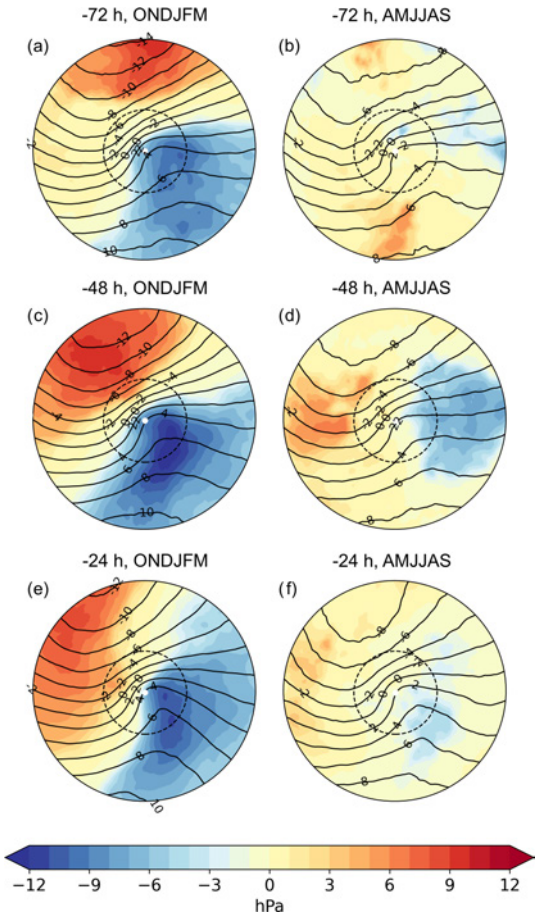

Figure 9. Sensitivity of the minimum MSLP to the 850 hPa potential temperature anomaly (colours; hPa) and the composite mean of the 850 hPa potential temperature anomaly (contours; 2 °C interval) **(a, b)** 72 h, **(c, d)** 48 h, and **(e, f)** 24 h before the occurrence of the minimum MSLP. Note that the colour scale here is double that in the other sensitivity figures. The radius of the plots is 18°, and the 6° radius is marked with a dashed circle.

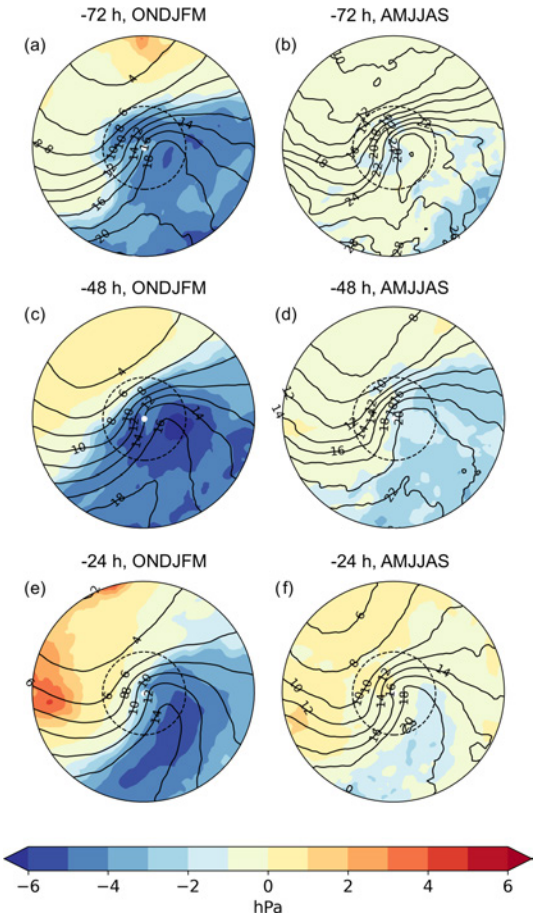

Figure 10. Sensitivity of the minimum MSLP to the TCWV (colours; hPa) and the composite mean of TCWV (contours; 2 kg m^{-2} interval) **(a, b)** 72 h, **(c, d)** 48 h, and **(e, f)** 24 h before the occurrence of the minimum MSLP. The radius of the plots is 18°, and the 6° radius is marked with a dashed circle.

The 300 hPa wind speed composites (contours in Fig. 11) show that the cyclone centre at −72 h is located in the centre of the poleward side of the jet stream, but at −48 and −24 h the cyclone centre is located at the left exit of the jet stream. The windstorm only starts strongly deepening at −48 h (not shown), when it moves into the left exit region (favourable region for cyclone development), and then 48 h later, at 0 h, the windstorm has its minimum MSLP. In the cold season at −72 h (Fig. 11a) and −48 h (Fig. 11c) offset times, the largest sensitivities are north-east of the cyclone centre. The strongest negative sensitivities in Fig. 11 mean that when the 300 hPa wind speeds increase by 1 standard deviation, it results in a decrease in minimum MSLP by 6 hPa. This implies that the minimum MSLP of a windstorm is deeper when the 300 hPa jet stream is extended north-east of the cyclone centre. A situation when the 300 hPa wind speed is stronger north-east of the cyclone centre suggests that the jet stream is tilted and thus more meridional. Furthermore, this implies that although at −72 h the cyclone centre is not located at the left exit of the jet, it possibly is in a region of cyclonic curvature vorticity advection. The 300 hPa wind speed at −24 h (Fig. 11e) has large sensitivities over the whole jet stream, meaning that the minimum MSLP decreases when the jet stream is stronger. In the warm season, there is more variability between the offset times than was observed in the cold season. The −24 h (Fig. 11f) sensitivity has a similar pattern to that of the cold season: a stronger jet stream is associated with a deeper windstorm. While the precursor at −48 h (Fig. 11d) shows some sensitivity for the north-east-extended jet stream, at −72 h (Fig. 11b) the field is more noisy and has no sensitivity. It is good to note that, climatologically, the jet stream is at a higher altitude in summer than in winter. However, the 300 hPa wind speed composites in the warm season do capture the jet streak, and the absolute 300 hPa wind speeds are not much weaker than in the cold season.

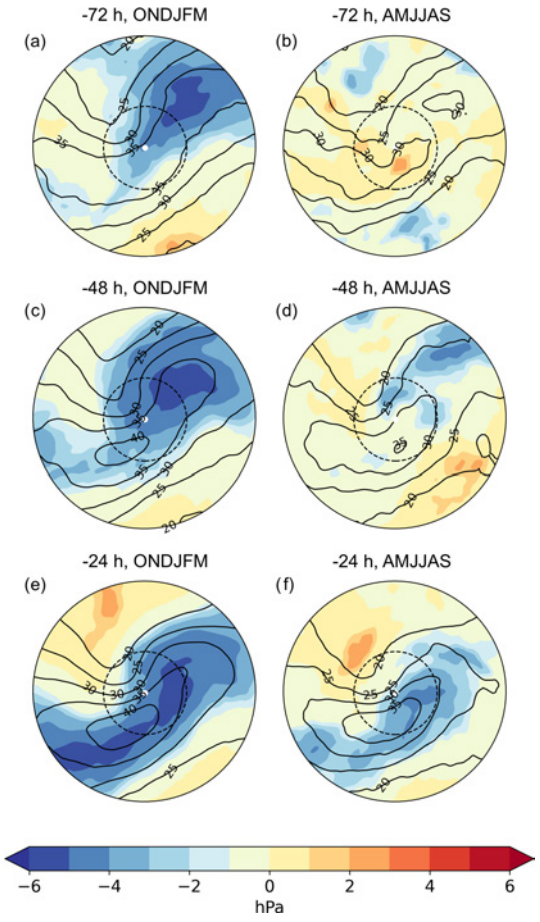

Figure 11. Sensitivity of the minimum MSLP to the 300 hPa wind speed (colours; hPa) and the composite mean of 300 hPa wind speed (contours; 5 m s^{-1} interval) **(a, b)** 72 h, **(c, d)** 48 h, and **(e, f)** 24 h before the occurrence of the minimum MSLP. The radius of the plots is 18°, and the 6° radius is marked with a dashed circle.

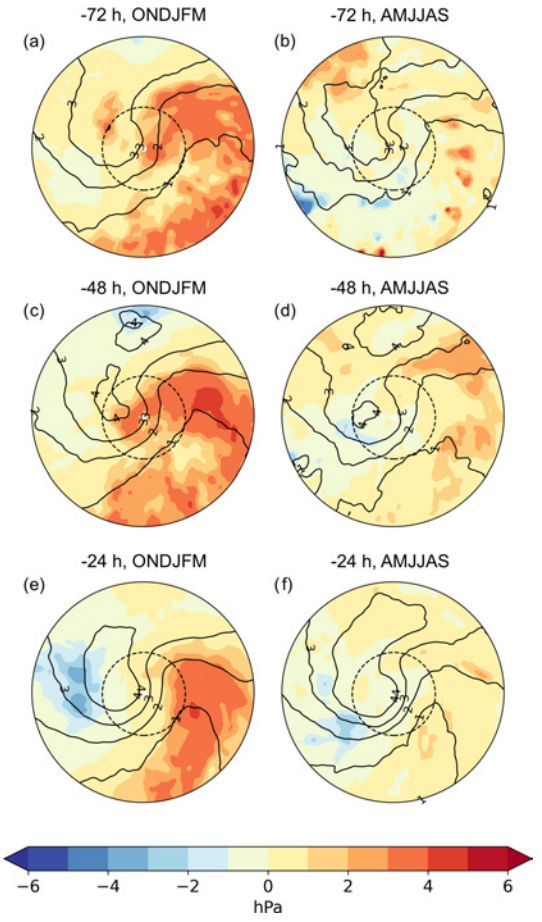

Figure 12. Sensitivity of the minimum MSLP to the 300 hPa PV (colours; hPa) and the composite mean of 300 hPa PV (contours; 1 PVU interval, 1 PVU $= 1.0 \times 10^{-6}$ m^2 s^{-1} K kg^{-1}) **(a, b)** 72 h, **(c, d)** 48 h, and **(e, f)** 24 h before the occurrence of the minimum MSLP. The radius of the plots is 18°, and the 6° radius is marked with a dashed circle.

The 300 hPa PV composites (contours in Fig. 12) show high PV values (> 2 PVU, indicating stratospheric air) that occur upstream and north of the cyclone centre, denoting an upper-level trough. This westward tilt between a surface cyclone and an upper-level trough is typical in intensifying extratropical cyclones. An upper-level ridge (low PV values) is also seen downstream of the cyclone centre, with a PV gradient between the trough and the ridge, which corresponds to a tilted tropopause and thus the location of the jet stream. In the cold season, all offset times show that there is positive sensitivity in the warm sector, meaning that higher 300 hPa PV in that region is associated with an increase in the minimum MSLP. Quantitatively, an increase of 1 standard deviation in the 300 hPa PV is associated with an increase in the minimum MSLP by up to 5 hPa. In other words, lower PV in the warm sector is associated with a deeper windstorm. Lower PV in the warm sector implies a stronger upper-level ridge or higher tropopause, and this increases the PV gradient, i.e. steepens the tropopause. This is in agreement with the 300 hPa wind speed (Fig. 11): a steeper tropopause is consistent with a stronger jet stream. In addition to being sensitive to a stronger upper-level ridge, at −24 h (Fig. 12e) the minimum MSLP is also sensitive to a stronger upper-level trough, which similarly increases the PV gradient. In the warm season, the 300 hPa PV sensitivities are rather noisy and weak. This may imply that warm-season windstorms are less controlled by the upper-level vorticity advection and more by the low-level thermal advection or diabatic heating (more discussion on this in Sect. 8). Some sensitivity is visible to a stronger upper-level ridge at −48 h offset (Fig. 12d) and a stronger upper-level trough at −24 h offset (Fig. 12f), but mostly the minimum MSLP is not sensitive to the upper-level PV in warm-season windstorms.

7.2 Sensitivity of the maximum 10 m wind gust

In the maximum 10 m wind gust sensitivities, the offset time is relative to the time when the maximum 10 m wind gust occurs when the cyclone centre is inside the northern Europe box. This means that the composite means are slightly different in this section compared to Sect. 7.1. The 850 hPa potential temperature anomaly composites (contours in Fig. 13) reveal that the frontal structure evolves within the 72 h before the maximum 10 m wind gust from a broad, large-scale temperature gradient with the beginnings of a frontal wave (Fig. 13a and b) to clearer frontal wave patterns (Fig. 13e and f). The sensitivity of the maximum 10 m wind gust has a similar dipole pattern to the sensitivity of the minimum MSLP, denoting that a stronger temperature gradient is associated with stronger gusts. This dipole pattern is visible in both seasons and all offset times. The strongest sensitivities are in the cold season and at −72 and −48 h offset times in two regions, in the warm sector and in the cold sector. An increase of 1 standard deviation in the 850 hPa potential temperature anomaly in the warm sector increases the maximum wind gust by 2.4 m s^{-1}. An increase of 1 standard deviation in the 850 hPa potential temperature in the cold sector anomaly decreases the maximum wind gust by 2.0 m s^{-1}.

The TCWV composites (Fig. 14) are consistent with the frontal structure, with the highest TCWV values found in the warm sector. TCWV sensitivities show that in the cold season more moisture south of the cyclone centre 72 h (Fig. 14a) and 48 h (Fig. 14c) before the maximum 10 m wind gust occurrence is associated with stronger gusts. As discussed above, moisture may lead to diabatically produced low-level PV that deepens the minimum MSLP of the windstorm and hence increases the pressure gradient. The stronger pressure gradient then is associated with stronger wind gusts. The high sensitivities at −72 h are found in a broader area than at −48 h, where they are more concentrated near the cold front. The strongest sensitivities at −48 h offset (Fig. 14c) indicate that an increase of 1 standard deviation in TCWV in the warm sector increases the maximum wind gust by 1.6 m s^{-1}. The TCWV sensitivities in the cold season at −24 h offset time and in the warm season at all offset times are weak, although the sensitivity patterns are similar.

The 300 hPa wind speed composites (contours in Fig. 15) show that in the cold season, the cyclone centre is located at the left exit region of the jet stream. The sensitivities in the cold season show that when the jet stream is farther north (and more downstream especially at −48 h), the wind gusts are stronger. An increase of 1 standard deviation in the 300 hPa wind speed north of the cyclone centre is associated with an increase in the maximum wind gusts by up to 1.6 m s^{-1}. This suggests that stronger wind gusts occur in cold-season windstorms possibly when the jet stream is more poleward relative to the cyclone centre. The maximum wind gust is more sensitive to the jet stream at −72 h (Fig. 15a) and −48 h (Fig. 15c) offset times than −24 h (Fig. 15e) offset time. In the warm season, the cyclone centre is located at the centre of the poleward side of the jet stream. The warm-season sensitivities have a similar pattern to the cold season, but they are weaker: an increase of 1 standard deviation in the 300 hPa wind speed in the warm season is associated with an increase in the maximum wind gusts by up to 1.2 m s^{-1}.

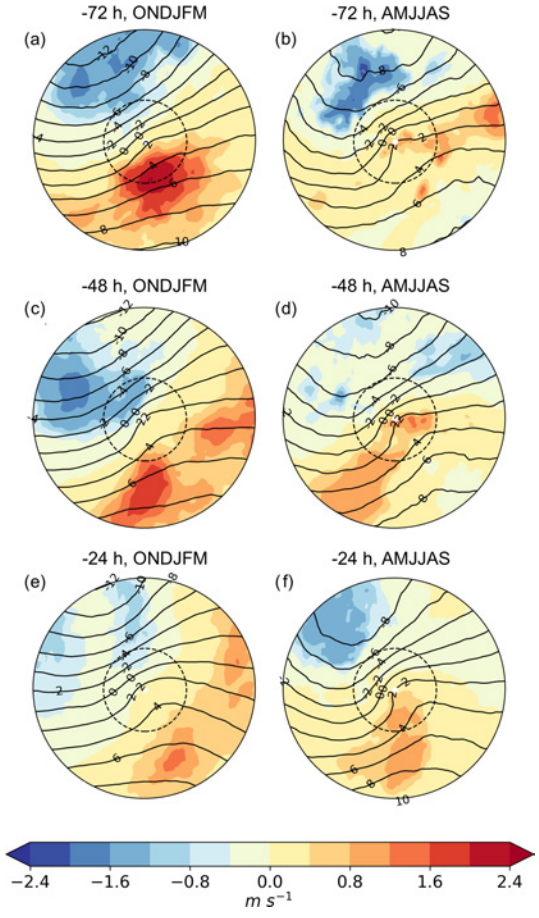

Figure 13. Sensitivity of the maximum 10 m wind gust to the 850 hPa potential temperature anomaly (colours; m s^{-1}) and the composite mean of 850 hPa potential temperature anomaly (contours; 2 °C interval) **(a, b)** 72 h, **(c, d)** 48 h, and **(e, f)** 24 h before the occurrence of the maximum 10 m wind gust in northern Europe. The radius of the plots is 18°, and the 6° radius is marked with a dashed circle.

Overall, the maximum 10 m wind gusts are weakly sensitive to the 300 hPa PV. In the cold season, −72 h (Fig. 16a) and −48 h (Fig. 16c) offset times show that a stronger upper-level ridge (i.e. lower PV values downstream of the cyclone centre) is associated with slightly stronger gusts. An increase of 1 standard deviation in the 300 hPa PV is associated with a decrease in the maximum wind gusts by 1.2 m s^{-1}. This is not visible at −24 h or at any offset times in the warm season. However, in the warm season at −48 h offset time (Fig. 16d), there is weak sensitivity north and upstream of the cyclone centre, where an increase of 1 standard devia-

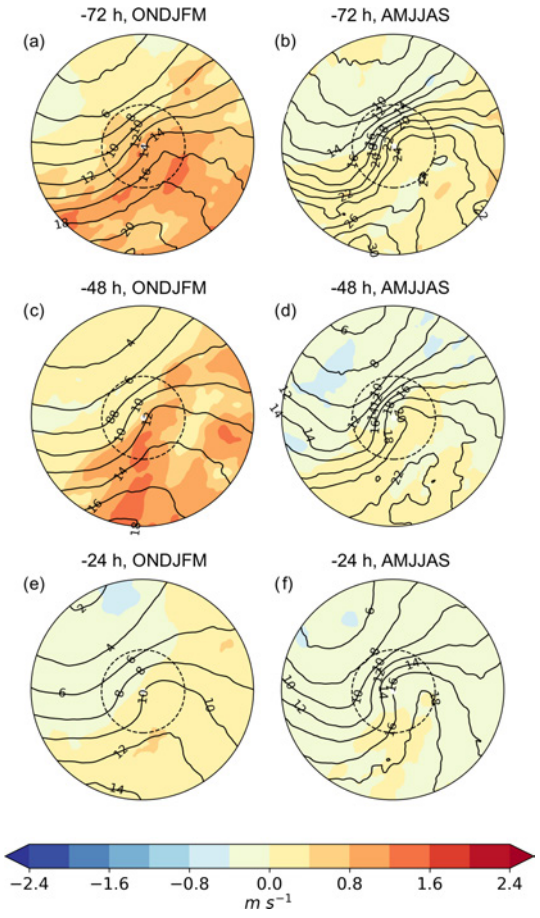

Figure 14. Sensitivity of the maximum 10 m wind gust to the TCWV (colours; $m\,s^{-1}$) and the composite mean of TCWV (contours; $2\,kg\,m^{-2}$ interval) **(a, b)** 72 h, **(c, d)** 48 h, and **(e, f)** 24 h before the occurrence of the maximum 10 m wind gust in northern Europe. The radius of the plots is 18°, and the 6° radius is marked with a dashed circle.

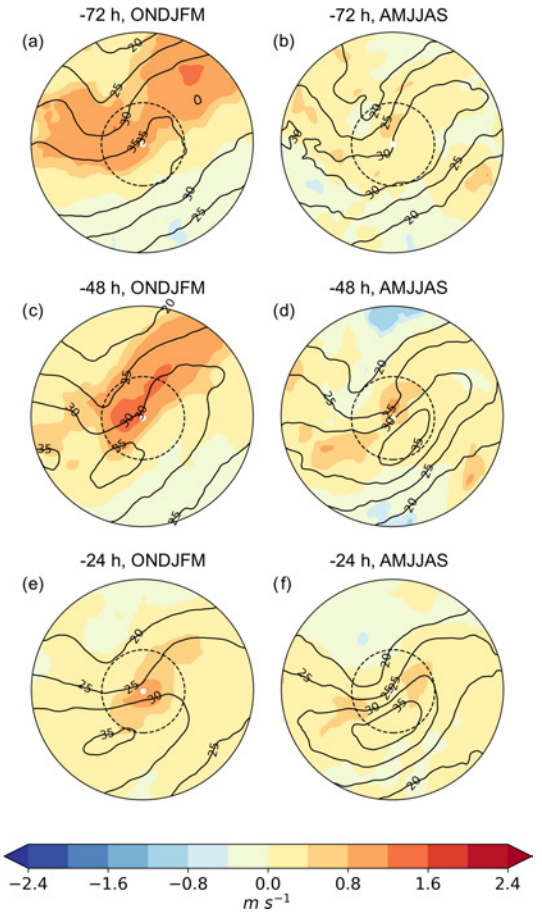

Figure 15. Sensitivity of the maximum 10 m wind gust to the 300 hPa wind speed (colours; $m\,s^{-1}$) and the composite mean of 300 hPa wind speed (contours; $5\,m\,s^{-1}$ interval) **(a, b)** 72 h, **(c, d)** 48 h, and **(e, f)** 24 h before the occurrence of the maximum 10 m wind gust in northern Europe. The radius of the plots is 18°, and the 6° radius is marked with a dashed circle.

tion in the 300 hPa PV (i.e. a stronger upper-level trough) is associated with an increase in the maximum wind gusts by $0.8\,m\,s^{-1}$.

8 Discussion and conclusions

This study investigated extratropical cyclones and windstorms in northern Europe and their characteristics, spatial and temporal evolution, and precursors. We tracked all extratropical cyclones in northern Europe during 1980–2019 and classified them into three classes: (1) all extratropical cyclones in northern Europe, (2) windstorms (i.e. extratropical cyclones which have strong wind gusts in northern Europe), and (3) non-windstorms (i.e. extratropical cyclones with no strong wind gusts in northern Europe). We investigated the cold season (October–March) and the warm season (April–September) separately to identify seasonal differences. We created cyclone composites to examine the cyclone evolution and used an ensemble sensitivity method to analyse precursors.

During the 40-year period, there is a large year-to-year variation in the annual number of extratropical cyclones, windstorms, and non-windstorms in northern Europe. The 40-year linear trends are not significant at the 95 % level; however, there is a decreasing trend in all extratropical cyclones (−3.7 cyclones per decade) that is significant at the 93 % level. Feser et al. (2015) reviewed the long-term trends of extratropical cyclone numbers over the North Atlantic and north-western Europe. They found that in their "Baltic Sea" region (covering the Baltic Sea; the Baltic states; and the major parts of Finland, Sweden, and Norway) there is no consensus on the long-term trends in reanalysis-, model- or, observation-based studies. Nonetheless, the sign and magnitude of linear trends depend strongly on the chosen time period and region, and therefore comparing different studies and results is difficult. In addition, it is important to note that

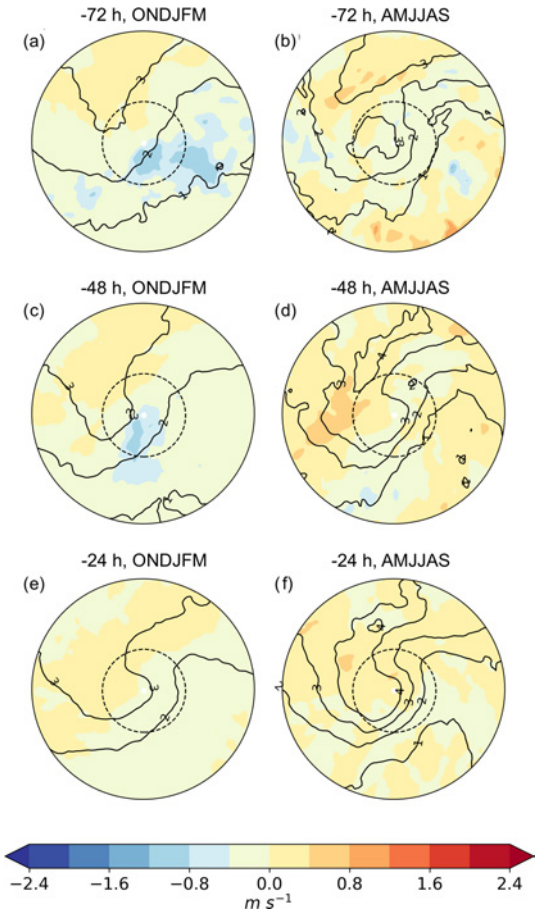

Figure 16. Sensitivity of the maximum 10 m wind gust to the 300 hPa PV (colours; $\mathrm{m\,s^{-1}}$) and the composite mean of 300 hPa PV (contours; 1 PVU interval, 1 PVU $= 1.0\times10^{-6}\,\mathrm{m^2\,s^{-1}\,K\,kg^{-1}}$) **(a, b)** 72 h, **(c, d)** 48 h, and **(e, f)** 24 h before the occurrence of the maximum 10 m wind gust in northern Europe. The radius of the plots is 18°, and the 6° radius is marked with a dashed circle.

a low number of windstorms in a specific year or decade does not mean that there could not be individual, strong windstorms. For example, our study shows that there were fewer windstorms than average between 1995–2005, while during this period a few extremely strong and damaging windstorms occurred in northern Europe: Storm Anatol in December 1999 (Ulbrich et al., 2001) and Storm Gudrun in January 2005 (Suursaar et al., 2006).

We found the well-known seasonality that windstorms are more common in winter, and extratropical cyclones in the warm season are weaker. However, a more unexpected result was that the overall number of extratropical cyclones per month in northern Europe does not differ much between months. This is contradictory to the general claim that there are less extratropical cyclones in the Northern Hemisphere during summer than winter (see for example the review by Ulbrich et al., 2009). However, this seasonal difference is most pronounced in the core of the North Atlantic storm track, while at the end of the storm track, i.e. in northern Europe, the difference is smaller (Hoskins and Hodges, 2019; Priestley et al., 2020). If considering the track densities in northern Europe, Hoskins and Hodges (2019) show mainly no difference between winter and summer, and Priestley et al. (2020) show only a small difference. Therefore, our finding does agree with other extratropical cyclone climatologies, but the other studies simply highlight more the general seasonality in the core of the storm track, although the seasonality has regional differences.

We investigated a set of cyclone characteristics to detect possible differences between windstorms and non-windstorms and between the cold and warm seasons. Windstorms tend to originate and occur over the sea areas (in the Norwegian and Barents seas), while non-windstorms originate and occur mostly over land in northern Europe. Partially, this is likely related to surface friction since we define windstorms based on their wind gusts, and winds are stronger over smooth surfaces, i.e. over sea areas. Moreover, the highest genesis densities of windstorms are co-located with the climatological left exit of the jet stream (Laurila et al., 2021), which is a favourable location for cyclone development. Our result also means that windstorms occur at higher latitudes than non-windstorms. This agrees with our composites, which showed that windstorms are located on the poleward side of the jet stream in both seasons. We additionally found that the maximum wind gusts occur approximately at the same time as the minimum MSLP regardless of the cyclone class or season.

The maximum wind gusts in windstorms move from the warm sector to behind the cold front during the cyclone evolution following the strongest pressure gradient. This shift in the maximum gust location during the cyclone evolution is in agreement with the shift in the maximum 900 hPa wind speeds of the 200 strongest extratropical cyclones in an aqua-planet study (Sinclair et al., 2020). In addition, the spatial patterns of MSLP and 850 hPa potential temperature in our composites are similar to the spatial patterns found by Catto et al. (2010) when they created composites of the 100 strongest extratropical cyclones in the Northern Hemisphere. This suggests that northern Europe windstorms have similar spatial and temporal structures to those found elsewhere in the Northern Hemisphere. Our results show that the wind gusts, pressure gradient, and temperature gradient are stronger, and the minimum MSLP is deeper in the cold season than in the warm season. The cold-season windstorms have their associated wind gusts covering a larger area and thus are spatially larger than warm-season windstorms. This is relevant when informing and preparing for likely impacts, yet it is important to note that our study only includes large-scale extratropical cyclones, whereas other weather systems (e.g. thunderstorms) can also cause strong winds and impacts.

Lastly, we investigated precursors to northern Europe windstorms for the minimum MSLP and the maximum 10 m

wind gust. The first main conclusion of our precursor results is that cold-season windstorms have higher sensitivities and thus are potentially easier to forecast than warm-season windstorms in terms of both the minimum MSLP and the maximum wind gusts. Possible reasons for this are a higher case-to-case variability and more rare occurrence of warm-season windstorms compared to cold-season windstorms. The second main conclusion is that the minimum MSLP of a windstorm has higher sensitivities than its associated maximum wind gust. This is possibly caused by the different nature of these variables: MSLP is a larger-scale field, while wind gusts are more localized and turbulent. The third and last main conclusion is that the best precursor for northern Europe windstorms is the 850 hPa potential temperature anomaly, i.e. the temperature gradient. This precursor outperformed the TCWV (moisture), the 300 hPa wind speed (jet stream), and the 300 hPa PV (upper-level trough and tropopause steepness). This means that the 850 hPa temperature gradient has the strongest impact on the resulting minimum MSLP and the maximum wind gusts, and thus the temperature gradient is an important variable to follow when forecasting windstorms in northern Europe. If we apply our sensitivity results to climate change, the low-level temperature gradient is expected to decrease (IPCC, 2013), which based on our results would indicate weaker windstorms in terms of the minimum MSLP and the maximum wind gusts. However, this is counteracted by the atmospheric moisture, which is predicted to increase (IPCC, 2013) and hence would, based on our results from the TCWV sensitivities, indicate stronger windstorms.

The 300 hPa PV shows sensitivities to the downstream ridge, which is not found in Dacre and Gray (2013), who used the ensemble sensitivity analysis to investigate precursors to extratropical cyclones in the west and east North Atlantic. This difference between our and their results may be because of the difference in the geographical location: blocking is more common over northern Europe and Russia than over the North Atlantic (Pelly and Hoskins, 2003; Rimbu and Lohmann, 2011). The 300 hPa PV also gives weak or nonexistent sensitivities in the warm season. Petterssen and Smebye (1971) and Deveson et al. (2002) developed a cyclone development classification based on the upper- and lower-level forcing mechanisms, and they identified three types of cyclones. Type A cyclones develop due to lower-level thermal advection in baroclinic regions without a pre-existing upper-level trough; type B cyclones develop due to upper-level vorticity advection, where a pre-existing upper-level trough moves over an area of warm advection; and type C cyclones are characterized by strong latent heat release with initiation of strong upper-level forcing and weak low-level baroclinicity (Petterssen and Smebye, 1971; Deveson et al., 2002; Plant et al., 2003). Therefore, our result may indicate that warm-season windstorms in northern Europe are type A or type C cyclones since they are not dominated by upper-level forcing. Our finding that the TCWV gives weak sensitivities in the warm season was surprising since typically there is more diabatic heating in the warm season than in the cold season. However, this may be a result of a low number of windstorms and a high case-to-case variability in the warm season. Our results also showed that the sensitivities are generally higher at -48 h than at -24 h. One possible explanation could be that 24 h is too short of a time for the atmospheric available potential energy to be converted to kinetic energy, an energy conversion known as the Lorenz energy cycle (Lorenz, 1955).

Our study has certain limitations. There are multiple ways to classify extratropical cyclones and to define windstorms (Catto, 2016), and therefore, our results may depend on our windstorm definition. Due to different extratropical cyclone and windstorm definitions, direct comparison of our climatology to previous studies is not simple. We also made a subjective choice about what geographic area to study, and our results are likely to be sensitive to our choice of the box over northern Europe. The area we considered included sea areas, and most windstorms we identified occurred over sea, making our results less applicable to windstorms over land areas. Furthermore, our analysis was based solely on ERA5 reanalysis, which may not accurately capture wind gusts due to the coarse resolution of the reanalysis (~ 31 km) and also because wind gusts are parameterized, not directly resolved. Another limitation is that composites (and climatological studies overall) smooth the case-to-case variability, and therefore there is still need for case studies to investigate different evolution paths in more detail. For example, Storm Aila occurred in Finland in September 2020 and developed in the right entrance of the jet stream (Rantanen et al., 2021), which is contradictory to our result that northern Europe windstorms occur poleward of the jet stream. On the other hand, Storm Aila formed in an area of a strong temperature gradient (Rantanen et al., 2021), which agrees with our results.

Despite the limitations noted above, our composite and sensitivity results highlight the common features of windstorms in northern Europe. This enhances our dynamical understanding of these potentially damaging weather systems and furthermore provides valuable guidance in the form of data-based "conceptual models" to weather forecasters in the region.

Appendix A

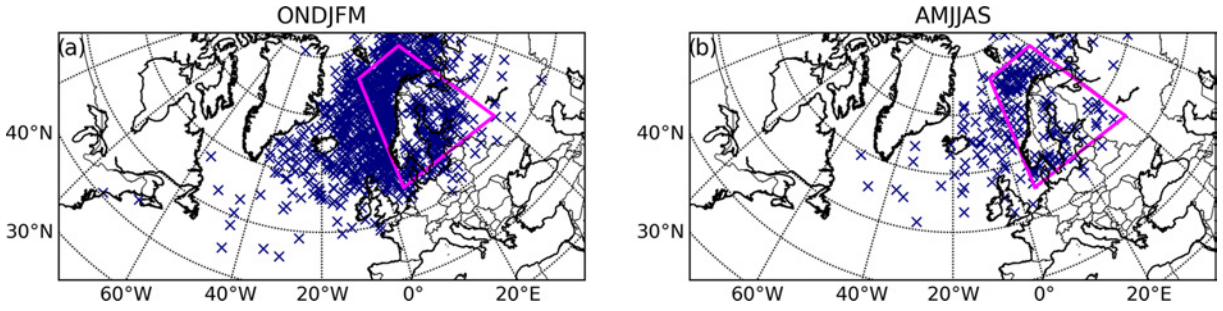

Figure A1. The locations of the minimum MSLP of windstorm tracks. The time of the minimum MSLP is the time when the absolute minimum of MSLP occurs along the cyclone track.

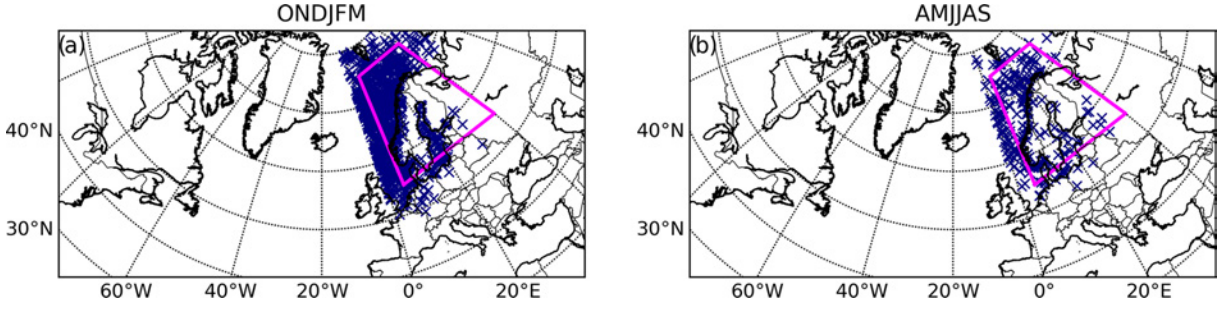

Figure A2. The locations of the maximum 10 m wind gust of windstorm tracks. The time of the maximum 10 m wind gust is the time when the maximum wind gust occurs while the cyclone centre is within the northern Europe box.

Code availability. Information on how to obtain the cyclone identification and tracking algorithm (TRACK) can be found from http://www.nerc-essc.ac.uk/~kih/TRACK/Track.html (last access: 18 November 2021, TRACK, 2021).

Data availability. ERA5 reanalysis is available from the Copernicus Climate Change Service Climate Data Store (https://cds.climate.copernicus.eu/#!/search?text=ERA5&type=dataset, last access: 18 November 2021) (DOIs: https://doi.org/10.24381/cds.adbb2d47, https://doi.org/10.24381/cds.bd0915c6; Hersbach et al., 2018a, b).

Author contributions. TKL performed most of the data analysis, interpreted the results, drew the main conclusions, and wrote the majority of the paper. JC contributed to the data analysis of the wind speed distributions and the cyclone characteristics presented in Sects. 4, 5, and 6. VAS performed the cyclone tracking. VAS and HG conceived the study, provided guidance on the interpretation of the results, and led the overall scientific investigation. All authors provided comments on drafts of the manuscript.

Competing interests. The contact author has declared that neither they nor their co-authors have any competing interests.

Disclaimer. Publisher's note: Copernicus Publications remains neutral with regard to jurisdictional claims in published maps and institutional affiliations.

Acknowledgements. We thank Kevin Hodges for providing the cyclone tracking code TRACK and Helen Dacre for providing an initial version of the cyclone composite code. The authors wish to acknowledge CSC – IT Center for Science, Finland, for computational resources and ECMWF for providing the ERA5 reanalysis, which is available from the Copernicus Climate Change Service Climate Data Store. This work was supported by the MONITUHO project, the ERA4CS WINDSURFER project, and Academy of Finland Flagship funding (grant nos. 337549 and 337552).

Financial support. This research has been supported by the Academy of Finland (grant nos. 337549 and 337552); the Maa- ja metsätalousministeriö (grant no. 647/03.02.06.00/2018); and the European Commission, Horizon 2020 Framework Programme (ERA4CS (grant no. 690462)).

Review statement. This paper was edited by Silvio Davolio and reviewed by two anonymous referees.

References

Ancell, B. and Hakim, G. J.: Comparing adjoint-and ensemble-sensitivity analysis with applications to observation targeting, Mon. Weather Rev., 135, 4117–4134, 2007.

Bjerknes, J.: On the structure of moving cyclones, Geofys. Publ., 1, 1–8, 1919.

Bjerknes, J. and Solberg, H.: Life cycle of cyclones and the polar front theory of atmospheric circulation, Geofys. Publ., 3, 3–18, 1922.

Blackmon, M. L.: A Climatological Spectral Study of the 500 mb Geopotential Height of the Northern Hemisphere, J. Atmos. Sci., 33, 1607–1623, https://doi.org/10.1175/1520-0469(1976)033<1607:ACSSOT>2.0.CO;2, 1976.

Catto, J. L.: Extratropical cyclone classification and its use in climate studies, Rev. Geophys., 54, 486–520, https://doi.org/10.1002/2016RG000519, 2016.

Catto, J. L., Shaffrey, L. C., and Hodges, K. I.: Can climate models capture the structure of extratropical cyclones?, J. Climate, 23, 1621–1635, 2010.

Charney, J. G.: The dynamics of long waves in a baroclinic westerly current, J. Atmos. Sci., 4, 136–162, https://doi.org/10.1175/1520-0469(1947)004<0136:TDOLWI>2.0.CO;2, 1947.

Dacre, H. F. and Gray, S. L.: Quantifying the climatological relationship between extratropical cyclone intensity and atmospheric precursors, Geophys. Res. Lett., 40, 2322–2327, https://doi.org/10.1002/grl.50105, 2013.

Dacre, H., Hawcroft, M., Stringer, M., and Hodges, K.: An extratropical cyclone atlas: A tool for illustrating cyclone structure and evolution characteristics, B. Am. Meteorol. Soc., 93, 1497–1502, 2012.

Dacre, H. F., Martinez-Alvarado, O., and Mbengue, C. O.: Linking atmospheric rivers and warm conveyor belt airflows, J. Hydrometeorol., 20, 1183–1196, 2019.

Deveson, A. C. L., Browning, K. A., and Hewson, T. D.: A classification of FASTEX cyclones using a height-attributable quasi-geostrophic vertical-motion diagnostic, Q. J. Roy. Meteor. Soc., 128, 93–117, https://doi.org/10.1256/00359000260498806, 2002.

Faranda, D., Messori, G., and Yiou, P.: Dynamical proxies of North Atlantic predictability and extremes, Scientific Reports, 7, 1–10, 2017.

Feser, F., Barcikowska, M., Krueger, O., Schenk, F., Weisse, R., and Xia, L.: Storminess over the North Atlantic and northwestern Europe–A review, Q. J. Roy. Meteor. Soc., 141, 350–382, https://doi.org/10.1002/qj.2364, 2015.

Field, P. R. and Wood, R.: Precipitation and cloud structure in midlatitude cyclones, J. Climate, 20, 233–254, 2007.

Garcies, L. and Homar, V.: Ensemble sensitivities of the real atmosphere: application to Mediterranean intense cyclones, Tellus A, 61, 394–406, https://doi.org/10.1111/j.1600-0870.2009.00392.x, 2009.

Gardiner, B., Schuck, A., Schelhaas, M.-J., Orazio, C., Blennow, K., and Bruce, N. (eds.): Living with storm damage to forests, What Science Can Tell Us 3, European Forest Institute, 2013.

Grönås, S.: Mesoscale phenomena induced by mountains over Scandinavia and Spitsbergen, in: Workshop on Orography, 10–12 November 1997, 165–181 pp., ECMWF, available at: https://www.ecmwf.int/node/9656, last access: 18 November 2021, Shinfield Park, Reading, 1997.

Hersbach, H., Bell, B., Berrisford, P., Biavati, G., Horányi, A., Muñoz Sabater, J., Nicolas, J., Peubey, C., Radu, R., Rozum, I., Schepers, D., Simmons, A., Soci, C., Dee, D., and Thépaut, J.-N.: ERA5 hourly data on single levels from 1979 to present, Copernicus Climate Change Service (C3S) Climate Data Store (CDS) [data set], https://doi.org/10.24381/cds.adbb2d47, 2018a.

Hersbach, H., Bell, B., Berrisford, P., Biavati, G., Horányi, A., Muñoz Sabater, J., Nicolas, J., Peubey, C., Radu, R., Rozum, I., Schepers, D., Simmons, A., Soci, C., Dee, D., and Thépaut, J.-N.: ERA5 hourly data on pressure levels from 1979 to present, Copernicus Climate Change Service (C3S) Climate Data Store (CDS) [data set], https://doi.org/10.24381/cds.bd0915c6, 2018b.

Hersbach, H., Bell, B., Berrisford, P., Hirahara, S., Horányi, A., Muñoz-Sabater, J., Nicolas, J., Peubey, C., Radu, R., Schepers, D., Simmons, A., Soci, C., Abdalla, S., Abellan, X., Balsamo, G., Bechtold, P., Biavati, G., Bidlot, J., Bonavita, M., De Chiara, G., Dahlgren, P., Dee, D., Diamantakis, M., Dragani, R., Flemming, J., Forbes, R., Fuentes, M., Geer, A., Haimberger, L., Healy, S., Hogan, R. J., Hólm, E., Janisková, M., Keeley, S., Laloyaux, P., Lopez, P., Lupu, C., Radnoti, G., de Rosnay, P., Rozum, I., Vamborg, F., Villaume, S., and Thépaut, J.-N.: The ERA5 Global Reanalysis, Q. J. Roy. Meteor. Soc., 146, 1999–2049, https://doi.org/10.1002/qj.3803, 2020.

Hodges, K. I.: A General Method for Tracking Analysis and Its Application to Meteorological Data, Mon. Weather Rev., 122, 2573–2586, https://doi.org/10.1175/1520-0493(1994)122<2573:AGMFTA>2.0.CO;2, 1994.

Hodges, K. I.: Feature Tracking on the Unit Sphere, Mon. Weather Rev., 123, 3458–3465, https://doi.org/10.1175/1520-0493(1995)123<3458:FTOTUS>2.0.CO;2, 1995.

Hodges, K.: Spherical nonparametric estimators applied to the UGAMP model integration for AMIP, Mon. Weather Rev., 124, 2914–2932, 1996.

Hodges, K. I.: Adaptive Constraints for Feature Tracking, Mon. Weather Rev., 127, 1362–1373, https://doi.org/10.1175/1520-0493(1999)127<1362:ACFFT>2.0.CO;2, 1999.

Hodges, K. I., Lee, R. W., and Bengtsson, L.: A comparison of extratropical cyclones in recent reanalyses ERA-Interim, NASA MERRA, NCEP CFSR, and JRA-25, J. Climate, 24, 4888–4906, 2011.

Holley, D. M.: The impacts of Storm Odette in eastern England, 24–26 September 2020, Weather, 76, 86–88, https://doi.org/10.1002/wea.3920, 2021.

Hoskins, B. J. and Hodges, K. I.: New Perspectives on the Northern Hemisphere Winter Storm Tracks, J. At-

mos. Sci., 59, 1041–1061, https://doi.org/10.1175/1520-0469(2002)059<1041:NPOTNH>2.0.CO;2, 2002.

Hoskins, B. J. and Hodges, K. I.: The Annual Cycle of Northern Hemisphere Storm Tracks. Part I: Seasons, J. Climate, 32, 1743–1760, https://doi.org/10.1175/JCLI-D-17-0870.1, 2019.

IPCC: Climate Change 2013: The Physical Science Basis. Contribution of Working Group I to the Fifth Assessment Report of the Intergovernmental Panel on Climate Change, Cambridge University Press, Cambridge, United Kingdom and New York, NY, USA, https://doi.org/10.1017/CBO9781107415324, 2013.

Kendall, M. G.: Rank Correlation Methods, Griffin, London, ISBN 978-0-8526-4199-6, 1970.

Krueger, O. and Von Storch, H.: Evaluation of an air pressure–based proxy for storm activity, J. Climate, 24, 2612–2619, 2011.

Kufeoglu, S. and Lehtonen, M.: Cyclone Dagmar of 2011 and its impacts in Finland, in: IEEE PES Innovative Smart Grid Technologies, Europe, 1–6 pp., https://doi.org/10.1109/ISGTEurope.2014.7028868, 2014.

Laurila, T. K., Sinclair, V. A., and Gregow, H.: Climatology, variability, and trends in near-surface wind speeds over the North Atlantic and Europe during 1979–2018 based on ERA5, Int. J. Climatol., 41, 2253–2278, https://doi.org/10.1002/joc.6957, 2021.

Lorenz, E. N.: Available potential energy and the maintenance of the general circulation, Tellus, 7, 157–167, 1955.

Mann, H. B.: Nonparametric tests against trend, Econometrica, 13, 245–259, https://doi.org/10.2307/1907187, 1945.

Pelly, J. L. and Hoskins, B. J.: A new perspective on blocking, J. Atmos. Sci., 60, 743–755, 2003.

Petterssen, S. and Smebye, S.: On the development of extratropical cyclones, Q. J. Roy. Meteor. Soc., 97, 457–482, 1971.

Pinto, J. G., Spangehl, T., Ulbrich, U., and Speth, P.: Sensitivities of a cyclone detection and tracking algorithm: individual tracks and climatology, Meteorol. Z., 14, 823–838, 2005.

Plant, R. S., Craig, G. C., and Gray, S. L.: On a threefold classification of extratropical cyclogenesis, Q. J. Roy. Meteor. Soc., 129, 2989–3012, https://doi.org/10.1256/qj.02.174, 2003.

Priestley, M. D. K., Ackerley, D., Catto, J. L., Hodges, K. I., McDonald, R. E., and Lee, R. W.: An Overview of the Extratropical Storm Tracks in CMIP6 Historical Simulations, J. Climate, 33, 6315–6343, https://doi.org/10.1175/JCLI-D-19-0928.1, 2020.

Rantanen, M., Räisänen, J., Sinclair, V. A., and Järvinen, H.: Sensitivity of idealised baroclinic waves to mean atmospheric temperature and meridional temperature gradient changes, Clim. Dyn., 52, 2703–2719, 2019.

Rantanen, M., Laurila, T. K., Sinclair, V. A., and Gregow, H.: Storm Aila: An unusually strong autumn storm in Finland, Weather, 76, 306–312, https://doi.org/10.1002/wea.3943, 2021.

Rimbu, N. and Lohmann, G.: Winter and summer blocking variability in the North Atlantic region – evidence from long-term observational and proxy data from southwestern Greenland, Clim. Past, 7, 543–555, https://doi.org/10.5194/cp-7-543-2011, 2011.

Rudeva, I. and Gulev, S. K.: Composite analysis of North Atlantic extratropical cyclones in NCEP–NCAR reanalysis data, Mon. Weather Rev., 139, 1419–1446, 2011.

Schultz, D. M., Keyser, D., and Bosart, L. F.: The effect of large-scale flow on low-level frontal structure and evolution in midlatitude cyclones, Mon. Weather Rev., 126, 1767–1791, 1998.

Shapiro, M. A. and Keyser, D.: Fronts, jet streams and the tropopause, in: Extratropical Cyclones: The Erik Palmén Memorial Volume, edited by: Newton, C. and Holopainen, E. O., American Meteorological Society, Boston, MA, 167–191, Online ISBN 978-1-944970-33-8, 1990.

Sinclair, V. A., Rantanen, M., Haapanala, P., Räisänen, J., and Järvinen, H.: The characteristics and structure of extra-tropical cyclones in a warmer climate, Weather Clim. Dynam., 1, 1–25, https://doi.org/10.5194/wcd-1-1-2020, 2020.

Suursaar, U., Kullas, T., Otsmann, M., Saaremae, I., Kuik, J., and Merilain, M.: Cyclone Gudrun in January 2005 and modelling its hydrodynamic consequences in the Estonian coastal waters, Boreal Environ. Res., 11, 143–159, 2006.

Tervo, R., Láng, I., Jung, A., and Mäkelä, A.: Predicting power outages caused by extratropical storms, Nat. Hazards Earth Syst. Sci., 21, 607–627, https://doi.org/10.5194/nhess-21-607-2021, 2021.

Tierney, G., Posselt, D. J., and Booth, J. F.: An examination of extratropical cyclone response to changes in baroclinicity and temperature in an idealized environment, Clim. Dynam., 51, 3829–3846, 2018.

TRACK: Homepage, available at: http://www.nerc-essc.ac.uk/~kih/TRACK/Track.html, last access: 18 November 2021.

Ulbrich, U., Fink, A., Klawa, M., and Pinto, J. G.: Three extreme storms over Europe in December 1999, Weather, 56, 70–80, 2001.

Ulbrich, U., Leckebusch, G., and Pinto, J. G.: Extra-tropical cyclones in the present and future climate: a review, Theor. Appl. Climatol., 96, 117–131, 2009.

Wang, C.-C. and Rogers, J. C.: A composite study of explosive cyclogenesis in different sectors of the North Atlantic. Part I: Cyclone structure and evolution, Mon. Weather Rev., 129, 1481–1499, 2001.

Reprinted, with permission, from
Monthly Weather Review, 148(1), 377–401,
doi:10.1175/MWR-D-19-0035.1

III

The Extratropical Transition of Hurricane Debby (1982) and the Subsequent Development of an Intense Windstorm over Finland

TERHI K. LAURILA

Finnish Meteorological Institute, Helsinki, Finland

VICTORIA A. SINCLAIR

Institute for Atmospheric and Earth System Research/Physics, Faculty of Science, University of Helsinki, Helsinki, Finland

HILPPA GREGOW

Finnish Meteorological Institute, Helsinki, Finland

(Manuscript received 7 February 2019, in final form 6 September 2019)

ABSTRACT

On 22 September 1982, an intense windstorm caused considerable damage in northern Finland. Local forecasters noted that this windstorm potentially was related to Hurricane Debby, a category 4 hurricane that occurred just 5 days earlier. Due to the unique nature of the event and lack of prior research, our aim is to document the synoptic sequence of events related to this storm using ERA-Interim reanalysis data, best track data, and output from OpenIFS simulations. During extratropical transition, the outflow from Debby resulted in a ridge building and an acceleration of the jet. Debby did not reintensify immediately in the midlatitudes despite the presence of an upper-level trough. Instead, ex-Debby propagated rapidly across the Atlantic as a diabatic Rossby wave–like feature. Simultaneously, an upper-level trough approached from the northeast and once ex-Debby moved ahead of this feature near the United Kingdom, rapid reintensification began. All OpenIFS forecasts diverged from reanalysis after only 2 days indicating intrinsic low predictability and strong sensitivities. Phasing between Hurricane Debby and the weak trough, and phasing of the upper- and lower-level potential vorticity anomalies near the United Kingdom was important in the evolution of ex-Debby. In the only OpenIFS simulation to correctly capture the phasing over the United Kingdom, stronger wind gusts were simulated over northern Finland than in any other simulation. Turbulent mixing behind the cold front, and convectively driven downdrafts in the warm sector, enhanced the wind gusts over Finland. To further improve understanding of this case, we suggest conducting research using an ensemble approach.

1. Introduction

On 22 September 1982, an intense windstorm affected northern Finland causing two fatalities and significant damage to forests destroying three million cubic meters of timber. The storm, which was given the name Mauri, is one of the most intense windstorms Finland has experienced. Windstorms in northern Europe and Finland are primarily caused by extratropical cyclones that have their genesis regions in the midlatitudes and develop due to baroclinic instability (Hoskins and Hodges 2002; Zappa et al. 2013). However, it was argued back in 1982 that Mauri was caused by the remnants of a category 4 hurricane, Debby, which had undergone extratropical transition (ET).

In the North Atlantic, almost half of hurricanes undergo ET; a process where a tropical cyclone transforms into an extratropical cyclone due to entering the midlatitude environment (Hart and Evans 2001; Jones et al. 2003; Evans et al. 2017). Tropical cyclones that undergo ET can occasionally lead to severe weather along the east coast of the United States and Canada (e.g., Palmén 1958; Ma et al. 2003; Galarneau et al. 2013) but there

Denotes content that is immediately available upon publication as open access.

Supplemental information related to this paper is available at the Journals Online website: https://doi.org/10.1175/MWR-D-19-0035.s1.

Corresponding author: Terhi K. Laurila, terhi.laurila@fmi.fi

DOI: 10.1175/MWR-D-19-0035.1

are also cases that have caused damage in Europe. For example, Hurricane Iris in 1995 became extratropical and its remnants reached northwest Europe (Thorncroft and Jones 2000) whereas Hurricane Lili underwent ET in October 1996 and then passed over the United Kingdom leading to heavy rain and strong wind gusts (Browning et al. 1998; Agustí-Panareda et al. 2005). More recently, in 2017, Hurricane Ophelia transitioned into an extratropical system and its hurricane-force winds caused significant damage in Ireland and the United Kingdom and three fatalities (Stewart 2018). However, it is rare that transitioned cyclones result in high-impact events in Fenno-Scandinavia. Thus, if storm Mauri did originate from Hurricane Debby it would be a unique storm. Despite this, and that Mauri is a well-known event in Finland, no in-depth dynamic study has yet been performed about Mauri.

During the ET process, the structural characteristics of the cyclone change. The cyclone transforms from being a symmetric, warm core cyclone to an asymmetric, cold core cyclone, and the spatial extent of the cloud and precipitation increases and fronts become evident (e.g., Klein et al. 2000; Hart and Evans 2001). The vertical structure of the potential vorticity (PV) field associated with the cyclone also undergoes notable changes during ET. In general, when the cyclone is tropical, a positive PV anomaly associated with latent heating is evident in the center of the cyclone (as a vertical ''PV tower'') (e.g., Hoskins et al. 1985; Jones et al. 2003). After ET, the PV structure of the cyclone is typically characterized by an upper-level positive PV anomaly that is tilted westward with height (e.g., Hoskins et al. 1985; Jones et al. 2003). A transitioned cyclone can then directly interact with an upper-level trough and reintensify (Evans et al. 2017). The upper-level PV anomaly of a preexisting trough might lead to a strong reintensification of the transitioned cyclone, however the phasing between these two systems is critical in determining whether or not reintensification will occur (Ritchie and Elsberry 2007). Scheck et al. (2011) developed the concept of bifurcation points to highlight that a track bifurcation can occur when a small change in one aspect of the flow (e.g., the midlatitude trough) can result in significant changes to the subsequent circulation. In an idealized modeling study, Riemer and Jones (2014) identified a bifurcation (stagnation) point at the base of the midlatitude upstream trough that governs the bifurcation of cyclone tracks into a regime where ET occurs and another when no ET occurs.

A tropical cyclone can also affect midlatitudes by directly modulating the downstream flow [see section 2a of Keller et al. (2019) for an overview]. This typically manifests as ridge building poleward and downstream of the transitioning tropical cyclone, downstream trough amplification, and jet streak modifications. These features have all been identified in idealized experiments (Riemer et al. 2008) and in a climatological study by Archambault et al. (2013) where time-lagged composites of the midlatitude flow were created. A case study of Hurricane Irene by Agustí-Panareda et al. (2004) highlighted that diabatically produced low-PV air at upper levels can be advected by the divergent outflow of a tropical cyclone leading to both ridge amplification and, by the subsequent steepening of the tropopause, an acceleration of the upper-level jet downstream. Similar results were also obtained more recently by Grams et al. (2013) for Typhoon Jangmi in which diabatic PV reduction at upper levels and the advection of low-PV air toward a jet streak by the tropical cyclone outflow resulted in weak ridge building. Furthermore, the impact of the transition of an extratropical cyclone on the midlatitude flow can also be transmitted farther downstream by modifying Rossby wave packets and leading to the development of new cyclones and anticyclones downstream (Riemer et al. 2008; Archambault et al. 2013). As an example, Supertyphoon Nuri (2014) amplified the downstream ridge–trough couplet that then resulted in a new cyclone developing farther downstream, amplifying the upper-level wave pattern even more and resulting in a heat wave and a cold air outbreak far downstream from the transitioned ex-Nuri (Keller et al. 2019).

In addition to direct interaction and downstream development, a less common way for a transitioned cyclone to regenerate and travel in the midlatitudes is as a diabatic Rossby wave (DRW). A DRW is a positive low-level PV anomaly embedded in a baroclinic and moist environment. Downstream of the vortex center, where poleward winds are present, isentropic ascent is induced, which leads to condensation and diabatic heating (e.g., Parker and Thorpe 1995; Moore and Montgomery 2004, 2005). Beneath the localized diabatic heating, there is a positive PV tendency, which generates positive PV downstream of the original position of the DRW. Thus, the DRW can maintain itself by this constant diabatic PV generation (Moore and Montgomery 2004). If a rapidly propagating DRW interacts with an upper-level trough it can result in an explosive intensification of the cyclone (Boettcher and Wernli 2013). Boettcher and Wernli (2013) developed an algorithm to objectively identify DRWs which states that a DRW must have the following characteristics: a closed sea level pressure contour, a positive low-level PV anomaly, substantial low-level baroclinicity, fast propagation, sufficient

moisture, and very weak upper-level forcing. An example case in which a DRW played an essential role was storm Lothar in 1999 where a positive low-level PV anomaly moved rapidly across the North Atlantic and intensified to become a damaging windstorm over Europe (Wernli et al. 2002).

In meteorological case studies, the evaluation of the synoptic-scale weather patterns is generally analyzed by using reanalysis datasets (e.g., Schenkel and Hart 2012; Hewson and Neu 2015). However, the relatively coarse resolution of most reanalysis datasets can result in small-scale cyclones, such as mesocyclones or polar lows, being completely absent or resolved but with intensities that are much weaker than observed (e.g., Uotila et al. 2009; Laffineur et al. 2014; Pezza et al. 2016). In addition, too low spatial resolution decreases the maximum wind speed and intensity of windstorms whereas too low temporal resolution may shift the location of the windstorm maximum impacts (Gregow 2013; Jokinen et al. 2014). Thus, in this study a reanalysis dataset is used only for examining the general synoptic-scale evolution whereas higher-resolution numerical simulations are employed to investigate the mesoscale features of storm Mauri.

The aims of this study are to 1) conduct a detailed analysis of the synoptic and dynamic evolution of Debby and Mauri, and 2) identify the reasons for the damaging winds over Finland on 22 September 1982. The data, model, and additional datasets used in this study are presented in section 2 and the analysis methods applied are described in section 3. Section 4 introduces the case with a brief synoptic overview based on ERA-Interim reanalysis and more in-depth analysis based on OpenIFS model simulations is presented in section 5. The conclusions are given in section 6.

2. Data, model simulations, and additional datasets

a. ERA-Interim reanalysis data

To give a general overview of this historic weather event, we use ERA-Interim reanalysis data from the European Centre for Medium-Range Weather Forecasts (ECMWF). ERA-Interim covers the years from 1979 onward, has a spatial resolution of approximately 80 km (T255 in spectral space) and there are 60 non-uniformly spaced levels with the model top at 0.1 hPa (Dee et al. 2011). The temporal resolution of the analysis fields is six hours. ERA-Interim uses a four-dimensional variational (4D-Var) data assimilation system. The limited spatial and temporal resolution of the analysis (6 h) and forecast (3 h) fields from ERA-Interim means that ERA-Interim alone cannot be used to fully understand the dynamic evolution of this weather event. Hence, numerical simulations of this case study are also performed with the OpenIFS model.

b. OpenIFS

ECMWF maintains and develops the Integrated Forecast System (IFS), which includes a data assimilation system, forecast systems for the atmosphere and ocean, as well as a wave and sea ice model. The IFS is a global, hydrostatic spectral model that uses semi-implicit semi-Lagrangian time stepping that enables long time steps while remaining numerically stable (Staniforth and Côté 1991; Ritchie et al. 1995; Temperton et al. 2001; Hortal 2002). Parameterizations for radiation, microphysics, turbulence, convection, gravity wave drag, and surface fluxes are included. The full IFS documentation is available online (ECMWF 2019). The IFS is used operationally to produce weather forecasts as well as extended-range and seasonal predictions. In addition, the IFS is also the forecast system used to produce the ERA-Interim reanalysis (Dee et al. 2011).

OpenIFS is a version of the IFS that is available to academic and research institutions free of charge but under license for use in research and teaching (Szépszó and Carver 2018; Szépszó et al. 2019). OpenIFS has exactly the same dynamics and physical parameterizations as the atmospheric model of the full version of the IFS and also includes the same wave model. However, OpenIFS does not contain the data assimilation system, sea ice model nor ocean model. OpenIFS version Cy40r1v1 is used in this study to perform numerical simulations of Hurricane Debby and its evolution into extratropical storm Mauri. The equivalent version of the IFS was operational between November 2013 and May 2015. All simulations included here are global simulations initialized from ERA-Interim reanalysis data and are run with a horizontal spatial resolution of approximately 16 km (T1279 in spectral space) and with 137 vertical levels. Coarser-resolution simulations, when compared to ERA-Interim reanalysis data, were found to not correctly capture the complete evolution of Hurricane Debby/extratropical storm Mauri (not shown). The simulations were run with a 10-min time step and model fields were output every hour.

c. 10-m wind speed and gust parameterization

The OpenIFS simulations are used to assess the physical mechanisms that resulted in the strong winds over northern Finland. Therefore, a brief overview of how the full IFS and thus OpenIFS parameterizes the 10-m wind speed and the 10-m wind gust is given here.

A full description is available in the IFS documentation (ECMWF 2015).

The method used to compute the 10-m wind in the operational IFS and thus OpenIFS is designed so that the resulting wind speeds are as comparable as possible to 10-m wind speeds measured at SYNOP stations. Official SYNOP stations are located in open terrain and are well exposed to the wind. Therefore, standard SYNOP observations of 10-m wind are not necessarily representative of a larger area, for example, the area of a grid box in a model. A model grid box is likely to be inhomogeneous and include rougher elements, for example forest, which results in a higher aerodynamics roughness value than for open homogeneous terrain. To account for this, an exposure correction is applied online during the model run (i.e., it is part of the OpenIFS model code) to grid boxes where the roughness length exceeds 0.03 m. This uses wind values at a level (40 m above ground level) that are not strongly affected by the surface and interpolates these to 10 m using an aerodynamic roughness length, which is representative of open terrain with grassland and thus comparable to the terrain at SYNOP stations. Therefore, it should be noted that 10-m wind speeds output from OpenIFS may be higher than reality at some locations but that overall they should compare well with observations.

Wind gusts are also computed by the OpenIFS code and the method employed is designed to ensure the model output is directly comparable to how wind gusts are observed following the World Meteorological Organization's recommendations. In OpenIFS, the wind gust (F_{gust}) is calculated as:

$$F_{\text{gust}} = F_{10} + C_{\text{ugn}} u_* + C_{\text{conv}} \max(0, U_{850} - U_{950}) \quad (1)$$

where F_{10} is the 10-m wind speed calculated as described above, C_{ugn} is an empirically derived parameter and has a value of 7.71, u_* is the friction velocity, C_{conv} is the convective mixing parameter and has a value of 0.6, and U_{850} and U_{950} are the wind speeds at 850 and 950 hPa, respectively (ECMWF 2015). The second term on the right-hand side represents turbulent driven wind gusts and thus includes the effects of surface friction (through surface roughness) and boundary layer stability. The third term represents wind gusts generated by the downward transport of higher momentum air that can occur in convective situations (Bechtold and Bidlot 2009), which may be organized downdrafts in a sheared environment or evaporatively driven downdrafts. This convective term only becomes active during time steps and at grid points where the horizontal wind speed increases with height and where the convection scheme is active. In practice, this term contributes to forecast wind gusts in frontal systems and in organized mesoscale convective systems.

The wind gust (F_{gust}) is computed every time step during the simulation and its maximum value since the last postprocessing is written to the output files. Here we output model variables every hour so the wind gusts we obtain are the maximum gust to have occurred in the previous hour. We do not directly output the turbulent or convective wind gust terms [second and third terms on the right-hand side of Eq. (1)]. Instead, these two terms are approximated offline from the hourly outputs of the instantaneous eastward and northward turbulent surface stress components and wind speeds at 850 and 950 hPa. Since the third term is active only during deep convection, we include only grid points where convective precipitation exceeds 1 mm per hour for this term.

d. Observations and additional datasets

IBTrACS (the International Best Track Archive for Climate Stewardship) best track dataset (Knapp et al. 2010) is used to identify the location of Hurricane Debby during the tropical phase and extratropical transition. The data includes longitude and latitude coordinates of the cyclone, the minimum sea level pressure and the 1-min averaged sustained surface wind speeds.

We also investigated SYNOP observations from Finnish Meteorological Institute (FMI) from the time the storm was over Finland (22 September 1982). We obtained 10-m wind speed observations in total from 130 automated and manual weather stations. In 1982, when storm Mauri occurred, wind speed observations were made as 10-min average SYNOP observations every 3 h or every 6 h. Therefore, taking into account the temporal (and spatial) resolution, the highest wind speeds associated with storm Mauri are likely to be missing from FMI's observational dataset. No wind gust observations were made at that time.

Additionally, we obtained several thermal infrared satellite images from the Advanced Very High Resolution Radiometer (AVHRR) from the NERC Satellite Receiving Station, Dundee University, Scotland.

3. Analysis methods

a. Cyclone space phase diagram

Hart (2003) developed an objective methodology that can be used to visually detect the evolution of the ET process through a phase diagram. A phase diagram has $-V_T^L$ values on the x axis and B values on the y axis, which represent the thermal wind and storm symmetry, respectively. ET onset is defined to occur when the storm symmetry parameter B becomes greater than

10 m denoting that the cyclone changes from symmetric to asymmetric. Tropical cyclones are warm cored and thus, the geostrophic wind decreases with height (negative thermal wind) whereas extratropical cyclones are cold cored and the geostrophic wind increases with height (positive thermal wind). Therefore, ET completion is defined to occur when $-V_T^L$ becomes negative denoting that the cyclone changes to cold cored.

b. Quasigeostrophic omega equation

The quasigeostrophic omega equation is a diagnostic equation which can be solved for the vertical velocity. The traditional form of the omega equation partitions the forcing for vertical motion into a thermal advection term and a differential vorticity advection term (Holton and Hakim 2013), which due to the linearity of the equation can be solved separately. Warm-air advection and vorticity advection increasing with height are forcings for ascent, whereas cold-air advection and vorticity advection decreasing with height are forcings for descent.

Here we solve the following version of the omega equation that is formulated in pressure coordinates:

$$\sigma_0(p)\nabla^2\omega + f^2\frac{\partial^2\omega}{\partial p^2} = f\frac{\partial}{\partial p}[\mathbf{V}\cdot\nabla(\zeta+\mathbf{f})] + \frac{R}{p}\nabla^2(\mathbf{V}\cdot\nabla T), \tag{2}$$

where σ_0 is the hydrostatic static stability, taken here to be the average on each pressure surface, p is pressure, ω is the vertical velocity in pressure coordinates (units Pa s^{-1}), f is the Coriolis parameter, $\mathbf{V}$ is the horizontal wind vector, ζ is the relative vorticity and T is temperature. In this formulation the full winds and relative vorticity are used, rather than the geostrophic values typically applied in the traditional formulation as this increases the agreement between the diagnosed omega and the model output omega. The vertical motion diagnosed with Eq. (2) was compared to the model output omega values (Fig. S1 in the online supplemental material) and in general a good agreement was found particularly on synoptic scales. Furthermore, in this version of the omega equation the contribution of friction and diabatic heating have been neglected.

OpenIFS model output on evenly spaced pressure surfaces every 50 hPa at the native model resolution (T1279) is used as input to Eq. (2). The terms on the right-hand side are first calculated in grid-point space and then the equation is solved in spectral space. Due to the high resolution, the resultant omega fields are rather noisy when calculated at T1279 resolution. Therefore, a smoothing is applied when solving the omega equation such that the Fourier coefficient associated with wavenumbers larger than T255 are set to zero. This effectively smooths the output from the omega equation to T255 resolution, approximately 80 km.

Sutcliffe's development theorem (Sutcliffe 1947) links vertical motions to surface development via the quasigeostrophic vorticity equation:

$$\frac{\partial\zeta_g}{\partial t} = -\mathbf{V}_g\cdot\nabla(\zeta_g+f) + f_0\frac{\partial\omega}{\partial p}. \tag{3}$$

Assuming the standard boundary condition that $\omega = 0$ at the surface, Eq. (3) shows that if there is ascent in the low-to-mid troposphere, $\partial\omega/\partial p > 0$, and thus this will cause an increase in low-level relative vorticity. Ascent therefore leads to the intensification of a surface cyclone, and therefore when vertical motions due to different forcings are diagnosed from the omega equation, we can subsequently infer how the surface cyclone will develop.

4. Synoptic overview

In this section, we provide a brief synoptic overview of Debby and other relevant synoptic-scale features in the North Atlantic based on ERA-Interim reanalysis. An animation of the 850-hPa relative vorticity with 6-hourly time steps is included in the supplemental material to show that a coherent low-level positive vorticity anomaly can be tracked from Hurricane Debby across the Atlantic and finally to northern Finland. Four distinct stages of the evolution of the hurricane and the extratropical windstorm are considered here: 1) Hurricane Debby, 2) extratropical transition, 3) reintensification over the United Kingdom, and 4) storm Mauri in northern Finland.

a. Hurricane Debby

Debby was a category 4 hurricane, with maximum sustained winds of 58 m s^{-1}, that formed from a tropical depression north of the Dominican Republic on 13 September 1982 (Clark 1983). It developed into a tropical storm at 1200 UTC 14 September and was upgraded to a hurricane 12 h later at 0000 UTC 15 September while moving north from the Bahamas (Clark 1983). Between 15 and 17 September, Debby took a more northeastward course both in the IBTrACS best track data and minimum central pressure track of ERA-Interim, which we produced manually by following the minimum mean sea level pressure center associated with Debby (Fig. 1a). The hurricane deepened rapidly, which was captured only in IBTrACS (Fig. 1b); reanalysis datasets, like ERA-Interim, are

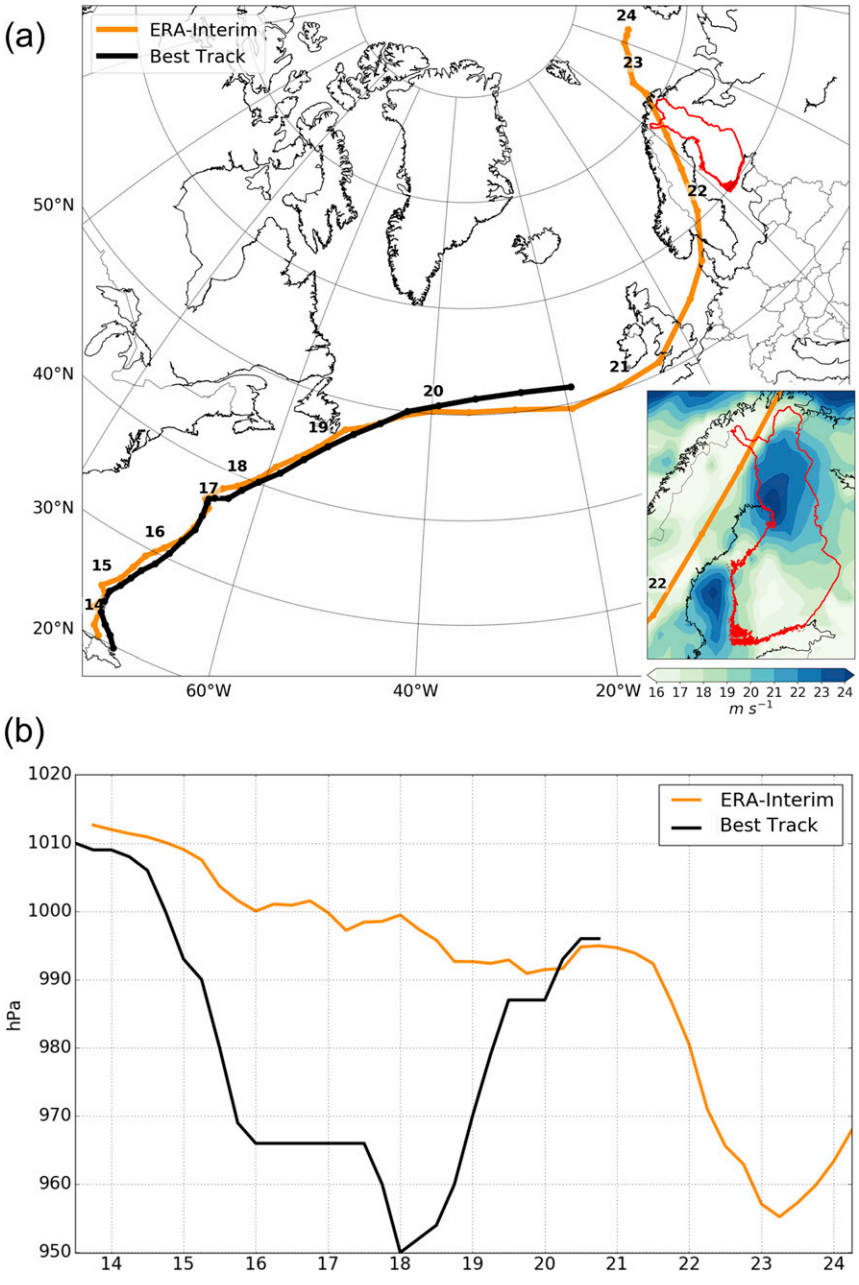

FIG. 1. (a) IBTrACS best track for Hurricane Debby (black) and ERA-Interim manual minimum sea level pressure track (orange). Dots are plotted every 6 h and the labeled numbers are days of September 1982 at 0000 UTC. The inset figure shows maximum 10-m wind gusts between 21 and 24 Sep 1982 from ERA-Interim (colors, m s^{-1}). Borders of Finland are colored red. (b) Time series of minimum mean sea level pressure for Hurricane Debby from IBTrACS best track (black) and ERA-Interim (orange).

known to often underestimate hurricane intensity (Schenkel and Hart 2012; Hodges et al. 2017). The phase diagram, created based on ERA-Interim data, shows that Debby had a warm core ($-V_T^L > 0$) and symmetric structure ($B < 10$ m) as typical for a tropical system (Fig. 2).

At 1200 UTC 16 September, Debby was located at 32°N, 65°W and the symmetrical vortex of the hurricane was visible in the 850-hPa relative vorticity and mean sea level pressure (MSLP) fields (Fig. 3a). At that time, there was a small, additional 850-hPa relative vorticity maximum evident at 47°N, 73°W that was in the

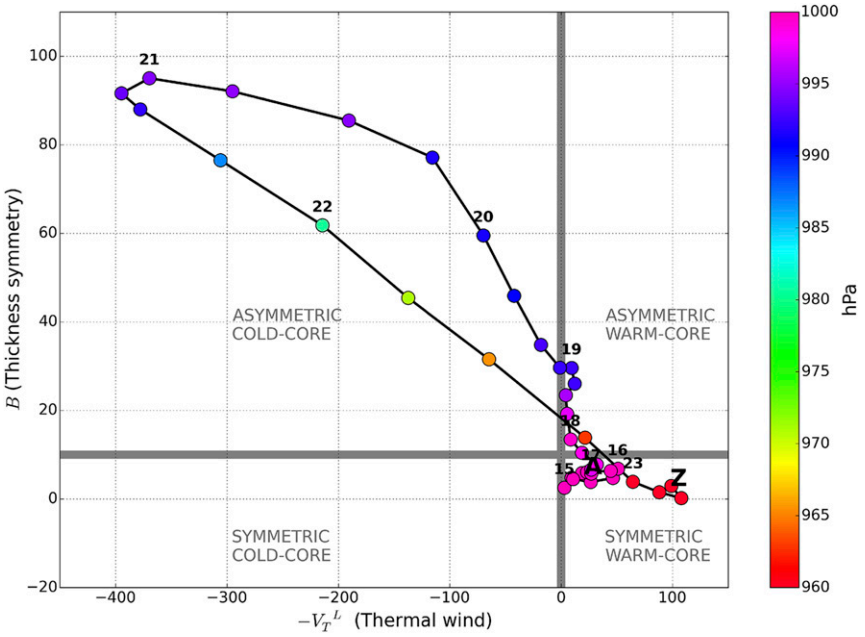

FIG. 2. Phase diagram of Hurricane Debby based on ERA-Interim. Dots are plotted every 6 h and the labeled numbers above the dots are days of September 1982 at 0000 UTC (starting with letter "A" at 1200 UTC 14 Sep and ending with letter "Z" at 1800 UTC 23 Sep). The dot colors indicate mean sea level pressure of the cyclone.

left-hand exit region of a jet streak, an ideal location for further development. Debby potentially enhanced the development of this feature by advecting warm and moist air poleward, although the favorable location relative to the jet streak likely contributed to the cyclone development. The jet streak over North America reached wind speeds of 50 m s^{-1} at 300 hPa and another jet streak with wind speeds exceeding 60 m s^{-1} at 300 hPa extended from the central North Atlantic to northern Europe. Twelve hours later, at 0000 UTC 17 September, Debby moved northward and a surface low (hereinafter referred to as "ETC1") became evident north of Debby at 50°N, 72°W (Fig. 3b). ETC1 traveled east and at 1200 UTC 17 September it had reached Newfoundland (Fig. 3c).

b. *Extratropical transition*

Based on the phase diagram, ET onset occurred at 1800 UTC 17 September as Debby became asymmetric i.e., the B value exceeded 10 m (Fig. 2). Debby reached a minimum surface pressure of 950 hPa at 0000 UTC 18 September (Fig. 1b) while located at 37°N, 62°W (Figs. 1a and 3d). The 850-hPa relative vorticity maximum related to ETC1 had increased and spatially extended, while another closed low center formed between Greenland and Iceland at 65°N, 35°W with a minimum MSLP of 1000 hPa (hereinafter referred to as "ETC2"). At 1200 UTC 18 September, Debby still had a rather symmetrical vortex noted from the 850-hPa relative vorticity and MSLP patterns (Fig. 4a). ETC1 traveled east over the Atlantic while ETC2 remained stationary. There was a jet streak that had wind speeds exceeding 60 m s^{-1} at 300 hPa over northern Europe and a weaker jet of 40 m s^{-1} at 300 hPa over the northeastern Atlantic.

Debby moved slowly toward the north and east, and by 0000 UTC 19 September it had reached Newfoundland (Figs. 1a and 4b). At 0600 UTC 19 September, the phase diagram shows Debby becoming cold cored ($-V_T^L$ turning negative) indicating the ET completion and a transformation of Hurricane Debby to an extratropical cyclone, now referred to as "ex-Debby" (Fig. 2). The shape of MSLP and 850-hPa relative vorticity near the center of the storm started to spread zonally (Figs. 4c,d). ETC2 moved east toward Iceland and at 1200 UTC 19 September it had intensified with the minimum MSLP of 996 hPa while ETC1, also deepening to a minimum of 998 hPa, rapidly traveled eastward across the Atlantic (Fig. 4c). ETC1 was located at the left exit of the intensifying jet, now exceeding 60 m s^{-1} at 300 hPa.

At 1200 UTC 19 September, ex-Debby came under the influence of the midlatitude westerlies and moved rapidly across the Atlantic; between 1200 UTC 19 September (Fig. 4c) and 0000 UTC 21 September (Fig. 4f) ex-Debby traveled almost 2700 km in 36 h.

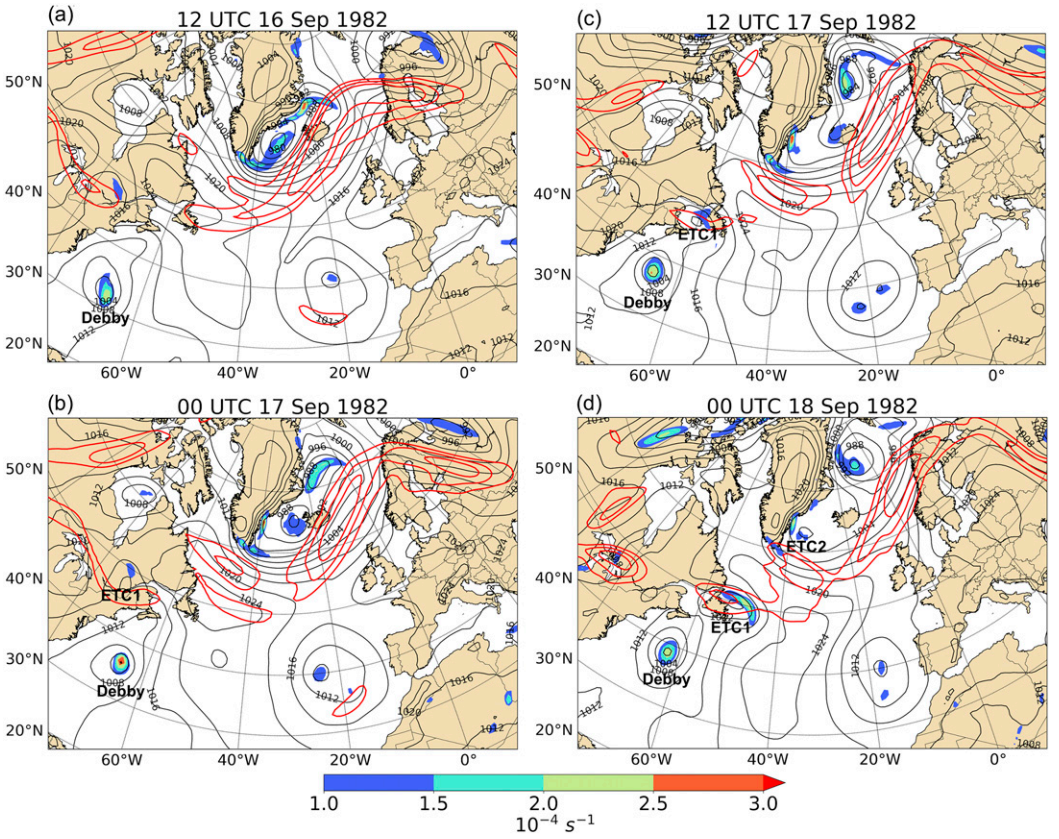

FIG. 3. 850-hPa relative vorticity (colors, s^{-1}), 300-hPa wind speed (red contours at 40, 50, and 60 m s^{-1}), and mean sea level pressure (black contours at 4-hPa interval) from ERA-Interim at (a) 1200 UTC 16 Sep, (b) 0000 UTC 17 Sep, (c) 1200 UTC 17 Sep, and (d) 0000 UTC 18 Sep.

By 1200 UTC 20 September, when located at 50°N, 25°W (Fig. 4e), ex-Debby had a much larger zonal than meridional extent, values of 850-hPa relative vorticity reaching $3 \times 10^{-4}\,s^{-1}$ and a minimum MSLP of 994 hPa. Farther east and north of ex-Debby, between Iceland and the United Kingdom, ETC1 merged with ETC2, leading to the development of a large intense low pressure system with 984-hPa minimum pressure.

c. *Reintensification over the United Kingdom*

At 0000 UTC 21 September, the 850-hPa positive vorticity anomaly associated with ex-Debby had a coherent structure (Fig. 4f) but 12 h later, the vorticity anomaly magnitude had decreased (Fig. 5a). Between those 12 h, 0000–1200 UTC 21 September, ex-Debby traveled from southwestern Ireland (50°N, 10°W, Fig. 4f) across the southern United Kingdom to the North Sea (55°N, 5°E, Fig. 5a). The MSLP pattern resembled a frontal trough rather than a closed low (Figs. 4f and 5a), which is also detected in the satellite image valid at 0422 UTC 21 September (Fig. 6); there was a frontal wave visible over the central United Kingdom alongside the cold front of the mature extratropical cyclone.

To the north of ex-Debby, the large low pressure system (merged ETC1 and ETC2) continued to intensify over the Norwegian Sea reaching a minimum MSLP of 968 hPa (Fig. 5a). The 850-hPa relative vorticity indicated a strong bent-back warm front to the north and east of the low pressure center and a cold front to the south. Such a frontal structure resembles the T-bone structure of the Shapiro–Keyser cyclone model (Shapiro and Keyser 1990). The occurrence of the mature extratropical cyclone is confirmed from the satellite image (Fig. 6) with a pronounced hook cloud and dry intrusion wrapping around the center of the cyclone.

At 1200 UTC 21 September, ex-Debby was situated beneath the right-hand side of jet entrance region, which likewise the left-hand side exit region is a favorable area for further cyclone development (Fig. 5a). At that time, the asymmetric and cold core structure of ex-Debby started to change as the high B values began to decrease and highly negative $-V_T^L$ values began to increase toward zero (Fig. 2). The surface pressure of ex-Debby

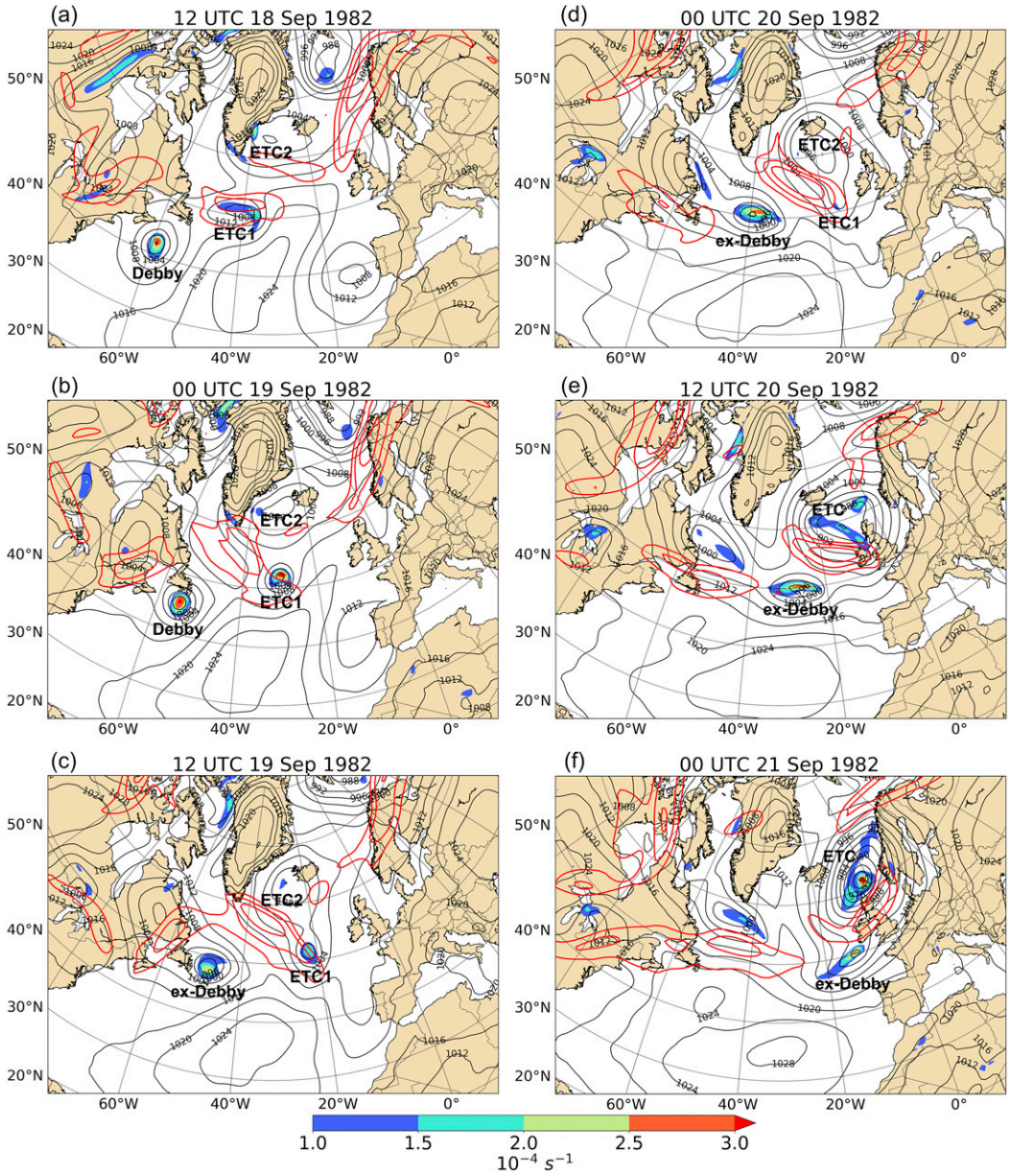

FIG. 4. 850-hPa relative vorticity (colors, s^{-1}), 300-hPa wind speed (red contours at 40, 50, and 60 $m\,s^{-1}$), and mean sea level pressure (black contours at 4-hPa interval) from ERA-Interim at (a) 1200 UTC 18 Sep, (b) 0000 UTC 19 Sep, (c) 1200 UTC 19 Sep, (d) 0000 UTC 20 Sep, (e) 1200 UTC 20 Sep, and (f) 0000 UTC 21 Sep.

started to rapidly deepen (Fig. 1b) and 12 h later, at 0000 UTC 22 September, the 850-hPa positive vorticity anomaly of ex-Debby had reintensified (Fig. 5b).

d. Storm Mauri in northern Finland

At 0000 UTC 22 September, there were two closed low pressure centers evident and three separate localized 850-hPa relative vorticity maxima (Fig. 5b). The relative vorticity maximum associated with ex-Debby was in southern Sweden at 61°N, 15°E and did not have a closed low pressure contour. The second relative vorticity maximum was located over the Norwegian Sea, related to the occlusion, and had a 972 hPa minimum pressure. The third relative vorticity maximum was north of 70°N, had a minimum MSLP of 976 hPa, and was related to the warm front extending toward the east in the Barents Sea. Twelve hours later at 1200 UTC, the low pressure center and vorticity maximum associated with ex-Debby had strengthened and moved northward (Fig. 5c). Two other vorticity

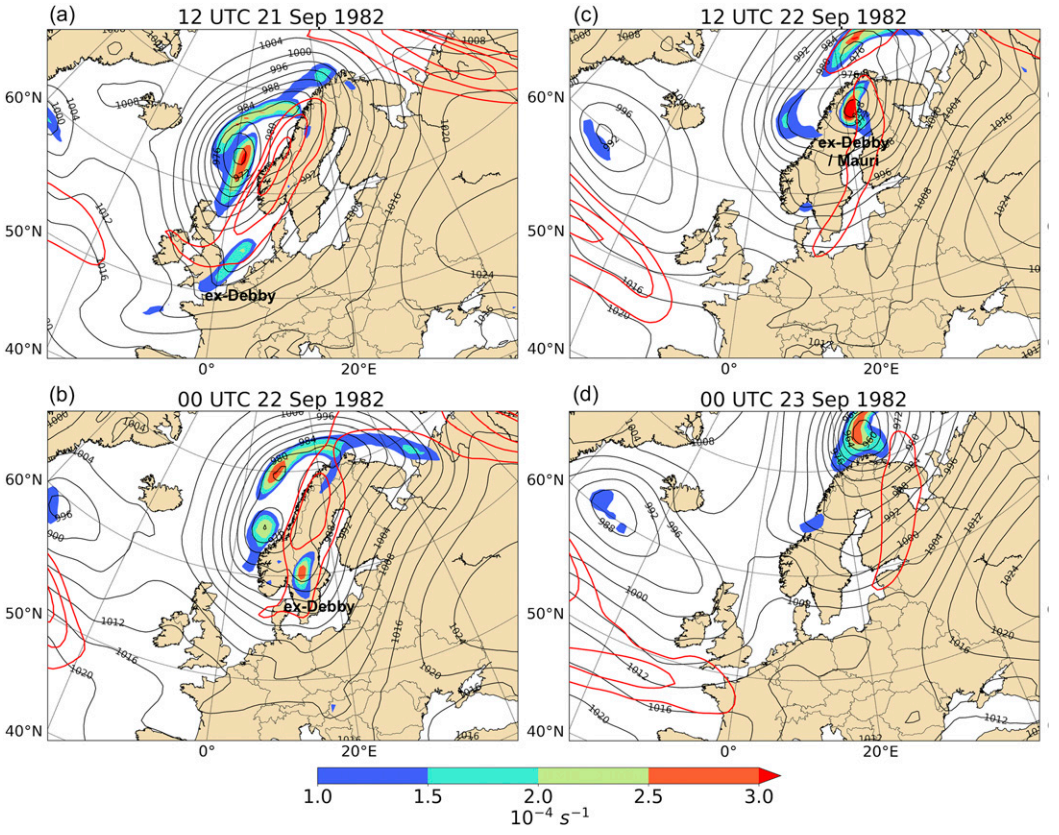

FIG. 5. 850-hPa relative vorticity (colors, s^{-1}), 300-hPa wind speed (red contours at 40, 50, and 60 $m\,s^{-1}$), and mean sea level pressure (black contours at 4-hPa interval) from ERA-Interim at (a) 1200 UTC 21 Sep, (b) 0000 UTC 22 Sep, (c) 1200 UTC 22 Sep, and (d) 0000 UTC 23 Sep.

centers, one in the Norwegian Sea and one in the Barents Sea, remained at this time but only the Barents Sea vorticity maximum was associated with a closed pressure contour (Fig. 5c). The low related to the remains of the warm front had moved farther north. The low center associated with ex-Debby, now located in northern Sweden at 68°N, 21°E, was clearly the more intense of the two with minimum pressure of 965 hPa. The region of 850-hPa relative vorticity maximum was widely spread and exceeded $3 \times 10^{-4}\,s^{-1}$. This strong low center moved over northern Finland and was named storm Mauri. The maximum 10-m wind gusts attained in ERA-Interim during storm Mauri were up to 26 $m\,s^{-1}$ and there was a large area over Finland where the gusts exceeded 20 $m\,s^{-1}$ (enlarged box in Fig. 1a). The phase diagram shows that ex-Debby/storm Mauri became warm cored at 1800 UTC 22 September and regained symmetric structure at 0000 UTC 23 September (Fig. 2). This change in the structure was due to the warm air seclusion, a feature typically observed in fully developed T-bone structure cyclones, which trapped the warm air in the center of the cyclone. The occluded phase of storm Mauri is evident in Figs. 5c and 5d and in the animation included in the supplemental material.

5. Meso- and synoptic-scale dynamic evolution

a. Overview and verification of OpenIFS simulations

We used OpenIFS to simulate the meso- and synoptic-scale dynamic evolution of ex-Debby and storm Mauri. Three simulations with different initialization dates were conducted. The first simulation was initialized at 0000 UTC 17 September and produces a cyclone track of Hurricane Debby that is in reasonable agreement with ERA-Interim for the first two days (Fig. 7). During those 48 h OpenIFS simulated Debby, still as a hurricane, to move northeast roughly parallel to the east coast of North America. After two days of simulation, errors develop in the OpenIFS forecast initialized on 17 September and ex-Debby is simulated to track farther south than in ERA-Interim. During 19 and 20 September, the minimum MSLP simulated is 3–15 hPa higher than in ERA-Interim. Therefore, the forecast from 17 September is only used to investigate how Debby modified the midlatitude flow in section 5b.

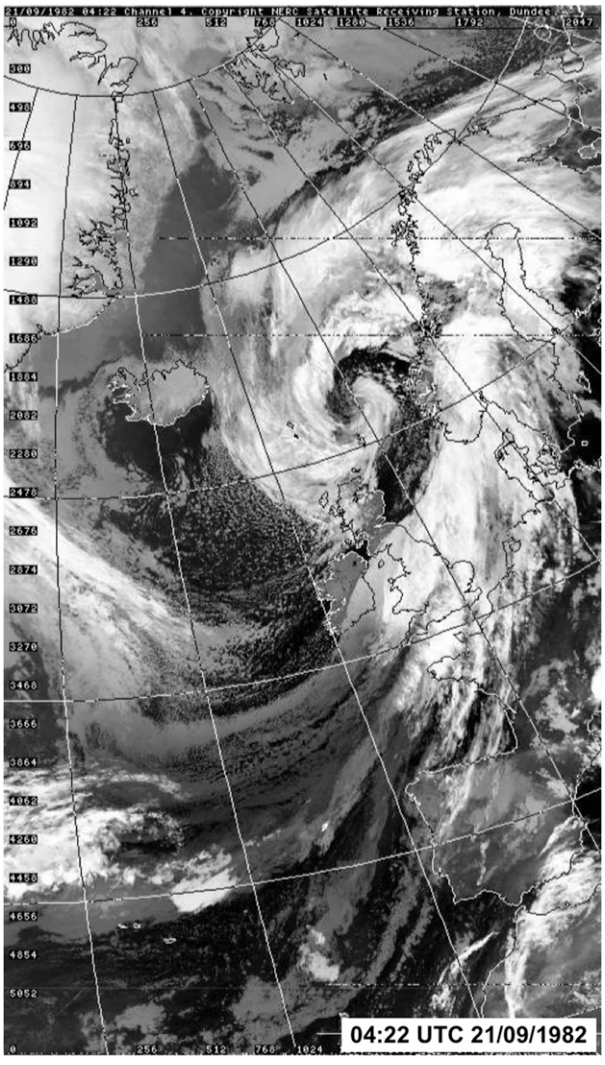

FIG. 6. Thermal infrared satellite image obtained from the Advanced Very High Resolution Radiometer (AVHRR) at 0422 UTC 21 Sep 1982. Copyright NERC Satellite Receiving Station, Dundee University, Scotland.

The second simulation was initialized at 0000 UTC 19 September; the track of ex-Debby in this OpenIFS forecast compares well against ERA-Interim for two days (19 and 20 September) during which time the cyclone traveled from Newfoundland across the Atlantic to the south of Ireland (Fig. 7). However, on 21 September when ex-Debby traveled over the south of the United Kingdom and reintensified, large differences appear between the OpenIFS forecast and ERA-Interim. The OpenIFS simulated track of ex-Debby is farther south than in ERA-Interim and the simulated minimum MSLP increases during 21 September demonstrating that the OpenIFS forecast initialized on 19 September cannot correctly capture the reintensification that took place over the United Kingdom. Hence, the forecast from 19 September is only used to analyze the large-scale flow and dynamical evolution and structure of ex-Debby as it traveled across the Atlantic in section 5c.

The third simulation was initialized at 0000 UTC 21 September. Both the simulated track location and intensity agree well with ERA-Interim during 21 and 22 September (Fig. 7). Therefore, the forecast from 21 September is used to investigate the reintensification of ex-Debby over the United Kingdom (section 5d) and the high winds over Finland (section 5e). Since in the OpenIFS forecast initialized on 19 September ex-Debby decayed and did not reintensify over the United Kingdom, we compared that to the forecast initialized on 21 September to attempt to identify the reasons for the redevelopment. In addition, as there was no ex-Debby over northern Finland in the forecast initialized on 19 September, we qualitatively estimate the role that ex-Debby played in leading to the strong winds and to the occurrence of storm Mauri by comparing the winds simulated in the forecast initialized on 19 September to those in the forecast initialized on 21 September (section 5f).

b. *Did Debby modulate the downstream upper-level flow?*

Debby did not begin the process of ET until 1800 UTC 17 September but had already started to impact the evolution of the midlatitude flow before this time. As noted in section 4a, Debby may have affected the midlatitude flow on 16 September by enhancing the development of ETC1. Later on Debby started to directly impact the midlatitude flow. At 0600 UTC 18 September, 12 h after the transition process began, Debby was located at 41°N, 60°W (Figs. 7a and 8a). The upper-level waveguide, indicated by the 2 potential vorticity unit (2 PVU) contour (1 PVU $= 1.0 \times 10^{-6}\,\mathrm{m^2\,s^{-1}\,K\,kg^{-1}}$) in Fig. 8a, was already somewhat amplified at this time. A trough, visible in the 200-hPa PV, was located upstream of Debby, a pronounced ridge was present to the north and downstream of Debby and ETC1 was at 51°N, 50°W collocated with a 200-hPa jet streak that had a maximum speed of $69\,\mathrm{m\,s^{-1}}$ (Fig. 8a). In addition, at 0600 UTC 18 September strong divergent (irrotational) winds at 200 hPa were associated with Debby. Directly above and slightly west of Debby's center, upper-level divergent winds, which were likely a result of the outflow from Hurricane Debby, were directed toward the west that may have impeded the eastward progression of the upstream trough. Strong divergent winds were also present to the north of Debby, over Newfoundland, and were almost perpendicular to the PV gradient at 200 hPa. The divergent winds were directed from a region of low-PV air at 200 hPa, which most likely arose due to diabatic heating in the low-to-mid troposphere, to an area of high

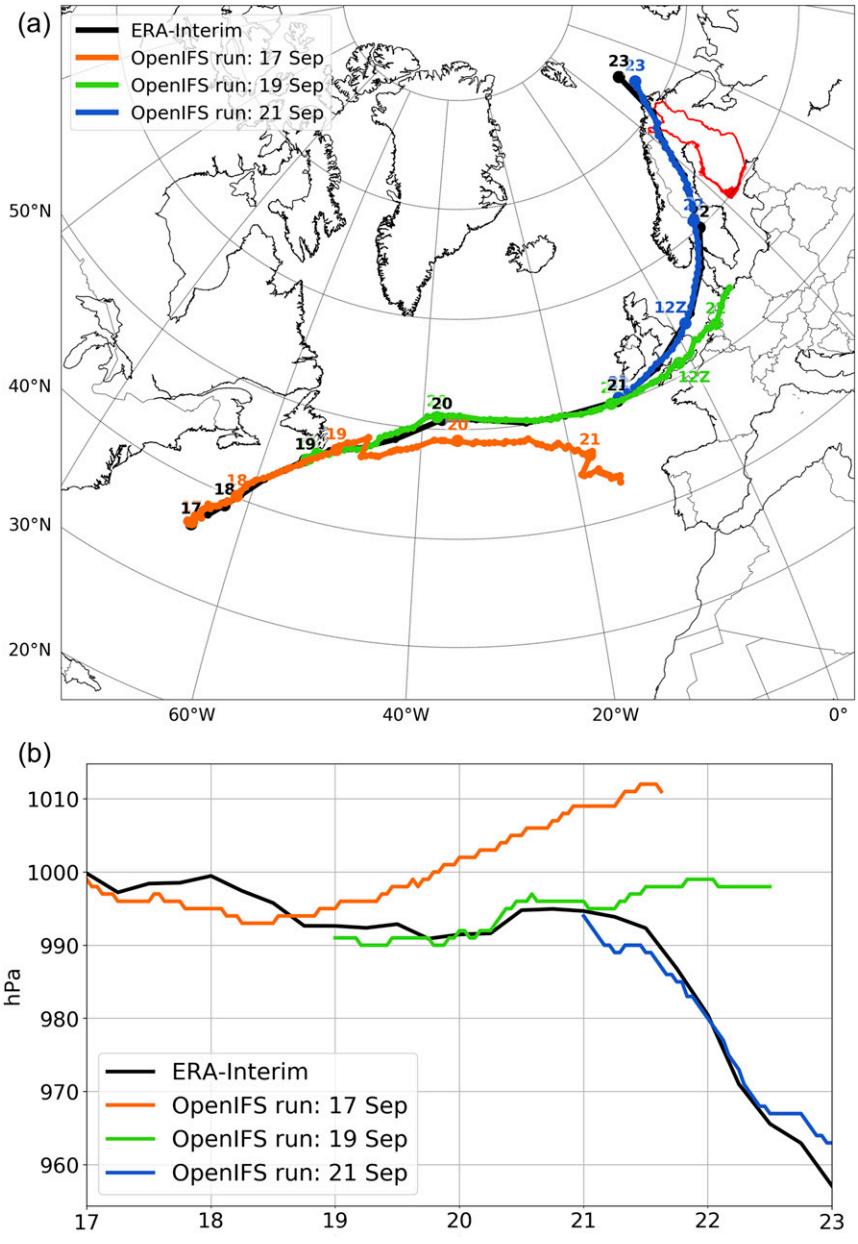

FIG. 7. (a) Manual 850-hPa maximum vorticity tracks from ERA-Interim (black) and OpenIFS simulations initialized on 17 Sep (orange), 19 Sep (green), and 21 Sep (blue). Dots are plotted every 6 h for ERA-Interim and every hour for the OpenIFS forecasts. The labeled numbers above the enlarged dots are days of September 1982 at 0000 UTC, in addition 1200 UTC 21 Sep is labeled. Borders of Finland are colored red. (b) Time series of minimum mean sea level pressure for ERA-Interim (black) and OpenIFS simulations initialized on 17 Sep (orange), 19 Sep (green), and 21 Sep (blue).

PV. Therefore, the upper-level divergent winds resulted in negative PV advection at upper levels.

At 1800 UTC 18 September, strong 200-hPa divergent winds remained collocated with the PV gradient, and the upper-level ridge to the north of Debby had amplified slightly (Fig. 8b). Furthermore, at 1800 UTC 18 September the jet streak had strengthened slightly and now had a maximum speed of 76 m s^{-1}. The jet likely accelerated due to the influx of low-PV air on the equatorward side of the jet, which would act to steepen the tropopause and consequently accelerate the jet stream. This sequence of events, namely weak ridge

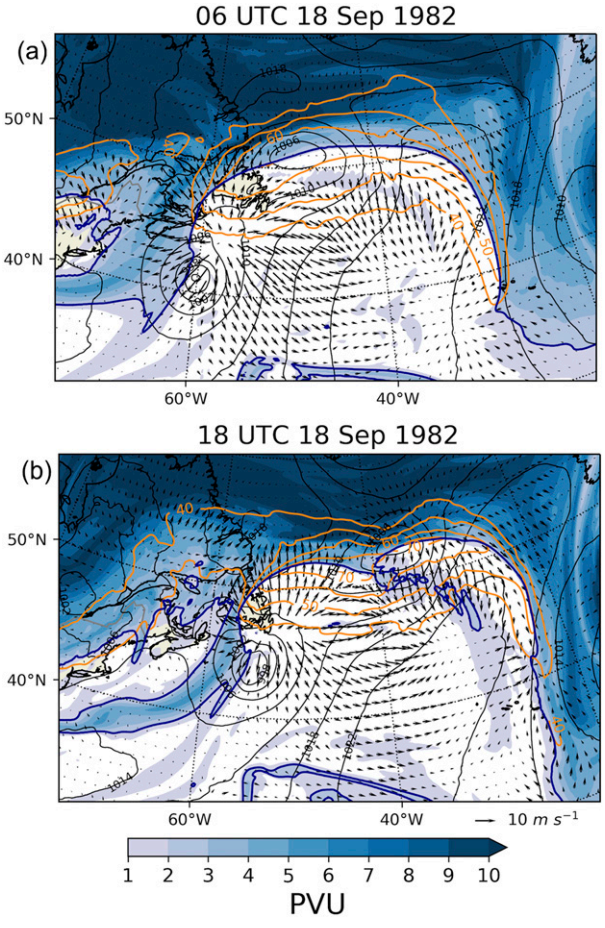

FIG. 8. OpenIFS simulation initialized on 17 Sep valid at (a) 0600 UTC 18 Sep, and (b) 1800 UTC 18 Sep. 200-hPa potential vorticity (colors, 2 PVU contour also in dark blue), 200-hPa divergent wind (vectors), 200-hPa wind speed (orange contours starting at 40 m s^{-1} with 10 m s^{-1} interval), and mean sea level pressure (black contours at 4-hPa interval).

building and jet streak acceleration, is similar to that observed during the transition of Typhoon Jangmi in 2008 (Grams et al. 2013). It is notable that the minimum MSLP of Debby did not decrease between 0600 and 1800 UTC 18 September despite the presence of an upper-level trough immediately to the west. Previous studies (e.g., Riboldi et al. 2019) have shown that reintensification of tropical cyclones can be very sensitive to the exact location and propagation speed of the trough axis. Thus, a small shift in the position of Debby, or the upper-level trough, could have easily resulted in a very different evolution of ex-Debby.

c. *Why was ex-Debby able to travel across the North Atlantic?*

Ex-Debby moved rapidly across the North Atlantic between 19 and 21 September 1982 in ERA-Interim and in the OpenIFS forecast initialized on 19 September (Fig. 7a) but did not intensify during this time (Fig. 7b). At 0000 UTC 19 September, Debby was located east of Newfoundland but during the next 48 h ex-Debby traveled almost 3200 km and by 0000 UTC 21 September was located south of Ireland. In this section, we address the cause of this rapid propagation and the cause for the lack of any intensification.

Ex-Debby had completed ET by 0600 UTC 19 September and was located at 46.5°N, 52.5°W, just east of Newfoundland (Fig. 9a). At this time, ex-Debby was positioned under a large-scale upper-level ridge with a trough to the west and another trough to the northeast. The trough to the west, which was associated with potential temperature values of ~300 K on the dynamic tropopause (Fig. 9a), was too far west relative to ex-Debby to provide notable upper-level forcing (this point is further discussed below). This explains the lack of intensification of ex-Debby at this point in time. The second trough, which was located to the east of Greenland at 0600 UTC 19 September, was also at this time unable to interact directly with ex-Debby. This second trough was intense, had closed contours of low (<290 K) potential temperature on the dynamic tropopause at its base (60.8°N, 39°W, Fig. 9a), and was collocated with a surface low pressure center (ETC2).

Twelve hours later, at 1800 UTC 19 September, ex-Debby had tracked eastward and slightly northward and was now located at 49.5°N, 44.8°W whereas the downstream trough had moved east and south (the base of the trough was now located at 58.0°N, 26.2°W) (Fig. 9b). Consequently, ex-Debby was still located under an upper-level ridge and lacked any interaction with this downstream trough. However, as the upper-level downstream trough approached the jet from the northern side it resulted in a further accelerate the jet: at 0600 UTC the maximum 200-hPa wind speed in this jet core was 64.3 m s^{-1} whereas 12 h later it was 70.1 m s^{-1}. This upper-level trough proves critical for the reintensification of ex-Debby over the United Kingdom, discussed below in section 5d.

At 0000 UTC 20 September, ex-Debby was located at 50°N, 40°W (Fig. 10a) and remained under the upper-level ridge (Fig. 10e). The minimum MSLP of ex-Debby had not changed over the preceding 24 h yet the PV anomaly and cyclonic circulation associated with ex-Debby remained (Fig. 10a). One physical reason that explains how a PV anomaly of a transitioned tropical cyclone can remain and subsequently redevelop in a baroclinic zone is a diabatic Rossby wave (DRW, e.g., Moore and Montgomery 2004, 2005). Using the criteria of DRW characteristics developed by Boettcher and

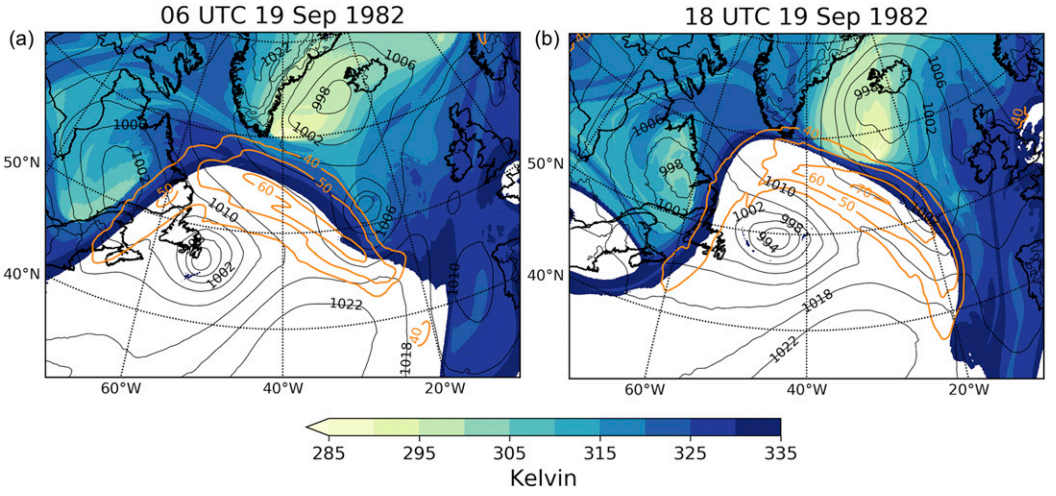

FIG. 9. OpenIFS simulation initialized on 19 Sep valid at (a) 0600 UTC 19 Sep, and (b) 1800 UTC 19 Sep. Potential temperature on the dynamic tropopause (PV = 2 PVU; colors, K), 200-hPa wind speed (orange contours starting at 40 m s^{-1} with 10 m s^{-1} interval), and mean sea level pressure (black contours at 4-hPa interval).

Wernli (2013) (and discussed in section 1), we now test our hypothesis that ex-Debby propagated rapidly across the Atlantic as a DRW.

The first requirement for a DRW is that the MSLP minima is enclosed by a closed MSLP contour. This requirement is clearly met by ex-Debby at both 0000 and 1200 UTC 20 September (Figs. 10a,b). The second requirement is that there must be a positive 850-hPa PV anomaly close to the MSLP minimum. Ex-Debby again meets this criterion as there is a strong positive 850-hPa PV anomaly at both 0000 and 1200 UTC 20 September (Figs. 10a,b), which at 0000 UTC exceeded 5 PVU near the center of the cyclone (Fig. 10a). Vertical cross sections of PV at 0000 UTC 20 September further confirm the presence of a low-level PV anomaly with maximum PV values exceeding 5 PVU between 900 and 700 hPa (Fig. 11). These cross sections also show that ex-Debby still had a vertically coherent PV tower structure remaining from the ET process and consequently the PV anomaly was deeper than typically found in DRWs.

The third requirement is that there must be substantial low-level baroclinicity. At 0000 UTC 20 September, there was a strong horizontal potential temperature gradient (and equivalent potential temperature gradient—not shown) downstream of ex-Debby (Fig. 10c). In the climatological study by Boettcher and Wernli (2013), the specific criteria for low-level baroclinicity is that the difference between the 10th and 90th percentile of 950-hPa potential temperature difference evaluated over a box downstream of the cyclone center must exceed 5 K. This box starts 1.2°E of the MSLP minima and extends a further 3.6°E and extends 1.8°S and 4.8°N of the cyclone center. However, in case studies values much higher than 5 K can occur. For example, a DRW event from December 2005 had baroclinicity values exceeding 14 K (Boettcher and Wernli 2011). The same method for estimating baroclinicity as used by Boettcher and Wernli (2011) and Boettcher and Wernli (2013) was applied to the OpenIFS output. At 0000 (1200) UTC 20 September a value of 15.5 K (12.3 K) was found that exceeds the threshold and confirms that the requirement of a strong baroclinic zone is also met.

The fourth requirement of Boettcher and Wernli (2013) is that the cyclone must travel more than 250 km within 6 h to meet the requirement of fast propagation. Between 0000 and 0600 UTC 20 September ex-Debby traveled 480 km and between 0600 and 1200 UTC 20 September ex-Debby traveled another 510 km (Fig. 7a). Hence, ex-Debby fulfills the fast propagation speed criterion. Ex-Debby also had sufficient moisture (the fifth requirement); 850-hPa relative humidity around the cyclone center exceeded 90% at both 0000 and 1200 UTC 20 September (Figs. 10c,d). In addition, at both 0000 and 1200 UTC 20 September, diabatic heating due to microphysics and convection averaged over the 900–700-hPa layer exceed 1 K h^{-1} immediately downstream of ex-Debby (Figs. 10e,f). Thus, based on the first five criteria, ex-Debby qualifies as a DRW at both 0000 and 1200 UTC 20 September and certainly at low-level has strong similarities with DRWs.

The final requirement of a DRW is that there is very weak upper-level forcing. Vertical cross sections indicate that there were strong, large-scale troughs (positive PV anomalies descending from the stratosphere) both to the northwest (Fig. 11a) and northeast (Fig. 11b) of ex-Debby but that neither of these

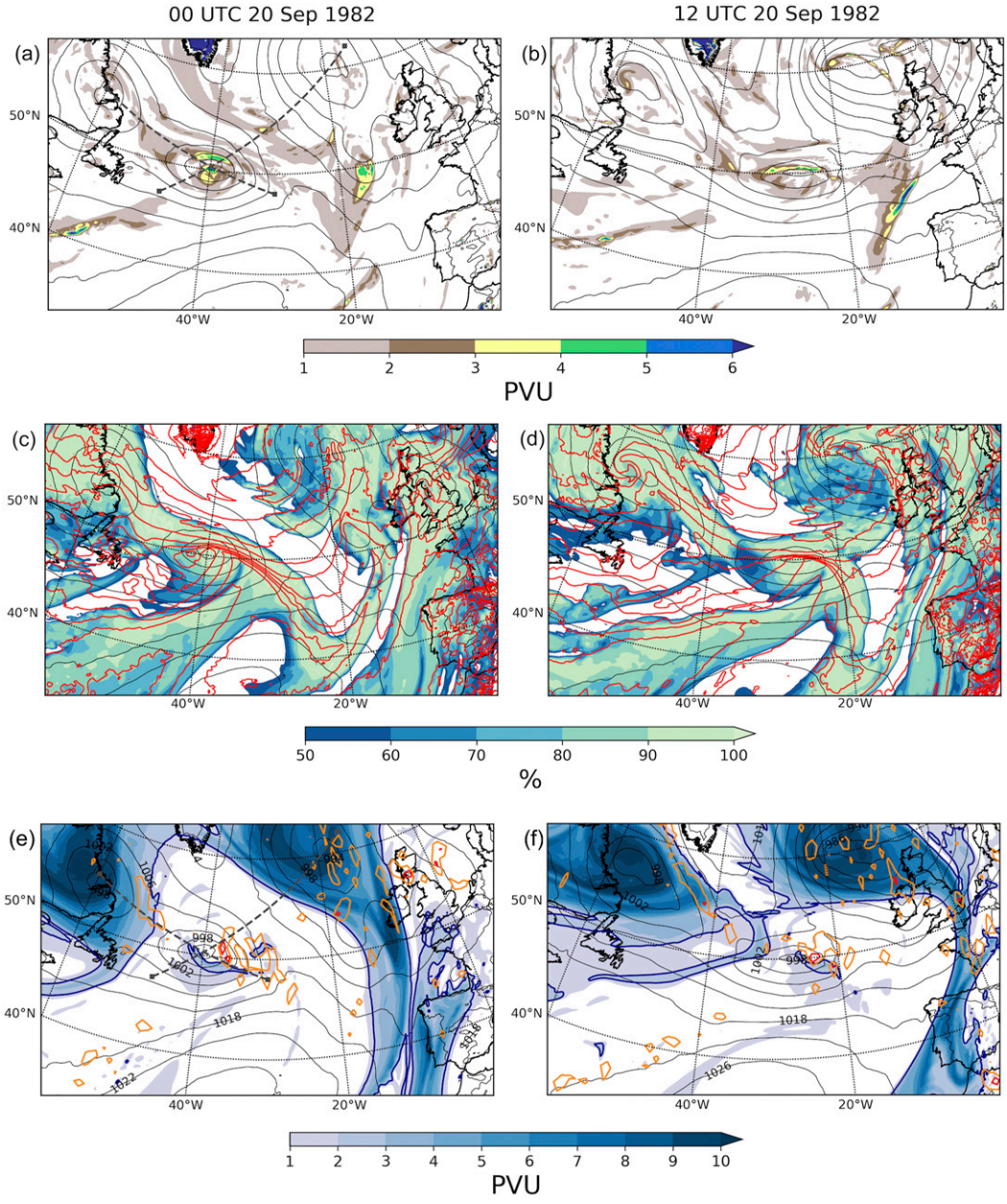

FIG. 10. OpenIFS simulation initialized on 19 Sep valid at (left) 0000 UTC 20 Sep and (right) 1200 UTC 20 Sep: (a),(b) 850-hPa potential vorticity (colors, PVU), and mean sea level pressure (black contours at 4-hPa interval). (c),(d) 850-hPa relative humidity (colors, %), 950-hPa potential temperature (red contours at 2-K interval), and mean sea level pressure (black contours at 4-hPa interval). (e),(f) 250-hPa potential vorticity (colors, 2 PVU contour also in dark blue), diabatic heating (sum of temperature tendencies from the microphysics and convection schemes) averaged over 900–700-hPa (orange contour at 0.2 K h^{-1}, red contour at 1.0 K h^{-1}), and mean sea level pressure (black contours at 4-hPa interval). Dashed lines in (a),(e) mark the locations of vertical cross sections shown in Fig. 11.

features connected directly to the low-level PV anomaly. In contrast, Fig. 10e indicates that although ex-Debby was situated beneath a large-scale ridge, there was a localized region to the south where the 250-hPa PV exceeded 2 PVU. This small-scale feature is also evident in vertical cross sections (Fig. 11a, top-right of the panel, Fig. 11b, top-left of the panel) and is relatively close to the low-level PV anomaly of ex-Debby. For the weak upper-level forcing criterion to be met Boettcher and Wernli (2013) require that the mean

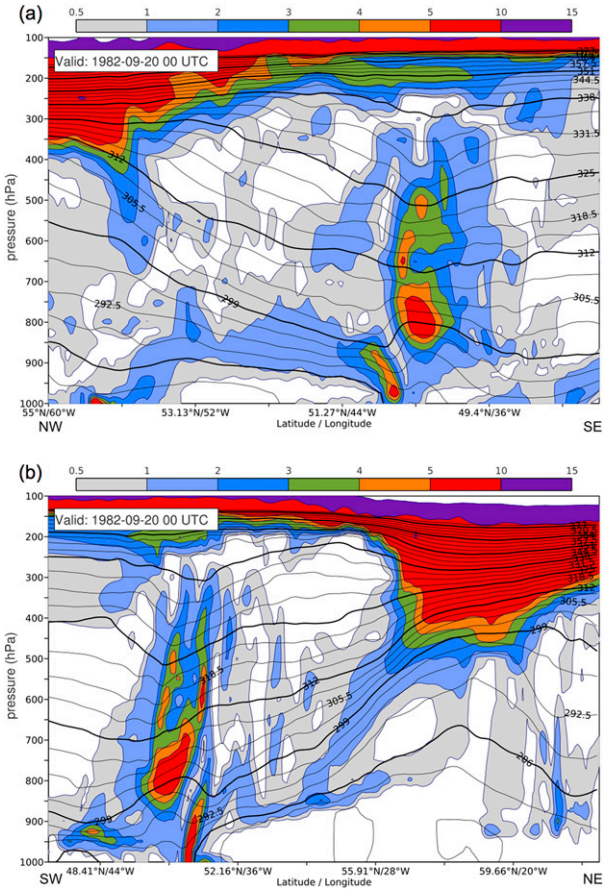

FIG. 11. Potential vorticity (colors, PVU) cross sections for the OpenIFS simulation initialized on 19 Sep valid at 0000 UTC 20 Sep: (a) (55°N, 60°W)–(48°N, 30°W), (b) (47°N, 47°W)–(62°N, 15°W). Black contours are potential temperature at 3.25-K interval.

250-hPa PV in a box that extends 4.8°E and 4.8°W, 3.6°S and 3.0°N of the cyclone center must be less than 1 PVU. Ex-Debby as simulated by OpenIFS meets this requirement between 1200 UTC 19 September and 1200 UTC 20 September but the averaged values of 250-hPa PV are close to the threshold and range from 0.89 to 0.97 PVU. Boettcher and Wernli (2013) also require that the averaged upper-level-induced quasigeostrophic ascent at 700 hPa in the same box as the PV was averaged over must be smaller than $0.5 \times 10^{-2}\,\mathrm{m\,s^{-1}}$. This diagnostic is not calculated from the OpenIFS simulation but in ERA-Interim, the upper-level-induced quasigeostrophic ascent at 700 hPa was less than $0.15 \times 10^{-2}\,\mathrm{m\,s^{-1}}$ between 1200 UTC 19 September and 1200 UTC 20 September (Maxi Boettcher, personal communication). However, the area-averaged 250-hPa PV in ERA-Interim had slightly larger values (0.89 to 1.17 PVU, Maxi Boettcher, personal communication) than in the OpenIFS simulation and was less than 1 PVU only at 1800 UTC 19 September. Ex-Debby therefore did not convincingly meet the requirements of very weak upper-level forcing for a prolonged period of time. Thus, ex-Debby was not a classical DRW as there was some (albeit weak) upper-level forcing and also because the PV tower was deeper than observed in other DRW cases (e.g., Wernli et al. 2002; Moore et al. 2008; Boettcher and Wernli 2011). Therefore, we conclude that ex-Debby traveled rapidly across the North Atlantic as a DRW-like feature between 1200 UTC 19 September and 1200 UTC 20 September.

d. *Why did ex-Debby reintensify over the United Kingdom?*

ERA-Interim reanalysis showed that ex-Debby rapidly reintensified on 21 and 22 September as it moved over the south of the United Kingdom and toward Finland. To investigate the reasons for ex-Debby's reintensification over the southern United Kingdom, we analyze the model output from the OpenIFS simulation initialized on 21 September. This forecast was able to capture the track of ex-Debby and the rapid decrease in MSLP on 21 and 22 September (Fig. 7).

At 0300 UTC 21 September, ex-Debby was located south of Ireland, had a MSLP minimum of 990 hPa and a strong 850-hPa PV anomaly which exceeded 5 PVU (enlarged box in Fig. 12b). This low-level PV anomaly was small in scale but a coherent feature that was likely present in this location as a result of ex-Debby traveling across the Atlantic as a DRW-like feature. The low-level PV anomaly could constantly regenerate itself due to diabatic processes. The continued presence of the low-level positive PV anomaly is also indicative of diabatic heating in the layer above 850 hPa. At upper levels, there was a pronounced trough, which is identified from the 2-PVU contour on the 315-K isentropic surface (Fig. 12b). This is the same feature that was first identified to the east of Greenland at 0600 UTC 19 September but did not interact with ex-Debby at that time (Fig. 9a). Between 1800 UTC 19 September (Fig. 9b) and 1200 UTC 20 September (Fig. 10f), this trough moved southeast while ex-Debby moved northeast. Ex-Debby propagated eastward faster than the upper-level trough and, hence, at 0300 UTC 21 September, the surface PV anomaly of ex-Debby was located ahead (east) of the trough (Fig. 12b). Thus, at 0300 UTC 21 September this upper-level trough could interact with, and intensify, the low-level anomaly. The trough, and associated upper-level positive PV anomaly, can also be inferred from the satellite image (Fig. 6), which shows relatively clear skies over Northern Ireland and to the north.

Figure 12e shows that at 0300 UTC 21 September, in the OpenIFS simulation initialized on 21 September,

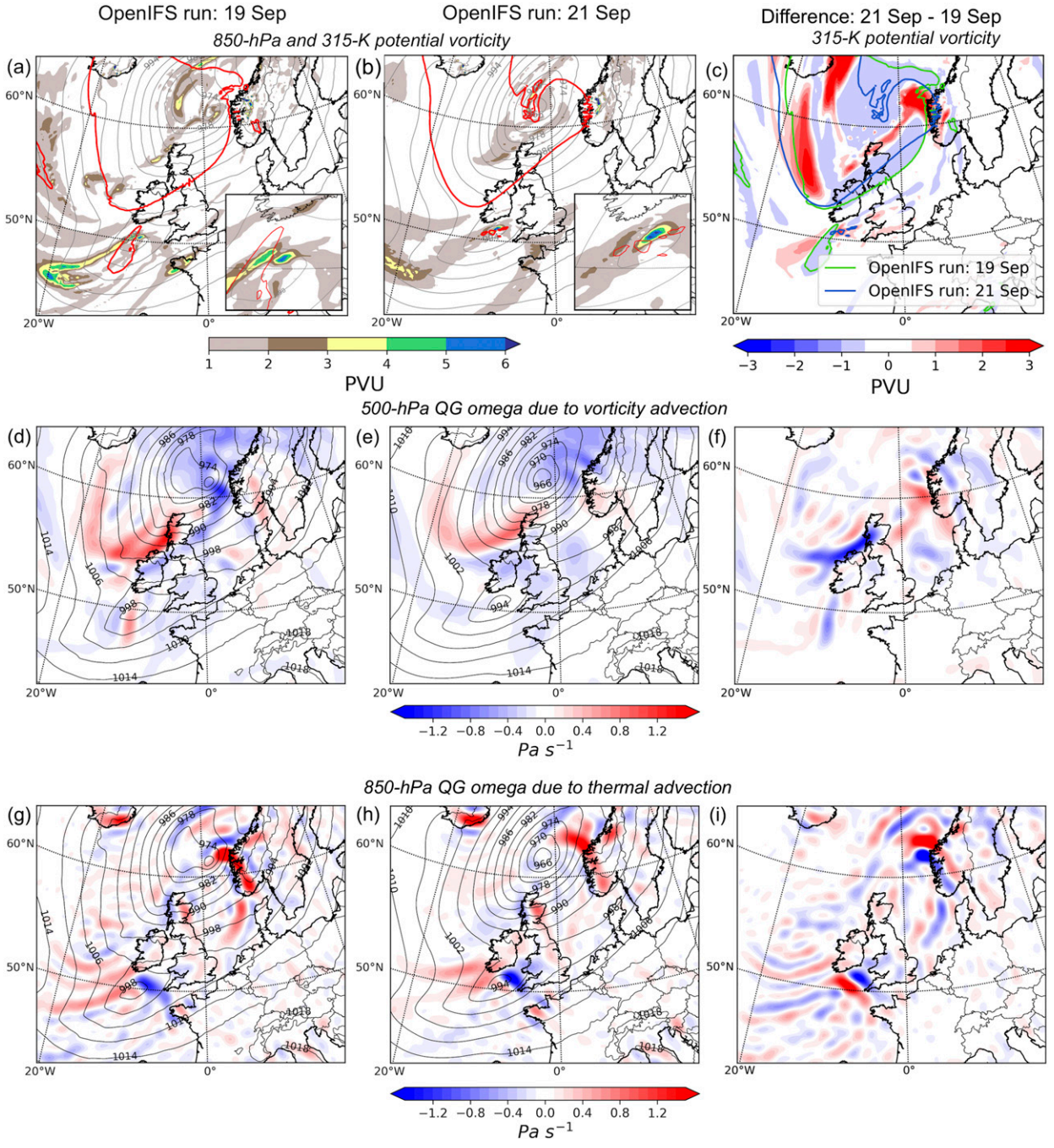

FIG. 12. OpenIFS simulations valid at 0300 UTC 21 Sep 1982, initialized on (left) 19 Sep, (middle) 21 Sep, and (right) the difference field 21 Sep minus 19 Sep: (a),(b) 850-hPa (colors, PVU) and 315-K (red contour at 2 PVU) potential vorticity, and mean sea level pressure (gray contours at 4-hPa interval). (c) 315-K potential vorticity at 2 PVU with 19 Sep (green contour) and 21 Sep (blue contour) simulations, and difference of 21 Sep–19 Sep (colors, PVU). (d),(e) 500-hPa quasigeostrophic omega due to vorticity advection (colors, Pa s^{-1}) and mean sea level pressure (black contours at 4-hPa interval). (f) Difference of 21 Sep–19 Sep of 500-hPa quasigeostrophic omega due to vorticity advection (colors, Pa s^{-1}). (g),(h) 850-hPa quasigeostrophic omega due to thermal advection (colors, Pa s^{-1}) and mean sea level pressure (black contours at 4-hPa interval). (i) Difference of 21 Sep–19 Sep of 850-hPa quasigeostrophic omega due to thermal advection (colors, Pa s^{-1}).

there was ascent due to vorticity advection at 500 hPa over Ireland and to the north and east of ex-Debby that had values of $-0.5\,\mathrm{Pa\,s^{-1}}$ (approximately $5\,\mathrm{cm\,s^{-1}}$). This suggests that relative vorticity will increase below this level in the area just north of ex-Debby [e.g., Eq. (3)]. The vertical velocity at 850 hPa due to thermal advection (Fig. 12h) shows there was strong ascent ($-1.5\,\mathrm{Pa\,s^{-1}}$, approximately $15\,\mathrm{cm\,s^{-1}}$) collocated and slightly downstream of ex-Debby that would also promote the intensification of the low-level cyclonic vorticity. This ascent at 850 hPa was east of the ascent at 500 hPa indicating a westward tilt with height. Finally, it should be noted that the low-level PV anomaly of ex-Debby was located in the right-hand side of the jet entrance (not shown). Thus, the rapid reintensification of ex-Debby over the United Kingdom occurred as the large-scale environment was favorable, with both warm-air and cyclonic vorticity advection present, and because the low-level and upper-level PV anomalies had now become constructively aligned, that is, the surface PV anomaly of ex-Debby was ahead of the upper-level trough, which enabled enhanced development.

To further elucidate the reasons why ex-Debby reintensified, the forecast initialized on 19 September, which did not show any reintensification (Fig. 7), is compared to the forecast from 21 September. Hence, by examining the differences between these two forecasts we can further clarify which factors likely led to the reintensification of ex-Debby.

When the left-hand column of Fig. 12 is compared to the middle column, no major differences are evident yet a number of small differences are present (difference fields are shown in the right-hand column). First, the 850-hPa PV anomaly in the forecast initialized on 19 September was weaker, less coherent, and located farther south and west than in the forecast initialized on 21 September. The 850-hPa PV values were more than 2 PVU higher in the simulation initialized on 21 September compared to the simulation initialized on 19 September (enlarged boxes in Figs. 12a and 12b). This difference suggests that more diabatic heating occurred at midlevels in the forecast initialized on 21 September, which subsequently increased the PV values below. The differences in the location, and also the strength, of the low-level PV anomaly may also result from earlier errors in the forecast when ex-Debby was simulated to travel rapidly across the Atlantic as a DRW-like feature.

The second notable difference between the two forecasts is the location of the low-level PV anomaly relative to the upper-level PV anomaly. There was a coherent positive PV anomaly on the 315-K isentrope directly above the surface anomaly in the forecast initialized on 19 September. This feature is evident as a dipole in the vertical motion due to vorticity advection (Fig. 12d). This suggests that the forecast initialized on 19 September did not predict rapid intensification of ex-Debby as the upper-level and low-level PV anomalies were already vertically stacked and thus unable to mutually enhance one another. Differences in location of the upper-level anomaly are confirmed when the red contours in Figs. 12a and 12b are considered that show that on synoptic scales the upper-level PV anomaly (associated with the trough that originated near Greenland) was farther west in the forecast initialized on 21 September compared to the forecast initialized on 19 September (Fig. 12c). This westward shift in the upper-level PV anomaly in the forecast from 21 September compared to the forecast initialized on 19 September, combined with an eastward shift in the lower-level PV anomaly, confirms that the vertical phasing differed between the two forecasts.

The third difference between the two forecasts is that the area of vertical motion due to thermal advection to the south of Ireland was shifted northeast in the simulation initialized on 21 September compared to 19 September (Figs. 12g–i). This displacement is directly related to the difference in the position of the surface low. However, the ascent due to thermal advection was stronger in the forecast from 21 September than from 19 September.

These differences discussed so far were valid at 0300 UTC 21 September, the time at which the two forecasts started to diverge. Additional times between 0600 and 1200 UTC were also considered. The ascent due to vorticity advection was further southwest and closer to ex-Debby particularly at 0600 and 0900 UTC in the forecast from 21 September (Fig. S2). This indicates that the more favorable phasing evident at 0300 UTC in the forecast from 21 September continued to exist at later times. The vertical velocity due to thermal advection is stronger at 0600, 0900, and 1200 UTC in the forecast from 21 September compared to the forecast from 19 September (Fig. S3). Furthermore, by 1200 UTC 21 September the vertical velocities due to thermal advection have started to weaken in the forecast from 19 September (Fig. S3), which demonstrates that ex-Debby weakens in this forecast due to limited coupling with upper levels.

e. What were the reasons for the strong winds over northern Finland?

On 22 September 1982, when storm Mauri traveled across northern Finland, the strongest observed 10-min average 10-m wind speeds were $23\,\mathrm{m\,s^{-1}}$, which were recorded by three weather stations located over

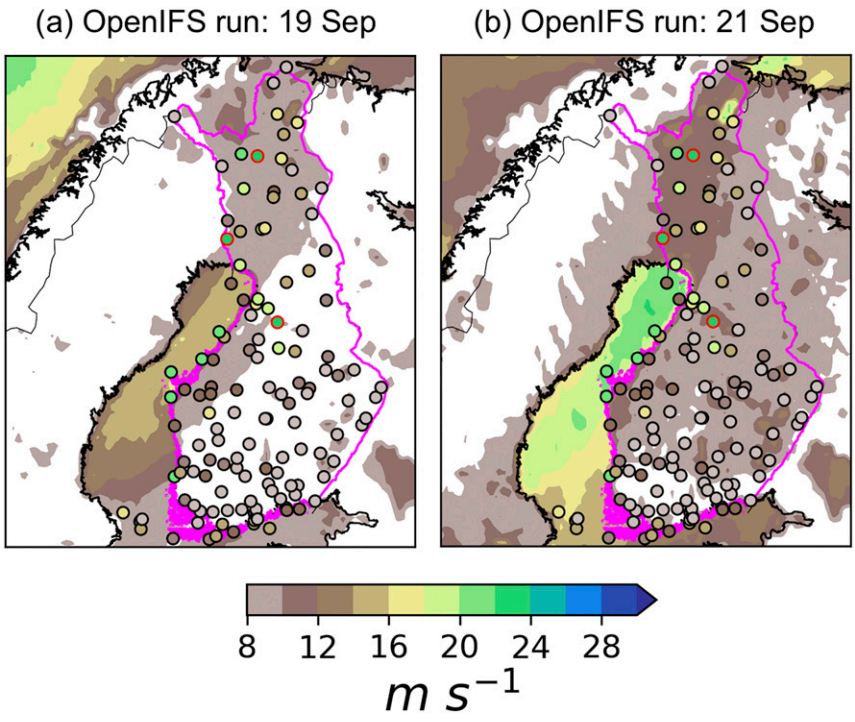

FIG. 13. Maximum observed 10-min average 10-m wind speeds during 22 Sep 1982 from Finnish Meteorological Institute's automated and manual weather stations (circles) and from OpenIFS simulations initialized on (a) 19 Sep, and (b) 21 Sep. The red circles denote the three stations that obtained the highest values of 23 m s^{-1}. Borders of Finland are colored magenta.

land in central and northern parts of Finland (Fig. 13). Nine stations in total, situated on the west coast and northern areas of Finland, observed wind speeds of 20 m s^{-1} or more. The OpenIFS simulation initialized on 21 September shows that on 22 September the simulated 10-m wind speeds were the strongest over the Bay of Bothnia with a maximum of 22 m s^{-1} and maximum values over land were up to 14 m s^{-1} (Figs. 13b and 14c). There is a strong gradient in the simulated 10-m wind speeds across the coastline that is due to changes in surface roughness; in OpenIFS the surface aerodynamic roughness over sea depends on wave parameters and is typically of order 1×10^{-4} m whereas over land the 10-m wind speed is calculated using a surface roughness of 0.03 m (see section 2c). The high winds simulated over the northern part of the Bay of Bothnia and nearby inland areas were collocated with a strong large-scale pressure gradient (Fig. 15b). When the simulated 10-m winds from the forecast initialized on 21 September are compared to the SYNOP observations from FMI (Fig. 13b), it is apparent that OpenIFS underestimates the wind speeds. The largest underestimation is over northern Finland where observed winds are 16–24 m s^{-1} but the model simulated values are only 10–12 m s^{-1}. The large underestimation of wind speeds in OpenIFS occurs mainly over land. Coastal locations and points near Lake Inari in the far northeast of Finland have better agreement between the observations and modeled values. Moreover, the regions of strongest modeled winds (dark brown areas in Fig. 13b) correspond well to the locations of the strongest observed winds. Hence, we can conclude that while at least over land areas the model forecast underestimates the magnitude of the wind speed it can correctly predict the location of the strongest winds.

In Finland, the volume of forest damage follows approximately a power relation as a function of wind gust speed with a power of ~10 (Valta et al. 2019). Considering European scales, it has been shown that wind gusts that exceed 35 m s^{-1} cause the largest damages (e.g., Gardiner et al. 2013). Therefore, wind gusts are considered here in addition to the sustained wind speeds as it is likely that wind gusts were responsible for most of the damage. The 10-m wind gust, from the OpenIFS forecast initialized on 21 September, shows extremely high values reaching up to 31 m s^{-1} over the Bay of Bothnia at 1200 UTC and also a considerable area over northern Finland where values exceed 24 m s^{-1} (Fig. 14a). The physical reasons for the cause of

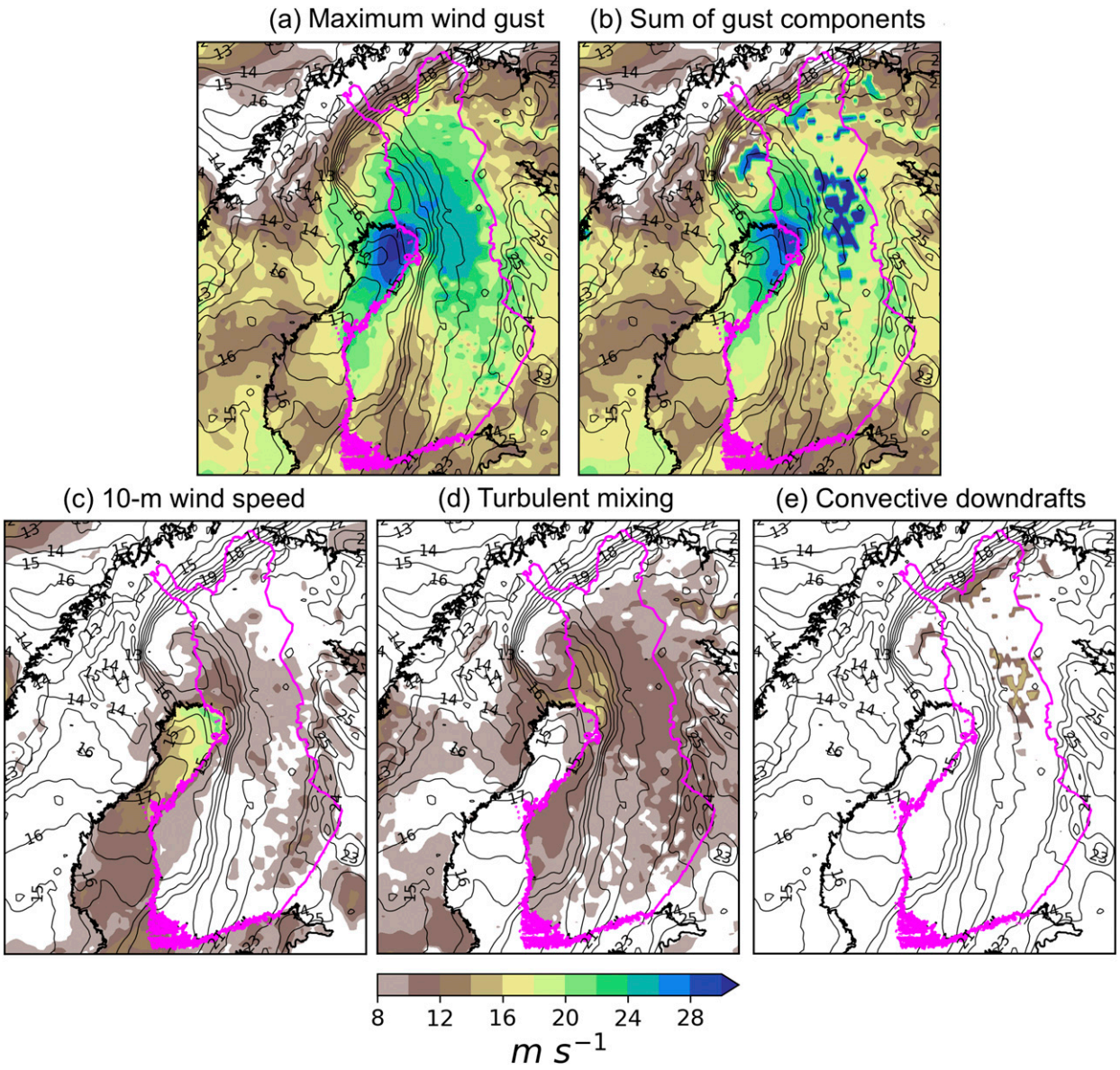

FIG. 14. OpenIFS simulation valid at 1200 UTC 22 Sep initialized on 21 Sep. (a) Maximum 10-m wind gust (colors, m s^{-1}) in the last 1 h. (b) Sum of all wind gust components in OpenIFS gust computation. (bottom) Wind gust components: (c) 10-m wind speed, (d) turbulent mixing term, and (e) convective downdrafts term. Black contours are 850-hPa potential temperature at 1°C interval. Borders of Finland are colored magenta.

these wind gusts are now examined using the wind gust parameterization [Eq. (1)] described in section 2c as a basis. This parameterization has contributions to the total wind gust from the 10-m wind speed, turbulent mixing and convective downdrafts.

With respect to the component of the total gust due to turbulent mixing, the highest values of 18 m s^{-1} at 1200 UTC were over land behind the cold front (Fig. 14d). The location of the cold front is evident from the 850-hPa potential temperature, which shows an enhanced gradient oriented north–south in western Finland (Fig. 14). The surface roughness generates more boundary layer turbulence over land than over sea and thus the turbulent gusts are larger over land. The turbulent gusts are also larger behind the cold front than ahead of it suggesting that the boundary layer is more unstable behind the cold front than ahead of it. This is supported by model soundings (vertical profiles—not shown), which confirm that there was a very steep lapse rate denoting an unstable boundary layer in the same location as the strongest turbulent driven gusts. This change in boundary layer

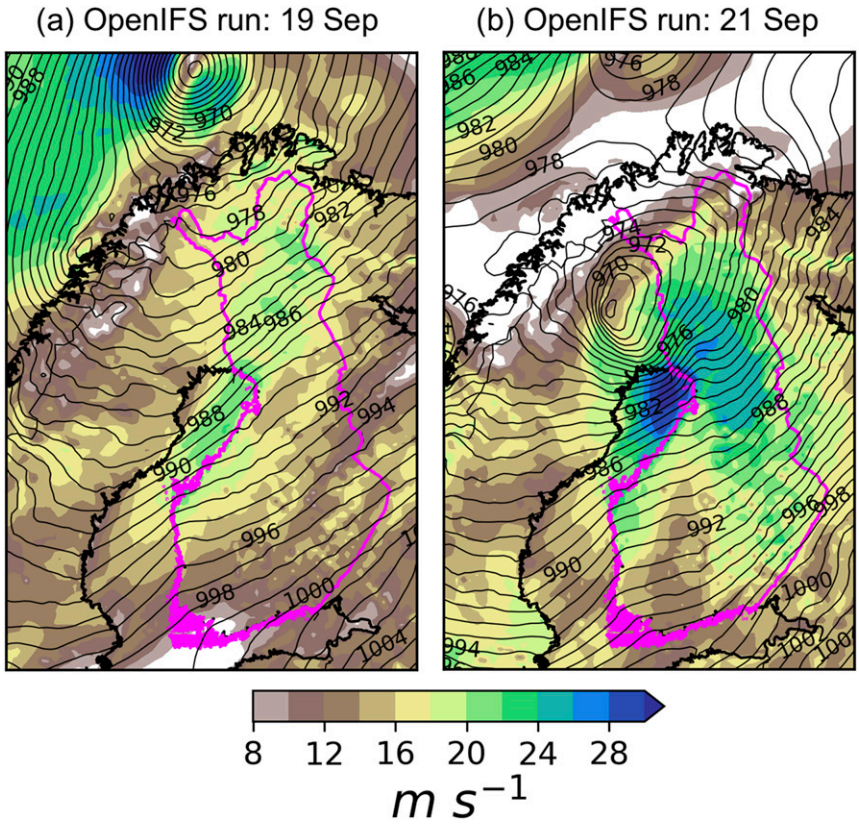

FIG. 15. Maximum 10-m wind gust (colors, $m\,s^{-1}$) during the previous hour and mean sea level pressure (contours at 1-hPa interval) at 1200 UTC 22 Sep 1982 from OpenIFS simulations initialized on (a) 19 Sep and (b) 21 Sep. Borders of Finland are colored magenta.

stability across cold fronts has been noted previously by Sinclair et al. (2010).

With respect to the 10-m wind gusts driven by convective downdrafts, the maximum values of 16 $m\,s^{-1}$ at 1200 UTC were ahead of the cold front, in the warm sector of Mauri, close to the Finnish–Russian border (Fig. 14e). In addition, there were weaker values behind the zonally extended warm front to the north. This indicates that in those regions there was strong vertical wind shear and convection present. Convective downdrafts in these regions likely induced downward mixing of high momentum air from upper levels allowing the winds reach such high values also near the surface. However, in comparison to the turbulent driven part of the 10-m wind gusts, the convective driven gusts occur in much more localized areas.

The model output gives the maximum 10-m wind gust since the previous output i.e., 1 h in this study. However, we estimated two of the three gust components from instantaneous values offline. Therefore, the sum of the three components does not exactly match with the direct model output of 10-m wind gust. By comparing Figs. 14a and 14b, we can still conclude that the patterns and magnitudes of these gusts are similar and thus the offline method can be used to identify the physical causes for the wind gusts in different regions. Three noticeable regions with elevated 10-m wind gusts were identified: 1) the Bay of Bothnia where the gusts are due to the strong large-scale pressure gradient and low surface roughness, 2) behind the cold front where turbulent mixing in an unstable boundary layer resulted in strong gusts, and 3) in the warm sector and on the warm side of the warm front where convective downdrafts likely caused the gusts.

f. What role did ex-Debby play in contributing to the strong winds?

As identified from Fig. 7, the OpenIFS forecast initialized on 21 September simulated ex-Debby to reintensify and travel to Finland whereas in the forecast initialized on 19 September ex-Debby was simulated to decay and did not travel to Fenno-Scandinavia. Therefore, by comparing these two OpenIFS forecasts, we attempt to make a first-order estimate of the possible role that ex-Debby played in the occurrence of storm Mauri and in the high winds in northern Finland.

At the time of the strongest observed winds in Finland (1200 UTC 22 September), the mean sea level pressure in both forecasts was broadly similar when only large scales are considered. Both forecasts simulated a low pressure center over the Barents Sea and a southwesterly flow over Finland (Fig. 15). However, there was one notable and critical smaller scale exception; the prominent low center of ex-Debby, which was present in the forecast initialized on 21 September was absent from MSLP pattern of the forecast from 19 September. Furthermore, there was a significant difference between the two simulations in terms of the simulated 10-m wind gust values. Although both forecasts had strong gusts, in the forecast initialized on 21 September, maximum wind gusts exceeded 31 m s^{-1} (Fig. 15b) whereas in forecast initialized on 19 September the gusts had values of up to 23 m s^{-1} (Fig. 15a). In addition, in the forecast initialized on 19 September, only a small area of land had gusts exceeding 20 m s^{-1} whereas in contrast, in the simulation from 21 September, almost all of Finland had simulated wind gusts exceeding this value (the exception being southwest inland areas). Moreover, in the forecast initialized on 21 September, there was a large area over land where the simulated wind gusts exceeded 24 m s^{-1}. In addition to wind gusts, also maximum wind speeds during 22 September were 6 m s^{-1} higher over sea and 2–4 m s^{-1} higher over land in the simulation from 21 September (Fig. 13b) compared to the one from 19 September (Fig. 13a).

Storm Mauri was a high-impact storm in Finland and almost all of the impacts (e.g., felled forest) were caused by the extreme winds. Based on the comparison of the two OpenIFS forecasts, one initialized on 19 September that did not correctly capture the evolution of ex-Debby and the other on 21 September that agrees better with reanalysis and surface wind observations, it is likely that without ex-Debby the winds observed in northern Finland on 22 September 1982 would have been weaker and hence, the impacts likely would have been smaller. Thus, we conclude that ex-Debby contributed to the damaging winds but the large-scale cyclone (merged ETC1 and ETC2), and its associated upper-level trough, played a nonnegligible role.

6. Conclusions

This study investigated the extratropical transition of Hurricane Debby and the subsequent evolution of an intense extratropical windstorm, Mauri, which occurred in Finland on 22 September 1982 and led to two fatalities and extensive forest damage. The main aims were to analyze the synoptic and dynamic evolution of Debby and Mauri and to examine the causes for the strong winds over Finland.

A brief synoptic overview based on ERA-Interim reanalysis was performed before the case was analyzed in more detail using OpenIFS model simulations that had a horizontal grid spacing of 16 km. The case proved very difficult to simulate accurately. To cover the whole evolution from Debby to Mauri, with good agreement between the model forecast and ERA-Interim reanalysis, three different simulations with initialization dates on 17, 19, and 21 September were required as all three OpenIFS forecasts diverged from reanalysis after only two days. One potential reason for this could be that there were notably fewer observations in 1982 than today and thus the initial states may be less accurate than for more recent case studies. Another likely reason is that the atmospheric state was characterized by intrinsic low predictability and was strongly sensitive to the positioning and speed of certain dynamical features.

Hurricane Debby began extratropical transition on 17 September 1982, five days before the damaging winds occurred in northern Finland. At the time of extratropical transition, the upper-level waveguide was already amplified, however the divergent outflow of Debby and negative PV advection resulted in weak ridge building and an acceleration of the jet. Previous studies have noted similar evolutions, for example, Typhoon Jangmi in the Pacific also resulted in weak ridge building and jet acceleration (Grams et al. 2013). Despite the presence of a positive PV anomaly at 200 hPa immediately to the west, Debby did not reintensify immediately in the midlatitudes. This was the first critical moment in the evolution of ex-Debby. Previous studies have indicated that subsequent development and downstream modifications can be very sensitive to the phasing between the low-level PV anomaly of the tropical cyclone and the upper-level trough/PV anomaly (Riemer et al. 2008; Riboldi et al. 2019). Thus, it is possible that a very small difference in the position of Debby or in the position, intensity or phase speed of the upper-level trough could have resulted in a very different synoptic evolution over the North Atlantic.

Ex-Debby did not decay as it moved into the midlatitudes and instead retained a strong positive PV anomaly in the lower troposphere, moved into a very moist and strongly baroclinic zone, maintained a closed pressure contour and traveled rapidly east. Using the objective criteria described by Boettcher and Wernli (2013) we determined that ex-Debby evolved into a DRW-like feature and could thus maintain itself via diabatic processes as it traveled across the Atlantic. At low levels ex-Debby had all the required characteristics of a DRW but due to the presence of some (albeit weak) upper-level forcing and a PV tower we conclude that ex-Debby differs somewhat from a classical DRW.

During 19 and 20 September as ex-Debby was propagating east as a DRW-like feature, a large-scale, intense trough became evident to the east of Greenland. Initially this feature was too far north and east of ex-Debby to provide any upper-level forcing for the reintensification of ex-Debby. However, by 21 September, this upper-level PV anomaly had moved slowly east and south and had eventually become constructively aligned with ex-Debby. Ex-Debby, which was located ahead (east) of the upper-level anomaly in a region of warm-air advection and positive vorticity advection, started rapidly intensifying near the United Kingdom on 21 September. This was the second critical point in the evolution of ex-Debby. The comparison of the OpenIFS forecasts initialized on 19 and 21 September revealed that the interaction between the upper-level trough and the low-level PV anomaly of ex-Debby was important for the reintensification of ex-Debby. In the forecast initialized on 21 September, in which ex-Debby did reintensify over the southern United Kingdom, the exact locations of ex-Debby and the upper-level PV anomaly were in a favorable position to enhance the redevelopment of ex-Debby. The subsequent development of Mauri over Finland was most likely very sensitive to this phasing that was less optimal in the forecast initialized on 19 September. Furthermore, the forecast evolution was likely also heavily dependent on the intensity and coherence of the low-level PV anomaly, which was the result of the DRW-like feature. These sensitivities were apparent in the OpenIFS forecasts with differing lead times: the strong winds over Finland only became evident with a lead time of ~2 days. To further understand the sensitivities in ex-Debby's evolution, an ensemble sensitivity analysis could be used to attain additional diagnostics.

During storm Mauri on 22 September 1982, the highest observed 10-min average 10-m wind speeds were $23\,m\,s^{-1}$ over central and northern Finland. Compared to the observations, the forecast initialized on 21 September underestimates the wind speeds although the locations of the highest values are similar. Since the damage was most likely caused by strong wind gusts, we also investigated these with the forecast from 21 September. There were three distinct regions with high wind gusts. The first was over the Bay of Bothnia and was related to the strong large-scale pressure gradient and low surface roughness. The second area was behind the cold front over land where the wind gusts were primarily related to turbulent mixing in an unstable boundary layer. The third and final area of strong gusts was in the warm sector and on the warm side of the warm front where the gusts were related to convectively driven downdrafts. By comparing these wind gusts to the forecast initialized on 19 September, in which ex-Debby did not travel to Fenno-Scandinavia, it is very likely that without ex-Debby the winds over Finland would have been weaker and that less damage would have occurred.

To conclude, this analysis has shown that storm Mauri was related to Hurricane Debby but in a complex manner: the interaction with the preexisting upper-level trough near the United Kingdom was as critical a part of Mauri's development as the occurrence of Hurricane Debby. During this critical part of the evolution of ex-Debby, the low-level PV anomaly was a small-scale feature. Such small features are particularly challenging to forecast accurately and we speculate that such anomalies, and therefore the rather unconventional way in which a damaging midlatitude windstorm Mauri evolved, may be difficult to capture in coarser-resolution models, such as climate models. This potential limitation of climate models should be considered when assessing future changes to winds and extratropical storms.

Acknowledgments. This work was supported by the Academy of Finland (Projects 303951 and 3073314), the SAFIR2018 program (The Finnish Nuclear Power Plant Safety Research Programme 2015-2018) through the EXWE project (Extreme weather and nuclear power plants), the Finnish Cultural Foundation (Satakunta Regional Fund/Aili Nurminen Fund), and by the EU through the ERA4CS Windsurfer project. We thank ECMWF for providing the ERA-Interim reanalysis and for making the OpenIFS model available for our use. We also thank the NERC Satellite Receiving Station, Dundee University, Scotland (http://www.sat.dundee.ac.uk/) for providing the AVHRR satellite images. We acknowledge Mika Rantanen for providing the code to solve the quasigeostrophic omega equation. We also thank Maxi Boettcher for providing advice concerning diabatic Rossby waves and for providing the upper-level forcing data from ERA-Interim for ex-Debby.

REFERENCES

Agustí-Panareda, A., C. D. Thorncroft, G. C. Craig, and S. L. Gray, 2004: The extratropical transition of Hurricane Irene (1999): A potential-vorticity perspective. *Quart. J. Roy. Meteor. Soc.*, **130**, 1047–1074, https://doi.org/10.1256/qj.02.140.

——, S. L. Gray, G. C. Craig, and C. Thorncroft, 2005: The extratropical transition of Tropical Cyclone Lili (1996) and its crucial contribution to a moderate extratropical development. *Mon. Wea. Rev.*, **133**, 1562–1573, https://doi.org/10.1175/MWR2935.1.

Archambault, H. M., L. F. Bosart, D. Keyser, and J. M. Cordeira, 2013: A climatological analysis of the extratropical flow response to recurving western North Pacific tropical cyclones. *Mon. Wea. Rev.*, **141**, 2325–2346, https://doi.org/10.1175/MWR-D-12-00257.1.

Bechtold, P., and J.-R. Bidlot, 2009: Parametrization of convective gusts. *ECMWF Newsletter*, No. 119, ECMWF, Reading, United Kingdom, 15–18, https://doi.org/10.21957/kfr42kfp8c.

Boettcher, M., and H. Wernli, 2011: Life cycle study of a diabatic Rossby wave as a precursor to rapid cyclogenesis in the North Atlantic—Dynamics and forecast performance. *Mon. Wea. Rev.*, **139**, 1861–1878, https://doi.org/10.1175/2011MWR3504.1.

——, and ——, 2013: A 10-yr climatology of diabatic Rossby waves in the Northern Hemisphere. *Mon. Wea. Rev.*, **141**, 1139–1154, https://doi.org/10.1175/MWR-D-12-00012.1.

Browning, K. A., P. Panagi, and G. Vaughan, 1998: Analysis of an ex-tropical cyclone after its reintensification as a warm-core extratropical cyclone. *Quart. J. Roy. Meteor. Soc.*, **124**, 2329–2356, https://doi.org/10.1002/qj.49712455108.

Clark, G. B., 1983: Atlantic hurricane season of 1982. *Mon. Wea. Rev.*, **111**, 1071–1079, https://doi.org/10.1175/1520-0493(1983)111<1071:AHSO>2.0.CO;2.

Dee, D. P., and Coauthors, 2011: The ERA-Interim reanalysis: Configuration and performance of the data assimilation system. *Quart. J. Roy. Meteor. Soc.*, **137**, 553–597, https://doi.org/10.1002/qj.828.

ECMWF, 2015: Subgrid-scale orographic drag. *IFS Documentation CY38R1*— Part IV: Physical processes, ECMWF, 57–65, https://www.ecmwf.int/node/9245.

——, 2019: Operational configurations of the ECMWF Integrated Forecasting System (IFS). ECMWF, accessed 15 May 2019, https://www.ecmwf.int/en/forecasts/documentation-and-support.

Evans, C., and Coauthors, 2017: The extratropical transition of tropical cyclones. Part I: Cyclone evolution and direct impacts. *Mon. Wea. Rev.*, **145**, 4317–4344, https://doi.org/10.1175/MWR-D-17-0027.1.

Galarneau, T. J., C. A. Davis, and M. A. Shapiro, 2013: Intensification of Hurricane Sandy (2012) through extratropical warm core seclusion. *Mon. Wea. Rev.*, **141**, 4296–4321, https://doi.org/10.1175/MWR-D-13-00181.1.

Gardiner, B., A. Schuck, M.-J. Schelhaas, C. Orazio, K. Blennow, and B. Nicoll, Eds., 2013: *Living with Storm Damage to Forests: What Science Can Tell Us 3*. European Forest Institute, 132 pp.

Grams, C. M., S. C. Jones, C. A. Davis, P. A. Harr, and M. Weissmann, 2013: The impact of Typhoon Jangmi (2008) on the midlatitude flow. Part I: Upper-level ridgebuilding and modification of the jet. *Quart. J. Roy. Meteor. Soc.*, **139**, 2148–2164, https://doi.org/10.1002/qj.2091.

Gregow, H., 2013: Impacts of strong winds, heavy snow loads and soil frost conditions on the risks to forests in Northern Europe. Ph.D. thesis, University of Eastern Finland, FMI Contributions 94, 44 pp. (with articles 178 pp.).

Hart, R. E., 2003: A cyclone phase space derived from thermal wind and thermal asymmetry. *Mon. Wea. Rev.*, **131**, 585–616, https://doi.org/10.1175/1520-0493(2003)131<0585:ACPSDF>2.0.CO;2.

——, and J. L. Evans, 2001: A climatology of the extratropical transition of Atlantic tropical cyclones. *J. Climate*, **14**, 546–564, https://doi.org/10.1175/1520-0442(2001)014<0546:ACOTET>2.0.CO;2.

Hewson, T. D., and U. Neu, 2015: Cyclones, windstorms and the IMILAST project. *Tellus*, **67A**, 27128, https://doi.org/10.3402/tellusa.v67.27128.

Hodges, K., A. Cobb, and P. L. Vidale, 2017: How well are tropical cyclones represented in reanalysis datasets? *J. Climate*, **30**, 5243–5264, https://doi.org/10.1175/JCLI-D-16-0557.1.

Holton, J. R., and G. J. Hakim, 2013: *An Introduction to Dynamic Meteorology*. 5th ed. Academic Press, 552 pp.

Hortal, M., 2002: The development and testing of a new two-time-level semi-Lagrangian scheme (SETTLS) in the ECMWF forecast model. *Quart. J. Roy. Meteor. Soc.*, **128**, 1671–1687, https://doi.org/10.1002/qj.200212858314.

Hoskins, B. J., and K. I. Hodges, 2002: New perspectives on the Northern Hemisphere winter storm tracks. *J. Atmos. Sci.*, **59**, 1041–1061, https://doi.org/10.1175/1520-0469(2002)059<1041:NPOTNH>2.0.CO;2.

——, M. E. McIntyre, and A. W. Robertson, 1985: On the use and significance of isentropic potential vorticity maps. *Quart. J. Roy. Meteor. Soc.*, **111**, 877–946, https://doi.org/10.1002/qj.49711147002.

Jokinen, P., H. Gregow, A. Venäläinen, and A. Laaksonen, 2014: Influence of resolution on storm studies. EGU General Assembly Conf. Abstracts, Vienna, Austria, European General Assembly, 16, 14299, https://www.egu2014.eu/.

Jones, S. C., and Coauthors, 2003: The extratropical transition of tropical cyclones: Forecast challenges, current understanding, and future directions. *Wea. Forecasting*, **18**, 1052–1092, https://doi.org/10.1175/1520-0434(2003)018<1052:TETOTC>2.0.CO;2.

Keller, J. H., and Coauthors, 2019: The extratropical transition of tropical cyclones. Part II: Interaction with the midlatitude flow, downstream impacts, and implications for predictability. *Mon. Wea. Rev.*, **147**, 1077–1106, https://doi.org/10.1175/MWR-D-17-0329.1.

Klein, P. M., P. A. Harr, and R. L. Elsberry, 2000: Extratropical transition of western North Pacific tropical cyclones: An overview and conceptual model of the transformation stage. *Wea. Forecasting*, **15**, 373–395, https://doi.org/10.1175/1520-0434(2000)015<0373:ETOWNP>2.0.CO;2.

Knapp, K. R., M. C. Kruk, D. H. Levinson, H. J. Diamond, and C. J. Neumann, 2010: The International Best Track Archive for Climate Stewardship (IBTrACS) unifying tropical cyclone data. *Bull. Amer. Meteor. Soc.*, **91**, 363–376, https://doi.org/10.1175/2009BAMS2755.1.

Laffineur, T., C. Claud, J.-P. Chaboureau, and G. Noer, 2014: Polar lows over the Nordic Seas: Improved representation in ERA-Interim compared to ERA-40 and the impact on downscaled simulations. *Mon. Wea. Rev.*, **142**, 2271–2289, https://doi.org/10.1175/MWR-D-13-00171.1.

Ma, S., H. Ritchie, J. Abraham, J. Gyakum, R. McTaggart-Cowan, and C. Fogarty, 2003: A study of the extratropical reintensification of former Hurricane Earl using Canadian Meteorological Centre regional analyses and ensemble forecasts. *Mon. Wea. Rev.*, **131**, 1342–1359, https://doi.org/10.1175/1520-0493(2003)131<1342:ASOTER>2.0.CO;2.

Moore, R. W., and M. T. Montgomery, 2004: Reexamining the dynamics of short-scale, diabatic Rossby waves and their role in midlatitude moist cyclogenesis. *J. Atmos. Sci.*, **61**, 754–768, https://doi.org/10.1175/1520-0469(2004)061<0754:RTDOSD>2.0.CO;2.

——, and ——, 2005: Analysis of an idealized, three-dimensional diabatic Rossby vortex: A coherent structure of the moist baroclinic atmosphere. *J. Atmos. Sci.*, **62**, 2703–2725, https://doi.org/10.1175/JAS3472.1.

——, ——, and H. C. Davies, 2008: The integral role of a diabatic Rossby vortex in a heavy snowfall event. *Mon. Wea. Rev.*, **136**, 1878–1897, https://doi.org/10.1175/2007MWR2257.1.

Palmén, E., 1958: Vertical circulation and release of kinetic energy during the development of Hurricane Hazel into an extratropical storm. *Tellus*, **10A**, 1–23, https://doi.org/10.1111/j.2153-3490.1958.tb01982.x.

Parker, D. J., and A. J. Thorpe, 1995: Conditional convective heating in a baroclinic atmosphere: A model of convective

frontogenesis. *J. Atmos. Sci.*, **52**, 1699–1711, https://doi.org/10.1175/1520-0469(1995)052<1699:CCHIAB>2.0.CO;2.

Pezza, A., K. Sadler, P. Uotila, T. Vihma, M. D. Mesquita, and P. Reid, 2016: Southern Hemisphere strong polar mesoscale cyclones in high-resolution datasets. *Climate Dyn.*, **47**, 1647–1660, https://doi.org/10.1007/s00382-015-2925-2.

Riboldi, J., C. M. Grams, M. Riemer, and H. M. Archambault, 2019: A phase locking perspective on Rossby wave amplification and atmospheric blocking downstream of recurving western North Pacific tropical cyclones. *Mon. Wea. Rev.*, **147**, 567–589, https://doi.org/10.1175/MWR-D-18-0271.1.

Riemer, M., and S. C. Jones, 2014: Interaction of a tropical cyclone with a high-amplitude, midlatitude wave pattern: Waviness analysis, trough deformation and track bifurcation. *Quart. J. Roy. Meteor. Soc.*, **140**, 1362–1376, https://doi.org/10.1002/qj.2221.

——, ——, and C. A. Davis, 2008: The impact of extratropical transition on the downstream flow: An idealized modelling study with a straight jet. *Quart. J. Roy. Meteor. Soc.*, **134**, 69–91, https://doi.org/10.1002/qj.189.

Ritchie, E. A., and R. L. Elsberry, 2007: Simulations of the extratropical transition of tropical cyclones: Phasing between the upper-level trough and tropical cyclones. *Mon. Wea. Rev.*, **135**, 862–876, https://doi.org/10.1175/MWR3303.1.

Ritchie, H., C. Temperton, A. Simmons, M. Hortal, T. Davies, D. Dent, and M. Hamrud, 1995: Implementation of the semi-Lagrangian method in a high-resolution version of the ECMWF forecast model. *Mon. Wea. Rev.*, **123**, 489–514, https://doi.org/10.1175/1520-0493(1995)123<0489:IOTSLM>2.0.CO;2.

Scheck, L., S. C. Jones, and M. Juckes, 2011: The resonant interaction of a tropical cyclone and a tropopause front in a barotropic model. Part II: Frontal waves. *J. Atmos. Sci.*, **68**, 420–429, https://doi.org/10.1175/2010JAS3483.1.

Schenkel, B. A., and R. E. Hart, 2012: An examination of tropical cyclone position, intensity, and intensity life cycle within atmospheric reanalysis datasets. *J. Climate*, **25**, 3453–3475, https://doi.org/10.1175/2011JCLI4208.1.

Shapiro, M. A., and D. A. Keyser, 1990: Fronts, jet streams and the tropopause. *Extratropical Cyclones: The Erik Palmén Memorial Volume*, C. W. Newton and E. O. Holopainen, Eds., Amer. Meteor. Soc., 167–191.

Sinclair, V. A., S. E. Belcher, and S. L. Gray, 2010: Synoptic controls on boundary-layer characteristics. *Bound.-Layer Meteor.*, **134**, 387–409, https://doi.org/10.1007/s10546-009-9455-6.

Staniforth, A., and J. Côté, 1991: Semi-Lagrangian integration schemes for atmospheric models—A review. *Mon. Wea. Rev.*, **119**, 2206–2223, https://doi.org/10.1175/1520-0493(1991)119<2206:SLISFA>2.0.CO;2.

Stewart, S. R., 2018: National Hurricane Center Tropical Cyclone Report: Hurricane Ophelia (9–15 October 2017). National Hurricane Center Rep. AL172017, 32 pp., https://www.nhc.noaa.gov/data/tcr/AL172017_Ophelia.pdf.

Sutcliffe, R. C., 1947: A contribution to the problem of development. *Quart. J. Roy. Meteor. Soc.*, **73**, 370–383, https://doi.org/10.1002/qj.49707331710.

Szépszó, G., and G. Carver, 2018: New forecast evaluation tool for OpenIFS. *ECMWF Newsletter*, No. 156, ECMWF, Reading, United Kingdom, 14–15, https://www.ecmwf.int/en/newsletter/156/news/new-forecast-evaluation-tool-openifs.

——, V. Sinclair, and G. Carver, 2019: Using the ECMWF OpenIFS model and state-of-the-art training techniques in meteorological education. *Adv. Sci. Res.*, **16**, 39–47, https://doi.org/10.5194/asr-16-39-2019.

Temperton, C., M. Hortal, and A. Simmons, 2001: A two-time-level semi-Lagrangian global spectral model. *Quart. J. Roy. Meteor. Soc.*, **127**, 111–127, https://doi.org/10.1002/qj.49712757107.

Thorncroft, C., and S. C. Jones, 2000: The extratropical transitions of Hurricanes Felix and Iris in 1995. *Mon. Wea. Rev.*, **128**, 947–972, https://doi.org/10.1175/1520-0493(2000)128<0947:TETOHF>2.0.CO;2.

Uotila, P., A. Pezza, J. Cassano, K. Keay, and A. Lynch, 2009: A comparison of low pressure system statistics derived from a high-resolution NWP output and three reanalysis products over the Southern Ocean. *J. Geophys. Res.*, **114**, D17105, https://doi.org/10.1029/2008JD011583.

Valta, H., I. Lehtonen, T. K. Laurila, A. Venäläinen, M. Laapas, and H. Gregow, 2019: Communicating the amount of windstorm induced forest damage by the maximum wind gust speed in Finland. *Adv. Sci. Res.*, **16**, 31–37, https://doi.org/10.5194/asr-16-31-2019.

Wernli, H., S. Dirren, M. A. Liniger, and M. Zillig, 2002: Dynamical aspects of the life cycle of the winter storm 'Lothar' (24–26 December 1999). *Quart. J. Roy. Meteor. Soc.*, **128**, 405–429, https://doi.org/10.1256/003590002321042036.

Zappa, G., L. C. Shaffrey, K. I. Hodges, P. G. Sansom, and D. B. Stephenson, 2013: A multimodel assessment of future projections of North Atlantic and European extratropical cyclones in the CMIP5 climate models. *J. Climate*, **26**, 5846–5862, https://doi.org/10.1175/JCLI-D-12-00573.1.

ILMATIETEEN LAITOS
METEOROLOGISKA INSTITUTET
FINNISH METEOROLOGICAL INSTITUTE

FINNISH METEOROLOGICAL INSTITUTE
Erik Palménin aukio 1
P.O. Box 503
FI-00560 HELSINKI
tel. +358 29 539 1000
WWW.FMI.FI

FINNISH METEOROLOGICAL INSTITUTE
CONTRIBUTIONS No. 181
ISSN 0782-6117
ISBN 978-952-336-155-3 (paperback)
ISBN 978-952-336-154-6 (pdf)
https://doi.org/10.35614/isbn.9789523361546

Helsinki 2022
Edita Prima Oy